QUANTUM LIQUIDS AND QUANTUM CRYSTALS

Three-phonon relaxation in isotropic and anisotropic phonon systems of liquid helium at different pressures

I. N. Adamenko*

Karazin Kharkov National University, 4 Svoboda Sq., Kharkov 61077, Ukraine; Electro-Physical Scientific and Technical Center National Academy of Sciences of Ukraine, 28 Chernyshevsky St., Kharkov 61002, Ukraine

K. E. Nemchenko and V. A. Slipko

Karazin Kharkov National University, 4 Svoboda Sq., Kharkov 61077, Ukraine

Yu. A. Kitsenko

Akhiezer Institute for Theoretical Physics National Scientific Center "Kharkov Institute of Physics and Technology" National Academy of Sciences of Ukraine 1 Academicheskaya St., Kharkov 61108, Ukraine

A. F. G. Wyatt

School of Physics, University of Exeter, Exeter, EX4 4QL, United Kingdom
(Submitted September 24; revised October 8, 2004)
Fiz. Nizk. Temp. **31**, 607–619 (June 2005)

Starting from the kinetic equation for phonons in superfluid helium, expressions for the rates of three-phonon scattering in isotropic and anisotropic phonon systems are obtained for different pressures. These expressions are valid in the whole range of energies where three-phonon processes are allowed. Limiting cases are analyzed and compared with the results of previous theoretical investigations. The obtained pressure and angular dependence of three phonon scattering rate allows one to explain the experimental data on interaction of phonon pulses. © *2005 American Institute of Physics.* [DOI: 10.1063/1.1943527]

1. INTRODUCTION

The dispersion relation of superfluid helium (He II) has an important role in determining the interactions in its phonon systems. The dispersion relation can be written as

$$\varepsilon(p)=cp(1+\psi(p)), \tag{1}$$

where ε is the phonon energy, p is its momentum, c is the sound velocity in He II, $\psi(p)\ll 1$ is the deviation of the spectrum from linearity, which is small but nevertheless completely determines the mechanisms of phonon interactions. We note that, as well as at $p=0$, there is a critical momentum p_c at which the function $\psi(p)$ is zero:

$$\psi(0)=\psi(p_c)=0. \tag{2}$$

When $p<p_c$ the function $\psi>0$ (anomalous dispersion). In this case the conservation laws of energy and momentum allow processes which do not conserve the numbers of phonons. The fastest of these processes is the three-phonon process in which one phonon decays into two or two interacting phonons combine into one phonon. This paper is devoted to the consideration of such processes.

When $p>p_c$ the function $\psi<0$. In this case the dispersion is normal and three-phonon processes are prohibited by the conservation laws of energy and momentum. Then the fastest processes are four-phonon processes.

Phonon systems can be isotropic or anisotropic, depending on whether or not there is a special direction in momentum space. Isotropic phonon systems can be easily created experimentally by heating a volume of fluid He II. These systems have been intensively investigated theoretically over several decades. Anisotropic phonon systems are a relatively new area of low-temperatures physics. In experiments they are created by a plane heater which injects a pulse of phonons into superfluid He II (see, for example, Refs. 1–3).

The stimulus for carrying out this investigation were the experiments of Refs. 4 and 5, where the interaction of phonon pulses was observed. These experiments have shown that pulses interact at pressures from 0 to 12 bar, and when the pressure is higher, for example, at 18 bar, there is no interaction. Also in these experiments the dependence of the interaction on the angle between the axes of the pulses was investigated. It was found that pulses interact strongly if the angle between their axes is 8.8°, but at 46° there is no interaction.

The purpose of this paper is to calculate the rate of three-phonon processes in isotropic and anisotropic phonon systems of superfluid helium at different pressures and to compare the results of the calculations with experimental data.[4,5]

2. THE MAIN CHARACTERISTICS OF THREE-PHONON PROCESSES

The dispersion relation (1) is very important for studying three-phonon processes. As the behavior at different pres-

 © 2005 American Institute of Physics

sures will be considered in this paper, it is necessary to take into account the pressure dependence of the parameters in expression (1).

For calculations in this paper we use a simple analytical approximation of the function ψ, which nevertheless describes all the available experimental data (see, for example, Refs. 6 and 7) rather well:

$$\psi(p,P)=4\psi_{\max}(P)\frac{p^2}{p_c^2(P)}\left(1-\frac{p^2}{p_c^2(P)}\right), \tag{3}$$

where $p_c(P)$ is the critical value of momentum, which depends on pressure P, and $\psi_{\max}(P)$ is the maximum value of the function $\psi(p,P)$, which is reached when $p=p_c/\sqrt{2}$. The expression for the function $\psi_{\max}(P)$ can be written as

$$\psi_{\max}(P)=4.551\cdot 10^{-2}-5.537\cdot 10^{-3}P+2.155\cdot 10^{-4}P^2 - 2.415\cdot 10^{-6}P^3. \tag{4}$$

Expression (4) is obtained from an analysis of Refs. 6, 8 and 9.

Expression (3) is valid in the region $p<p_c$ for any pressures up to $P=19$ bar, the pressure at which the dispersion becomes normal. To calculate the rate of three phonon processes in isotropic and anisotropic phonon systems at different pressures, it is necessary to have the dependences $c(P)$ and $\tilde{p}_c(P)=c(P)p_c(P)/k_B$, which can be written as

$$c(P)=10^2(238.3+7.33146P-0.09141P^2), \tag{5}$$

$$\tilde{p}_c(P)=10-0.20915P-0.01669P^2. \tag{6}$$

Expressions (5) and (6) are obtained from analysis of the experimental data of Ref. 10 and Refs. 7–9, 11, 12, respectively. Here and below, values of the variables are given in CGS units except that $\tilde{p}_c$ is in kelvin and pressure in bar.

We write out the dependences of the density $\rho(P)$ and the Grüneisen constant $u=(\rho/c)(\partial c/\partial\rho)$ on pressure, as they will be necessary for our further calculations:

$$\rho(P)=0.14513+0.00171P-3.7661\cdot 10^{-5}P^2+5.2994\cdot 10^{-7}P^3, \tag{7}$$

$$u(P)=2.84-0.05537P+0.00201P^2-3.24998\cdot 10^{-5}P^3. \tag{8}$$

These dependences were found from experimental data of Ref. 10 as well as expression (5).

It has long been realized that three-phonon processes cannot take place all the way to the critical momentum p_c. From the conservation laws of momentum and energy which must apply in such processes:

$$\mathbf{p}'+\mathbf{p}''=\mathbf{p}. \tag{9}$$

$$\varepsilon(p')+\varepsilon(p')=\varepsilon(p), \tag{10}$$

and also from expression (1) we obtain restrictions on the momenta of the interacting phonons. Starting from (1), (9) and (10), we calculate the angles between phonons with momenta $\mathbf{p}',\mathbf{p}''$ and $\mathbf{p},\mathbf{p}'$. As a result we have:

$$\zeta_{p'p''}=\frac{p'+p''}{p'p''}[(p'+p'')\psi(p'+p'')-p'\psi(p') - p''\psi(p'')], \tag{11}$$

$$\zeta_{pp'}=\frac{p-p'}{pp'}[p\psi(p)-p'\psi(p')-(p-p')\psi(p-p')], \tag{12}$$

where $\zeta_{p'p''}=1-\cos\theta_{p'p''}$, $\zeta_{pp'}=1-\cos\theta_{pp'}$ and $\theta_{p'p''}$, $\theta_{pp'}$ are the angles between $\mathbf{p}',\mathbf{p}''$ and $\mathbf{p},\mathbf{p}'$, respectively.

The values $\zeta_{p'p''}$ and $\zeta_{pp'}$ should be greater than or equal to zero, in order that three-phonon processes be allowed by the conservation laws (9) and (10). Having put quantities $\zeta_{p'p''}$ and $\zeta_{pp'}$ equal to zero, we obtain the boundaries of the regions in which three-phonon processes can take place.

Substituting (3) into (12) and equating the resulting expression to zero, we obtain an equation in the fourth power of $p'(p)$. Its solutions are

$$p'_{\pm}(p)=\frac{1}{2}(p\pm\sqrt{3}\sqrt{p_{\max}^2-p^2}),\quad p'(p)=p, \tag{13}$$

where

$$p_{\max}=\sqrt{\frac{4}{5}}p_c. \tag{14}$$

Only three solutions of the quartic equation are written because the solution $p'(p)=p$ is a 2-fold root.

Having equated expression (11) to zero, after substituting relation (3) in it, we have an equation of the fourth power in $p'(p'')$. The solutions of this equation are:

$$p'_{\pm}(p'')=\frac{1}{2}(-p''\pm\sqrt{3}\sqrt{p_{\max}^2-p''^2}),\quad p'(p'')=-p''. \tag{15}$$

Here the solution $p'(p'')=-p''$ is also a 2-fold root. We note that the only physical solution in this case is $p'_+(p'')$ because other solutions have one or both momenta with negative values.

Relations (13)–(15) determine the boundaries of regions where three-phonon processes are allowed. In Figs. 1a,b, based on (13) and (15), the area where three-phonon processes are allowed is shown shaded. As we have used the dimensionless variable normalized to p_c, the specified area does not depend on pressure.

From relations (13)–(15) (see Fig. 1) it follows that values of the momentum of phonons participating in three-phonon processes can vary in the ranges:

$$0<(p',p'')<\sqrt{\frac{3}{5}}p_c=p_{\min}, \tag{16}$$

$$0<p<p_{\max}. \tag{17}$$

At saturated vapor pressure we have $\tilde{p}_{\min}=7.7$ K and $\tilde{p}_{\max}=8.9$ K.

We note that $p_{\min}$ and $p_{\max}$ can be expressed in terms of the function ψ and its first derivative. From the conservation laws (9) and (10) it follows that when $p'\to p_{\min}$, $p''\to 0$. As a result of the fact that $p''\to 0$, we find from (9) that $\mathbf{p}'=\mathbf{p}$ and consequently $\zeta_{pp'}=0$. Then, taking into account that $p\to p_{\min}+p''$, we expand expression (12) as a series in p'', with the result

$$\{\psi+pd\psi/dp\}|_{p=p_{\min}}=0. \tag{18}$$

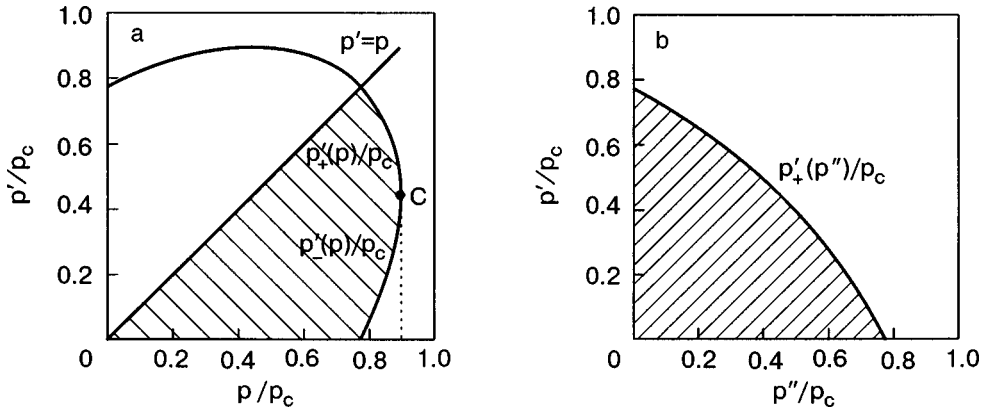

FIG. 1. The restrictions on the momenta of phonons participating in three-phonon processes. Three-phonon processes are allowed in the shaded areas.

Taking into account expression (3), we have

$$p_{\min}=\sqrt{\frac{3}{5}}p_c, \tag{19}$$

as obtained above.

The maximum value of the momentum of a phonon p which is created as a result of combining phonons p' and p'', in accordance with Ref. 13, is defined by the equality

$$\psi(p_{\max}/2)=\psi(p_{\max}), \tag{20}$$

from which, taking into account (3), we obtain relation (14).

Boundary values of the momenta of phonons participating in three-phonon processes were studied in Refs. 7 and 14–17; however, except in Ref. 16, the regions of momenta where three-phonon processes are allowed (see Fig. 1) were not obtained. In Ref. 16 an area similar to that shown in Fig. 1a was shown. Nevertheless it has some difference with Fig. 1a, apparently because a less adequate approximation to the phonon spectrum was used for the computer evaluations. In Refs. 7 and 14–17 analytical relations for the boundaries of the areas and the expression (18) for the boundary momentum of phonon p' expressed in terms of the function ψ and its first derivative were not obtained.

The probability density of three-phonon process, according to Ref. 18, can be written as

$$W(\mathbf{p}|\mathbf{p}'\mathbf{p}'')=\frac{\pi c}{p\hbar}pp'p''(u+1)^2\delta_{\mathbf{p}'+\mathbf{p}'',\mathbf{p}}. \tag{21}$$

From (21) it is clear that the probability density does not depend on the angles between the momenta of the interacting phonons as long as such processes are allowed by the conservation laws (9) and (10). It follows from (21) that the most probable process is when

$$\varepsilon'=\varepsilon''=\varepsilon/2. \tag{22}$$

Starting from relation (11), we calculate the angle between phonons with momenta $\mathbf{p}'$ and $\mathbf{p}''$ as function of p and the relation between the momenta of phonons p' and p''. For that we need the dependences of p' and p'' on p and $m=p'/p''$, which, taking into account (10), can be written, in the zeroth approximation of ψ, as

$$p'=\frac{m}{m+1}p, \tag{23}$$

$$p''=\frac{1}{m+1}p. \tag{24}$$

Substituting (3) into (11), taking into account (23) and (24), and expanding the resulting expression $\zeta_{p'p''}$ as a series in the small parameter $\theta_{p'p''}$ up to second-order terms, we get

$$\theta_{p'p''}=\sqrt{8\psi_{\max}\frac{p^2}{p_c^2}\left[3-5\frac{p^2}{p_c^2}\left(1-\frac{m}{(m+1)^2}\right)\right]}. \tag{25}$$

From (25), it follows that when the value of m is fixed, the function $\theta_{p'p''}$ reaches the maximum value

$$\theta_{p'p''}(p\approx p_{\theta\max})=3(m+1)\sqrt{\frac{2\psi_{\max}}{5(m^2+m+1)}} \tag{26}$$

at

$$p_{\theta\max}=\sqrt{\frac{3}{10}}\frac{m+1}{\sqrt{m^2+m+1}}p_c. \tag{27}$$

In accordance with (26), the function $\theta_{p'p''}$ reaches the maximum value at $m=1$, i.e., when the requirement (22) is satisfied. We note that at $m=1$

$$p_{\theta\max}=\sqrt{\frac{2}{5}}p_c \tag{28}$$

and

$$\theta_{p'p''\max}=\sqrt{\frac{24}{5}\psi_{\max}}. \tag{29}$$

In Fig. 2 we show the dependence of the relation $\theta_{p'p''}/\theta_{p'p''\max}$ on p/p_c, for different relations between the momenta of phonons p' and p'', which we get from (25). Here $\theta_{p'p''\max}$ is the maximum angle between the momenta of the phonons participating in the three-phonon process, which is defined by Eq. (29). We note that in the chosen variables, the form of this curve does not depend on pressure.

In Table I, numerical values of the angle $\theta_{p'p''\max}$ and the critical momentum $\tilde{p}_c$ are given for different pressures which correspond to the experimental conditions of Ref. 4.

It can be seen from Table I that the maximum angle of three-phonon processes decreases with increasing pressure. From (29) this can be explained as $\psi_{\max}$ decreasing with

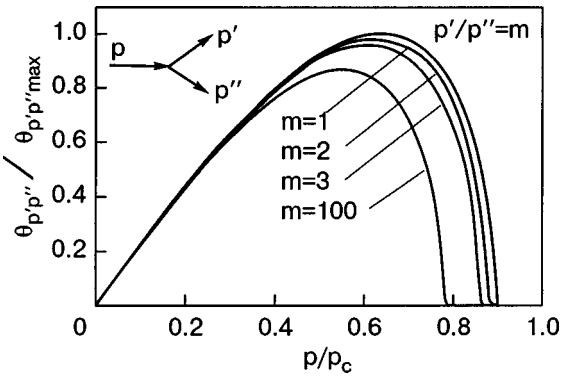

FIG. 2. The dependence of the angle $\theta_{p'p''}$ between phonons with momenta $\mathbf{p}'$ and $\mathbf{p}''$, on the momentum of the decay phonon p for different ratios of the momenta of the created phonons $m=p'/p''$.

increasing pressure. Also when the value of pressure increases, the value of p_c, which determines the maximum values of the momenta of phonons which can participate in three-phonon interactions, decreases. These two factors lead to a reduction of the volume of momentum space in which three-phonon processes are allowed by the conservation laws of energy and momentum.

3. THE RATES OF THREE-PHONON PROCESSES IN ISOTROPIC PHONON SYSTEMS

The rates of three phonon processes in isotropic phonon systems, at the saturated vapor pressure, were calculated in Ref. 18. Experiments[4] were carried out at pressures of 0, 5, 12 and 18 bar, so in this work we investigate the rates at different pressures. Besides this the expression obtained in Ref. 18 for the rate of three-phonon processes is valid only in the range $0<p<p_{\min}$. Here we shall carry out a detailed analysis of the rate of three-phonon processes in the range of momenta $p_{\min}<p<p_{\max}$ in which the rate of three-phonon processes changes from the maximum value to zero. Some results of this section were reported on International Conference Phonons 2004 (see Ref. 19) and were partly published in Ref. 20.

We follow the scheme of the Ref. 18 to calculate the rate of three phonon processes, starting from the kinetic equation:

TABLE I. The pressure dependences of the maximum angle $\theta_{p'p''\,\max}$ [see Eq. (29)] between two phonons created in a $3pp$ decay process and the critical momentum $\tilde{p}_c$ (see Eq. (6)).

P, bar	$\theta_{p'p''\max}$, deg	$\tilde{p}_c$, K
0	27	10
5	19	8.54
10	12	6.24
12	10	5.09
18	5	0.83

$$\frac{dn_1}{dt}=\frac{1}{2}\int\frac{W(\mathbf{p}_1|\mathbf{p}_2\mathbf{p}_3)}{(2\pi\hbar)^3}[n_2n_3(1+n_1)-n_1(1+n_2)(1+n_3)]\times\delta[\varepsilon(\mathbf{p}_1)-\varepsilon(\mathbf{p}_2)-\varepsilon(\mathbf{p}_3)]\delta(\mathbf{p}_1-\mathbf{p}_2-\mathbf{p}_3)d^3p_2d^3p_3+\int\frac{W(\mathbf{p}_3|\mathbf{p}_1\mathbf{p}_2)}{(2\pi\hbar)^3}[n_3(1+n_1)(1+n_2)-n_1n_2(1+n_3)]\times\delta[\varepsilon(\mathbf{p}_3)-\varepsilon(\mathbf{p}_1)-\varepsilon(\mathbf{p}_2]\delta(\mathbf{p}_3-\mathbf{p}_1-\mathbf{p}_2)d^3p_2d^3p_3, \tag{30}$$

where $n_i=n(\mathbf{p}_i)$ is the number of phonons in the given quantum state, and $W(\mathbf{p}_3|\mathbf{p}_1\mathbf{p}_2)$ is the probability density of transitions in phase space, which is defined by expression (21).

To calculate the typical rate of three-phonon processes in isotropic phonon systems, we follow Refs. 18 and substitute in Eq. (30):

$$n_1=n_{10}+\delta n,\quad n_2=n_{20},\quad n_3=n_{30}, \tag{31}$$

where the subscript "0" specifies an equilibrium distribution

$$n_0(p)=\{\exp[\varepsilon(p)/k_BT]-1\}^{-1}, \tag{32}$$

and δn is the deviation of the distribution function from equilibrium.

The typical rate of three-phonon processes ν_{3pp} is naturally defined by the equation

$$\nu_{3pp}(\mathbf{p}_1)=-\frac{1}{\delta n}\frac{d\,\delta n}{dt}. \tag{33}$$

Starting from expressions (21) and (30)–(33), we have

$$\nu_{3pp}(\mathbf{p}_1)=\frac{(u+1)^2}{4\pi\rho\hbar^4}\left\{\frac{1}{2}J_1(\mathbf{p}_1)+J_2(\mathbf{p}_1)\right\}, \tag{34}$$

where

$$J_1(\mathbf{p}_1)=\frac{cp_1}{n_{10}}\int_0^{p_1}dp_2\int_0^2d\zeta_{12}p_2^3|\mathbf{p}_1-\mathbf{p}_2|n_0(p_2)n_0(p_1-p_2)\times\delta(\varepsilon(p_1)-\varepsilon(p_2)-\varepsilon(|\mathbf{p}_1-\mathbf{p}_2|)), \tag{35}$$

$$J_2(\mathbf{p}_1)=cp_1\int_{p_1}^{p_{\max}}dp_3\int_0^2d\zeta_{13}p_3^3|\mathbf{p}_3-\mathbf{p}_1|\{n_0(p_3-p_1)-n_0(p_3)\}\delta[\varepsilon(p_3)-\varepsilon(p_1)-\varepsilon(|\mathbf{p}_3-\mathbf{p}_1|)]. \tag{36}$$

Here

$$\zeta_{12}=1-\frac{\mathbf{p}_1\mathbf{p}_2}{p_1p_2}, \tag{37}$$

$$\zeta_{13}=1-\frac{\mathbf{p}_1\mathbf{p}_3}{p_1p_3}. \tag{38}$$

Doing the integration on ζ_{12} and ζ_{13} with the help of the δ functions in Eqs. (35) and (36), we obtain for $\nu_{3pp}(\mathbf{p}_1)$ from (34) the following relation:

$$\nu_{3pp}(\tilde{p}_1)=\frac{(u+1)^2}{4\pi\rho\hbar^4}\left(\frac{k_B}{c}\right)^5\left\{\frac{1}{2}\xi(\tilde{p}_1)+\beta(\tilde{p}_1)\right\}, \tag{39}$$

where $\tilde{p}_i=cp_i/k_B$,

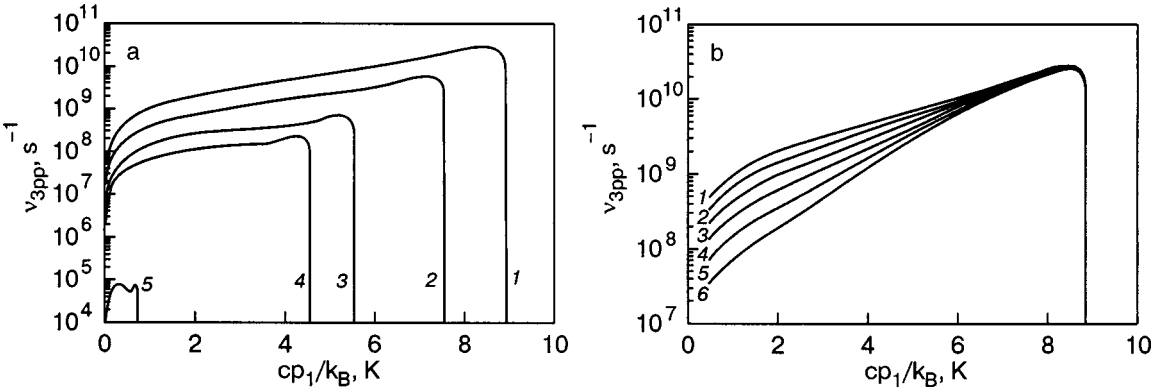

FIG. 3. The dependence of the relaxation rate in isotropic phonon systems ν_{3pp} on momentum p_1. In panel (a) curves *1–5* are for pressures 0, 5, 10, 12, 18 bar, respectively, at $T=1$ K. In panel (b) curves *1–6* are for temperatures 1, 0.9, 0.8, 0.7, 0.6, 0.5 K, respectively, at the saturated vapor pressure.

$$\xi(\tilde{p}_1)=\int_0^{\tilde{p}_1} d\tilde{p}_2\tilde{p}_2^2(\tilde{p}_1-\tilde{p}_2)^2(1+2\tilde{n}_0(\tilde{p}_2))\,\eta(\zeta(\tilde{p}_1,\tilde{p}_2)), \tag{40}$$

$$\beta(\tilde{p}_1)=\int_{\tilde{p}_1}^{\tilde{p}_{\max}} d\tilde{p}_3\tilde{p}_3^2(\tilde{p}_3-\tilde{p}_1)^2\{\tilde{n}_0(\tilde{p}_3-\tilde{p}_1)-\tilde{n}_0(\tilde{p}_3)\}\,\eta(\zeta(\tilde{p}_3,\tilde{p}_1)). \tag{41}$$

Here

$$\tilde{n}_0(\tilde{p})=[\exp(\tilde{p}/T)-1]^{-1}, \tag{42}$$

$$\zeta(\tilde{p}_i,\tilde{p}_j)=\frac{\tilde{p}_i-\tilde{p}_j}{\tilde{p}_i\tilde{p}_j}(\tilde{p}_i\psi(k_B\tilde{p}_i/c)-\tilde{p}_j\psi(k_B\tilde{p}_j/c)-(\tilde{p}_i-\tilde{p}_j)\psi(k_B(\tilde{p}_i-\tilde{p}_j)/c)) \tag{43}$$

and

$$\eta(x)=\begin{cases}1, & x\geqslant 0,\\ 0, & x<0.\end{cases} \tag{44}$$

Expression (39), together with (40)–(44), completely determines the typical rate of three-phonon relaxation in isotropic phonon systems. We underline the fact that the final result (39) contains parameters that describe the nonlinearity of the phonon spectrum of He II. Mathematically this fact is expressed by the appearance of η functions which restrict the integration range. The rates represented in Ref. 18 do not contain these η functions. We note that these η functions cause the rapid decrease of the rates near the boundary momentum $p_{\max}$.

Starting from expression (39), we get an analytical expression for rate of a three-phonon scattering in the case $p_{\min}<p_1<p_{\max}$. When $p_1>p_{\min}$ the term $\beta(\tilde{p}_1)$ is equal to zero because phonons with momentum $p_1>p_{\min}$ cannot participate in combining processes (see Fig. 1b). In this case expression (39) will have only the first term $\xi(\tilde{p}_1)$, which is defined by expression (40). It corresponds to the decay of a phonon with momentum p_1. We note that the term $\xi(\tilde{p}_1)$ describes the stimulated decay of a phonon with momentum p_1 which corresponds to the term with the Bose function, in the brackets of the integrand of (40), and spontaneous decay of a phonon with momentum p_1 which corresponds to the first term, unity, in the brackets. In our case $p_{\min}<p_1<p_{\max}$ we do not take into account stimulated decay, because its rate is much smaller than the rate of spontaneous decay. If the momentum of one of the phonons created as a result of decay is small, then the contribution of such decay processes in expression (40) is small, too. Also when the momenta of both phonons are significant, the term with the Bose function is much smaller than unity. As a result, we can neglect the term that contains the Bose function in the brackets of the integrand (40). On integrating we have:

$$\nu_{3pp}=\frac{(u+1)^2}{240\pi\rho\hbar^4}\sqrt{3}\sqrt{p_{\max}^2-p_1^2}(9p_1^4-14p_1^2p_{\min}^2+6p_{\min}^4), \tag{45}$$

Expression (45), in the range $p_1\to p_{\max}$, decreases rapidly and goes to zero at $p_1=p_{\max}$ due to the radicand going to zero. The expression in the brackets increases but tends to a finite value equal to $1.2p_c^4$. As a result, the rate decreases from a maximum to zero in a small range of momenta (see Fig. 3). The change of the rate is determined by a competition between the expression under square root, which decreases as $p_1\to p_{\max}$, and the factor in the brackets. As a result of the competition, expression (45) reaches a maximum value at $p_1\approx 0.84p_c$, and at $p_1\approx 0.89p_c$ it is equal to zero. Therefore the rate changes from the maximum value to zero in a small momentum range.

We now consider the typical time of three-phonon processes. Equation (39) can be interpreted as the reciprocal lifetime of a phonon with momentum p_1 in an equilibrium field of thermal phonons with temperature T. Let us consider the limiting cases which follow from Eq. (39). First, we consider the hypersound limit, when $\tilde{p}_1/T\gg 1$. Thus

$$\beta(\tilde{p}_1)\approx 0 \tag{46}$$

and

$$\xi(\tilde{p}_1)\approx\int_0^{\tilde{p}_1} d\tilde{p}_2\tilde{p}_2^2(\tilde{p}_1-\tilde{p}_2)^2=\frac{\tilde{p}_1^5}{30}. \tag{47}$$

Substitution of relations (46) and (47) in (39) gives

$$\nu_{3pp}^{(\infty)}(p_1)=\frac{(u+1)^2}{240\pi\rho\hbar^4}p_1^5. \tag{48}$$

This expression was obtained in Ref. 21 for the first time. From relations (46) and (47) it is clear that this limiting case corresponds only to decay processes as $\mathbf{p}_1 \rightarrow \mathbf{p}_2 + \mathbf{p}_3$. It is should be noted that formula (48) has actually a rather restricted area of application. This is because two requirements must be satisfied: $\tilde{p}_1/T \gg 1$ and $\tilde{p}_1 < \tilde{p}_{\min}$; therefore it can be used for numerical evaluations for pressures up to 12 bar at temperatures up to 1 K, and at lower pressures if the temperature is higher.

The other limiting case is $\tilde{p}_1/T \ll 1$, corresponding to the absorption of acoustic sound waves by an equilibrium phonon field with temperature T. In this case

$$\xi(\tilde{p}_1) \approx 0 \tag{49}$$

and

$$\beta(\tilde{p}_1) \approx \frac{\tilde{p}_1}{T} \int_0^\infty \frac{\tilde{p}_3^4 \exp(\tilde{p}_3/T)}{(\exp(\tilde{p}_3/T)-1)^2}\, d\tilde{p}_3 = T^4 \frac{4\pi^4}{15} \tilde{p}_1. \tag{50}$$

Substituting (49) and (50) into (39), we have

$$\nu_{3pp}^{(0)}(p_1) = \frac{\pi^3 (u+1)^2}{15\rho\hbar^4} \left(\frac{k_B}{c}\right)^4 T^4 p_1, \tag{51}$$

and thus we come to the result obtained in Refs. 22 and 23. We note that in expression (50) we replace $\tilde{p}_{\max}$ by ∞. Such a replacement can be made when $\tilde{p}_{\max}/T \gg 1$. There was no such requirement in Ref. 18 because the condition is always satisfied at the saturated vapor pressure. However, with increasing pressure it starts to play an important role and restricts the area of applicability of expression (51).

In contrast to the process of decay of high-energy phonons [see (48)], mentioned above, the limiting case (51), which follows from relations (49), (50), corresponds only to combining processes such as $\mathbf{p}_1 + \mathbf{p}_2 \rightarrow \mathbf{p}_3$. Equation (51) has been used many times for the description of various relaxation processes in pure He II and also in superfluid mixtures of ^{3}He-^{4}He (see Ref. 24).

It is important to note that equation (39), with dependences (3)–(8) taken into account, is valid for any pressure at which the dispersion is anomalous. In Fig. 3, rates for three-phonon processes are shown for different pressures and temperatures. In Fig. 3a it can be seen that with increasing pressure, the rate begins to decrease. This is caused by the decreasing of value p_c, and by the change in the parameters u, ρ, and c of superfluid helium. As pressure increases from 0 up to 12, at fixed value of p_c, the rates decrease by approximately 5 times, and as the pressure is further increased up to 18, the rate decreases by approximately 2 times. Another cause of decreasing rates with increasing pressure is the decreasing momentum range in which three-phonon processes are allowed. This is due to the decreasing value of p_c, which leads to a reduction of the phase volume in the integration.

We note that the decreasing of the rates, which is connected with the decreasing of p_c, has a strong temperature dependence: at temperatures $T \sim 1$ K, the decrease of p_c with growth of pressure from 0 to 12 bar, at fixed parameters u, ρ, and c, leads to the rates decreasing by up to 2 times, and for a further increase of pressure to 18 bar, the rate decreases up to 300 times. At temperatures $T < 0.1$ K, the decreasing of p_c with growth of pressure from 0 to 18 bar does not affect the rates of three-phonon relaxation, which in this case are influenced only by the change in the parameters of liquid helium. Such a temperature dependence can be explained by presence of the Bose-Einstein functions which contain the expression $\exp(\tilde{p}/T)$ in the integrands.

The temperature dependence of the rate, ν_{3pp}, in the limiting cases (48) and (51), as one can see in Fig. 3b, is as follows: at small values of p_1, $\nu_{3pp} \approx T^4$, and at large values of p_1, ν_{3pp} has practically no temperature dependence.

4. PHONON DISTRIBUTION FUNCTION OF AN ANISOTROPIC PHONON SYSTEM

Systems with an anisotropic distribution of phonons in momentum space are created in experiments (see, for example, Refs. 1–5) using a heater immersed in superfluid helium ^{4}He, which is at such a low temperature that the effect of thermal excitations can be neglected. The heater is a metal film evaporated onto glass. When current flows through the metal film, phonons are created in the superfluid helium within a narrow cone with a solid angle $\Omega_p \ll 1$ and with an axis perpendicular to the surface of the heater. The dimensions in coordinate space of this strongly anisotropic phonon system are defined by the area of the heater and the duration of the thermal pulse.

Such anisotropic phonon systems can be described with a help of approximate quasi-equilibrium distribution function (see, for example, Refs. 25–28), which can be written as

$$n_p(\mathbf{p}) = \eta(\theta_p - \theta)[\exp(\varepsilon/k_B T_p) - 1]^{-1}. \tag{52}$$

This distribution function has simple physical meaning and includes all the necessary parameters of anisotropic phonon systems: the temperature T_p and the value of anisotropy given by the angle θ_p. The approximation (52) has allowed the successful solution of a number of problems.[20,25–28]

However, this function does not make the three-phonon collision integral equal to zero. The exact equilibrium distribution function of phonons in anisotropic phonon systems, in accordance with Ref. 29, is

$$n_u(\mathbf{p}) = \left\{ \exp\left(\frac{\varepsilon - \mathbf{p}\cdot\mathbf{u}}{k_B T} \right) - 1 \right\}^{-1}, \tag{53}$$

where

$$\mathbf{u} = \mathbf{N} c (1 - \chi), \tag{54}$$

is the drift velocity, $\mathbf{N}$ is the unit vector directed along the total momentum of the phonon system, which defines the axis of anisotropy of phonon system, and χ is the parameter of anisotropy. It is obvious that function (53) makes the three-phonon collision integral equal to zero. In order to derive the further results we use exact equilibrium distribution function (53).

In a weakly anisotropic case the parameter χ is close to unity. In our case, which corresponds to the experiments of Refs. 4 and 5, the phonon pulses are strongly anisotropic phonon systems, and $\chi \ll 1$.

The expression (53), taking into account (1) and (54), can be written as

$$n_u(p,\zeta)=\left\{\exp\left(\frac{cp}{k_BT}(\psi+\chi+\zeta-\zeta\chi)\right)-1\right\}^{-1}, \qquad (55)$$

where $\zeta=1-\mathbf{p}\cdot\mathbf{N}/p$.

The values of the parameter of anisotropy χ and temperature T, which are contained in the distribution function (55), can be related to the values of the parameters θ_p and T_p of the approximate distribution functions (52), which have a clear physical meaning. Starting from the equality of energies and momenta of anisotropic phonon systems, calculated with the help of distribution functions (52) and (55), we have a system of two equations which connects the parameters θ_p and T_p with the parameters χ and T:

$$\int \varepsilon n_p d^3p=\int \varepsilon n_u d^3p, \qquad (56)$$

$$\int \mathbf{p} n_p d^3p=\int \mathbf{p} n_u d^3p. \qquad (57)$$

This system can be solved numerically, relating the parameters χ and T, to values of the parameters $\zeta_p=1-\cos\theta_p$ and T_p. In the following calculations we always use the relation

$$\zeta_p=\psi_{\max}/2, \qquad (58)$$

which is a good approximation to the real situation and represents a pressure dependence of ζ_p. Values of parameters χ and T which correspond to parameters ζ_p and T_p can be obtained by solving the combined equations (56), (57). These values will be used in our further calculations and are presented in Table II. We note that the choice of pressures in this paper corresponds to the choice of pressures in the experiments of Ref. 4.

The value $\langle\tilde{p}\rangle$ given in Table II corresponds to the average momentum of phonons in a pulse and is determined by the expression

$$\langle\tilde{p}\rangle=\frac{\int\tilde{p}n_u d^3p}{\int n_u d^3p} \qquad (59)$$

and θ_{eff} is an angle between the two interacting phonons with momenta $\langle\tilde{p}\rangle$ which is defined by conservation laws of energy and momentum.

TABLE II. The relation between parameters ζ_p, T_p of the approximate distribution function (51) and the parameters χ, T of the local equilibrium distribution function (54) at different pressures. The dependence of the average momentum $\langle\tilde{p}\rangle$ on the parameters χ, T and the angle θ_{eff} at which two phonons combine with momenta $\langle\tilde{p}\rangle$.

P, bar	ζ_p	T_p, K	χ	T, K	$\langle\tilde{p}\rangle$, K	θ_{eff}, deg
0	0.023	0.5	0.019	0.016	0.934	11
		0.6	0.020	0.021	1.075	13
		0.7	0.019	0.025	1.207	14
		0.8	0.020	0.030	1.317	15
		0.9	0.020	0.036	1.462	17
		1	0.020	0.041	1.581	18
5	0.011	0.5	0.0093	0.0084	0.906	9
		0.6	0.013	0.012	0.992	10
		0.7	0.010	0.014	1.183	11
		0.8	0.010	0.016	1.28	12
		0.9	0.010	0.019	1.424	13
		1	0.010	0.022	1.569	14
10	0.0046	0.5	0.0043	0.0041	0.835	7
		0.6	0.0044	0.0053	0.964	8
		0.7	0.0045	0.0064	1.085	9
		0.8	0.0044	0.0076	1.232	10
		0.9	0.0043	0.0086	1.361	10
		1	0.0041	0.0095	1.492	11
12	0.003	0.5	0.0029	0.0029	0.788	6
		0.6	0.0029	0.0037	0.919	7
		0.7	0.0028	0.0044	1.074	8
		0.8	0.0027	0.0050	1.208	9
		0.9	0.0025	0.0056	1.349	9
		1	0.0024	0.0060	1.442	10
18	0.00079	0.5	0.00018	0.00057	0.368	5
		0.6	0.000092	0.00062	0.403	5
		0.7	0.000037	0.00066	0.429	5
		0.8	0.000011	0.00071	0.455	4
		0.9	0.0000034	0.00078	0.484	4
		1	0.0000022	0.00084	0.506	3

5. RELAXATION IN ANISOTROPIC PHONON SYSTEMS, CAUSED BY THREE-PHONON PROCESSES

The expression for the rate of three-phonon processes in anisotropic phonon systems can be obtained from the kinetic equation (30) in a way similar to obtaining expression (39) for the rate of three-phonon processes in isotropic phonon systems:

$$\nu_{3pp}(\tilde{p}_1,\zeta_1)=\frac{(u+1)^2}{4\pi\rho\hbar^4}\left(\frac{k_B}{c}\right)^5\left\{\frac{1}{2}\xi_a(\tilde{p}_1,\zeta_1)+\beta_a(\tilde{p}_1,\zeta_1)\right\}, \qquad (60)$$

where

$$\xi_a(\tilde{p}_1,\zeta_1)=\int_0^{\tilde{p}_1}d\tilde{p}_2\tilde{p}_2^2(\tilde{p}_1-\tilde{p}_2)^2\eta(\zeta(\tilde{p}_1,\tilde{p}_2))\times\left(1+\frac{2}{\pi}\int_{\zeta_{1,2-}}^{\zeta_{1,2+}}d\zeta_2 n_u(k_B\tilde{p}_2/c,\zeta_2)\{(\zeta_{1,2+}-\zeta_2)\times(\zeta_2-\zeta_{1,2-})\}^{-1/2}\right), \qquad (61)$$

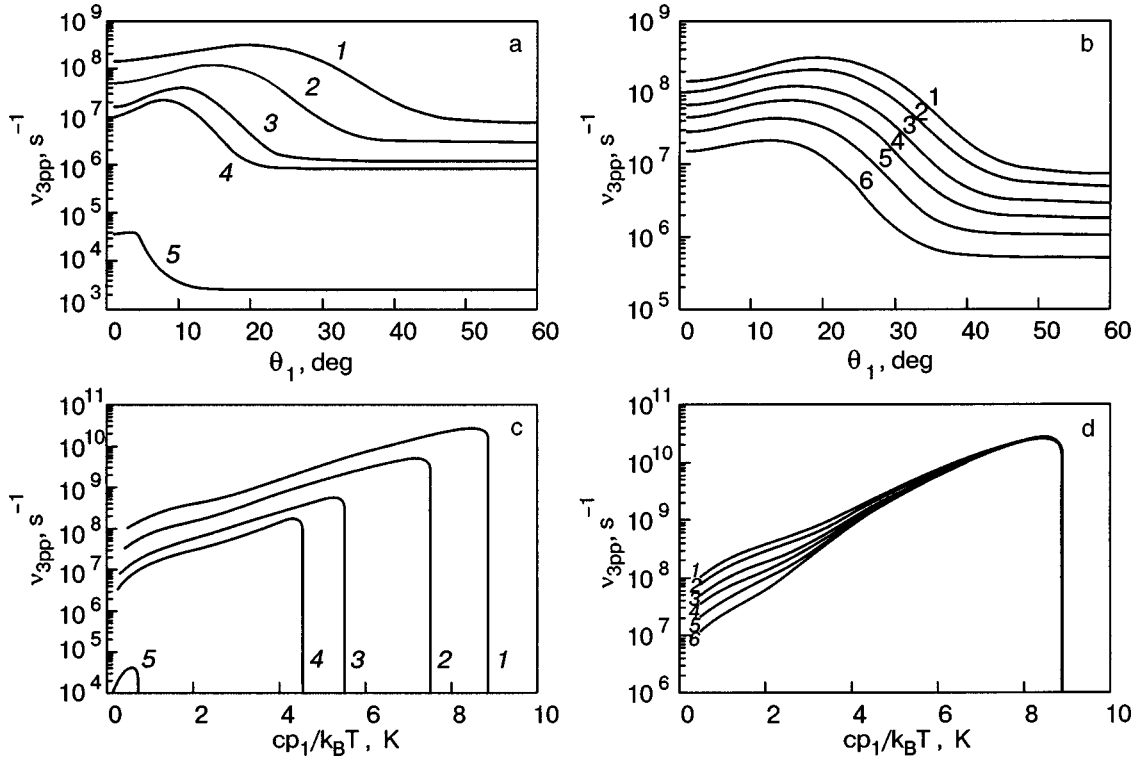

FIG. 4. The relaxation rates ν_{3pp} in anisotropic phonon systems. Panel (a) presents the dependence of ν_{3pp} on θ_1 at different pressures. Curves *1–5* are for pressures 0, 5, 10, 12, and 18 bar, respectively, at $T_p=1$ K and values of ζ_p which were defined from Eq. (57) (see Table II). The momentum $\tilde{p}_1$ was considered to be equal to the average value of the momentum $\langle\tilde{p}\rangle$ of the phonons in a pulse. Panel (b) shows the dependence of ν_{3pp} on θ_1 at different temperatures. Curves *1–6* are for temperatures of 1, 0.9, 0.8, 0.7, 0.6, and 0.5 K, respectively, at the saturated vapor pressure and when $\tilde{p}_1=\langle\tilde{p}\rangle$ (see Table II) at $\zeta_p=0.023$. Panels (c) and (d) show the dependence of ν_{3pp} on $\tilde{p}_1$, at the angle corresponding to the maximum of the curves in panels (a) and (b). The value of ζ_p was defined from equality (57). Panel (c) shows the effect of different pressures (0, 5, 10, 12, and 18 bar) at $T_p=1$ K and panel (d) shows the effect of different temperatures (1, 0.9, 0.8, 0.7, 0.6, 0.5 K) at the saturated vapor pressure.

$$\beta_a(\tilde{p}_1,\zeta_1)=\int_{\tilde{p}_1}^{\tilde{p}_{\max}} d\tilde{p}_3\tilde{p}_3^2(\tilde{p}_3-\tilde{p}_1)^2\,\eta(\zeta(\tilde{p}_3,\tilde{p}_1))(\beta_2-\beta_3). \tag{62}$$

Here $\zeta_i=1-\mathbf{p}\cdot\mathbf{N}/p_i$,

$$\beta_2=\frac{1}{\pi}\int_{\zeta_{1,(3,1)-}}^{\zeta_{1,(3-1)+}} d\zeta_2\frac{n_u(k_B(\tilde{p}_3-\tilde{p}_1)/c,\zeta_2)}{\sqrt{(\zeta_{1,(3-1)+}-\zeta_2)(\zeta_2-\zeta_{1,(3-1)-})}}, \tag{63}$$

$$\beta_3=\frac{1}{\pi}\int_{\zeta_{3,1-}}^{\zeta_{3,1+}} d\zeta_3\frac{n_u(k_B\tilde{p}_3/c,\zeta_3)}{\sqrt{(\zeta_{3,1+}-\zeta_3)(\zeta_3-\zeta_{3,1-})}}, \tag{64}$$

$$\zeta_{i,j\pm}=\zeta_1+\zeta(\tilde{p}_1,\tilde{p}_j)-\zeta_1\zeta(\tilde{p}_i,\tilde{p}_j) \pm\sqrt{(2\zeta_1-\zeta_1^2)[2\zeta(\tilde{p}_i,\tilde{p}_j)-\zeta^2(\tilde{p}_i,\tilde{p}_j)]}, \tag{65}$$

and $\zeta(\tilde{p}_i,\tilde{p}_j)$ is defined by relation (43).

As in the isotropic case, the first term in expression (60) corresponds to the decay of a phonon with momentum $\mathbf{p}_1$, and the second to the combining of a phonon with momentum $\mathbf{p}_1$ with phonons of the anisotropic phonon system. The relation for the rate of three-phonon processes in the anisotropic case differs from the isotropic case only by the dependence of phonon distribution function on the angle ζ. As a consequence, the integration cannot now be done analytically. We note that if we substitute the distribution function (55) with the distribution function of phonons in the isotropic phonon system (32) in expression (60), then the integration over angles can be done, and expression (60) for the rates of three-phonon processes in anisotropic phonon systems will turn into expression (39).

Figures can be obtained with the help of expression (60). Figure 4a shows the dependence of the relaxation rate of a phonon with momentum $\mathbf{p}_1$ in anisotropic phonon systems on the angle θ_1 between the axis of anisotropy of phonon system $\mathbf{N}$ and the phonon momentum $\mathbf{p}_1$ at $T_p=1$ K and different pressures. Values of ζ_p corresponding to different pressures are calculated with the help of relation (58) (see Table II). The phonon momentum p_1 is considered to be equal to the average momentum of phonons in a pulse $\langle p\rangle$. It follows from Fig. 4a that the rates of three-phonon processes decrease with increasing pressure. This has the same cause as for the isotropic case. We note that with the growth of angle θ_1 the rate ν_{3pp} increases, reaching a maximum value, and then decreases and ceases to depend on an angle. In order to understand such angular dependence of the rates we turn to Fig. 5. In Fig. 5, curve *1+2* is the same as curve *1* in Fig. 4a. It is the sum of curves *1* and *2*, which correspond to the first and the second terms of expression (60), respectively. Curve *1* in Fig. 5 corresponds to the decay of a phonon with momentum $\mathbf{p}_1$, and curve *2*, to the combining of a phonon with momentum $\mathbf{p}_1$ with a phonon of the anisotropic phonon system. The increase in the rates, which is represented by curve *1* at small values of angle, is caused by stimulated decay of a phonon with momentum $\mathbf{p}_1$ due to the presence of the aniso-

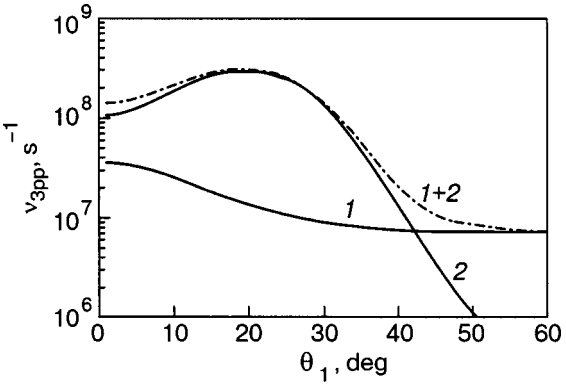

FIG. 5. The dependence of the three-phonon process rate on the angle between the axis of anisotropy and the momentum of the relaxing phonon $\tilde{p}_1=\langle\tilde{p}\rangle$ at $P=0$ bar, $T_p=1$ K, and $\zeta_p=0.023$. Curve *1* shows the rate of decay of a phonon with momentum $\mathbf{p}_1$, curve *2* shows the rate of combining of a phonon with momentum $\mathbf{p}_1$ with a phonon of the anisotropic phonon system, curve *1+2* is the sum of curves *1* and *2* and corresponds to the full relaxation rate of a phonon with momentum $\mathbf{p}_1$ in the anisotropic phonon system.

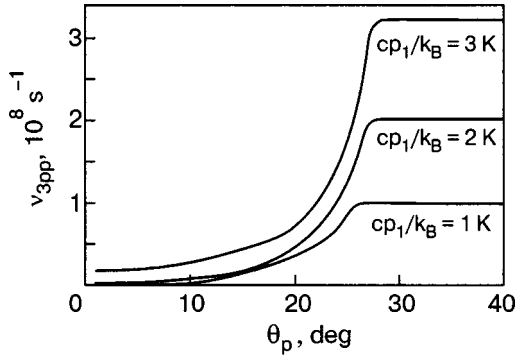

FIG. 6. The dependence of the rate ν_{3pp} on the angle θ_p occupied by the anisotropic phonon system in momentum space for different values of $\tilde{p}_1$ at $T=1$ K and $P=0$ bar.

tropic phonon system. At greater values of the angle between phonon momentum and the axis of anisotropy, the phonon ceases ''to feel'' the presence of the anisotropic phonon system, and as a result there is no angular dependence. In this case the rate of decay corresponds to the rate of spontaneous decay of a phonon. The maximum of curve *2* can be explained in the following way. We replace the anisotropic phonon system by a monochromatic phonon pulse which moves along the z axis. Then the average momentum of phonons in such pulse is equal to 1.581 K (see Table II). We calculate the interaction angle of such phonons and see from Table II that $\theta_{\text{eff}}=18°$. This is in good agreement with the location of the maximum in Fig. 4a. The locations of the maxima of the other curves in Fig. 4a can be calculated in a similar way and they are given in Table II. Figure 4b shows the effect of different temperatures at the saturated vapor pressure and $\zeta_p=0.023$. The curves in this case have an angular dependence which is similar to that shown in Fig. 4a. The locations of the maxima in this case are also given in Table II. Figures 4c and 4d show the dependence of the rate ν_{3pp} on momentum p_1 at $\theta_1=\theta_{\text{eff}}(P,T)$ at different pressures and temperatures. The value of ζ_p was defined by expression (58) (see Table II). We note that the dependences represented in Fig. 4c and 4d look like the dependences of the rates on momentum p_1 for relaxation in isotropic systems. However, in this case the rates are smaller.

The dependence of the rate of three-phonon processes on the value of anisotropy of phonon system can be obtained by calculating the rate of three-phonon processes in anisotropic phonon systems with the distribution function (52) instead of (53). Calculating the rates in this way makes it possible to see the transition from anisotropic phonon system to isotropic. This transition is shown in Fig. 6, where θ_p is the typical angle that the anisotropic phonon system occupies in momentum space. When the angle is zero, there is no anisotropic phonon system. In this case this rate corresponds to the rate of decay of a phonon with momentum p_1 originally obtained in Ref. 21. As the angle increases, the rate begins to increase, reaching the isotropic value when $\theta_p\approx 27°$. Such a result is connected with the fact that phonons can interact with each other if the angle between their momenta does not exceed the maximum angle for three-phonon processes. In this case the value of this angle equals 27°.

6. COMPARISON OF THE THEORY WITH EXPERIMENTAL DATA ON INTERACTION OF PHONON PULSES

In the experiments of Refs. 4 and 5 the interaction of two phonon pulses was studied. In this connection the problem of calculating of the rate of their interaction is of undoubted interest. The calculation of these rates is based on the above solution of the problem of one phonon relaxing in an anisotropic phonon system. In Fig. 7 the dependence of the rate of such an interaction on the angle between the axes of anisotropy of the phonon systems is shown. This angle is shown in the inset in the right upper corner of Fig. 7a (anisotropic phonon systems are represented by cones). This rate was obtained from relation (60) in the following way: the value of the relaxing phonon momentum was considered to be equal to the average value of the momentum of phonons in a pulse, and the averaging over angle was done in order to take into account that actually we are dealing not with one phonon but with an anisotropic phonon system. To average over angles, we took three values of the rate at values of angle $\theta_{\mathbf{uu}'}-\theta_p$, $\theta_{\mathbf{uu}'}$, $\theta_{\mathbf{uu}'}+\theta_p$ and calculated their simple average value. We note that such an approach does not take into account spontaneous decays of a phonon with momentum $\mathbf{p}_1$, because anisotropic phonon systems by themselves are in equilibrium. However, it is necessary to take into account the decay stimulated by the anisotropic phonon system, which, as follows from our calculations (see Fig. 5), gives a small contribution compared to phonon-combining processes.

Phonon pulses have enough time to interact if the time to cross the region where the two sheets overlap, τ_{cross}, is greater than the phonon relaxation time ν_{3pp}^{-1}. The expression for τ_{cross}, according to Ref. 29, can be written as

$$\tau_{\text{cross}}=t_p(2\sin^2(\theta_{\mathbf{uu}'}/2))^{-1}, \tag{66}$$

where t_p is the duration of the thermal pulse that creates the phonon pulse. In this case in the volume where the pulses intersect there is enough time for three-phonon processes to occur and create a new formation, which, following the terminology of Ref. 5, we call a hot line.

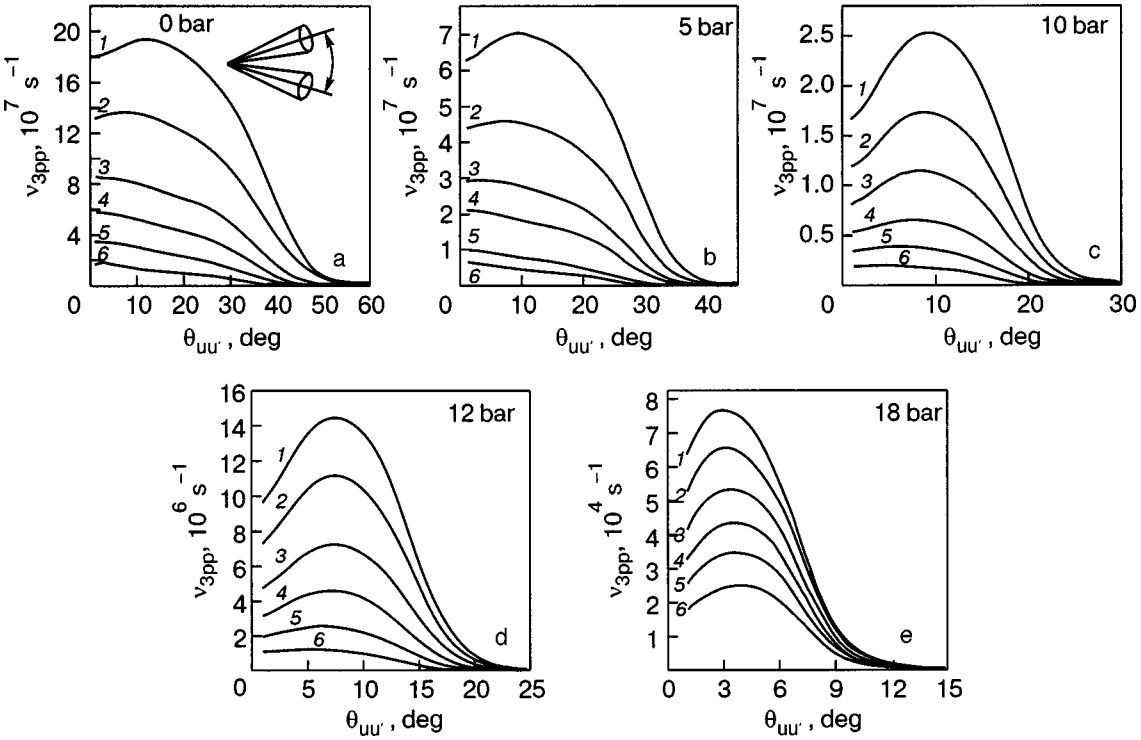

FIG. 7. The rate of three-phonon processes ν_{3pp} as a function of an angle between the axes of the two interacting anisotropic phonon systems. Curves *1–6* of each panel are for temperatures $T_p = 1$, 0.9, 0.8, 0.7, 0.6, and 0.5 K. Panels a, b, c, d, and e are for pressures of 0, 5, 10, 12, and 18 bar, respectively. The value of ζ_p is defined by Eq. (57) (see Table II).

The formation of a hot line was experimentally observed in Refs. 4 and 5, and it was shown that at high pressures and at large values of the angles between pulses, a hot line is not formed. Such a situation can be explained with the help of Fig. 7. At the values of the angle $\theta_{\mathbf{uu}'}$ in the experiments,[4,5] i.e., 8.8°, 26°, and 46°, the time τ_{cross} at $t_p = 100$ ns is equal to 8.5×10^{-6} s, 9.88×10^{-7} s, and 3.28×10^{-7} s, respectively. Then, as shown in Fig. 7e, when the pressure is 18 bar, at all values of angle and temperature, the inequality

$$\tau_{\text{cross}} < \nu_{3pp}^{-1} \tag{67}$$

is satisfied. Thus the pulses have no time to interact and a hot line is not formed.

We note also that at the saturated vapor pressure and at an angle equal to 46° and $T_p = 0.7$ K, the inequality (67) is satisfied and the hot line does not have time to form. At a temperature T_p of 1 K, the given angle is about 50° (see Fig. 7a), and again no hot line is formed.

At the saturated vapor pressure, for $\theta_{\mathbf{uu}'} = 8.8°$ and 26°, for all six values of temperature which are represented on Fig. 7a by curves *1–6* the inequality

$$\tau_{\text{cross}} > \nu_{3pp}^{-1} \tag{68}$$

is satisfied. In this case pulses have enough time to interact.

Our results on the dependence of the interaction of two phonon pulses on the angle between their axes at different values of pressure and temperature are in full agreement with the results of experiments.[4,5]

We note that in the experiments[4,5] the angle between pulses $\theta_{\mathbf{uu}'}$ and the temperature of the pulses change during motion of the pulses from the heater to the detector. An account of these effects was given in Ref. 29. However, the comparisons carried out above answer the question about the possibility of pulses interacting under the conditions of the experiments.[4,5]

7. CONCLUSION

In this paper three-phonon processes in isotropic and anisotropic phonon systems of superfluid helium at different pressures were investigated. The approximate dependences (5)–(8) of He II parameters on pressure were obtained. Restrictions on the momenta of the phonons participating in three-phonon processes (see Fig. 1) were studied, and analytical expressions (13)–(19) for the boundaries of regions in which three-phonon processes are allowed by the conservation laws of energy and momentum were obtained. The dependence (25) on the angle $\theta_{p'p''}$ between phonons with momenta $\mathbf{p}'$ and $\mathbf{p}''$ created as a result of the decay of a phonon with momentum $\mathbf{p}$, using different relations between the momenta of the created phonons, was obtained. This dependence is represented on Fig. 2. The maximum angle (29) of three-phonon processes at different pressures was found. Also it was shown that this angle decreases as pressure increases.

Starting from the kinetic equation, the expression (39) for the rate of three-phonon relaxation in isotropic phonon systems valid for all phonon energies at which three-phonon processes are allowed by conservation laws at different pres-

sures was obtained. The results of rates evaluated using (39) for different pressures and temperatures are shown in Fig. 3. Also the analytical expression (45) which describes the behavior of rates in the range $p_{\min}<p_1<p_{\max}$ was found. Starting from (45), it was shown that the rates of three-phonon processes in a small interval of momentum reach a maximum value and then rapidly vanish.

The pressure dependence of the rate of three-phonon processes in isotropic phonon systems was investigated, and it was shown that the rates decrease with increasing pressure. The reasons for this decrease were explained. Starting from expression (39), the regions in which the limiting cases (48) and (51) are valid were found.

In this paper the relaxation rates (60) in anisotropic phonon systems at different pressures were calculated for the first time. Dependences of these rates on the energy of a relaxing phonon (Fig. 4c,d) and on the direction of its motion relative to an axis of anisotropy (Fig. 4a,b) were found. Dependences of the rates on the angle between an axis of anisotropy of the phonon system and on the momentum of the relaxing phonon were investigated, and the presence of a maximum in this dependence was explained. The terms corresponding to combining of a phonon with momentum $\mathbf{p}_1$ with a phonon of the anisotropic phonon system and to the decay of a phonon with momentum $\mathbf{p}_1$ (see Fig. 5) were compared.

The transition from an anisotropic phonon system to an isotropic one (Fig. 6) was investigated. It was shown that, starting at some value of θ_p, the rate of three-phonon processes becomes saturated.

Based on the solution of a problem of relaxation in anisotropic phonon system, the rates of two interacting anisotropic phonon systems (see Fig. 7) were calculated and compared with experimental data.[4,5]

In conclusion, we note that three-phonon relaxation causes the dissipative coefficients of He II and superfluid mixtures of ^{3}He-^{4}He (see, for example, Ref. 24). The pressure dependence of three-phonon processes rate obtained here allows the determination of the change of this contribution with increasing pressure.

We express our gratitude to GFFI of Ukraine (grant N02.07/000372), and to EPSRC of the UK (grant EP/C523199/1) for support of this work.

*E-mail: i.n.adamenko@mail.ru

[1] A. F. G. Wyatt, N. A. Lockerbie, and R. A. Sherlock, J. Phys.: Condens. Matter **1**, 3507 (1989).
[2] M. A. H. Tucker and A. F. G. Wyatt, J. Phys.: Condens. Matter **6**, 2813 (1994).
[3] M. A. H. Tucker and A. F. G. Wyatt, J. Low Temp. Phys. **113**, 621 (1998).
[4] D. H. S. Smith, R. Vovk, C. D. H. Williams, and A. F. G. Wyatt, Submitted to Phys. Rev. B.
[5] R. Vovk, C. D. H. Williams, and A. F. G. Wyatt, Phys. Rev. Lett. **91**, 235302 (2003).
[6] W. Stirling, *Proceedings of the 75th Jubilee Conference on* ^{4}He, J. G. M. Armitage (ed.), World Scientific, Singapore (1983), p. 109.
[7] R. C. Dynes and V. Narayanamurti, Phys. Rev. B **12**, 1720 (1975).
[8] C. H. Aldrich III and D. Pines J. Low Temp. Phys. **25**, 677 (1976).
[9] C. H. Aldrich III, C. J. Pethick, and D. Pines, J. Low Temp. Phys. **25**, 691 (1976).
[10] B. M. Abraham, Y. Eckstein, J. B. Ketterson, M. Kuchnir, and P. R. Roach, Phys. Rev. A **1**, 250 (1970).
[11] R. C. Dynes and V. Narayanamurti, Phys. Rev. Lett. **33**, 1195 (1974).
[12] R. Sridhar, Phys. Rep. **146**, 259 (1987).
[13] L. P. Pitayevski and Y. B. Levinson, Phys. Rev. B **14**, 263 (1976).
[14] R. A. Sherlock, N. G. Mills, and A. F. G. Wyatt, J. Phys. C: Solid State Phys. **8**, 2575 (1975).
[15] J. Jackle and K. W. Kehr, Phys. Rev. Lett. **27**, 654 (1971).
[16] C. I. Um, S. Y. Lee, S. K. Yoo, T. F. George, L. N. Pandey, and I. N. Adamenko, Fiz. Nizk. Temp. **23**, 537 (1997) [Low Temp. Phys. **23**, 397 (1997)].
[17] T. J. Sluckin and R. M. Bowley, J. Phys. C: Solid State Phys. **7**, 1779 (1974).
[18] M. A. H. Tucker, A. F. G. Wyatt, I. N. Adamenko, A. V. Zhukov, and K. E. Nemchenko, Fiz. Nizk. Temp. **25**, 657 (1999) [Low Temp. Phys. **25**, 488 (1999)].
[19] I. N. Adamenko, Yu. A. Kitsenko, K. E. Nemchenko, V. A. Slipko, and A. F. G. Wyatt, *Abstacts of 11th International Conference on Phonon Scattering in Condensed Matter "Phonons 2004,"* St. Petersburg (2004), p. 218.
[20] Yu. A. Kitsenko and V. A. Slipko, The Journal of Kharkov National University, Physical Series ''Nuclei, Particles, Fields,'' No. 619, Issue 1(23), 81 (2004) [in Russian].
[21] S. Halvin and M. Luban, Phys. Lett. A **42**, 133 (1972).
[22] H. J. Maris, Phys. Rev. A **8**, 1980 (1973).
[23] H. J. Maris, Phys. Rev. A **9**, 1412 (1974).
[24] I. N. Adamenko and E. Ya. Rudavskii, Fiz. Nizk. Temp. **13**, 3 (1987) [Low Temp. Phys. **13**, 1 (1987)].
[25] A. F. G. Wyatt, M. A. H. Tucker, I. N. Adamenko, K. E. Nemchenko, and A. V. Zhukov, Phys. Rev. B **62**, 9402 (2000).
[26] I. N. Adamenko, K. E. Nemchenko, V. A. Slipko, and A. F. G. Wyatt, Phys. Rev. B **68**, 134507 (2003).
[27] A. F. G. Wyatt, M. A. H. Tucker, I. N. Adamenko, K. E. Nemchenko, and A. V. Zhukov, Phys. Rev. B **62**, 3029 (2000).
[28] I. N. Adamenko, K. E. Nemchenko, and A. F. G. Wyatt, Fiz. Nizk. Temp. **29**, 16 (2003)] [Low Temp. Phys. **29**, 11 (2003)].
[29] I. N. Adamenko, Yu. A. Kitsenko, K. E. Nemchenko, V. A. Slipko, and A. F. G. Wyatt, Submitted to Phys. Rev.

This article was published in English in the original Russian journal. Reproduced here with stylistic changes by AIP.

Heat capacity of a p-H_2–p-D_2–Ne solid solution: Effect of (p-D_2)Ne clusters

M. I. Bagatskii,* I. Ya. Minchina, and V. M. Bagatskii

B. Verkin Institute for Low Temperature Physics and Engineering of the National Academy of Sciences of Ukraine, 47, Lenin Ave., Kharkov 61103, Ukraine
(Submitted October 26, 2004)
Fiz. Nizk. Temp. **31**, 620–623 (June 2005)

The heat capacity of a solid solution of 1% p-D_2 and 0.25% Ne in p-H_2 is investigated in the interval $\Delta T = 0.5$–4 K. An excess heat capacity ΔC_{Ne} of this solution exceeding the heat capacity of the solution of 1% p-D_2 in p-H_2 is detected and analyzed. It is found that below 2 K the dominant contribution to the heat capacity ΔC_{Ne} is made by the rotation of the p-D_2 molecules in (p-D_2) Ne-type clusters. The number of (p-D_2) Ne clusters in the solid sample is strongly dependent on the conditions of preparation. The splitting of the $J=1$ level of the p-D_2 molecules in the (p-D_2) Ne clusters, $\Delta = 3.2$ K, is consistent with the theoretical estimate. © *2005 American Institute of Physics.* [DOI: 10.1063/1.1943528]

INTRODUCTION

Heavy impurities in quantum crystals of hydrogen isotopes affect the phonon spectrum of the crystal and disturb the zero (quantum) vibrations of the lattice and rotation of the molecules. Local changes in the lattice structure and the formation of new quantum objects (molecular clusters and complexes[1–8]) are also possible in the vicinity of heavy impurities, which can produce considerable changes in the physical properties of crystals. These phenomena have recently been a focus of intensive investigations.[8,9]

The excess heat capacity ΔC_{Ne} of a solution of 2.5% o-H_2 and xNe ($x = 0.5\%$, 2%) in solid p-H_2 due to the heavy quasi-isotopic Ne impurity introduced into a 2.5% o-H_2–p-H_2 solid solution was first observed in Ref. 1 at $T = 2$–6 K. Near $T = 2$ K ΔC_{Ne} is an order of magnitude larger than the results calculated in the harmonic approximation for $\Delta C_{L,Ne}$ caused by the heavy quasi-isotopic Ne impurity changing the phonon spectrum of the crystal.

A theory was put forward in Ref. 2 to explain this anomaly. Along with the anomalous heat capacity of solid H_2–Ne solutions attendant upon the change in the phonon spectrum of the crystal, there is an anomaly in the rotational component of $C_{R,Ne}$ which is due to the contribution from the rotational degrees of freedom of the H_2 molecules in the lowest state with the rotational quantum number $J=1$ (o-H_2). The strong perturbation of zero (quantum) lattice vibrations by the Ne atoms in the (o-H_2) Ne-type clusters disturbs the local symmetry of the crystal field,[2] causing the $J=1$ level of the o-H_2 molecules to split into two levels with the degeneracies $g_0 = 1$ and $g_1 = 2$ (see Fig. 1). When the (o-H_2) Ne cluster is formed, the energy of the subsystem decreases by $2\Delta/3$ (Δ is the splitting value). $C_{R,Ne}(T)$ exhibits a Schottky-type anomaly. The equilibrium contents of o-H_2–o-H_2 and (o-H_2) Ne clusters in this system depends on temperature. As the temperature changes due to quantum diffusion of the angular momentum of the o-H_2 molecules, the number of clusters varies with time (configurational relaxation). The value of the heat capacity is therefore dependent on the time t_m of the (single) heat capacity measurement and the temperature prehistory. In Ref. 1 the heat capacity was measured above the temperature of the $C_{R,Ne}(T)$ maximum in the Schottky curve. The splitting $2.5\ \text{K} < \Delta < 5\ \text{K}$ of the $J=1$ level of the o-H_2 molecules in the neighborhood of the Ne impurity was estimated roughly[2] from analysis the results obtained in Ref. 1.

This study is concentrated on the contribution of the rotational motion of the p-D_2 molecules to the heat capacity of a 1% p-D_2–p-H_2 solid solution doped with 0.25% Ne in the interval $\Delta T = 0.5$–4 K. The choice of impurity concentration and the temperature interval was dictated by the following considerations. First, quantum diffusion of the p-D_2 molecules is impossible in the p-H_2 lattice,[10] and conversion of the p-D_2 molecules during the experiment is negligible. Second, with the splitting $\Delta > 2$ K of the $J=1$ level of the p-D_2 molecules in the neighborhood of the Ne impurity the temperature of the maximum in the Schottky curves enters the temperature region of this investigation. Third, earlier we investigated the heat capacity of the solution of 1% p-D_2 in

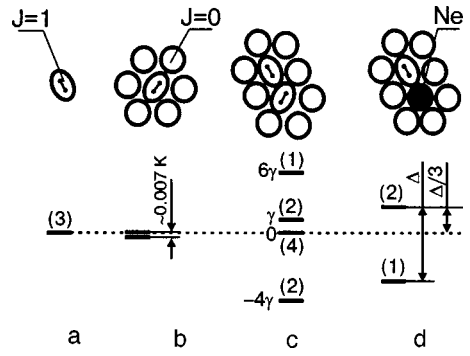

FIG. 1. Schematic arrangement of lower energy levels of o-H_2 (p-D_2) ($J=1$) molecules as a function of molecular surroundings (level degeneracy is indicated in brackets): (a) free molecule; (b) twelve p-H_2 molecules ($J=0$) of the first coordination sphere of an hcp lattice (only six molecules are shown);[15] (c) two nearest neighboring o-H_2 molecules (cluster o-H_2-o-H_2, $\gamma = 0.83$ K), p-D_2 (cluster p-D_2–p-D_2, $\gamma = 0.95$ K) surrounded by the nearest neighboring p-H_2 molecules of the hcp lattice (eight molecules are shown);[15] (d) the nearest neighboring Ne atom and p-D_2 molecule [(p-D_2) Ne cluster] surrounded by the nearest neighboring p-H_2 molecules of the hcp lattice (eight molecules are shown).[2]

 © 2005 American Institute of Physics

TABLE I. Time t_i during which the sample was kept in the liquid phase near T_i before its crystallization and the subsequent series of heat capacity measurement.

Series	t_i, min	T_i, K
2	40	14.5
3	90	16
4	120	18

solid p-H_2 using the same calorimeter.[10] This permits us to separate accurately the excess heat capacity ΔC_{Ne} caused by 0.25% Ne introduced into the 1% p-D_2–p-H_2 solid solution.

EXPERIMENT

The heat capacity of the solid solution of 0.94 mole % p-D_2 and 0.06 mole % o-D_2 in parahydrogen (below referred to as 1% p-D_2 in p-H_2) doped with 0.25% Ne has been measured using an adiabatic calorimeter[11] in the interval $\Delta T = 0.5$–4 K. The gas compositions were H_2–99.99% (99.985% the isotope and 0.015% HD); D_2–99.99% (99.9% the isotope and 0.1% HD); Ne–99.99%. The starting ortho-para composition of hydrogen $\approx 1\times 10^{-2}$% o-H_2 was obtained by keeping hydrogen in catalytic $Fe(OH)_3$ for 24 h at a constant temperature (the triple point of H_2). p-D_2 was obtained in an adsorption column by the technique described in Ref. 12. The p-D_2 concentration (94%) in deuterium was estimated from the thermal conductivity of D_2 gas at nitrogen temperatures using an analyzer which we made and calibrated following the configuration in Ref. 13. Four measurement series were performed. Series 1 was made on a sample prepared in the calorimetric vessel by condensing the gas mixture to the solid phase at $T \approx 9.5$ K. The other series were made on solid samples prepared by crystallization from the liquid phase. After each series of measurements, the sample was melted, kept in the liquid state during a period of t_i at temperature T_i, crystallized, and cooled. Then the next run of measurements was performed.

The heat capacities measured at $T \leqslant 4$ K are independent of the temperature prehistory of the sample. The measurement error was ± 6% at 0.5 K, ± 2% at 1 K, and ± 1% at $T > 2$ K.

RESULTS AND DISCUSSION

The experimental results on heat capacity per mole of the solution 1% p-D_2 and 0.25% Ne in solid p-H_2 can be written as

$$C = C_1 + \Delta C_{Ne} = C_1 + \Delta C_{L,Ne} + C_{R,Ne}. \quad (1)$$

Here C_1 is the heat capacity of the 1% p-D_2–p-H_2 solid solution,[10] ΔC_{Ne} is the excess heat capacity of the solution 1% p-D_2 and 0.25% Ne in solid p-H_2 over the heat capacity of the solution 1% p-D_2 in solid p-H_2. We assume that $\Delta C_{Ne} = \Delta C_{L,Ne} + C_{R,Ne}$, where $\Delta C_{L,Ne}$ is the increment in the heat capacity of the lattice produced by the quasi-local frequencies in the phonon spectrum of hydrogen, which appear when the heavy quasi-isotopic Ne impurity is introduced into the lattice of p-H_2; $C_{R,Ne}$ is the rotational heat capacity of the p-D_2 molecules caused by the 0.25% Ne impurity introduced into the p-H_2–1%p-D_2 solution. $\Delta C_{L,Ne}$ was calculated in the harmonic approximation using the technique developed by Peresada *et al.*[14]

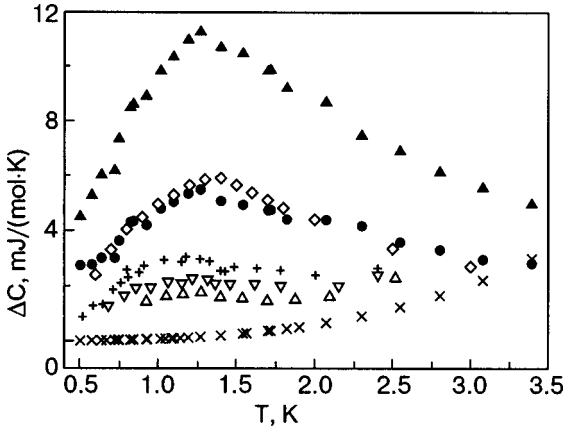

FIG. 2. Temperature dependences of excess heat capacities: (▲) is a solution of 1% p-D_2 and 0.25% Ne in solid p-H_2 over that of pure p-H_2 (series 1); (●), (+), (▽), (△) are the values for solutions of 1% p-D_2 and 0.25% Ne in solid p-H_2 in excess of that for solutions of 1% p-D_2 in solid p-H_2 (series 1–4, respectively); (◇) is for solutions of 1% p-D_2 in solid p-H_2 in excess of that for pure p-H_2 (Ref. 10); (×) is $\Delta C_{L,Ne}$ induced by the change in the phonon spectrum of the crystal due to introduction of heavy quasi-isotopic Ne impurity to the lattice of p-H_2.

The temperature dependences of the excess heat capacities $\Delta C_{Ne}(T) = C - C_1$ taken in series 1–4 are shown in Fig. 2. The figure also shows the temperature dependences of the excess heat capacity of solid solution of 1% p-D_2 and 0.25% Ne in p-H_2 in comparison with the heat capacity of pure p-H_2 (series 1), the excess heat capacity $\Delta C_{p-D_2}(T)$ of the 1% p-D_2–p-H_2 solid solution in comparison with the heat capacity of pure p-H_2, and the increment in the lattice heat capacity $\Delta C_{L,Ne}$. Note that at $T < 2$ K the contribution of $\Delta C_{L,Ne}$ to ΔC_{Ne} is negligible (see Fig. 2). Therefore, the excess heat capacity ΔC_{Ne} is practically determined by the rotational motion of the p-D_2 molecules in the (p-D_2) Ne type clusters. The temperature dependences $C_{R,Ne}(T)$ and $C_{R,p-D_2}(T)$ from Ref. 10 ($C_{R,p-D_2}$ is the heat capacity of the rotational subsystem of the 1% p-D_2–p-H_2 solution) are shown in Fig. 3.

The excess heat capacity $C_{R,Ne}$ was analyzed within the theoretical model of Ref. 2. A number of new phenomena have been observed, which are induced by doping the solid solution of 1% p-D_2 in p-H_2 with 0.25% Ne.

1. An anomalously high excess heat capacity ΔC_{Ne} is observed after the addition of 0.25% Ne to the 1% p-D_2–p-H_2 solid solution. It is found that below 2 K the dominant contribution ($C_{R,Ne}$) to the heat capacity ΔC_{Ne} is made by the rotation of the p-D_2 molecules in the (p-D_2) Ne clusters (Fig. 2).

2. The heat capacity ΔC_{Ne} is strongly dependent on the method of preparation of a solid sample. Note that the excess heat capacity of the p-H_2-1% p-D_2 solid solution over that of pure p-H_2 is independent of the method of solid sample preparation.

3. At $T < 3$ K the temperature dependence of the excess heat capacity $C_{R,Ne}$ has the form of the Schottky curve and is described by the theory.[2] The splitting $\Delta = 3.2 \pm 0.1$ K of the

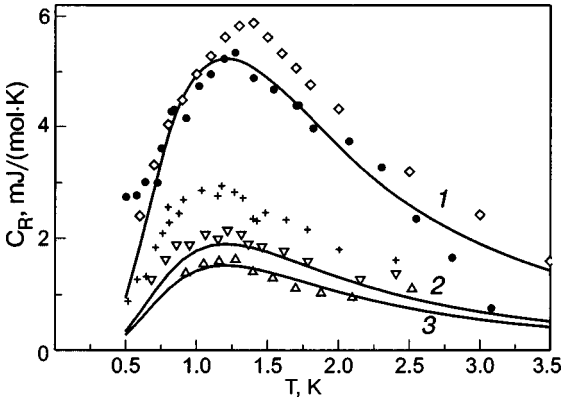

FIG. 3. Temperature dependences of heat capacities determined by the rotation of p-D_2 molecules. Experiment: (●), (+), (△), (▽) are in (p-D_2) Ne clusters, solid solution 1% p-D_2, 0.25% Ne in p-H_2, series 1, 2, 3, 4, respectively; (◇) is in p-D_2–p-D_2 clusters, solid solution 1% p-D_2 in p-H_2 (Ref. 10). The curves show the calculated heat capacities $C_{R,Ne}$ for different contents of (p-D_2) Ne clusters: curve *2* is for a number of clusters equal to N_R for a random distribution of Ne and p-D_2 impurities; curve *1* is for a number of clusters 2.8 times larger than N_R; curve *3* is for a number of clusters 1.25 times smaller than N_R.

$J=1$ level of the p-D_2 molecules in the (p-D_2) Ne type clusters was obtained from the analysis of $C_{R,Ne}(T)$ and is consistent with the theoretical estimate.[2] The number of (p-D_2) Ne clusters in the samples measured in series 1 and 4 is 2.8 times larger and 1.25 times smaller than that in the case of randomly distributed p-D_2 and Ne impurities (see Fig. 3).

The effects observed are evidence in favor of the existence of new condensable systems formed by the van der Waals complexes of the $Ne(H_2)_n$ or $Ne(D_2)_n$ type.[6,7] It has been found[3–7] that mixtures of quantum substances (e.g., helium and hydrogen) with inert elements or simple molecular substances can form van der Waals complexes which make a basis for a new type of solids. X-ray investigations of Ne-containing H_2 and D_2 polycrystalline samples prepared by condensation of gas mixtures onto a substrate at $T\approx 5$ K show that in addition to the hexagonal and cubic phases based on the H_2 and Ne lattices, the samples contain hcp inclusions (even at the 0.25% Ne concentration[6,7]) whose lattices have somewhat larger (by 1.5%–0.7%) volumes than that of pure Ne. The authors believe that the additional hcp phase in these systems is formed on the basis of the $Ne(H_2)_n$ or $Ne(D_2)_n$ types of van der Waals complexes. We can assume that in the solution of 1% p-D_2 and 0.25% Ne in p-H_2 the solid p-D_2 concentration produced by complexes of the $Ne(p\text{-}H_2)_n$ type and the amount of this phase are strongly dependent on the preparation conditions. This is because the formation of the (p-D_2) Ne clusters decreases the energy of the system by $2\Delta/3$ and, hence, the total (elastic) energy of dilatation. In a liquid sample, the phase formed by the $Ne(p\text{-}H_2)_n$ complexes dissociates rather slowly, which reduces the number of (p-D_2) Ne clusters.

The authors are indebted to A. I. Prokhvatilov and M. A. Strzhemechny for helpful discussions. The study was supported by the Ukraine Ministry of Education and Science, State Foundation for Basic Research (Project No. 02.07/00391-2004).

*E-mail: bagatskii@ilt.kharkov.ua

[1] V. G. Manzhelii, V. A. Popov, G. P. Chausov, and L. I. Vladimirova, J. Low Temp. Phys. **14**, 397 (1974).
[2] V. B. Kokshenev, Fiz. Nizk. Temp. **2**, 236 (1976) [Sov. J. Low Temp. Phys. **2**, 118 (1976)].
[3] R. Boltnev, E. B. Gordon, I. N. Krushinskaya, A. A. Pal'menev, E. A. Popov, O. F. Pugachev, and V. V. Khmelenko, Fiz. Nizk. Temp. **18**, 819 (1992) [Sov. J. Low Temp. Phys. **18**, 576 (1992)].
[4] W. L. Vos, L. W. Finger, R. J. Hemley, J. Z. Hu, H. K. Mao, and J. A. Schouten, Nature (London) **358**, 46 (1992).
[5] P. Loubeyer, M. Jean-Louis, R. LeToullec, and L. Charon-Gerard, Phys. Rev. Lett. **70**, 178 (1993).
[6] A. S. Barylnik, A. I. Prokhvatilov, M. A. Strzhemechny, and G. N. Shcherbakov, Fiz. Nizk. Temp. **19**, 625 (1993) [Low Temp. Phys. **19**, 447 (1993)].
[7] A. S. Barylnik, A. I. Prokhvatilov, and G. N. Shcherbakov, Fiz. Nizk. Temp. **21**, 787 (1995) [Low Temp. Phys. **21**, 607 (1995)].
[8] M. A. Strzhemechny, N. N. Galtsov, and A. I. Prokhvatilov, Fiz. Nizk. Temp. **29**, 699 (2003) [Low Temp. Phys. **29**, 522 (2003)].
[9] N. N. Galtsov, A. I. Prokhvatilov, G. N. Shcherbakov, and M. A. Strzhemechny, Fiz. Nizk. Temp. **29**, 1036 (2003) [Low Temp. Phys. **29**, 784 (2003)].
[10] A. I. Krivchikov, M. I. Bagatskii, V. G. Manzhelii, and P. I. Muromtsev, Fiz. Nizk. Temp. **15**, 3 (1989) [Sov. J. Low Temp. Phys. **15**, 1 (1989).
[11] M. I. Bagatskii, I. Ya. Minchina, and V. G. Manzhelii, Fiz. Nizk. Temp. **10**, 1039 (1984) [Sov. J. Low Temp. Phys. **10**, 542 (1984)].
[12] D. A. Depatie and R. L. Mills, Rev. Sci. Instrum. **39**, 106 (1968).
[13] T. W. Bradshaw and J. O. W. Norris, Rev. Sci. Instrum. **58**, 83 (1987).
[14] V. I. Peresada and V. P. Tolstoluzhskii, Fiz. Nizk. Temp. **3**, 788 (1977) [Sov. J. Low Temp. Phys. **3**, 378 (1977)].
[15] W. N. Hardy, A. J. Berlinsky, and A. B. Harris, Can. J. Phys. **55**, 1150 (1977).

This article was published in English in the original Russian journal. Reproduced here with stylistic changes by AIP.

Multi-echo in phase-separated ^{3}He–^{4}He solid solutions under NMR conditions

N. P. Mikhin* and V. A. Maidanov

B. Verkin Institute for Low Temperature Physics and Engineering, National Academy of Sciences of Ukraine, pr. Lenina 47, Kharkov 61103, Ukraine

(Submitted October 29, 2004)
Fiz. Nizk. Temp. **31**, 624–628 (June 2005)

A pulsed NMR method is used to make the first observation and study of the multi-echo in a phase-separated ^{3}He–^{4}He solid solution. Analysis of the behavior of the second echo under these conditions in comparison with the results obtained in samples of liquid and solid ^{3}He reveals the presence of a significant amount of liquid ^{3}He in a fine-grained ^{3}He phase and offers a new explanation of the origin of the unusual damping of the first echo observed previously under these conditions. © *2005 American Institute of Physics.* [DOI: 10.1063/1.1943529]

1. INTRODUCTION

In the pulsed NMR technique developed by Hann[1] a sample containing nuclei with half-integer spin is placed in a magnetic field $\mathbf{H}_0$ and acted upon by short radio pulses whose frequency band includes the resonant frequency. Hann showed that in the presence of a magnetic-field gradient G the action of a pair of such pulses separated by an interval τ will produce a spin echo in the sample, with an amplitude h given by

$$h(\tau)=\frac{1}{2}\sin\Theta_1(1-\cos\Theta_2)h_0 \times\exp\left(-\frac{2\tau}{T_2}-\frac{2}{3}\gamma^2G^2\tau^3D\right), \quad (1)$$

where $\Theta=\gamma H_1 t_P$ is the angle of rotation of the magnetization vector of the sample after the action of a radio pulse with alternating magnetic field amplitude H_1 and duration t_P (γ is the gyromagnetic ratio), T_2 is the spin-spin relaxation time, and D is the spin diffusion coefficient. Hann's calculations were based on an idealized model under the assumption that the ensemble of nuclei with magnetic moment μ is an ideal paramagnet ($\mu H_0 \ll kT$) with a negligible degree of magnetic polarization, that there is no nuclear magnetic order in it, and that the spin interaction processes are isotropic.

The successful use of pulsed NMR in experimental physics, chemistry, biology, medicine, and geology over the last 50 years has demonstrated the adequacy of the model proposed by Hann. Nevertheless, it has been shown comparatively recently that for polarized nuclear paramagnets under conditions of intense spin-spin interaction of the nuclei at high magnetic-field gradients, the equations describing the dynamics of the motion of the magnetization of the sample acquire additional nonlinear terms that can be interpreted as a manifestation of additional effective demagnetizing fields. In this case, instead of the usual spin echo (1), a sequence of responses of the nuclear system at the resonant frequency appears, at times $(n+1)\tau$ ($n=2,3,\ldots$), i.e., a multi-echo, the amplitude of which is much less than that of an ordinary echo. In particular, the amplitude of the second echo ($n=2$; see, e.g., Ref. 2) is

$$h_2=\frac{1}{2}\sin^2\Theta_1\sin\Theta_2(1-\cos\Theta_2)h_0\beta\exp\left(-\frac{7D^*}{3}\right) \times\left(\frac{\mathrm{erf}(\sqrt{D^*})\sqrt{\pi}}{2\sqrt[6]{D^*}}\right), \quad (2)$$

where $\beta=\gamma\mu_0M_0\tau/\sqrt{D^*}$ and $D^*=G^2\gamma^2\tau^3D$. It is seen from Eq. (2) that, first, unlike the ordinary echo, the maximum of which is reached at $\Theta_1=90°$ and $\Theta_2=180°$, the second echo reaches its maximum value at $\Theta_2=120°$ second, the dependence of h_2 on τ, G, and D^* is a nonmonotonic function with a maximum.

Until recently the multi-echo effect had been studied in solid, liquid, and superfluid helium-3 and in dilute liquid solutions of helium-3 in helium-4.[2–7]

In this paper we report the first observation and study of the multi-echo effect in a phase-separated ^{3}He–^{4}He solid solution. In this case investigation of the behavior of the second echo made it possible to explain the origin of the singularities of the damping of the first echo as being due to the presence of an appreciable amount of liquid ^{3}He in a fine-grained ^{3}He phase of the phase-separated solid solution revealed in Ref. 8.

2. EXPERIMENTAL TECHNIQUE

In this paper we have investigated samples of solid helium with an initial concentration of 0.54% ^{3}He. The samples were grown by blocking of a capillary in the cell described previously.[8] The sample cell was in good thermal contact with the mixing chamber of the refrigerator. The final pressure in the homogeneous samples annealed at a submelting temperature was around 31 atm, corresponding to molar volumes $V_m=20.55\pm0.05$ cm^3/mole. On cooling below the phase separation temperature the samples separated into two daughter phases having high and low ^{3}He concentrations. The separated sample consists of fine-grained bcc crystals of almost pure ^{3}He, 1–4 μm in size,[8–11] immersed in a bulk hcp host crystal of almost pure ^{4}He. Under these conditions the molar volume of solid ^{3}He should amount to 24.6 cm^3/mole.

The measurements were mainly done after completion of the phase separation at a temperature of 100 mK at a reso-

 © 2005 American Institute of Physics

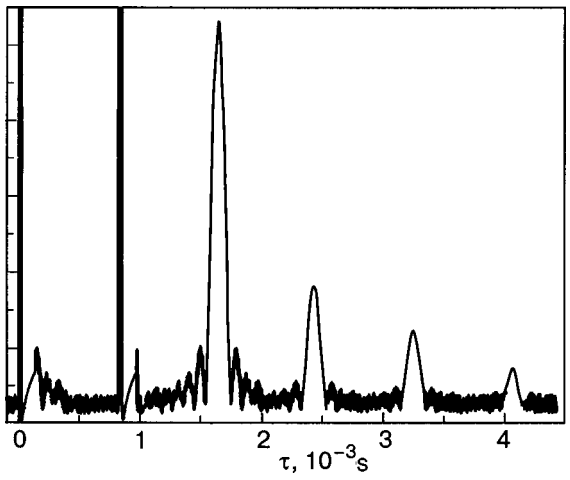

FIG. 1. Oscilloscope trace of the multi-echo ($n=1,2,3,4$; $\tau=0.82$ ms, $\Theta_2=120'$) in a phase-separated ^{3}He–^{4}He solid solution at $T=100$ mK.

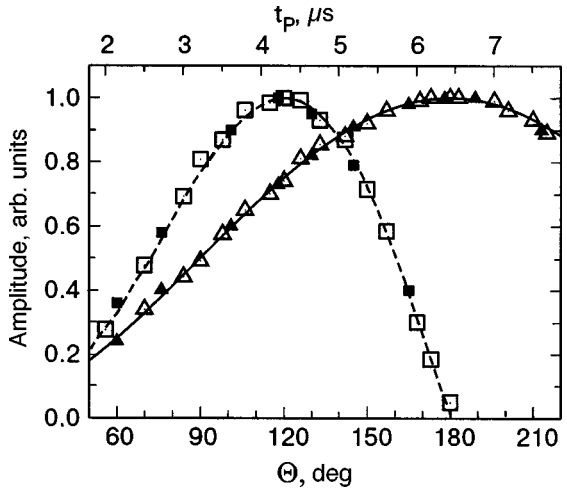

FIG. 2. Dependence of the normalized amplitude of the first and second echoes on the duration of the second rf pulse (upper scale). First echo: △—in bulk liquid ^{3}He, ▲—in a phase-separated solid solution. Second echo: □—in bulk liquid ^{3}He, ■—in a phase-separated solid solution. The curves show the result of a fitting of the trigonometric factors from formulas (1) and (2), respectively (lower scale).

nance frequency of 9.15 MHz with the use of $\Theta_1-\tau-\Theta_2$ pulse trains. In such a heterophase sample the spin-lattice relaxation time T_{1B} in the ^{3}He clusters was around 1 s,[12] and therefore the waiting time between measurements was chosen an order of magnitude greater than T_{1B} so that the magnetization of the sample would have time to reach its equilibrium value. In this case there is no contribution to the NMR signal from the host (where, according to estimates, T_{1H} should be several orders of magnitude greater than T_{1B}) because of its negligibly small ^{3}He content.

The multi-echo in the phase-separated sample was first observed in this study after a $90°-\tau-180°$ pair of pulses, and then the duration of the second pulse was adjusted to obtain the maximum amplitude of the second echo. Figure 1 shows the form of the echo signals arising after a $90°-\tau-120°$ train with $\tau=0.82$ ms in a phase-separated solid solution at 100 mK.

As part of this study we also carried out a number of calibration experiments with pure liquid and solid ^{3}He at pressures of 28–37 atm in the temperature range 40–450 mK. This permitted a more precise adjustment of the duration of the second pulse, since the signal/noise ratio in this case was two orders of magnitude higher.

Figure 2 shows how the amplitudes of the first and second echoes in bulk ^{3}He and in the phase-separated solid solution depended on the duration of the second pulse. A least-squares processing of the experimental results showed that the broad maximum for the first echo corresponds to 6.44 μs, and the sharper maximum for the second echo, to 4.29 μs. The ratio 6.44/4.29 is close to 1.5, and it can therefore be assumed that 6.44 μs corresponds to 180° and 4.29 μs corresponds to 120°.

This result and also the agreement between the results of measurements made in pure ^{3}He and in heterophase separated crystals provide proof of the observation of a multi-echo.

3. EXPERIMENTAL RESULTS AND DISCUSSION

The dependence of the amplitude h_2 of the second echo on τ in the calibration experiments is shown in Fig. 3. In liquid ^{3}He at a pressure of 28 atm and a temperature of 100 mK the dependence $h_{2L}(\tau)$ is well described by expression (2) with parameters $G=14$ G/sm and $D=1.8\times10^{-5}$ cm^2/s and practically coincides with the data of Ref. 7.

In bulk solid ^{3}He with a molar volume of 23.6 cm^3/mole at $T=400$ mK our results are in good agreement with the data of Ref. 4, obtained on samples of the same density. Here the $h_{2S}(\tau)$ curves obtained in both studies are well described by expression (2). Therefore all of our subsequent data processing was done using formula (2), which seems to us more convenient than the function $h_2(\tau)$ used in Ref. 4.

As is seen in Fig. 3, relation (2) also gives a good description of the data of the calibration experiment for solid ^{3}He at $V_m=24.6$ cm^3/mole and $T=100$ mK ($D=1.25\times10^{-7}$ cm^2/s, $G=14$ G/cm).

The dependence of the amplitude of the second echo on τ in the phase-separated ^{3}He–^{4}He solid solution at 100 mK

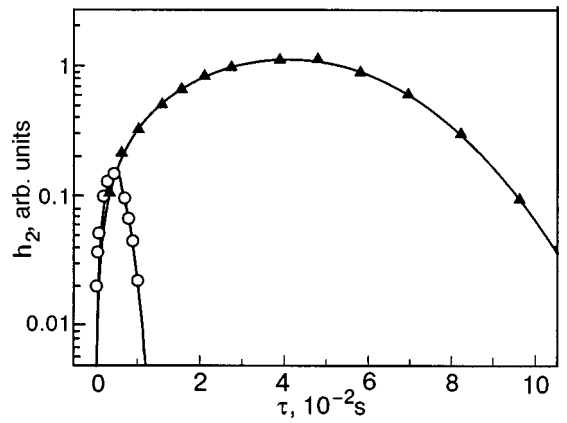

FIG. 3. Dependence on τ of the amplitude of the second echo in bulk ^{3}He at $T=100$ mK. ○—h_{2L} (liquid helium, $P=28$ atm, $G=14$ G/cm), ▲—h_{2S} (solid helium, $V=24.6$ cm^3/mole, $G=5$ G/cm). The curves are calculated according to formula (2) for $D=1.8\times10^{-5}$ cm^2/s and 1.25×10^{-7} cm^2/s, respectively. The amplitudes are normalized to the maximum value of h_{2S}.

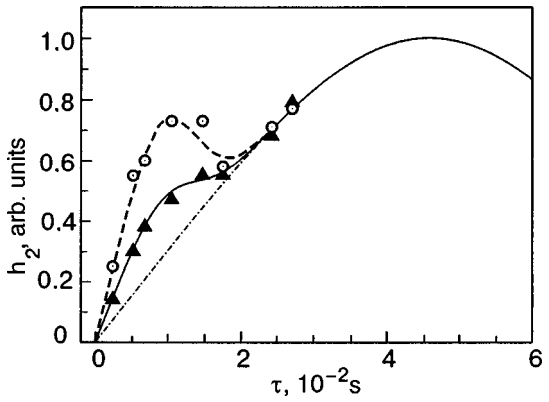

FIG. 4. Dependence on τ of the amplitude of the second echo in a phase-separated ^{3}He–^{4}He solid solution at $T=100$ mK, obtained for two different crystals. The curves show the result of a processing of the experimental data on the assumption that $h_2=\alpha h_{2L}+(1-\alpha)h_{2S}$. ▲—$\alpha=0.5$ (solid curve); ○—$\alpha=0.7$ (dashed curve). The dotted line shows the normalized function $h_{2S}(\tau)$ according to Eq. (2).

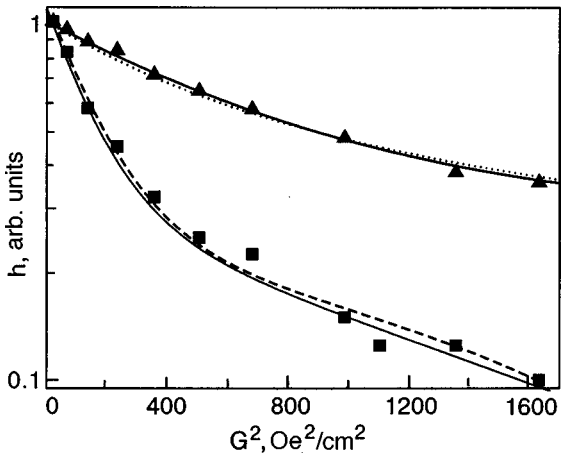

FIG. 5. Damping of the amplitude of the first echo in a phase-separated ^{3}He–^{4}He solid solution at $T=100$ mK (data of Ref. 8): ▲—$\tau=40$ ms; ■—$\tau=105$ ms. The solid curves show the calculation according to formula (3) for $\alpha=0.7$, $D_L=1.8\times10^{-5}$ cm^2/s, and $D_S=1.25\times10^{-7}$ cm^2/s. The dashed curve shows a calculation according to formula (4) with $D=1\times10^{-5}$ cm^2/s.

is presented in Fig. 4. A comparison of the characteristic maximum at $\tau<10$ ms with the results obtained in experiments on pure ^{3}He (see Fig. 3) suggests that it is due to the presence of both solid and liquid ^{3}He in the sample. We therefore processed the experimental data obtained on two different samples by the least-squares method under the assumption that $h_2=\alpha h_{2L}+(1-\alpha)h_{2S}$, where the free parameter $\alpha<1$ is the liquid fraction contained in the sample.

It should be noted that relations (1) and (2) for $h(\tau,D,G)$ were obtained for the case of unrestricted diffusive motion, when the length of the diffusion path of an atom over the measurement time $\sim\sqrt{2\tau D}$ is less than the characteristic size of the particle in which the diffusion occurs. It is easy to see that in the case of liquid diffusion ($D\sim10^{-5}$ cm^2/s) in a fine-grained ^{3}He phase with a characteristic particle size $\sim4\times10^{-4}$ cm (Ref. 8) the condition of unrestricted diffusive motion begins to fail at $\tau>10$ ms. The transition to the regime of restricted diffusion length leads to an effective decrease of the diffusion coefficient calculated from the relation $h(G)$ using Eq. (1), and at sufficiently large τ the diffusion coefficient becomes inversely proportional to τ^2 (see, e.g., Ref. 13). With such a decrease of D the maximum of $h_{2L}(\tau)$ in accordance with Eq. (2) grows and shifts to larger τ. Therefore at long τ the values of h_2 were not processed in this case.

Thus, as a result of our processing of the data shown in Fig. 4 we obtained the values $\alpha=0.5$ and $\alpha=0.7$.

Such large values of α are easily explained. To obtain such a large ratio of liquid to crystal for bulk solid ^{3}He on isochoric cooling along the melting curve it is necessary to reduce the temperature to 0 K.[14] However, small inclusions of ^{3}He surrounded by the ^{4}He host, which has a high compressibility coefficient, are found more nearly under isobaric than isochoric conditions, and it is therefore easily shown that the change of their molar volume on melting leads to growth of the pressure in the whole sample, $\Delta P_X\approx\Delta P_{\rm melt}X_3$, where $\Delta P_{\rm melt}$ is the change in pressure under isochoric melting of bulk ^{3}He, and X_3 is the ^{3}He concentration in the initial solution. Indeed, in our experiments the change of pressure in the samples after phase separation did not exceed a few hundredths of an atmosphere. Simple estimates show that under conditions of a phase-separated solid solution with $X_3=0.5\%$ a supercooling of 2–3 mK below the melting curve of ^{3}He is sufficient for complete melting of the ^{3}He crystallites.

It should be noted that the sample with the lower liquid content was investigated at 100 mK immediately after the end of the phase separation process, whereas the second sample after phase separation at 100 mK was cooled to 50 mK over the course of two hours, and the inclusions of the ^{3}He phase could have melted completely in the process. The larger amount of liquid ^{3}He observed in the latter agrees with the conclusions of Ref. 15 that the crystallization of the liquid contained in the ^{3}He inclusions on heating is more difficult than melting on cooling. This is due in part to the large deforming stresses that arise in the crystalline matrix of the dilute phase on account of the appreciable difference of the molar volumes of the liquid and solid phases of ^{3}He.

The evidence obtained for the existence of liquid in the fine-grained ^{3}He phase allows us to reexamine afresh the results of Ref. 8. The nonexponential damping of the first echo observed in that study was explained a quasi-one-dimensional distribution of ^{3}He in the concentrated phase. In the light of what we have said above, one can attempt to explain the $h(G^2)$ curves obtained in Ref. 8 by a partial melting of ^{3}He in the phase-separated solid solution. Here in each sample containing two phases with different diffusion coefficients the damping of the first spin echo is described by a sum of two exponentials:

$$h(\tau)=h_0\left[\left(\alpha\exp\left(-\frac{2\tau}{T_{2L}}-\frac{2}{3}\gamma^2G^2\tau^3D_L\right)\right.\right.$$
$$\left.\left.+(1-\alpha)\exp\left(-\frac{2\tau}{T_{2S}}-\frac{2}{3}\gamma^2G^2\tau^3D_S\right)\right)\right], \qquad (3)$$

where the subscripts L and S refer to the liquid and solid phases, respectively. Figure 5 shows the results of a least-

squares processing of the original data of Ref. 8 using formula (3) with the parameters $\alpha=0.7$, $D_L=1.8\times10^{-5}$ cm^2/s, and $D_S=1.25\times10^{-7}$ cm^2/s in comparison with the processing done in Ref. 8 ($D=1\times10^{-5}$ cm^2/s) under the assumption of a quasi-one-dimensional character of the ^{3}He diffusion:[16]

$$h=h_0\frac{\sqrt{\pi}\,\mathrm{erf}\left(\sqrt{\frac{2}{3}G^2\gamma^2\tau^3D}\right)}{2\sqrt{\frac{2}{3}G^2\gamma^2\tau^3D}}. \tag{4}$$

Formally the two approaches both describe the experimental results equally well, but the data of the present study, attesting to an appreciable liquid content in the fine-grained ^{3}He phase in a phase-separated solid solution, provide a more natural explanation.

The authors thank B. P. Cowan, G. Eska, V. N. Grigor'ev, W. J. Mullin, E. Ya. Rudavskii, and D. A. Tayurskii for interest in this study and helpful discussions.

This study was supported by the Ukrainian Foundation for Basic Research, 02.07./00391 (Project No. F7/286-2004).

*E-mail: mikhin@ilt.kharkov.ua

[1] E. L. Hann, Phys. Rev. **4**, 580 (1950).
[2] G. Eska, H. G. Willers, B. Amend, and W. Widemann, Physica B **108**, 1155 (1981).
[3] D. Einzel, G. Eska, Y. Hirayoshi, T. Kopp, and P. Wölfle, Phys. Rev. Lett. **53**, 2312 (1984).
[4] G. Deville, M. Bernier, and J. M. Delrieux, Phys. Rev. B **19**, 5666 (1979).
[5] A. S. Bedford, R. M. Bowley, J. R. Owers-Bradley, and D. Wightman, Physica B **169**, 190 (1990).
[6] G. Nunes, Jr., C. Jin, A. M. Putman, and D. M. Lee, Physica B **169**, 546 (1991).
[7] A. S. Bedford, R. M. Bowley, J. R. Owers-Bradley, and D. Wightman, J. Low Temp. Phys. **83**, 389 (1991).
[8] V. A. Mikheev, V. A. Maidanov, N. P. Mikhin, S. E. Kal'noi, and N. F. Omelaenko, Fiz. Nizk Temp. **14**, 564 (1988) [Sov. J. Low Temp. Phys. **14**, 309 (1988)].
[9] N. Alikasem, Ph. D. Thesis, University of Sussex (1989).
[10] S. C. J. Kingsley, I. Kosarev, L. Roobol, V. Maidanov, J. Sauders, and B. Cowan, J. Low Temp. Phys. **110**, 34 (1998).
[11] S. C. J. Kingsley, V. Maidanov, J. Sauders, and B. Cowan, J. Low Temp. Phys. **113**, 1017 (1998).
[12] N. P. Mikhin, V. A. Maidanov, and A. V. Polev, Fiz. Nizk. Temp. **28**, 344 (2002) [Low Temp. Phys. **28**, 239 (2002)].
[13] B. Robertson, Phys. Rev. **151**, 273 (1966).
[14] W. P. Halperin, F. B. Rasmussen, C. N. Archie, and R. C. Richardson, J. Low Temp. Phys. **31**, 617 (1978).
[15] E. Rudavskii, A. Ganshin, V. Grigoriev, V. Maidanov, N. Omelaenko, A. Penzev, and A. Rybalko, J. Low Temp. Phys. **121**, 713 (2000).
[16] V. A. Mikheev and V. A. Slyusarev, Fiz. Nizk. Temp. **7**, 379 (1981) [Sov. J. Low Temp. Phys. **7**, 186 (1981)].

Translated by Steve Torstveit

SUPERCONDUCTIVITY, INCLUDING HIGH-TEMPERATURE SUPERCONDUCTIVITY

Electrical resistivity of $Ti_{41.5}Zr_{41.5}Ni_{17}$ quasicrystals in the temperature region 0.3–300 K

V. M. Azhazha

National Science Center "Kharkov Institute of Physics and Technology," 1 Academicheskaya St., Kharkov, 61108, Ukraine

G. Ya. Khadzhay* and B. A. Merisov

Physics Department, Kharkov National University, 4 Svobody Sq., Kharkov, 61077, Ukraine

S. V. Malikhin and A. T. Pugachov

National Technical University "Kharkov Polytechnical Institute," 21 Frunze Str., Kharkov, Ukraine

H. R. Ott and A. V. Sologubenko

Laboratorium für Festkörperphysik, ETH Hönggerberg, CH-8093, Zürich, Switzerland

(Submitted October 20, 2004)
Fiz. Nizk. Temp. **31**, 629–633 (June 2005)

The electrical resistivity of icosahedral quasicrystals $Ti_{41.5}Zr_{41.5}Ni_{17}$ is investigated in the temperature region between 0.3 and 300 K on samples of different quality. At temperatures between 0.3 and 2 K the influence of external magnetic fields up to 16 kOe on the superconducting transition of these materials is investigated. The temperature dependence of the resistivity in the region of the superconducting transition varies in a step-like manner. The data of the x-ray analysis imply the presence of several different quasicrystalline phases. Above the superconducting transition a resistivity minimum is observed. © *2005 American Institute of Physics.* [DOI: 10.1063/1.1943530]

1. INTRODUCTION

Quasicrystals are a relatively new type of conducting solids with long range order but no periodicity in the crystal structure. The conductivity and especially superconductivity of quasicrystals has not ben studied in great detail in the past, and therefore new efforts along those lines seem of interest.

The conductivity of quasicrystals is determined by both their electronic structure and by electron-scattering effects.[1] All known quasicrystalline superconductors—Al–Zn–Mg;[2] Al–Cu–Mg, Al–Cu–Li;[3] Ti–Zr–Ni[4,5]—belong to the so-called TC type, which is characterized by high (in comparison to the MI type) values of the electron concentration ($e/a \geqslant 2.1$) and of the ratio of the quasicrystallinity parameter to the average atomic diameter ($a_q/d \sim 1.75$).[6] Regarding the temperature dependence of the electrical resistivity of these TC-type quasicrystals, the derivative $d\rho/dT > 0$ in a broad range of temperature and, in general, the resistivity $\rho \leqslant 300\ \mu\Omega \cdot$cm. Thus, in the corresponding temperature region the electrical resistivity of these systems is mainly determined by the mean free path of the conduction electrons.[1]

In Ref. 5 we reported a low-temperature ($T \approx 20$ K) minimum in the temperature dependence of the resistivity of icosahedral quasicrystalline and superconducting alloys of the Ti–Zr–Ni family. In the present work we report an investigation of the electrical conductivity of alloys of the system Ti–Zr–Ni in a broad temperature range, including a study of the superconducting transition in magnetic fields.

2. EXPERIMENT

2.1. Samples

Thin ribbons of quasicrystalline $Ti_{41.5}Zr_{41.5}Ni_{17}$ were obtained by quenching the corresponding liquid on a rapidly rotating copper disk in a pure argon atmosphere. As initial elements we used Ti, Zr, and Ni of 99.9 purity.[4] The tangential velocity of the disk surface at quenching was $v = 19.5$ and 25 m/s (samples S19 and S25, respectively). X-ray fluorescence chemical composition control showed less than 0.5% deviation of the resulting sample composition from the nominal one. The electrical resistivity measurements were done on ribbons with an approximate size of $15 \times 2 \times (0.02-0.04)$ mm.

2.2. Measurements

The phase composition of the samples was determined by x-ray diffraction using Cu-K_α and Fe-K_α radiation. The quasicrystalline phase was identified following the method described in Refs. 7–9. Indices for each diffraction peak of the icosahedral structure were attributed following the scheme proposed by Cahn *et al.*[7] According to this scheme, the six-index reflection representation (n_1, n_2, n_3, n_4, n_5, n_6) is replaced, for simplicity, by a two-index version—(N,M). For characterizing the quasicrystalline structure we used the quasicrystallinity parameter a_q which is related to the modulus of the diffraction vector, $|\mathbf{Q}|$, as

 © 2005 American Institute of Physics

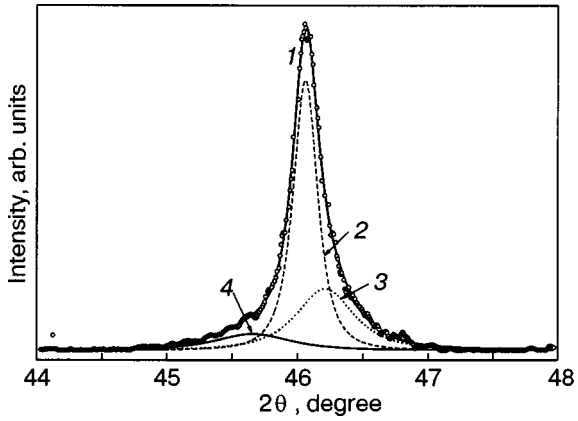

FIG. 1. Experimental distribution of intensity of the diffraction peak (18,29) for sample S25 in λ_{K_α}–Fe radiation (*1*) and the results of a full-profile computer analysis. Curves *2*, *3*, and *4* correspond to the maxima F1, F2, and F3, respectively.

$$Q=\frac{4\pi\sin\theta}{\lambda}=\frac{\pi}{a_q}\sqrt{\frac{N+M\tau}{2+\tau}}, \tag{1}$$

where $\tau=1.618\ldots$ is the irrational ''golden'' mean.

The coherence length, L, was estimated from the width of the diffraction lines.

The measurements of the electrical resistivity were done using a standard four-point arrangement. The temperature was measured with ruthenium-oxide thermometers in the interval 0.3–2 K and with rhodium-iron thermometers in the interval 1.5–300 K.

3. RESULTS

3.1. X-ray characteristics of the samples

The x-ray analysis of the samples in a wide range of diffraction angles revealed no admixture of crystalline phases.

A typical feature of the diffraction pictures is the observed asymmetry of the diffraction profiles in the shape of pronounced ''tails.'' For the sample S19, such a ''tail'' appears at high diffraction angles, but for S25 the ''tail'' is more pronounced on the small-angle side. The asymmetry is more substantial if the profiles are recorded using softer Fe–K_α radiation. The observed diffraction peak intensity distribution is typical for all observed reflections and it can be related to the presence of weak unresolved lines.

A part of the typical diffraction pattern taken with Fe–K_α radiation for sample S25 is presented in Fig. 1. It includes one of the strongest reflections with the attributed indices (18,29). The separation of diffraction peaks into components was done using a full-profile analysis after a standard treatment involving a background separation and the subtraction of the $K_{\alpha 2}$ doublet. The complex diffraction profile was simulated as a sum of separate peaks described by the Cauchy functions of first and second order. The minimum number of peaks providing the minimum deviation of the summary profiles from the experimental intensity distribution was equal to three for both samples. For each peak, we determined the position, the width and the integral intensity. The results of the signal separation into three components are displayed in Fig. 1.

TABLE I. Average values of the quasicrystallinity parameter, a_q, the line half-width B, and the volume portions of different phases in the samples.

Phase	S19, v = 19,5 m/s			S25, v = 25 m/s		
	a_q, Å	B, deg	Volume portion	a_q, Å	B, deg	Volume portion
P1	5.217	0.22	0.75	5.214	0.13	0.73
P2	5.184	0.33	0.22	5.188	0.32	0.17
P3	5.267	0.49	0.03	5.282	0.36	0.10

We denote the most intensive (main) peak as P1 and the weak additional peaks as P2 (left) and P3 (right). All additional peaks have the same indices as the main peaks, for all reflections in the spectrum. This implies that the sample contains three quasicrystalline phases with slightly different compositions.

It cannot be ruled out, however, that one of the phases may be a crystalline approximant W1/1. From the results of the separation, the quasicrystallinity parameter a_q and the phase volume portions were determined; they are presented in Table I.

Phase P2 (peak F2) is observed in both samples, although there is more of it in S19. The content of phase P3 is significant in S25, while its contribution in S19 is below the limit of experimental uncertainty. The volume portions of phases P2 and P3 are increasing towards the free surface within a subsurface layer of 2–3 μm. The lines of phase P2 are observed near all the main reflections [for example, (18,29), (20,32), (52,84), (136,220)] and give the same value of the parameter a_q. Therefore, we can conclude that this phase is indeed quasicrystalline.

As is seen from Table I, the volume portions of P1 and P2 as well as the corresponding a_q values are practically equal for both samples. In addition, we note that in sample S25, the linewidth is smaller and hence, the structural perfection is higher.

3.2. Temperature dependence of the electrical resistivity

The experimental data are presented in Fig. 2. We notice the following features in the temperature dependence of the electrical resistivity for the investigated quasicrystals $Ti_{41.5}Zr_{41.5}Ni_{17}$.

i) Shallow minima in $\rho(T)$ are observed near 20 and 50 K for samples S19 and S25, respectively.

ii) At temperatures above the minima ($T>20$ K for S19 and $T>50$ K for S25), a metallic behavior of the resistivity ($d\rho/dT>0$) is observed. The increase of the resistivity in the temperature range between $T_{\min}$ and 300 K is of the order of 3%.

iii) At temperatures below 1.6 K, onsets of transitions to superconductivity are identified. Zero resistivity was only observed for sample S25 at $T\approx 0.35$ K (Fig. 3b).

3.3. The influence of magnetic field on the superconducting transition temperature

In Fig. 3, the transitions to the superconducting state for samples S19 (a) and S25 (b) in magnetic fields up to 16 kOe are shown. The multistep character of the transitions is most

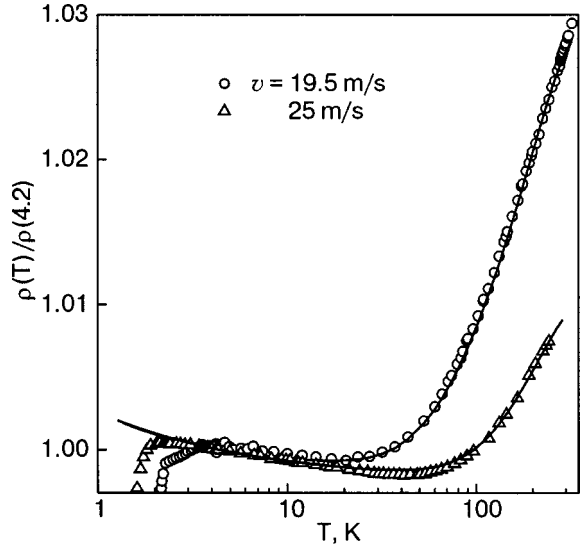

FIG. 2. The temperature dependence of the electrical resistivity of icosahedral quasicrystals $Ti_{41.5}Zr_{41.5}Ni_{17}$. The lines are to guide the eye.

likely caused by inhomogeneities of the samples' phase compositions. The upper limits for the values of the upper critical fields, H_{c2}, were determined from the onset of the deviation of $\rho(T)$ from the normal-state level. The resulting diagrams $H_{c2}(T)$ are presented in Fig. 4.

4. DISCUSSION

4.1. The composition of phases

It is known[10] that, in first approximation, the quasicrystallinity parameter is equal to the radius of the Bergman's cluster. This cluster is a structural unit of Ti–Zr–Ni icosahedral quasicrystals. It is clear that its size depends on which kind of atoms and how many of them form the cluster. Figure 5 shows the value a_q as a function of the average atomic radius of the alloy, according to our data and data from the literature.[3,11,12]

From this plot one can determine the average atomic radii for phases P1, P2, and P3. Here one has to take into account the following: 1) the dependence in Fig. 5 corresponds to compounds in a rather narrow homogeneity region of the *i*-QC phase, and 2) differences in the magnitude of a_q for three phases under consideration cannot be large. Taking into account the above-mentioned arguments, one can practically unambiguously identify the composition of the phases with an accuracy of $\sim$0.5 at.%. The reliability criterion for the selection is the coincidence of the nominal $Ti_{41.5}Zr_{41.5}Ni_{17}$ sample composition with the value calculated by adding up the three identified phases with their volume portions. The best agreement is obtained if the phases have the following compositions: P1—$Ti_{40}Zr_{42.5}Ni_{17.5}$, P2—$Ti_{40}Zr_{40}Ni_{20}$, and P3—$Ti_{43.5}Zr_{43.5}Ni_{13}$.

Note that, according to the equilibrium diagram for Ti–Zr–Ni system, the phase compositions P1 and P2 are in the stability region of the quasicrystalline phase. The phase P3 composition lies within the existence region of the 1/1 approximant.[13,14]

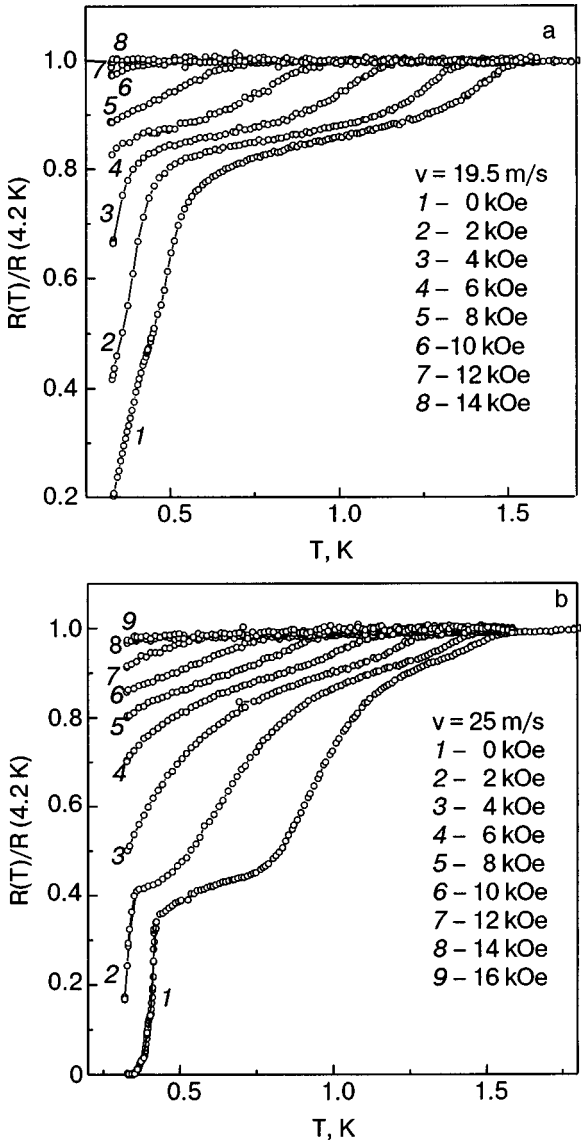

FIG. 3. Electrical resistivity of icosahedral quasicrystals $Ti_{41.5}Zr_{41.5}Ni_{17}$ in magnetic field: S19 (a), S25 (*b*).

4.2. The superconducting transition

The multistep behavior of $\rho(T)$ at low temperatures, which is observed for both samples, is consistent with the

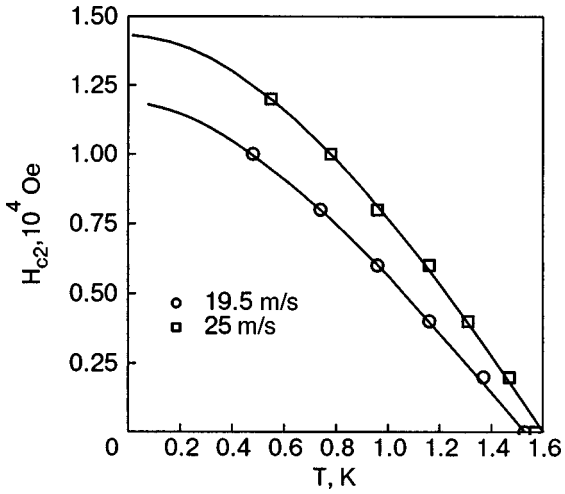

FIG. 4. Temperature dependence of the upper critical field of icosahedral quasicrystals $Ti_{41.5}Zr_{41.5}Ni_{17}$. The lines are to guide the eye.

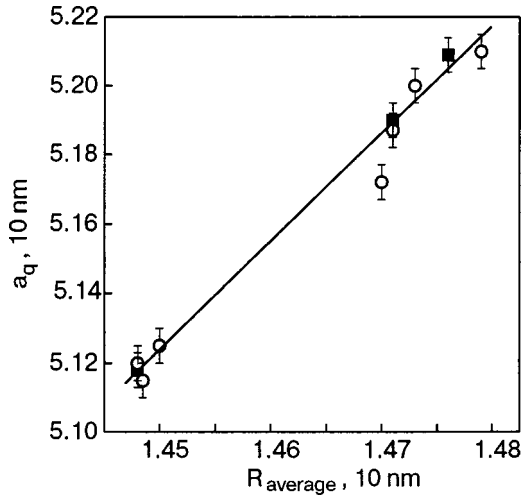

FIG. 5. Quasicrystallinity parameter as a function of the average atomic radius. Solid symbols are our data; open symbols are data from the literature.[3,11,12]

data of the x-ray phase analysis. In zero magnetic field there are three steps in the resistivity drop for sample S25, which we interpret as superconducting transitions in each phase. For S19, only two such steps are observed because one of the phases (P3) is practically absent in this specimen (Fig. 3). It is difficult to ascribe each $\rho(T)$ step to a particular phase because of the complex interconnection between regions of various size and different phases and the associated proximity effect. However, since the resistivity reaches zero only for sample S25 at $T<0.4$ K (Fig. 3b), it is plausible that it is phase P1 which is the main component of this sample that is responsible for the relatively sharp step in the region $T<0.4$ K, leading to the zero resistivity. Because in sample S19 the phase structure is less perfect than in S25, the superconducting transition for the P1 phase in S19 is broader, and in the covered temperature range ($T>0.3$ K), zero resistance is not achieved.

The broader superconducting transitions in phases P1 and P2 seem to lead to the step-like features in the temperature dependence of the electrical resistivity.

4.3. The temperature dependence of the upper critical field

In Fig. 4, the temperature dependences of the upper critical field $H_{c2}(T)$ are shown for phase P2, which has the maximum superconducting critical temperature in both samples. One can see that $H_{c2}(T)$ is higher for the structurally more perfect sample S25. Our data are qualitatively similar to the $H_{c2}(T)$ curves for icosahedral quasicrystals Al–Cu–Li and Al–Cu–Mg, obtained in Ref. 3. However, the critical fields at low temperatures for quasicrystals of system Ti–Zr–Ni are considerably higher than those for Al–Cu–Li and Al–Cu–Mg, in spite of the similar values of T_c of these alloys, between 0.8 and 1.5 K.[3]

4.4. The temperature dependence of the resistivity

The minima in $\rho(T)$ may be caused by the influence of weak localization of electrons at low temperatures.[6] Above $T_{\min}$, the temperature variation of the resistivity is close to $\rho(T)\propto T^3$. For metallic systems this is usually related to electron-phonon s-d scattering, although in our case its contribution to the total resistivity is largely masked by much stronger scatterings caused by the structural disorder, the electron-electron interaction, and localization effects.

We note that for sample S25, which appears to be structurally more perfect, the resistivity minimum appears at a distinctly higher temperature ($T_{\min}\approx 50$ K) than for the less perfect sample S19 ($T_{\min}\approx 20$ K).

5. CONCLUSIONS

We have investigated the phase composition, the structure and the temperature dependence of electrical resistivity of icosahedral quasicrystals of nominal composition $Ti_{41.5}Zr_{41.5}Ni_{17}$ in the region 0.3–300 K. In the region 0.3–1.6 K, the influence of magnetic fields up to 16 kOe on the superconducting transition was investigated.

The x-ray analysis revealed the existence of three phases with almost equal chemical composition, two of which are icosahedral and the third phase can be associated with the 1/1 approximant. The volume concentration of the phases was estimated, and the superconducting temperatures were determined.

The upper critical field obtained for the phase with the highest Tc is higher for the structurally more perfect sample.

The temperature dependence of the resistivity in the region between T_c and $T_{\min}$ is probably determined by effects of weak localization of conduction electrons. At $T>T_{\min}$, the influence of the scattering of electrons by phonons is also observed. The resistivity minimum for the more perfect sample is shifted to higher temperatures in comparison to the less perfect sample.

This work was supported by Swiss National Science Foundation as part of Joint Research Project No. 7UKPJ062171.

*E-mail: George.Ya.Khadjai@univer.kharkov.ua

[1] U. Mizutani, Mater. Sci. Eng. **294–296**, 464 (2000).
[2] J. F. Graebner and H. S. Chen, Phys. Rev. Lett. **58**, 1945 (1987).
[3] J. L. Wagner, B. D. Bigs, K. M. Wong, and S. J. Poon, Phys. Rev. Lett. B **38**, 7436 (1988).
[4] V. Azhazha, A. Grib, G. Khadzhay, S. Malikhin, B. Merisov, and A. Pugachov, Phys. Lett. A **303**, 87 (2002).
[5] V. Azhazha, G. Khadzhay, S. Malikhin, B. Merisov, and A. Pugachov, Phys. Lett. A **349**, 539 (2003).
[6] Z. M. Stadnik (ed.), *Physical Properties of Quasicrystals*, Springer, Berlin (1999).
[7] J. W. Cahn, D. Shechtman, and D. Gratias, J. Mater. Res. **1**, 13 (1986).
[8] S. Ebalard and F. Spaepen, J. Mater. Res. **4**, 39 (1989).
[9] P. J. Lu, K. Deffeyes, P. J. Steinhardt, and N. Yao, Phys. Rev. Lett. **87**, 275507-1 (2001).
[10] V. Azhazha, S. Dub, G. Khadzhay, B. Merisov, S. Malykhin, and A. Pugachov, Philos. Mag. **84**, 983 (2004).
[11] A. M. Viano, E. H. Majzoub, R. M. Stroud, M. J. Kramer, S. T. Misture, P. C. Gibbons, and K. F. Kelton, Philos. Mag. A **78**, 131 (1998).
[12] R. Nicula, A. Jianu, and A. R. Biris, Eur. Phys. J. B **3**, 1 (1998).
[13] I. Davis, E. Majzoub, J. Simmons, and K. Kelton, Mater. Sci. Eng. **296**, 104 (2000).
[14] K. F. Kelton, A. K. Gangopadhyay, G. W. Lee, L. Hannet, R. W. Hyers, S. Krishnan, M. B. Robinson, J. Rogers, and T. J. Rathz, J. Cryst. Solids **312–314**, 305 (2002).

This article was published in English in the original Russian journal. Reproduced here with stylistic changes by AIP.

Stationary Josephson effect in a weak link between nonunitary triplet superconductors

G. Rashedi*

Institute for Advanced Studies in Basic Sciences, Zanjan, 45195-1159, Iran; Department of Physics, Faculty of Science, University of Shahrekord, P.O. Box 115, Shahrekord, Iran

Yu. A. Kolesnichenko

B. Verkin Institute for Low Temperature Physics and Engineering of National Academy of Sciences of Ukraine, 47, Lenin Ave., Kharkov 61103, Ukraine

(Submitted November 5, 2004)
Fiz. Nizk. Temp. **31**, 634–639 (June 2005)

A stationary Josephson effect in a weak link between misoriented nonunitary triplet superconductors is investigated theoretically. The non-self-consistent quasiclassical Eilenberger equation for this system is solved analytically. As an application of this analytical calculation, the current-phase diagrams are plotted for the junction between two nonunitary bipolar f-wave superconducting banks. A spontaneous current parallel to the interface between superconductors is observed. Also, the effect of misorientation between crystals on the Josephson and spontaneous currents is studied. Such experimental investigations of the current-phase diagrams can be used to test the pairing symmetry in the above-mentioned superconductors. © *2005 American Institute of Physics.* [DOI: 10.1063/1.1943531]

1. INTRODUCTION

In recent years, triplet superconductivity has become a popular subject for research in the field of superconductivity.[1–3] Particularly, the nonunitary spin triplet state in which Cooper pairs may carry a finite averaged intrinsic spin moment has attracted much attention in the last decade.[4,5] A triplet state in the momentum space $\mathbf{k}$ can be descbribed by the order parameter $\hat{\Delta}(\mathbf{k})=i(\mathbf{d}(\mathbf{k})\cdot\hat{\sigma})\hat{\sigma}_y$ in a 2×2 matrix form in which the $\hat{\sigma}_j$ are 2×2 Pauli matrices $(\hat{\sigma}=(\hat{\sigma}_x,\hat{\sigma}_y,\hat{\sigma}_z))$. The three-dimensional complex vector $\mathbf{d}(\mathbf{k})$ (gap vector) describes the triplet pairing state. In the nonunitary state, the product $\hat{\Delta}(\mathbf{k})\hat{\Delta}(\mathbf{k})^{\dagger}=\mathbf{d}(\mathbf{k})\cdot\mathbf{d}^*(\mathbf{k})+i(\mathbf{d}(\mathbf{k})\times\mathbf{d}^*(\mathbf{k}))\cdot\hat{\sigma}$ is not a multiple of the unit matrix. Thus in a nonunitary state the time reversal symmetry is necessarily broken spontaneously and a spontaneous moment $\mathbf{m}(\mathbf{k})\times i\mathbf{d}(\mathbf{k})\times\mathbf{d}^*(\mathbf{k})$ appears at each point $\mathbf{k}$ of the momentum space. In this case the macroscopically averaged moment $\langle\mathbf{m}(\mathbf{k})\rangle$ integrated on the Fermi surface does not vanish. The value $\mathbf{m}(\mathbf{k})$ is related to the net spin average by $\mathrm{Tr}[\hat{\Delta}(\mathbf{k})^{\dagger}\hat{\sigma}_j\hat{\Delta}(\mathbf{k})]$. It is clear that the total spin average over the Fermi surface can be nonzero. As an application, the nonunitary bipolar state of f-wave pairing symmetry has been considered for the B phase of superconductivity in the compound UPt_3 which has been created at low temperatures T and small values of the magnetic field H.[5,6]

In the present paper, the ballistic Josephson weak link via an interface between two superconducting bulks with different orientations of the crystallographic axes is investigated. This type of weak-link structure can be used for the demonstration of the pairing symmetry in the superconducting phase.[7] Consequently, we generalize the formalism of Ref. 8 for the weak link between triplet superconducting bulks with a nonunitary order parameter. In the Ref. 8 the Josephson effect at a point contact between unitary f-wave triplet superconductors was studied. Also, the effect of misorientation on the charge transport was investigated, and a spontaneous current tangential to the interface between the f-wave superconductors was observed.

In this paper the nonunitary bipolar f-wave model of the order parameter is considered. It is shown that the current-phase diagrams are totally different from the current-phase diagrams of the junction between the unitary triplet (axial and planar) f-wave superconductors.[8] Roughly speaking, these different characters can be used to distinguish between nonunitary bipolar f-wave superconductivity and the other types of superconductivity. In the weak-link structure between the nonunitary f-wave superconductors, the spontaneous current parallel to the interface has been observed as a fingerprint for unconventional superconductivity and spontaneous time reversal symmetry breaking. The effect of misorientation on the spontaneous and Josephson currents is investigated. It is possible to find a value of the phase difference at which the Josephson current is zero but a spontaneous current, which is produced by the interface and is tangential to the interface, is present. In some configurations and at the zero phase difference, the Josephson current is not generally zero but has a finite value. This finite value corresponds to a spontaneous phase difference which is related to the misorientation between the gap vectors $\mathbf{d}$.

The arrangement of the rest of this paper is as follows. In Sec. 2 we describe the configuration that we have investigated. For a non-self-consistent model of the order parameter, the quasiclassical Eilenberger equations[9] are solved and suitable Green functions are obtained analytically. In Sec. 3 the formulas obtained for the Green functions are used for the calculation of the current densities at the interface. An analysis of numerical results will be presented in Sec. 4 together with some conclusions in Sec. 5.

 © 2005 American Institute of Physics

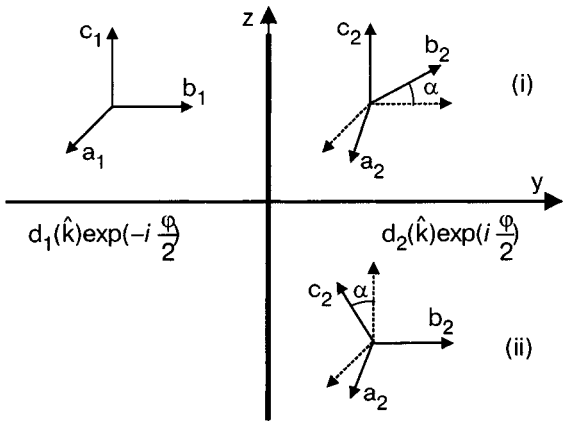

FIG. 1. Scheme of a flat interface between two superconducting bulks which are misoriented as much as α.

2. FORMALISM AND BASIC EQUATIONS

We consider a model of a flat interface $y=0$ between two misoriented nonunitary f-wave superconducting half-spaces (Fig. 1) as a ballistic Josephson junction. In the quasiclassical ballistic approach, in order to calculate the current, we use ''transport-like'' quasiclassical Eilenberger equations[9] for the energy-integrated Green functions $\check{g}(\hat{\mathbf{v}}_F,\mathbf{r},\varepsilon_m)$

$$v_F\cdot\nabla\check{g}+[\varepsilon_m\check{\sigma}_3+i\check{\Delta},\check{g}]=0, \tag{1}$$

and the normalization condition $\check{g}\check{g}=\check{1}$, where $\varepsilon_m=\pi T(2m+1)$, with $m=1,2,\ldots$, are discrete Matsubara energies, T is the temperature, $\mathbf{v}_F$ is the Fermi velocity, and $\check{\sigma}_3=\hat{\sigma}_3\otimes\hat{I}$, in which the $\hat{\sigma}_j$ $(j=1,2,3)$ are Pauli matrices. The Matsubara propagator $\check{g}$ can be written in the form:

$$\check{g}=\begin{pmatrix} g_1+g_1\cdot\hat{\sigma} & (g_1+g_2\cdot\hat{\sigma})i\hat{\sigma}_2 \\ i\hat{\sigma}_2(g_1+g_3\cdot\hat{\sigma}) & g_4-\hat{\sigma}_2 g_4\cdot\hat{\sigma}\hat{\sigma}_2 \end{pmatrix}, \tag{2}$$

where the matrix structure of the off-diagonal self-energy $\check{\Delta}$ in the Nambu space is

$$\check{\Delta}=\begin{pmatrix} 0 & \mathbf{d}\cdot\hat{\sigma}i\hat{\sigma}_2 \\ i\hat{\sigma}_2\mathbf{d}^*\cdot\hat{\sigma} & 0 \end{pmatrix}. \tag{3}$$

The nonunitary states, for which $\mathbf{d}\times\mathbf{d}^*\neq 0$ are investigated. Fundamentally, the gap vector (order parameter) $\mathbf{d}$ has to be determined numerically from the self-consistency equation,[1] while in the present paper, we use a non-self-consistent model for the gap vector which is much more suitable for analytical calculations.[10] Solutions to Eq. (1) must satisfy the following conditions for the Green functions and the gap vector $\mathbf{d}$ in the bulks of the superconductors far from the interface:

$$\check{g}=\frac{1}{\Omega_n}\begin{pmatrix} \varepsilon_m(1-\mathbf{A}_n\cdot\hat{\sigma}) & [i\mathbf{d}_n-\mathbf{d}_n\times\mathbf{A}_n]\cdot\hat{\sigma}i\hat{\sigma}_2 \\ i\hat{\sigma}_2[i\mathbf{d}_n^*+\mathbf{d}_n^*\times\mathbf{A}_n]\cdot\hat{\sigma} & -\varepsilon\hat{\sigma}_2(1+\mathbf{A}_n\cdot\hat{\sigma})\hat{\sigma}_2 \end{pmatrix}, \tag{4}$$

where

$$\mathbf{A}_n=\frac{i\mathbf{d}_n\times\mathbf{d}_n^*}{\varepsilon_m^2+\mathbf{d}_n\cdot\mathbf{d}_n^*+\sqrt{(\varepsilon_m^2+\mathbf{d}_n\cdot\mathbf{d}_n^*)^2+(\mathbf{d}_n\times\mathbf{d}_n^*)^2}} \tag{5}$$

and

$$\Omega_n=\sqrt{\frac{2[(\varepsilon_m^2+\mathbf{d}_n\cdot\mathbf{d}_n^*)^2+(\mathbf{d}_n\times\mathbf{d}_n^*)^2]}{\varepsilon_m^2+\mathbf{d}_n\cdot\mathbf{d}_n^*+\sqrt{(\varepsilon_m^2+\mathbf{d}_n\cdot\mathbf{d}_n^*)^2+(\mathbf{d}_n\times\mathbf{d}_n^*)^2}}} \tag{6}$$

$$\mathbf{d}(\pm\infty)=\mathbf{d}_{1,2}(T,\hat{\mathbf{v}}_F)\exp\left(\mp\frac{i\varphi}{2}\right), \tag{7}$$

where φ is the external phase difference between the order parameters of the bulks and $n=1,2$ labels the left and right half-spaces, respectively. It is clear that poles of the Green function in the energy space are at

$$\Omega_n=0. \tag{8}$$

Consequently,

$$(-E^2+\mathbf{d}_n\cdot\mathbf{d}_n^*)^2+(\mathbf{d}_n+\mathbf{d}_n^*)^2=0 \tag{9}$$

and

$$E=\pm\sqrt{\mathbf{d}_n\cdot\mathbf{d}_n^{*2}\pm i\mathbf{d}_n\times\mathbf{d}_n^*} \tag{10}$$

in which E is the energy value of the poles. Equation (1) has to be supplemented by the continuity conditions at the interface between superconductors. For all quasiparticle trajectories, the Green functions satisfy the boundary conditions both in the right and left bulks as well as at the interface. The system of equations (1) and the self-consistency equation for the gap vector $\mathbf{d}$ (Ref. 1) can be solved only numerically. For unconventional superconductors such solution requires information about the interaction between the electrons in the Cooper pairs and the nature of unconventional superconductivity in novel compounds which in most cases is unknown. Also, it has been shown that the absolute value of a self-consistent order parameter is suppressed near the interface and at the distances of the order of the coherence length, while its dependence on the direction in the momentum space almost remains unaltered.[11] This suppression of the order parameter changes the amplitude value of the current, but does not influence the current-phase dependence drastically. For example, it has been verified in Ref. 12 for the junction between unconventional d-wave superconductors, in Ref. 11 for the case of unitary ''f-wave'' superconductors, and in Ref. 13 for pinholes in ^{3}He, that there is good qualitative agreement between self-consistent and non-self-consistent results for not very large angles of misorientation. It has also been observed that the results of the non-self-consistent model in Ref. 14 are similar to experiment.[15] Consequently, despite the fact that this solution cannot be applied directly to a quantitative analysis of a real experiment, only a qualitative comparison of calculated and experimental current-phase relations is possible. In our calculations, a simple model of the constant order parameter up to the interface is considered, and the pair-breaking and scattering on the interface are ignored. We believe that under these strong assumptions our results describe the real situation qualitatively. In the framework of such a model, analytical expressions for the current can be obtained for a certain form of the order parameter.

3. ANALYTICAL RESULTS

The solution of Eq. (1) allows us to calculate the current densities. The expression for the current is

$$\mathbf{j}(\mathbf{r})=2i\pi eTN(0)\sum_m \langle \mathbf{v}_F g_1(\hat{\mathbf{v}}_F,\mathbf{r},\varepsilon_m)\rangle, \tag{11}$$

where $\langle ...\rangle$ stands for averaging over the directions of an electron momentum on the Fermi surface $\hat{\mathbf{v}}_F$ and $N(0)$ is the electron density of states at the Fermi level of energy. We assume that the order parameter is constant in space and in each half-space it equals its value (7) far from the interface in the left or right bulks. For such a model, the current-phase dependence of a Josephson junction can be calculated analytically. It enables us to analyze the main features of current-phase dependence for any model of the nonunitary order parameter. The Eilenberger equations (1) for Green functions $\check{g}$, which are supplemented by the condition of continuity of solutions across the interface, $y=0$, and the boundary conditions at the bulks, are solved for a non-self-consistent model of the order parameter analytically. In the ballistic case the system of equations for functions g_i and $\mathbf{g}_i$ can be decomposed into independent blocks of equations. The set of equations which enables us to find the Green function g_1 is:

$$v_F\hat{\mathbf{k}}\nabla\mathbf{g}_1=i(\mathbf{d}\cdot\mathbf{g}_3-\mathbf{d}^*\cdot\mathbf{g}_2); \tag{12}$$

$$v_F\hat{\mathbf{k}}\nabla\mathbf{g}_-=-2(\mathbf{d}\times\mathbf{g}_3+\mathbf{d}^*\times\mathbf{g}_2); \tag{13}$$

$$v_F\hat{\mathbf{k}}\nabla\mathbf{g}_2=-2\varepsilon_m\mathbf{g}_2+2ig_1\mathbf{d}+\mathbf{d}\times\mathbf{g}_-; \tag{14}$$

$$v_F\hat{\mathbf{k}}\nabla\mathbf{g}_3=2\varepsilon_m\mathbf{g}_3-2ig_1\mathbf{d}^*+\mathbf{d}^*\times\mathbf{g}_-, \tag{15}$$

where $\mathbf{g}_-=\mathbf{g}_1-\mathbf{g}_4$. Equations (12)–(14) can be solved by integrating over the ballistic trajectories of electrons in the right and left half-spaces. The general solution satisfying the boundary conditions (4) at infinity is

$$g_1^{(n)}=\frac{\varepsilon_m}{\Omega_n}+a_n\exp(-2s\Omega_n t); \tag{16}$$

$$\mathbf{g}_-^{(n)}=-2\frac{\varepsilon_m}{\Omega_n}\mathbf{A}_n+\mathbf{C}_n\exp(-2s\Omega_n t); \tag{17}$$

$$\mathbf{g}_2^{(n)}=\frac{i\mathbf{d}_n-\mathbf{d}_n\times\mathbf{A}_n}{\Omega_n}-\frac{2ia_n\mathbf{d}_n+\mathbf{d}_n\times\mathbf{C}_n}{2s\eta\Omega_n-2\varepsilon_m}\mathrm{e}^{-2s\Omega_n t}; \tag{18}$$

$$\mathbf{g}_3^{(n)}=\frac{i\mathbf{d}_n^*+\mathbf{d}_n^*\times\mathbf{A}_n}{\Omega_n}+\frac{2ia_n\mathbf{d}_n^*-\mathbf{d}_n^*\times\mathbf{C}_n}{2s\eta\Omega_n+2\varepsilon_m}\mathrm{e}^{-2s\Omega_n t}, \tag{19}$$

where t is the time of flight along the trajectory, $\mathrm{sgn}(t)=\mathrm{sgn}(y)=s$ and $\eta=\mathrm{sgn}(v_y)$. By matching the solutions (16)–(19) at the interface ($y=0,t=0$), we find the constants a_n and $\mathbf{C}_n$. Indices $n=1,2$ label the left and right half-spaces, respectively. The function $g_1(0)=g_1^{(1)}(-0)=g_1^{(2)}(+0)$ which is a diagonal term of the Green matrix and determines the current density at the interface, $y=0$, is as follows:

$$g_1(0)=\frac{\eta[\mathbf{d}_2\cdot\mathbf{d}_2(\eta\Omega_1+\varepsilon)^2-\mathbf{d}_1\cdot\mathbf{d}_1(\eta\Omega_2-\varepsilon)^2+B]}{[\mathbf{d}_2(\eta\Omega_1+\varepsilon)+\mathbf{d}_1(\eta\Omega_2-\varepsilon)]^2}, \tag{20}$$

where $B=i\mathbf{d}_1\times\mathbf{d}_2\cdot(\mathbf{A}+\mathbf{A}_2)(\eta\Omega_2-\varepsilon)(\eta\Omega_1+\varepsilon)$. We consider a rotation $\check{R}$ only in the right superconductor (see Fig. 1), i.e., $\mathbf{d}_2(\hat{\mathbf{k}})=\check{R}\mathbf{d}_1(\check{R}^{-1}\hat{\mathbf{k}})$; $\hat{\mathbf{k}}$ is the unit vector in the momentum space. The crystallographic c axis in the left half-space is selected parallel to the partition between the superconductors (along the z axis in Fig. 1). To illustrate the results obtained by computing the formula (20), we plot the current-phase diagrams for two different geometries. These geometries correspond to the different orientations of the crystals in the right and left sides of the interface (Fig. 1).

(i) The basal ab plane in the right side has been rotated around the c axis by α; $\hat{\mathbf{c}}_1\|\hat{\mathbf{c}}_2$.

(ii) The c axis in the right side has been rotated around the b axis by α; $\hat{\mathbf{b}}_1\|\hat{\mathbf{b}}_2$.

Further calculations require a certain model of the gap vector (order parameter) **d**.

4. ANALYSIS OF NUMERICAL RESULTS

In the present paper, the nonunitary f-wave gap vector in the B phase (low temperature T and low field H) of superconductivity in the compound UPt_3 has been considered. This nonunitary bipolar state which explains the weak spin-orbit coupling in UPt_3 is:[5]

$$\mathbf{d}(T,\mathbf{v}_F)=\Delta_0(T)k_z(\hat{\mathbf{x}}(k_x^2-k_y^2)+\hat{\mathbf{y}}2ik_xk_y). \tag{21}$$

The coordinate axes $\hat{\mathbf{x}},\hat{\mathbf{y}},\hat{\mathbf{z}}$ are chosen along the crystallographic axes $\hat{\mathbf{a}},\hat{\mathbf{b}},\hat{\mathbf{c}}$ in the left side of Fig. 1. The function $\Delta_0=\Delta_0(T)$ describes the dependence of the gap vector on the temperature T (our numerical calculations are done at the low value of temperature $T/T_c=0.1$). Using this model of the order parameter (21) and solution to the Eilenberger equations (20), we have calculated the current density at the interface numerically. These numerical results are listed below.

1. The nonunitary property of Green's matrix diagonal term consists of two parts. An explicit part, which is contained in the mathematical expression B in Eq. (20), and an implicit part in the $\Omega_{1,2}$ and $\mathbf{d}_{1,2}$ terms. These $\Omega_{1,2}$ and $\mathbf{d}_{1,2}$ terms are different from their unitary counterparts. In the mathematical expression for $\Omega_{1,2}$ the nonunitary mathematical terms $\mathbf{A}_{1,2}$ are presented. The explicit part will be present only in the presence of misorientation between gap vectors, $B=i\mathbf{d}_1\times\mathbf{d}_2\cdot(\mathbf{A}_1+\mathbf{A}_2)(\eta\Omega_2-\varepsilon)(\eta\Omega_1+\varepsilon)$, but the implicit part will be present always. So, in the absence of misorientation ($\mathbf{d}_1\|\mathbf{d}_2$), although the implicit part of nonunitary exists the explicit part is absent. This means that in the absence of misorientation, current-phase diagrams for planar unitary and nonunitary bipolar systems are the same, but the maximum values are slightly different.

2. For geometry (i) one of the current components parallel to the interface, j_z, is zero, as in the unitary case,[8] while the other parallel component j_x has a finite value (see Fig. 4). This last is a difference between the unitary and nonunitary cases. Because in the junction between unitary f-wave superconducting bulks all parallel components of the current (j_x and j_z) for geometry (i) are absent.[8]

3. In Figs. 2 and 3 the Josephson current j_y is plotted for a certain nonunitary f-wave model in different geometries. Figures 2 and 3 are plotted for the geometries (i) and (ii), respectively. They are completely unusual and totally different from their unitary counterparts which were obtained in Ref. 8.

4. In Fig. 2 for geometry (i), it is observed that by increasing the misorientation, some small oscillations appear in the current-phase diagrams as a result of the nonunitary

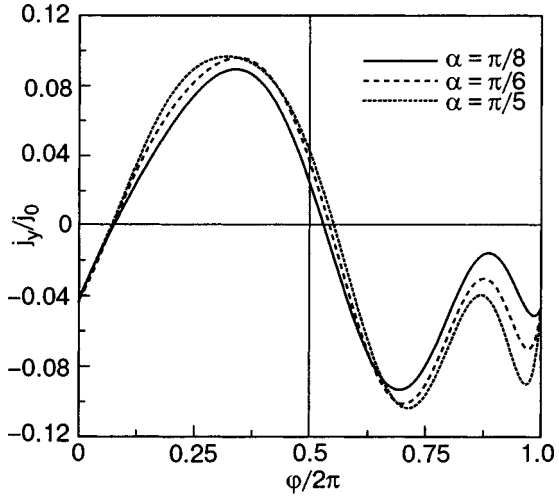

FIG. 2. Component of the current normal to the interface (Josephson current) versus the phase difference ε for the junction between nonunitary bipolar f-wave bulks, $T/T_c=0.15$, geometry (i), and different misorientations. Currents are given in units of $j_0=(\pi/2)\,eN(0)v_F\Delta_0(0)$.

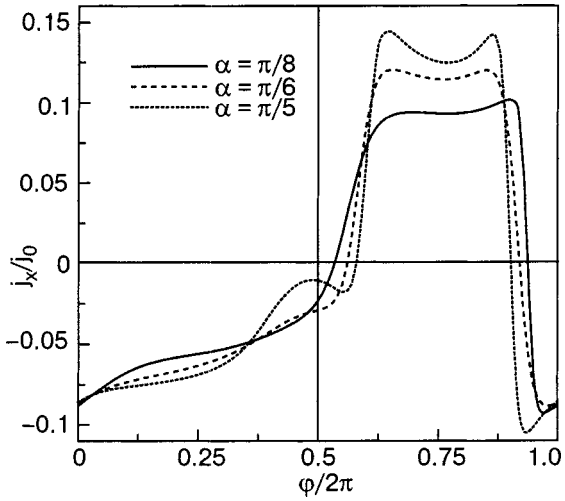

FIG. 4. The x component of the current tangential to the interface versus the phase difference ε for the junction between nonunitary bipolar f-wave superconducting bulks, $T/T_c=0.15$, geometry (i), and the different misorientations.

property of the order parameter. Also, the Josephson current at the zero external phase difference $\varphi=0$ is not zero but has a finite value. The Josephson current will be zero at the some finite values of the phase difference.

5. In Fig. 3 for geometry (ii), it is observed that by increasing the misorientation, new zeros appear in the current-phase diagrams, and the maximum value of the current will be change nonmonotonically. In contrast to the case for geometry (i) (Fig. 2), the Josephson currents at the phase differences $\varphi=0$, $\varphi=\pi$, and $\varphi=2\pi$ are exactly zero.

6. The current-phase diagram for geometry (i) and the x component (Fig. 4) is totally unusual. By increasing the misorientation, the maximum value of the current increases. The components of current parallel to the interface for geometry (ii) are plotted in Figs. 5 and 6. All the terms are zero at the phase differences $\varphi=0$, $\varphi=\pi$, and $\varphi=2\pi$. The maximum value of the current-phase diagrams is not a monotonic function of the misorientation.

5. CONCLUSIONS

Thus we have studied theoretically the supercurrents in a ballistic Josephson junction in the model of an ideal transparent interface between two misoriented UPt_3 crystals with nonunitary bipolar f-wave superconducting bulks which are subject to a phase difference φ. Our analysis has shown that misorientation between the gap vectors creates a current parallel to the interface and that different misorientations between gap vectors influence the spontaneous parallel and normal Josephson currents. These have been shown separately in Ref. 8 for the currents in point contacts between two bulk unitary axial superconductors and between two bulk planar f-wave superconductors. We have also shown that the misorientation of the superconductors leads to a spontaneous

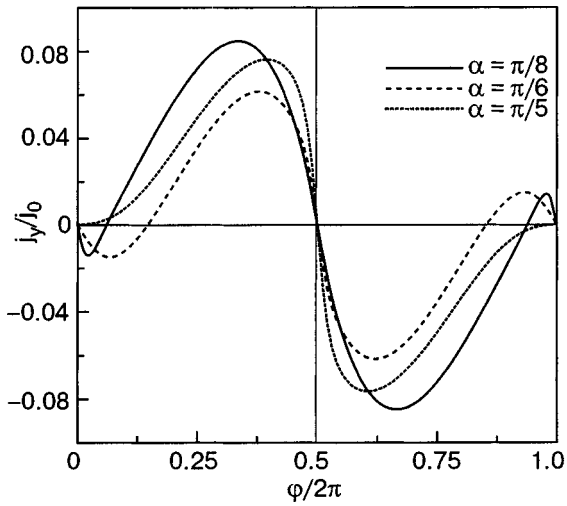

FIG. 3. Component of the current normal to the interface (Josephson current) versus the phase difference ε for the junction between nonunitary bipolar f-wave bulks, $T/T_c=0.15$, geometry (ii), and different misorientations.

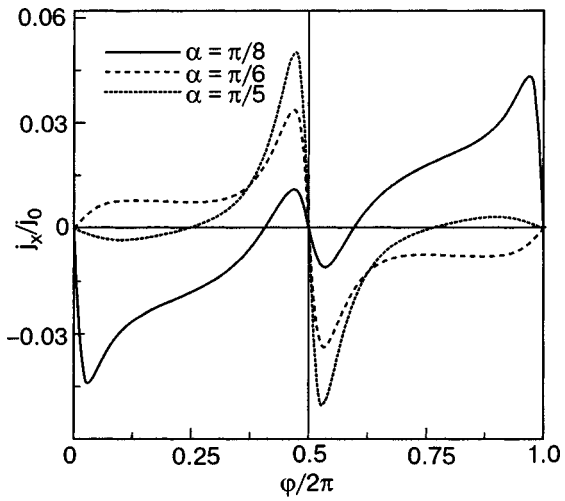

FIG. 5. Current tangential to the interface versus the phase difference ε for a junction between nonunitary bipolar f-wave superconducting bulks, $T/T_c=0.15$, geometry (ii), and the different misorientations (x component).

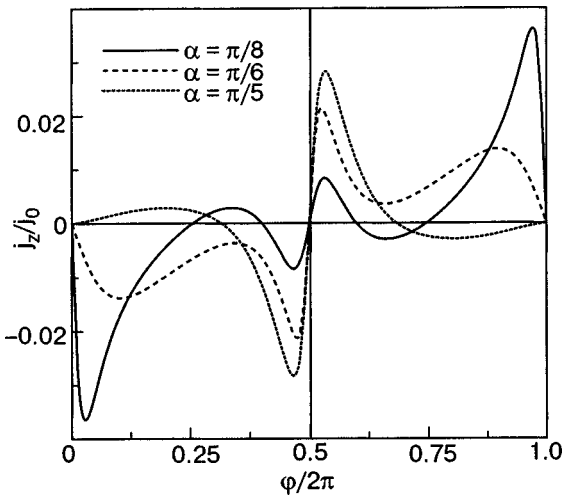

FIG. 6. Current tangential to the interface versus the phase difference ε for the junction between nonunitary bipolar f-wave superconducting bulks, $T/T_c = 0.15$, geometry (ii), and the different misorientations (z component).

phase difference that corresponds to zero Josephson current and to the minimum of the weak-link energy in the presence of a finite spontaneous current. This phase difference depends on the misorientation angle. The tangential spontaneous current is not generally equal to zero in the absence of the Josephson current. The difference between unitary planar and nonunitary bipolar states can be used to distinguish between them. This experiment can be used to test the pairing symmetry and recognize the different phases of UPt_3.

*E-mail: rashedy@www.iasbs.ac.ir

[1] M. Sigrist and K. Ueda, Rev. Mod. Phys. **63**, 239 (1991).
[2] Y. Maeno, H. Hashimoto, K. Yoshida, S. Nashizaki, T. Fujita, J. G. Bednorz, and F. Lichenberg, Nature (London) **372**, 532 (1994).
[3] A. P. Mackenzie and Y. Maeno, Rev. Mod. Phys. **75**, 657 (2003).
[4] H. Tou, Y. Kitaoka, K. Ishida, K. Asayama, N. Kimura, Y. Onuki, E. Yamamoto, Y. Haga, and K. Maezawa, Phys. Rev. Lett. **80**, 3129 (1998).
[5] K. Machida, T. Nishira, and T. Ohmi, J. Phys. Soc. Jpn. **68**, 3364 (1999).
[6] T. Ohmi and K. Machida, Phys. Rev. Lett. **71**, 625 (1993).
[7] N. Stefanakis, Phys. Rev. B **65**, 064533 (2002).
[8] R. Mahmoodi, S. N. Shevchenko, and Yu. A. Kolesnichenko, Fiz. Nizk. Temp. **28**, 262 (2002) [Low Temp. Phys. **28**, 184 (2002)].
[9] G. Eilenberger, Z. Phys. **214**, 195 (1968).
[10] I. O. Kulik and A. N. Omelyanchouk, Fiz. Nizk. Temp. **4**, 296 (1978) [Sov. J. Low Temp. Phys. **4**, 142 (1978)].
[11] Yu. S. Barash, A. M. Bobkov, and M. Fogelström, Phys. Rev. B **64**, 214503 (2001).
[12] M. H. S. Amin, M. Coury, S. N. Rashkeev, A. N. Omelyanchouk, and A. M. Zagoskin, Physica B **318**, 162 (2002).
[13] J. K. Viljas, cond-mat/0004246.
[14] S.-K. Yip, Phys. Rev. Lett. **83**, 3864 (1999).
[15] S. Backhaus, S. Pereverzev, R. W. Simmonds, A. Loshak, J. C. Davis, and R. E. Packard, Nature (London) **392**, 687 (1998).

This article was published in English in the original Russian journal. Reproduced here with stylistic changes by AIP.

On the influence of magnetic and nonmagnetic impurities on the properties of yttrium-based high-T_c superconductors

J. G. Sanikidze, R. G. Kokhreidze, A. N. Mestvirishvili, G. A. Mumladze, S. V. Odenov, N. A. Papunashvili, and M. Ya. Chubabria

*Cybernetics Institute of the Georgian Academy of Sciences, 5 S. Euli St., Tbilisi 0186, Georgia**

(Submitted November 17, 2004)
Fiz. Nizk. Temp. **31**, 640–644 (June 2005)

The influence of impurities on the physical properties of $YBa_2Cu_3O_{7-\delta}$ superconducting ceramics is investigated. Samples of yttrium ceramics with different Ni, Zn, Co, Fe, and Ga impurity contents were prepared for this study, and the superconducting fraction, the low-frequency susceptibility in an external dc field, and the temperature dependence of the magnetic susceptibility in a weak ac field were measured for each sample. The last of these measurements permits a more precise determination of the critical temperature (the start of the transition) without regard for percolation effects. The experimental results show a stronger suppression of the superconducting state by nonmagnetic impurities, thus confirming the presence of *d*-state pairs in these superconductors. The degree of suppression of superconductivity by magnetic impurities depends on the preference of the impurities to locate in Cu(1) or Cu(2) sites. © *2005 American Institute of Physics.* [DOI: 10.1063/1.1943532]

INTRODUCTION

The nature of high-temperature superconductivity (HTSC) remains a topic of numerous studies. Its mechanism remains unclear, as do certain fundamental questions, i.e., concerning the relative contributions of the *s* and *d* states. In a number of theoretical papers these aspects of superconductivity are considered in connection with the influence of Ni and Zn impurities on the critical temperature (in the so-called *p-d* multiband models). On the other hand there exist percolation polaron models that also imply a dependence of the critical temperature on the Ni and Zn doping.

It is of interest that in some HTSC models of the *p* type the influence of magnetic impurities is weaker than that of nonmagnetic ones (unlike the case of low-temperature superconductors). This effect is observed in experiments.

In the general case the wave function of a pair can be written in the form of a product of two factors:[1]

$$\Psi = \Psi(\mathbf{R})\varphi(\mathbf{r}),$$

where $\Psi(\mathbf{R})$ describes the motion of the center of mass, with coordinate $\mathbf{R}$, and $\varphi(\mathbf{r})$ describes the motion of the electrons within the pair, with relative coordinate $\mathbf{r}$.

The microscopic properties of a high-T_c superconductor, such as the symmetry of the energy gap and the critical current, are described by the function $\varphi(\mathbf{r})$. As in ordinary low-temperature superconductors, in cuprate-based HTSCs the spin of a pair is equal to zero. This means that

$$\varphi(\mathbf{r}) = \varphi(-\mathbf{r}) = (-1)^l \varphi(\mathbf{r}),$$

where $l = 0,2,4,\ldots$ (*s*-, *d*-, *g*-wave states). In classical superconductors $l = 0$ (*s* state), so that the function $\varphi(\mathbf{r})$ is isotropic with a maximum at $\mathbf{r} = 0$, and has an isotropic energy gap. If $l = 2$, then $\varphi(\mathbf{r})$ describes a *d* state and transforms according to the law $x^2 - y^2$, where *x* and *y* are the axes corresponding to the Cu—O bonds in the CuO_2 plane.

The possibility of *d* symmetry in HTSCs was first analyzed by Scalapino.[2] In recent years research has shown that in HTSCs the gap in $\mathbf{k}$ space is highly anisotropic, which is inconsistent with an *s* state. Apparently the gap in HTSCs has $d_{x^2-y^2}$ symmetry. The symmetry of the wave function has a substantial influence on the scattering of carriers by point defects lying in the CuO_2 plane. Contrary to the case of an *s* state, nonmagnetic impurities strongly disrupt the $d_{x^2-y^2}$ ordering, and that, of course, leads to strong suppression of superconductivity.

The first experiments[3] investigating the influence of transition-metal impurities on the superconductivity in the Y-Ba-Cu-O system showed that nonmagnetic impurities (Zn) suppressed the superconductivity more strongly than magnetic impurities (Ni). A similar influence of impurities is also observed in superconductors of the La-Sr-Cu-O system.[4,5] These experiments have stimulated serious theoretical calculations devoted to elucidating the influence of magnetic and nonmagnetic impurities on HTSC.[6–10] Ovchinnikov made a detailed study[6,7] of the influence of impurities on the critical temperature T_c in a multielectron, multiband model. He showed that in systems with *p*-type coordination a Zn impurity causes electron doping, which gives rise to additional states within the gap, whereas a Ni impurity causes additional hole doping. Since the residual resistivity is due to the scattering of carriers on impurities, the lowering of T_c is proportional to the growth of the residual resistivity ρ_{res}. It follows from the calculation that for a *p*-type HTSC $\rho_{\text{res}}(\text{Zn}) \gg \rho_{\text{res}}(\text{Ni})$. At low impurity concentrations

$$\frac{dT_c(\text{Ni})/dx}{dT_c(\text{Zn})/dx} = \frac{\rho_{\text{res}}(\text{Ni})}{\rho_{\text{res}}(\text{Zn})}.$$

Analysis of the suppression of superconductivity of the $d_{x^2-y^2}$ type in Y(1-2-3) HTSCs upon substitution of Cu by Zn shows[8] that scattering on Ni impurities in systems with *p*-type conductivity is significantly weaker than the scatter-

 © 2005 American Institute of Physics

ing on Zn impurities, because it is of a nonresonant character. For *n*-type conductivity the situation is the opposite.

For a detailed study of the given situation we investigated the superconducting properties of specially prepared samples of $YBa_2(Cu_{1-x}M_x)_3O_{7-\delta}$ samples in which the copper was partially substituted by another metal (M=Zn, Ni, Co, Fe, Ga) in various concentrations.

MEASUREMENT TECHNIQUE

The ceramics were synthesized at a temperature of 950 °C for 30 hours: 20 g of the reaction mixture was annealed in alundum forms. The initial materials were chemically pure stocks of the oxides Y_2O_3, CuO, ZnO, Ni_2O_3, Co_3O_4, Fe_2O_3, and Ga_2O_3 and the carbonate $BaCO_3$. The components were first dried at 150 °C for 4 hours. Tablets were pressed from the prepared powders under a pressure of 900 MPa and were then annealed at 950 °C for 5 hours.

We first measured the low-frequency magnetic susceptibility χ (the real part) of the prepared samples in an external dc magnetic field of 0–3 kOe. In addition to the field dependence $\chi(H)$, these measurements permitted a quantitative determination of the superconducting fraction x_s of the samples both by volume and by mass. In addition, from the dependence of the superconducting fraction x_s on the impurity concentration one can make a quantitative assessment of the suppression of the superconducting state by impurities and compare the results with theoretical models.

We also made magnetic measurements of χ in a low dc field in the temperature range from liquid-nitrogen to room temperature, making it possible to determine, in particular, the dependence of the critical temperature on the impurity concentration. Measurements were made with a vibrating magnetometer in a special cryostat for intermediate temperatures.[11] The temperature was measured by a resistance thermometer with an accuracy of 0.1 K or better.

From the curves obtained we could estimate the degree to which the superconductivity was suppressed by the impurities and investigate how the suppression is influenced by the presence or absence of a magnetic moment on the impurity.

DISCUSSION OF THE RESULTS

Below we present some of the results obtained. Figure 1 shows the dependence of the magnetic susceptibilities for samples with the nonmagnetic impurity Zn (Fig. 1a) and the magnetic impurity Ni (Fig. 1b) for various impurity concentrations, and Fig. 2 shows the dependence of the ratio of the superconducting fraction of the sample to the fraction in a control sample, x_s/x_{s0}, as a function of the atomic concentration of the impurity. It is seen from Fig. 1 that the weak links are already almost completely suppressed by relatively low external fields, and the magnetic susceptibility is determined practically entirely by the diamagetism due to the superconducting grains and is nearly independent of the field up to 3 kOe. Using the curves given in Fig. 1 one can determine the dependence of the superconducting fraction in the samples on the corresponding atomic concentration of the impurity (Fig. 2), which is done by extrapolating the tangent line of the function $-4\pi\chi$ at high fields to zero field.[12]

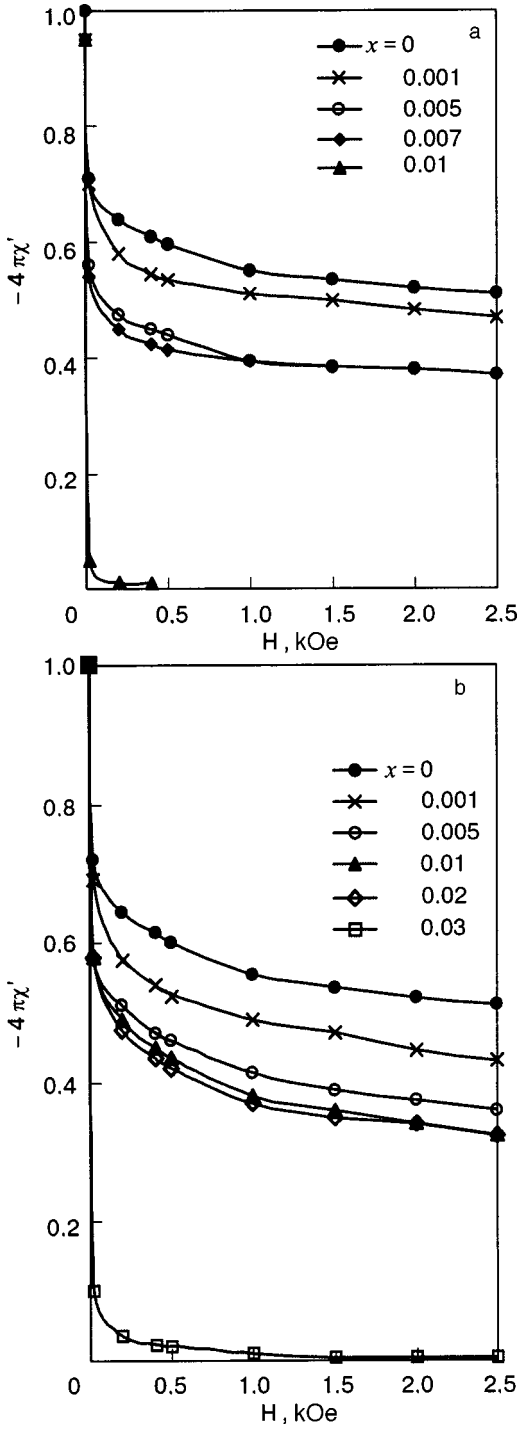

FIG. 1. Dependence of the low-frequency susceptibilities of $YBa_2Cu_{3-x}Zn_xO_{7-\delta}$ (a) and $YBa_2Cu_{3-x}Ni_xO_{7-\delta}$ (b) on the dc magnetic field for various impurity concentrations.

The curves in Fig. 2 for Co, Fe, and Ga differ substantially from the corresponding curves for Ni and Zn in that they do not have the initial sharp drop nor the plateau at intermediate impurity concentrations.

Figure 3 shows the concentration dependence of the ''magnetic'' critical temperature T_{cm} (determined from measurements of the magnetic susceptibility at a low dc field) for different impurities. In this case the dependence for Co and Fe is much weaker than for Ni and Zn, especially at low impurity concentrations.

It is seen in Figs. 2 and 3 that a Zn impurity suppresses

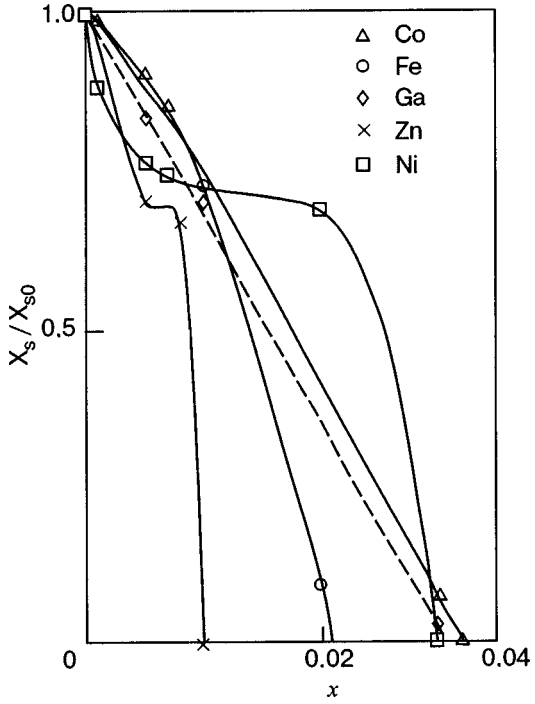

FIG. 2. Ratio of the superconducting fraction in the samples to the fraction in a control sample as a function of the impurity concentration.

the superconducting state much more strongly than Ni, Fe, and Co impurities. The magnetic method of determining the critical temperature was chosen for the obvious reason that it permits determination of the point at which the superconducting phase appears, unlike the resistive method, which determines only the point at which weak links between grains appear, allowing the percolation of supercurrent. The point determined by the resistive method reflects not the onset of superconductivity but the suppression of weak links in the sample, which we determine directly in measurements of the low-frequency susceptibility in a dc external field.

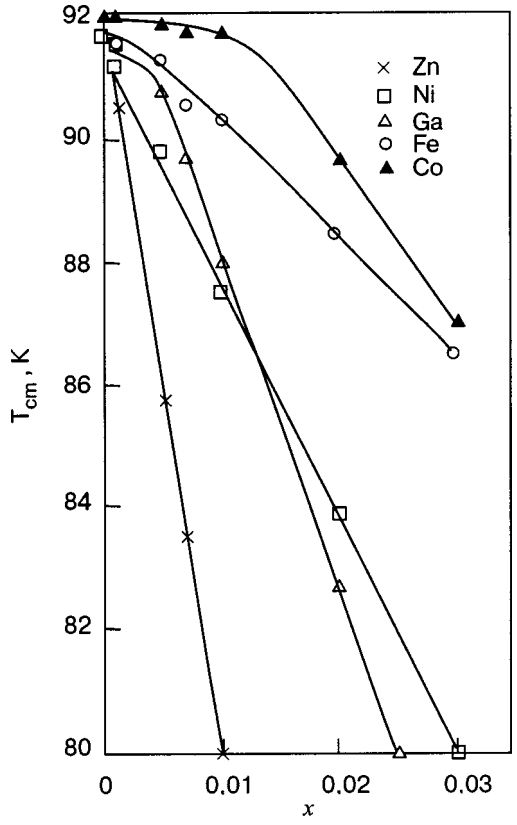

FIG. 3. Dependence of the critical temperature on the impurity concentration in the samples.

Thus we can see that for the same amount of impurity the lowering of the critical temperature in the cases of Ni, Fe, and Co is weaker than in the case of Zn, once again confirming the validity of models of superconductivity based on a d-state contribution.

The difference in the influence of impurities can apparently be explained qualitatively by the fact that in p-type superconductors impurities of Ni, Fe, and Co increase the number of carriers (holes), whereas Zn and Ga increase the number of electrons, which creates additional levels within the gap. This leads to different resonance scattering of carriers on impurities, which is weaker in the case of paramagnetic impurities[6–8] and, accordingly, to different lowering of the critical temperature in the two cases.

The different degree of influence of nonmagnetic impurities (Zn and Ga) is apparently due to the circumstance that they occupy the Cu(1) and Cu(2) cells with different probability: Zn^{2+} always occupies the Cu(2) cell, and Ga occupies both Cu(1) and Cu(2). Substitution of Cu in the CuO_2 planes suppresses the superconductivity more strongly, while the suppression in the chains is due to carrier hopping. Ga^{3+} ions suppress the superconductivity more than magnetic impurities of $3d$ elements, which have different preferences for the Cu cells.[13–15] Co^{3+} ions prefer Cu(1), while Ni^{3+} ions prefer the Cu(2) cells, and Fe ions can occupy either cell, and therefore the degree of suppression by iron also varies depending on the preferential occupation of the cells in the planes or chains.

The reduction of the superconducting fraction in the samples is also different, and that should lead to additional lowering of the critical temperature measured from the resistance in accordance with the percolation model, which is to some degree independent of the mechanism of superconductivity.

CONCLUSION

It follows from our experiments that the magnetic critical temperature in the case of Ni and Zn impurities varies in such a way that

$$\frac{dT_c(\mathrm{Ni})/dx}{dT_c(\mathrm{Zn})/dx} \cong \frac{1}{3}.$$

This agrees well the theory of the d state. The influence of nonmagnetic Zn and Ga on the transition temperature is considerably stronger than that of magnetic impurities. The different degree of suppression of the superconductivity by Ni, Co, and Fe impurities is apparently due to their different preferences for the Cu(1) or Cu(2) cells, as mentioned above. However, open questions remain as to the details of the mechanism of suppression of the superconductivity: dependence on the band structure, density of states on the Fermi surface, carrier density, etc. To elucidate these question it will be necessary, in particular, to have data on the influence of impurities on HTSCs of the n type. These and other issues

which are under intensive study at the present time will be the subject of our next papers. A more detailed analysis of this question will be carried out after completion of the series of measurements necessary for a deeper investigation of the problem.

*E-mail: juniko@posta.ge

[1] K. A. Müller and H. Keller, in *High-T_c Superconductivity 1996: Ten Years after Discovery*, Kluwer Acad. Publ., North Holland (1997), p. 7.
[2] D. J. Scalapino, Phys. Rep. **250**, 329 (1995).
[3] Gang Xiao, F. H. Streitz, A. Gavrin, Y. W. Du, and C. L. Chien, Phys. Rev. B **35**, 8782 (1987).
[4] Gang Xiao, Morta Z. Cieplak, J. Q. Xiao, and C. L. Chien, Phys. Rev. B **42**, 8752 (1990).
[5] G. L. Basilia, G. A. Kharadze, K. A. Kvavadze, M. N. Nadareishvili, D. F. Brewer, G. Ekosipedidis, and A. L. Thomson, Fiz. Nizk. Temp. **24**, 726 (1998) [Low Temp. Phys. **24**, 547 (1998)].
[6] S. G. Ovchinnikov, Fiz. Tverd. Tela (St. Petersburg) **37**, 3645 (1995) [Phys. Solid State **37**, 2007 (1995)].
[7] S. G. Ovchinnikov, Fiz. Tverd. Tela (St. Petersburg) **41**, 596 (1999) [Phys. Solid State **41**, 534 (1999)].
[8] L. S. Bozkovski and P. J. Hirchfeld, Phys. Rev. B **49**, 15404 (1994).
[9] O. Mihailovic, V. V. Kabanov, and K. A. Müller, cond-mat/0111083, v. 1, No. 6 (2001).
[10] T. Xiang, I. H. Su, C. Panagopoulos, Z. B. Su, and L. Yu, cond-mat/0111083, v. 1, May 29 (2002).
[11] D. Z. Sanikidze, S. V. Odenov, R. G. Kokhreidze, O. E. Modebadze, R. A. Tatulov, and N. G. Birkaya, Sverkhprovodimost' (KIAE) **4**, 1218 (1991) [Superconductivity **4**, 1218 (1991)].
[12] J. Sanikidze, S. Odenov, R. Kokhreidze, G. Mumladze *et al.*, in *Proceedings of Tbilisi University*, **333**, Physics (N.Y.) **34,** 4 (1999).
[13] T. J. Kistenmacher, Phys. Rev. B **38**, 8862 (1988).
[14] R. S. Howland, T. H. Geballe, S. S. Laderman, A. Fischer-Colbrie, M. Scott, J. M. Tarascon, and P. Barboux, Phys. Rev. B **39**, 9017 (1989).
[15] A. Dogra, S. Rayaprol, N. Shah *et al.*, cond-mat/0404558 (2004).

Translated by Steve Torstveit

On the theory of the electron spectrum and superconductivity of copper oxides as antiferromagnetic metals

V. M. Loktev*

N. N. Bogolyubov Institute of Theoretical Physics, National Academy of Sciences of Ukraine, ul. Metrologicheskaya 14-b, Kiev 03143, Ukraine

(Submitted December 8, 2004)
Fiz. Nizk. Temp. **31**, 645–655 (June 2005)

The electron spectrum of doped copper oxides is considered on the basis of explicitly taking into account the antiferromagnetic structure of their ground state. It is shown that the spin conservation law imposes certain restrictions on the motion of the carriers, making it impossible for a carrier to leave the magnetic sublattice in which it was created. An attempt is made to compare the resulting dispersion of the hole conductivity with the available experimental data. © *2005 American Institute of Physics.* [DOI: 10.1063/1.1943533]

1. Research on the processes and interactions underlying the formation of the electron spectrum of high-temperature superconducting copper oxides (HTSCs) is still among the topical problems of condensed matter physics. In particular, data from angle-resolved photoelectron spectroscopy (ARPES) measurements of the energy dispersion curves $\varepsilon(\mathbf{k})$ for mobile (doped) carriers in HTSC systems have been presented in a number of works (see, e.g., the recent reviews[1,2]). It was found that within the first Brillouin zone, which pertains to the paramagnetic (magnetically ordered) state of a HTSC, the corresponding curves have a maximum not at its edge [i.e., at the points $\mathbf{k}=(\pm\pi,\pm\pi)$ for dimensionless wave vectors], as is implied by band calculations in the linear density approximation (LDA), but at the points $\mathbf{k}=(\pm\pi/2,\pm\pi/2)$.

In principle, this sort of behavior of the electron dispersion seen in cuprates has long been known in the theory of small-radius excitons in molecular crystals with two (or more) molecules in the unit cell.[3] When the spectrum of elementary excitations (primarily excitons) is calculated in the ''extended''[1)] zone scheme, one is readily convinced that a maximum (which is not to say an extremum) of the unified dispersion curve $\varepsilon(\mathbf{k})$ can occur away from the edges (i.e., inside) the Brillouin zone of the undoubled lattice only in the case of small Davydov splitting. A small splitting of the exciton bands in the case of molecular crystals means that the contribution to the total dispersion, i.e., to $\varepsilon(\mathbf{k})$, from the so-called intersublattice resonant transfer of Frenkel excitation is smaller than the intrasublattice contribution. Therefore it would seem that the natural explanation for the aforementioned behavior of $\varepsilon(\mathbf{k})$ in HTSC systems, due solely to the rolling up (reduction) of this zone or the multiplication of the crystal cell in the ordered phase, although necessary, as is stated in Ref. 2, cannot be deemed completely sufficient.

The relationship between the probabilities (or amplitudes) of the different processes governing the motion of an excitation through the lattice is also important. In particular, the formation of a maximum on the $\varepsilon(\mathbf{k})$ curve for a wave vector $\mathbf{k}=(\pi/2,\pi/2)$ and other equivalent wave vectors [the complete star comprises the values $\mathbf{k}=(\pm\pi/2,\pm\pi/2)$] is possible only in the case when there is no Davydov splitting, as is easily confirmed by a simple calculation.

Indeed, we consider a two-dimensional nonmagnetic lattice, which, without loss of generality, can be assumed square for simplicity, and we assume that molecules (ions) of different sublattices lie at the nearest-neighbor distances in the **a** and **b** directions ($\mathbf{a}\perp\mathbf{b}$, $|\mathbf{a}|=|\mathbf{b}|$). We write the Hamiltonian of an electronic excitation that can move both with a change of sublattices (the parameter corresponding to this motion, t_{NN}, determines the Davydov splitting of the energy bands in the crystal) and within the confines of each sublattice. Then in the case of a unmultiplied (one-site) periodic structure this operator (in the tight binding approximation, which is valid for narrow-band crystals) can be represented by the expression

$$H=-\sum_{\mathbf{n},\mathbf{m}} t_{\mathbf{nm}} B_{\mathbf{n}}^{+} B_{\mathbf{m}}, \tag{1}$$

where we have neglected [as unimportant for calculating the dispersion $\varepsilon(\mathbf{k})$] the energy of excitation of the molecule in the crystal. In Eq. (1) we used the following notation: $t_{\mathbf{nm}}$ is the amplitude of the resonant interaction between molecules **n** and **m**, and $B_{\mathbf{n}}^{+}$ and $B_{\mathbf{n}}$ are the creation and annihilation operators of a molecular electronic excitation. Going to plane waves in (1) and restricting consideration to the simplest approximation of only nearest neighbors (NN) and next-nearest neighbors (NNN), we quickly obtain the desired dispersion relation:

$$\varepsilon(\mathbf{k})\equiv\varepsilon(k_x,k_y)=-2t_{NN}(\cos k_x+\cos k_y) -4t_{NNN}\cos k_x\cos k_y, \tag{2}$$

in which t_{NNN} (unlike t_{NN}) determines the amplitude of the intrasublattic hop.

In this representation the energy values $\varepsilon(0,0)=-4(t_{NN}+t_{NNN})$ and $\varepsilon(\pi,\pi)=4(t_{NN}-t_{NNN})$ specify a Davydov doublet, the splitting $|\varepsilon(\pi,\pi)-\varepsilon(0,0)|$ between components[2)] of which is completely determined by the value of t_{NN}, as it should be. The values of $\varepsilon(0,\pi)=\varepsilon(\pi,0)=4t_{NNN}$, on the contrary, are independent of that parameter. Finally, at the point $\mathbf{k}=(\pi/2,\pi/2)$ the energy

 © 2005 American Institute of Physics

$\varepsilon(\pi/2,\pi/2)=0$, and in order for the inequality $\varepsilon(\pi,\pi)<\varepsilon(\pi/2,\pi/2)$, corresponding to the appearance of a maximum on the $\varepsilon(\mathbf{k})$ curve within the first (doubled in the present case) Brillouin zone, to hold, it is necessary that the condition $t_{NN}<t_{NNN}$ be satisfied, assuring the relative weakness of the intersublattice resonant migration of excitation. It should be added that taking the neighbors on more remote coordination spheres into account does not affect qualitatively the statements made as to the shape of the dispersion curve, provided that t_{NN} is understood to mean the total contribution to the expression for $\varepsilon(\mathbf{k})$ from intersublattice processes and t_{NNN} that from intrasublattice processes.

In molecular crystals both of these ''hopping'' parameters are, as a rule, of a dipole-dipole (or multipole-multipole) character and for this reason depend rather strongly on the mutual orientation of the molecules. Therefore the above inequality attesting to the stronger interaction of more distant molecules cannot be dismissed out of hand. Its satisfaction does not imply that the maximum on the dispersion curve occurs directly at the point $\mathbf{k}=(\pi/2,\pi/2)$; this is achieved only in the limiting case $t_{NN}=0$ or, as was stated above, when for some reason intersublattice excitation transfer cannot occur.

Such a situation is actually realized in collinear antiferromagnetic insulators with a Néel ground state, where excitons (including magnons) can be regarded as a small-radius state.[4–6] In narrow-band systems with with such a magnetic structure an electronic (or a spin[3)]) excitation of the d or f shell of a paramagnetic ion, in migrating through the crystal, cannot move coherently (in our case that would mean resonantly) from one magnetic sublattice to the other because to do so is spin forbidden. Strict satisfaction of the spin conservation law in the motion of Frenkel excitations along the magnetic sublattices of isotropic and slightly anisotropic antiferromagnetic insulators based on transition-metal ions is unambiguously confirmed by numerous experimental results, which demonstrate the presence of a magnetic (excitonic) Davydov splitting effect.[7] In complete agreement with theory (see the monographs[4,5]) this splitting (or, equivalently, the suppression of intersublattice excitation transfer) is possible only in noncollinear spin structures and is absent in the initial collinear structures.

In the optical studies mentioned the noncollinearity of the Néel sublattices was induced by an external influence—a strong magnetic field, and it was reversible and well controllable. It presence leads to a splitting of the degenerate exciton bands relative to each other which depends quadratically on the external field (and on the modulus of the wave vector $\mathbf{k}$). In the absence of noncollinearity these bands form in each sublattice independently and are degenerate for all $\mathbf{k}$. We also note that in the model of a crystal with an unmultiplied (in other words, undoubled) unit cell this corresponds [see Eq. (2) under the condition $t_{NN}=0$] the equality $\varepsilon(0,0)=\varepsilon(\pi,\pi)$ or again to an $\varepsilon(\mathbf{k})$ curve that is completely symmetric with respect to the point $\mathbf{k}=(\pi/2,\pi/2)$; some reasons for the appearance of this curve are discussed in reviews.[1,2]

2. Returning to the cuprates, it is appropriate at this point to ask how an electronic excitation in an antiferromagnetic insulator differs physically (in any case, from the standpoint of propagation through a magnetically ordered space) from a carrier injected into its lattice.[4)] It can be assumed that there is essentially no difference, since in both situations in one way or another one is talking about the transfer from site to site of an ionic state that formally corresponds to an uncharged (neutral or, more precisely, currentless) excitation in the first case and a charged (current) excitation in the second. Also, in both of these cases the same relationship holds between the parameters t_{NN} and t_{NNN},[5)] the exchange nature of which in antiferromagnetically ordered crystals suggests that most likely $t_{NN}>t_{NNN}$ for both excitons and doped carriers. Nevertheless, this inequality does not enable the coherent transfer of the corresponding quasiparticle (uncharged or charged) from one magnetic sublattice to the other. The absence of such transfer is due to the spin part of the total matrix element (amplitude) of the intersublattice transition and not to a zero value of t_{NN}, which is actually finite and not small.

The transition of an excitation between collinear sublattices (including, obviously, nearest neighbors) can be brought about only in the presence of a ''contractor,'' a spin wave, which converts such a transition to incoherent. This possibility, however, does not fulfill the prerequisites for a direct contribution from hops of this kind to the width of the band of free motion of the quasiparticles.

In the above discussions for molecular (nonmagnetic) and ionic (magnetic) crystals it was implicitly assumed that the excitations reside on the molecules (ions) (i.e., are created there and remain there), forming sublattices that are translationally inequivalent in the orientational (magnetic) sense. Therefore in relation to HTSCs a much more complex and fundamental question is, how is a carrier created (we are talking primarily about holes) specifically at the ions of the copper subsystem, whose spins constitute a Néel (and not some other) ground state.[10]

In the standard scheme of doped HTSC compounds with their layered structure and current-carrying cuprate CuO_2 planes it is usually assumed that a hole introduced by doping belongs to the oxygen subsystem, which does not have a direct relationship to the magnetism (the two-band Emery model[11] or the more general multiband Gaididei-Loktev pd model[12,13]). If this picture is adopted and the holes in the HTSC are indeed created and move via oxygen ions (i.e., are ''assigned'' to the oxygen band) then it must be noted that the unit cell of even the paramagnetic (i.e., undoubled) square CuO_2 lattice has two translationally inequivalent oxygen ions. In this case the interoxygen hopping parameters [see Eq. (2)] shaping the dispersion of the oxygen bands, including the conduction band, are such that most likely $t_{NNN}^{O^-O}=0$ (or $t_{NNN}^{O^-O}\ll t_{NN}^{O^-O}$), which rules out an interpretation of the behavior of the dispersion of an isolated hole in a HTSC matching that which is observed in ARPES.[1,2]

The difficulty that arises (directly or indirectly) is avoided by specially constructed states known as Zhang-Rice singlets[14] (see also Refs. 15–20). They prescribe that the oxygen hole introduced by doping (depending on its spin direction) be found in an exchange bond with the nearest ion of that copper sublattice with which it lowers its self-energy by forming a singlet. Such charge states spin-correlated with the antiferromagnetic ordering can move along the cuprate

plane, each being bound only with a definite magnetic sublattice. It is easily verified, however, that such a quantum-mechanical construction is unstable, since in the formation of a singlet state the ''up'' and ''down'' spins of the hole enter the linear combination equiprobably, and after a dynamic interchange the oxygen hole with the opposite spin projection ''wants'' to form the same singlet with the neighboring localized spin of a copper ion of the other magnetic sublattice.

In addition, the oxygen in the cuprate plane is arranged absolutely symmetrically geometrically between the paramagnetic copper ions belonging to different magnetic sublattices. This, in turn, means that the exchange field produced by them at the doped hole cancels out exactly and that hole to a certain degree is frustrated from the standpoint of the choice of quantization axis for its spin. Its direction, which is equivalent for the two sublattices, is not hard to establish,[13] but here an oxygen hole, even when hybridized with the states of copper, can easily propagate through along the cuprate plane without perceiving the magnetic ordering of the latter; this, as we have said, does not permit an explanation of the aforementioned ARPES data.

3. For these reasons a search for other probable causes that would make compounds of the family of copper-oxide HTSCs to undergo a transition to a metallic state in such a way that mobile holes appear in the paramagnetic and not in the ligand subsystem. It is of interest here to note the following: cuprates belong to the same family of perovskites as manganites,[9] the doping of which causes metallization of the manganese subsystem, or the charge exchange $Mn^{3+} \rightarrow Mn^{4+}$.

If such a similarity is present, then that would imply directly that hole doping in the CuO_2 plane is nothing more than a Cu^{3+} ion or the valence state, which, because of the large ionization potential of divalent copper Cu^{2+}, is ordinarily ruled out from consideration of actual states. Although this state of affairs corresponds to reality, and this potential is deep enough, the aforementioned experimental evidence[1,2] of dispersion of isolated carriers gives weighty grounds for the view that situations that might bring about stabilization and the existence of specifically copper holes in HTSCs merit analysis.

For example, there has been incomplete discussion of the role of the inter-ion Coulomb interaction, which, as is well known, can directly determine which ionic states of combining chemical elements are energetically favorable and which are not. In this connection it is not groundless to assume that this Coulomb interaction can stabilize the copper holes in the CuO_2 lattice, the existence of these holes having been not so much demonstrated as postulated back in the first theoretical paper devoted to HTSC.[21] The precise answer to this many-electron problem, judging from everything, can be found only as a result of complex (possibly numerical[18]) calculations taking different p and d states into account, but on a qualitative level it appears to be affirmative in the sense that the role of the Coulomb interaction is decisive for the formation of copper holes to be favorable in comparison to oxygen holes.

In fact the ionic compositions of HTSCs has been considered numerous times (see, e.g., the reviews[13,17]) and it is considered to be well established. Copper, as we know, can be found in three (besides neutral) charge states: Cu^+, Cu^{2+}, and (more rarely) Cu^{3+}. The first corresponds to a completely filled $3d$ shell, or an electronic configuration $3d^{10}$, sometimes considered to be the vacuum configuration;[18] the second corresponds to the presence of one hole in it and the configuration $3d^9$; the third corresponds to two holes, $3d^8$. The oxygen in the lattice practically always has a valence equal to two, or is found in the state O^{2-}.

Undoped cuprate planes exhibit an ionic state in which the presence of divalent ions of both copper and oxygen are present, i.e., the ground state is $Cu^{2+}O^{2-}$. The charge-transfer configuration Cu^+O^- is an excited state; in itself, i.e., without the Coulomb component, this state has lower energy than the first. In other words, in the absence of static Coulomb attraction these configurations would switch places on the energy scale. This conclusion is obvious in view of the fact that the higher the degree of positive ionization, the larger the work function for the removal of an electron from a given atomic shell.

The creation of negatively charged ions, on the contrary, raises the energy. Therefore, in the electronic representation (rather than the usual hole one) the energies of the actual ionic states obey the inequalities $E_{Cu^{3+}} > E_{Cu^{2+}} > E_{Cu^+}$ and $E_O < E_{O^-} < E_{O^{2-}}$ (the latter is even positive, and in the free state the O^{2-} ion is absolutely unstable). An estimate based on these inequalities and the binding energies for the $3d$ and $2p$ shells of copper and oxygen, respectively, shows that for noninteracting ions the state Cu^+O^- is energetically preferable, since the energies satisfy the relation $E^+_{Cu} + E^-_O < E_{Cu^2} + E_{O^{2-}}$, but the Coulomb attraction in the $Cu^{2+}O^{2-}$ configuration is four times stronger than in the configuration Cu^+O^-, where it is also far from small (at interatomic scales $V_C^{Cu^+O^-} \sim e^2/a \sim -(5-6)$ eV). It is the Coulomb shift that ultimately makes the initial (i.e., in the static, first approximation in the Coulomb contribution) state $Cu^{2+}O^{2-}$ lower in energy than the ground state itself.

Importantly, further quantum-mechanical pd hybridization, while it undoubtedly mixes different states, and the valence of some ion in the crystal is, strictly speaking, noninteger, does not alter their relative position. This means that only the ionic bonding, when all of the intra- and inter-ion Coulomb terms are consistently taken into account, alters the content of the previous inequality, reversing its sense: $E_{Cu^{2+}} + E_{O^{2-}} + V_C^{Cu^{2+}O^{2-}} < E_{Cu^+} + E_{O^-} + V_C^{Cu^+O^-}$. The contribution of the excited configuration Cu^+O^-, owing to its admixture to the ground state, remains, but it can no longer become prevalent. Its presence can, in particular, be reflected in the value (including the contraction) of the mean spin of the copper ion in the magnetically ordered state, which will be determined not only by the quantum fluctuations that are highly developed in low-dimensional antiferromagnets but also by the contribution of the Cu^+O^- configuration.

It can be assumed approximately, however, that in its (insulating) ground state the cuprate planes contain Cu^{2+} and O^{2-} ions or one copper hole per unit cell. Heterovalent doping alters the valence of some ions in the crystal, giving rise to mobile charged, including hole, states in the CuO_2 plane. The appearance of a doped hole is nothing more than a positive change of the valence of some ion of the cuprate plane.

It is known that there are only two possibilities: charge exchange $Cu^{2+} \rightarrow Cu^{3+}$, i.e., the appearance of a predominantly copper hole in the crystal, or the process $O^{2+} \rightarrow O^{-}$, the appearance of an oxygen hole. Then, comparing the energy of the configurations $Cu^{3+}O^{2-}$ and $Cu^{2}O^{-}$ on the basis of the same arguments, one can tell that beyond a doubt the first of these has the higher energy and therefore is an excited state in the doped system (without allowance for the Coulomb attraction).

However, if it is taken into account that $V_C^{Cu^{3+}O^{2-}} \approx 3V_C^{Cu^{2+}O^{-}} \approx 6V_C^{Cu^{+}O^{-}}$, and also the circumstance that in the cuprate plane each of the copper ions has 4 nearest oxygen ions, whereas the oxygen ion has 2 nearest copper ions, it can be hoped that the difference of the static Coulomb contributions that arises, which, as is easily verified, amounts to $\approx 20V_C^{Cu^{+}O^{-}}$, can become decisive here. In other words, it is quite probable that among the possible ionic configurations in copper oxide HTSC systems, $Cu^{3+}O^{2-}Cu^{2+}$, $Cu^{2+}O^{-}Cu^{2+}$, $Cu^{3+}O^{-}Cu^{+}$, etc., containing a doped hole, the first, owing to the effect known as the crystalline shift in the theory of excitons, turns out to lie below the others if hybridization is not taken into account. Only such a position of the energies of the initial configurations can bring about the existence of ''copper-like'' carriers in the cuprate layers of HTSCs and their propagation along the two-sublattice antiferromagnetically ordered collinear structure in accordance with the rules governing the motion of magnetic excitons or magnons in it.

To some degree or other such a picture is reflected in the long-familiar tJ model,[14–20,22] in which the motion of the carriers on antiferromagnetic square lattices is studied but without making direct use of the concept of coherent intra- and incoherent intersublattice transfer. Nevertheless, it is appropriate to remark here that the spectrum of free (doped) carriers in the conduction band of this model is often specified by expression (2), which, as we have said, does not agree with the ARPES data.

On the whole, it should be kept in mind that when deriving the second-quantized Hamiltonian it is convenient to use a basis of one-site states. Here, because of pd hybridization (or, in other words, covalent bonding) these states are insufficiently well defined. Therefore attempts have been made and continue to be made to simplify the problem, e.g., restricting consideration to the rather popular cluster approximation[18–20] or working with Wannier functions.[19,20] Here, as a rule, one ignores the Coulomb component, which competes with covalency effects in the sense that it promotes an increase in the energy distance between different one-ion p and d states (see above). On the basis of such an assumption one can consider the use of the one-ion basis to be physically justified. One can then relatively simply generalize to doped HTSC systems the approach developed for the description of current-free excitations in (anti)ferromagnetic insulators containing elements (in particular, transition metals) with an unfilled electron shell.

One cannot fail to notice here that magnetic insulators (along with molecular crystals) belong to a class of highly correlated (and, hence, as we have said, narrow-band) systems in which the relatively large distance between different electron states (terms) is substantially larger than the width of the corresponding bands. Therefore, regardless of whether one considers a neutral or charged state of the transition ion, one can use as the zeroth approximation the one-ion states in which the Hubbard interaction is ''masked'' by the energy separating the different discrete levels corresponding to them (if collectivization processes are ignored).

4. For calculating the dispersion of a doped carrier we assume that the plane under consideration is the antiferromagnetic CuO_2 plane, in which the copper ion is found in the $3d_{x^2-y^2}$ state,[6)] while the oxygen ions are in $2p$ states, forming σ bonds with the nearest copper ions. Then, as is well known,[11–13,17] the main kinetic processes involving both the initial and introduced electrons are the hybridization pd hops and direct pp hops. The latter are responsible for the formation of comparatively wide p bands of free motion of the oxygen carriers (4 or 2, depending on whether the doubled or undoubled lattice is used in the calculation). There are also virtual hops occurring across these bands, bringing about an indirect—Anderson—exchange of localized (due to the one-site—Hubbard—repulsion) d electrons in the insulating phase and which are such that they correspond to the current motion of doped holes, since the direct overlap of the d states is negligibly small.

The preservation of the hybridized p and d bands in the Hamiltonian with simultaneous allowance for the strong one-site and intersite electronic correlations makes calculating its spectrum a very complicated problem. Therefore the p bands are usually eliminated in accordance with the putative small ratio $t_{\mathbf{n}}^{pd}(\mathbf{k})/\Delta E$, where $t_{\mathbf{n}}^{pd}(\mathbf{k})$ is the parameter characterizing the pd hybridization of the copper ion found at the **n**th site with the oxygen band, and ΔE is the characteristic energy difference between the initial ionic and virtual band states, including all the necessary Coulomb interactions. This procedure in essence leads to the Hamiltonian of the tJ model with allowance for the rather narrow bands of motion of the doped charges through the magnetically ordered space. This spin space has the feature that the effective transfer of collectivized (doped) d holes (ions in the $3d^8$ state) and the Heisenberg interaction between components of its localized spins (belonging to ions of the same copper but in the $3d^9$ state) is brought about not only between nearest neighbors but also between more remote neighbors, this being a direct consequence of the overlap or collectivization of the virtual p states.

Then, assuming the pd hybridization processes are ruled out, one can write the effective ''d-hole'' Hamiltonian of a HTSC system in the form

$$H_d = \varepsilon_d \sum_{\mathbf{n}} \sum_{\sigma_{\mathbf{n}}} d^{+}_{\mathbf{n}\sigma_{\mathbf{n}}} d_{\mathbf{n}\sigma_{\mathbf{n}}} + \frac{1}{2} \sum_{\mathbf{n},\mathbf{m}} \sum_{\sigma_{\mathbf{n}},\sigma_{\mathbf{m}}} t_{\mathbf{nm}} \langle \sigma_{\mathbf{n}} | \sigma_{\mathbf{m}} \rangle d^{+}_{\mathbf{n}\sigma_{\mathbf{n}}} d_{\mathbf{m}\sigma_{\mathbf{m}}}, \quad (3)$$

where ε_d is the density of the d level of an ion in the crystal; $d^{+}_{\mathbf{n}\sigma_{\mathbf{n}}}$ and $d_{\mathbf{n}\sigma_{\mathbf{n}}}$ are the Fermi creation and annihilation operators of a d electron at site **n** with spin projection $\sigma_{\mathbf{n}}(=\pm 1/2)$ in the proper (local) reference frame, $t_{\mathbf{nm}}$ is the matrix element for the transition of a carrier between ions **n** and **m**, and $\langle \sigma_{\mathbf{n}} | \sigma_{\mathbf{m}} \rangle$ is the ''overlap integral'' of the spin functions at different sites. Since the motion of a carrier oc-

curs in a magnetically ordered medium, it can be characterized by a Hamiltonian of the Heisenberg type:[10,23]

$$H_{\text{exch}}=\frac{1}{2}\sum_{\mathbf{n},\mathbf{m}}(J_{\mathbf{nm}}S_{\mathbf{n}}S_{\mathbf{m}}+\Delta J_{\mathbf{nm}}S_{\mathbf{n}}^{Z}S_{\mathbf{m}}^{Z}). \tag{4}$$

In operator (4) $J_{\mathbf{nm}}$ is the exchange integral between the spin $S=1/2$ copper ions localized at sites **n** and **m**, which for the same reason as for $t_{\mathbf{nm}}$ can be nonzero for non-nearest neighbors also, $\Delta J_{\mathbf{nm}}$ is the anisotropy constant, which according to the experimental data corresponds to an easy-plane type of initial magnetic structure of HTSC systems, and $S_{\mathbf{n}}$ and $S_{\mathbf{n}}^{Z}$ are the operators of the **n**th spin and its Z projection.

Since the carrier is created and moves in a medium in which spins are distributed over all sites, this circumstance must be taken into account directly. As in the theory of excitons, the magnetic order can be included in a consistent manner in the treatment by introducing, in place of the operators $d_{\mathbf{n}\sigma_{\mathbf{n}}}^{+}$ or $d_{\mathbf{n}\sigma_{\mathbf{n}}}$, the Hubbard operators $X_{\mathbf{n}}^{q_1q_2}$ $(=(X_{\mathbf{n}}^{q_2q_1})^{+}$ Ref. 24); here q_1 and q_2 correspond to the quantum numbers (including spin) of the ion with different numbers of electrons (differing by one or two). It is between such states that the ''transitions'' occur under the action of the Fermi operators $d_{\mathbf{n}\sigma_{\mathbf{n}}}^{+}$ and $d_{\mathbf{n}\sigma_{\mathbf{n}}}$.

In the case when acceptors are introduced into the system, as in the case of HTSCs with hole-type doping, the number of holes at a site when a carrier is created at it changes from one to two. Since it can be assumed to sufficient accuracy that $d_{\mathbf{n}\sigma_{\mathbf{n}}}=X_{\mathbf{n}}^{2\overline{\sigma}_{\mathbf{n}}}$, where the 2 corresponds to the occupation of this state by two carriers, and $\overline{\sigma}_{\mathbf{n}}\equiv-\sigma_{\mathbf{n}}$ by one. Here the pd hybridization manifests itself in the circumstance that a hole appearing at some ions in the crystal does not remain localized but begins to move according to processes allowed by the Hamiltonian (3). We note that in the hybrid tJ model, where only singly and doubly occupied states, one sometimes speaks of their belonging to a singlet (in the hybrid tJ model one sometimes speaks of double occupation of the states in a singlet pd band).[17,19] The Hamiltonian (3) describing the motion of the doped and mutually noninteracting carriers of the hole type takes the form

$$H_{d}^{\text{hole}}=\varepsilon_{d}\sum_{\mathbf{n}}X_{\mathbf{n}}^{22}+\frac{1}{2}\sum_{\mathbf{n},\mathbf{m}}\sum_{\sigma_{\mathbf{n}},\sigma_{\mathbf{m}}}t_{\mathbf{nm}}\langle\sigma_{\mathbf{n}}|\sigma_{\mathbf{m}}\rangle X_{\mathbf{n}}^{2\overline{\sigma}_{\mathbf{n}}}X_{\mathbf{m}}^{\overline{\sigma}_{\mathbf{m}}2}. \tag{5}$$

This expression differs somewhat from that used, e.g., by Plakida[25] in a study of the exchange mechanism of HTSC in the limit of strong interelectron correlations, which corresponds to the assumption of the absence of ions without carriers in the doped initially magnetic system, or, more precisely, of the presence of carriers of the electron type in the system. The difference we have in mind consists in the fact that the operator (5) explicitly—in terms of the overlap integrals $\langle\sigma_{\mathbf{n}}|\sigma_{\mathbf{m}}\rangle$—contain information about the initial $\overline{\sigma}_{\mathbf{m}}=\pm1/2$ and final $\overline{\sigma}_{\mathbf{n}}=\pm1/2$ projections of the ions at the sites **n** and **m** between which the hopping takes place. This, in turn, allows one to determine the spin projection of a carrier moving through the magnetic lattice. With the aid of the same quantities (overlap integrals) in the next stages of the calculation (see Refs. 5 and 6) one can express the character of the magnetic ordering (including the absence of such) in the crystal.

To find these integrals we assume that the spins of all the ions in the ground state (without the doping-introduced carriers) have projection $\sigma_{\mathbf{n}}=1/2$, which pertains by definition to the proper quantization axes, and we go over from the local coordinate systems corresponding to them to the laboratory reference frame. Then on the assumptions that the axes of quantization of the laboratory and **n**th local reference frames are directed at an angle $\theta_{\mathbf{n}}$ with respect to each other, we write the spin functions in the laboratory frame: $|\sigma_{\mathbf{n}}\rangle=|\sigma\rangle\cos(\theta_{\mathbf{n}}/2)+2\sigma|\sigma\rangle\sin(\theta_{\mathbf{n}}/2)$, where the spinor variable $\sigma=\pm1/2$ specifies the spin projections in the laboratory frame. Using this representation in expression (5), we arrive at the Hamiltonian

$$\begin{aligned}H_{d}^{\text{hole}}=&(\varepsilon_{d}-\mu)\sum_{\mathbf{n}}X_{\mathbf{n}}^{22}\\&+\frac{1}{2}\sum_{\mathbf{n},\mathbf{m}}\sum_{\sigma_{\mathbf{n}},\sigma_{\mathbf{m}}}t_{\mathbf{nm}}\Bigg[\cos\frac{\theta_{\mathbf{n}}-\theta_{\mathbf{m}}}{2}(X_{\mathbf{n}}^{2,1/2}X_{\mathbf{m}}^{1/2,2}\\&+X_{\mathbf{n}}^{2,\overline{1/2}}X_{\mathbf{m}}^{\overline{1/2},2})+\sin\frac{\theta_{\mathbf{n}}-\theta_{\mathbf{m}}}{2}(X_{\mathbf{n}}^{2,1/2}X_{\mathbf{m}}^{\overline{1/2},2}\\&-X_{\mathbf{n}}^{2,\overline{1/2}}X_{\mathbf{m}}^{1/2,2})\Bigg],\end{aligned} \tag{6}$$

in which for completeness we have included the chemical potential μ, which is needed for studying the conducting and superconducting properties of metallic systems regardless of whether they are metals by nature or have somehow acquired conductivity. The Hamiltonian operator obtained for copper oxides in this way is practically the same as the Hamiltonian of the double-exchange model valid for manganites. This agreement again underscores the similarity noted in Ref. 9 between these, generally speaking, different physical systems containing as the basic elements transition metals and oxygen and which are *doped* metals. The angles $\theta_{\mathbf{n}}$ and $\theta_{\mathbf{m}}$ in (6) pertain to local and not sublattice coordinate systems. It is seen that the amplitudes of processes that conserve the carrier spin projection and those that occur with a spin flip depend on the mutual directions of the spin in the initial and final states. The similar written form is not only a consequence of the use of local axes of quantization but also a reflection of a certain physics, making it possible, it would seem, at the level of the single-particle Hamiltonian to distinguish one-particle, two-particle, and other processes.

In fact, suppose that the doped cuprate plane retains (at least the short-range) antiferromagnetic order. If this is the case, then for the two-sublattice case this immediately implies that there is a (dimensionless) magnetic structure vector $\mathbf{Q}_{\text{AFM}}=(\pm\pi,\pm\pi)$ (Ref. 26) which determines the direction of the local quantization axes: $\theta_{\mathbf{n}}\approx\mathbf{Q}_{\text{AFM}}\cdot\mathbf{n}$, where equality corresponds to long-range order. Since here the spin variables of the Hubbard operators pertain to the local coordinate systems, one can see that only the first term in the second sum in expression (6) corresponds to the so-called resonant inter-ion transitions (or coherent transport) of a carrier. The nonresonant (incoherent) transitions can be separated out in this Hamiltonian by using the following well-known

property[17,24] of the Hubbard operator algebra: $X_{\mathbf{n}}^{q_1q_2}=X_{\mathbf{n}}^{q_1q_3}X_{\mathbf{n}}^{q_3q_2}$. It allows one formally to introduce the spin operators exactly, according to the relations $X_{\mathbf{n}}^{2,\overline{1/2}}=X_{\mathbf{n}}^{2,1/2}X_{\mathbf{n}}^{1/2,\overline{1/2}}\equiv X_{\mathbf{n}}^{2,1/2}S_{\mathbf{n}}^{+}$ and analogously $X_{\mathbf{n}}^{\overline{1/2},2}=S_{\mathbf{n}}^{-}X_{\mathbf{n}}^{1/2,2}$, and with the aid of these to reduce (now approximately) the Hamiltonian (6) to the form

$$H_d^{\text{hole}}=H_{\text{coh}}+H_{\text{int}}^{(1)}+H_{\text{int}}^{(2)}, \tag{7}$$

in which

$$H_{\text{coh}}=(\varepsilon_d-\mu)\sum_{\mathbf{n}} X_{\mathbf{n}}^{2,2} + \frac{1}{2}\sum_{\mathbf{n},\mathbf{m}} t_{\mathbf{nm}}\cos\frac{\mathbf{Q}_{AFM}\cdot(\mathbf{n}-\mathbf{m})}{2}X_{\mathbf{n}}^{2,1/2}X_{\mathbf{m}}^{1/2,2} \tag{8}$$

is the operator of the free motion of a hole through an antiferromagnetically ordered medium:

$$H_{\text{int}}^{(1)}=\frac{1}{2}\sum_{\mathbf{n},\mathbf{m}} t_{\mathbf{nm}}\sin\frac{\mathbf{Q}_{AFM}\cdot(\mathbf{n}-\mathbf{m})}{2}(X_{\mathbf{n}}^{2,1/2}X_{\mathbf{m}}^{1/2,2}S_{\mathbf{m}}^{-} - X_{\mathbf{n}}^{2,1/2}X_{\mathbf{m}}^{1/2,2}S_{\mathbf{n}}^{+}) \tag{9}$$

and

$$H_{\text{int}}^{(2)}=\frac{1}{2}\sum_{\mathbf{n},\mathbf{m}} t_{\mathbf{nm}}\cos\frac{\mathbf{Q}_{AFM}\cdot(\mathbf{n}-\mathbf{m})}{2}X_{\mathbf{n}}^{2,1/2}X_{\mathbf{m}}^{1/2,2}S_{\mathbf{n}}^{+}S_{\mathbf{m}}^{-} \tag{10}$$

are the operators of the incoherent inter-ion transitions involving one and two spin excitations, respectively. Operators (9) and (10) can be regarded as possible sources of exchange—one- and two-magnon (first studied in Ref. 27)—mechanisms of superconductivity with a high critical temperature. However, as was recently shown by Valkov *et al.*[28] the three-center terms that govern the electron-spin interaction processes, $H_{\text{int}}^{(1)}$, lead to a substantial decrease of the temperature at which the superconducting phase with a *d*-wave type of order-parameter symmetry appears.[7)] Here the source of attraction is assumed to be the Heisenberg inter-spin interaction, or operator (4), which appears in the total Hamiltonian of a doped antiferromagnet,[17,25,28,29] where $J_{\mathbf{nm}}$ is not restricted to nearest neighbors. It should be noted here that as they were obtained by perturbation theory, this interaction and, accordingly, the constant $J_{\mathbf{nm}}$ in essence pertain only to the initial localized spins and describe specifically their (and not that of the *mobile* carriers) direct energy coupling.

Nevertheless, a specific attraction arises between doped carriers in an antiferromagnet, as was pointed out (apparently for the first time) in Ref. 32 (see also Refs. 22, 33, and 34). We are talking about an exchange interaction but only for those carriers which are found in different magnetic sublattices and are *nearest* neighbors, i.e., $\mathbf{n}-\mathbf{m}=\pm\mathbf{a}$ or $\mathbf{n}-\mathbf{m}=\pm\mathbf{b}$. It is easily checked that the value of the attraction in such a (singlet) pair of carriers is equal to the Heisenberg exchange J $(=J_{\mathbf{nn}\pm\mathbf{a}}=J_{\mathbf{nn}\pm\mathbf{b}})$, and the operator corresponding to it can be represented by the expression

$$H_{\text{attr}}=-J\sum_{\mathbf{n},\rho=\mathbf{a},\mathbf{b}} X_{\mathbf{n}}^{2,2}X_{\mathbf{n}+\rho}^{2,2}. \tag{11}$$

It is independent of both the spin variables and the angles $\theta_{\mathbf{n}}$ and $\theta_{\mathbf{n}+\boldsymbol{\rho}}$, since doped holes (and electrons, too) in an antiferromagnet with $S=1/2$ pertain to those ionic states which are spinless (we recall that in the simplest one-band Hubbard model their spins $S=0$). It is clear that the operator H_{attr} brings about a *nonretarded* attraction between carriers moving along different magnetic sublattices, including such a one that leads to an anisotropic superconducting order parameter. The total Hamiltonian of doped carriers in an antiferromagnet is the sum of expressions (7) and (11), and for a coherently moving carrier it has the form

$$H=H_{\text{coh}}+H_{\text{attr}}. \tag{12}$$

From here on, the superconducting properties of a doped antiferromagnetic system described by Hamiltonian (12) can be treated in the standard way (see, e.g., Refs. 13, 17, and 25), and we shall not discuss it further. We note only that the absence of long-range magnetic order in a metal (analogous to the case of excitons in insulators with partial magnetic or orientational disordering[35,36]) causes both the normal and anomalous fermion Green functions to be transformed to a convolution, one of the constituents of which is determined by the correlator of the spin projections at different lattice sites. As was shown in Ref. 37, taking it into account can lead to non-pole behavior of the Green function and, hence, to non-Fermi-liquid behavior of the subsystem of doped carriers in an antiferromagnetic metal with long-range spin ordering. We also note that if it has a reduced spatial dimension, then in the calculation of the aforementioned Green functions it is necessary to take into account one more cofactor: the correlator of the phases of the order parameter.[37] However, analysis of the influence of the two types of (dis-)ordering on the superconducting properties of a two-dimensional magnetic metal, the model of which is appropriate to the case of copper oxides, goes beyond the framework of this paper and will be carried out separately.

5. Finally, let us consider the dispersion characteristics of free carriers given by operator (8). Then, as is readily verified, the coordination "spheres" in the square lattice are defined by the vectors $\boldsymbol{\rho}_j$; here $\boldsymbol{\rho}_1=\pm\mathbf{a}\pm\mathbf{b}$, $\boldsymbol{\rho}_2=\pm(\mathbf{a}\pm\mathbf{b})$, $\boldsymbol{\rho}_3=\pm2\mathbf{a}\pm2\mathbf{b}$, etc. Now transforming to the Fourier components in the second term of the operator H_{coh} and taking into account that in a translationally invariant medium $t_{\mathbf{nm}}=t(|\mathbf{n}-\mathbf{m}|)=t(\rho_j)\equiv t_j$, we arrive at the simple relation

$$\varepsilon(\mathbf{k})=\varepsilon_d+\sum_j t_j\cos\mathbf{k}\cdot\rho_j\cos\frac{\mathbf{Q}_{AFM}}{2}\cdot\rho_j. \tag{13}$$

It follows directly from this that only those neighbors for which $\cos(\mathbf{Q}_{AFM}\cdot\boldsymbol{\rho}_j/2)\neq0$ contribute to the formation of the dispersion relation of a free carrier. In the present case of a two-sublattice antiferromagnet with a square lattice the second- and third-nearest neighbors are of this kind, which belong to the same magnetic sublattice as the spin of the initial ion. Using the explicit form of the vectors $\boldsymbol{\rho}_2$ and $\boldsymbol{\rho}_3$, we easily obtain (cf. Eq. (2)):

$$\varepsilon(\mathbf{k})=\varepsilon_d-4t_2\cos k_x\cos k_y-2t_3(\cos2k_x+\cos2k_y), \tag{14}$$

or, in other words, a spectrum that corresponds completely to the condition (long known in the theory of biexcitons in

antiferromagnets[6]) which was recently used by Andreev[33] (see also Ref. 34) for justification of the simple physical picture of superconductivity with pre-existing (i.e., formed above T_c) electron pairs. Such superconductivity, having the traits of HTSC, will necessarily lead to the existence of a pseudogap.[37]

Let us now suppose that the dispersion curves observed in ARPES[1,2] are described by relation (14) and assume that the amplitudes t_2 and t_3 can be treated as adjustable fitting parameters. In such a case one is readily convinced that in order to reconcile (at least qualitatively) the experimental curves exhibiting maxima at the point $k_x=k_y=\pi/2$ in both the diagonal direction $k_x=k_y$ and in the coordinate directions $k_x=0$ or $k_y=0$, it is necessary to set $t_2 \ll t_3$. Taking into account the nearest neighbor, characterized by the quantity t_1, which, as we have said, specifies the incoherent transfer (see Eq. (9)) cannot alter the inequality obtained. As a result, a spectrum of the form (14) formally corresponds to the spectrum of carriers in the so-called $tt'J$ model,[17] where, however, the first term with amplitude t contains not the sum of cosines but the sum of cosines of twice the argument. Such a conclusion is a direct consequence of the spin conservation law in the motion of charge carriers of either sign through an antiferromagnetically ordered square crystal lattice.

6. The simple calculations we have carried out show that the initial magnetic (and, in particular, antiferromagnetic) order imposes substantial restrictions on the behavior of an isolated carrier introduced into the system. Here in the region of underdoping (and, possibly, optimal doping), when one can still speak of antiferromagnetism of the medium, the motion of a carrier should and will determined by the character of its ordering. When the number of carriers (holes or electrons) introduced into the system reaches a level such that the magnetic ordering itself is destroyed and becomes conditional, the role of the restrictions due to the conservation law discussed in this paper decreases, and the dispersion (14) will no longer correspond to that observed in Refs. 1 and 2.

Also, as the doping is increased, the exchange attraction described by the operator H_{attr} (11) gradually falls. Ultimately, the problem of the appearance and, judging from everything, suppression of superconductivity in doped antiferromagnet requires a self-consistent treatment, where a variable number of carriers is determined not only by the position of the one-electron Fermi level but also by the properties of the space through which they move and also the strength of the pair—direct or indirect—interaction. Here the doping, by altering the mutual disposition and ''partial'' contribution of the p or d states in the crystal, can also be reflected in the nature of the carriers. Such a problem requires special study. Our goal was to analyze the situation corresponding to the low-doping limit.

Finally, it is important to note that it would be necessary and, seemingly, easy to check the results by measuring the dispersion relation of the conduction band in cuprates in an external magnetic field **H** (say, by the same ARPES method). Then, judging from (2), in expression (14) there should be a term containing t_1 ($\equiv t_{NN}$), which, like the Davydov splitting mentioned in Sec. 1, introduces to $\varepsilon(\mathbf{k})$ an asymmetry relative to the points $\mathbf{k}=(\pm\pi/2,\pm\pi/2)$. The specifics of a doped antiferromagnet consists only in the fact that in it this asymmetry is proportional to $\mathbf{H}^2$.

I thank Profs. Yu. B. Gaididei and A. A. Kordyuka for critical discussion of the questions touched upon here.

*E-mail: vloktev@bitp.kiev.ua

[1]The quotation marks are used because real (mostly classical) molecular crystals lack a so-called paraphase (i.e., high-symmetry structure) in which the translational symmetry for nearest neighbors could be recovered. For them such symmetry does not exist, as a rule, and the spectra of such crystals are therefore always (adequately) considered in a nonextended Brillouin zone scheme, i.e., in a model in which the unit cell is expanded as necessary but remains essentially regular.

[2]In the model of a crystal with a doubled lattice (see Ref. 3) they are both long-wavelength and, in the majority of known cases for molecular crystals with two molecules in the unit cell, optically active.

[3]Recall that the name spin excitation is customarily applied to an excitation of an electronic nature in which only the projection of an ion's spin changes; the so-called electronic excitations are accompanied by a change of the magnitude of the spin itself and/or other quantum numbers.[5,6]

[4]We are leaving aside such special cases as the formation of ferrons in magnetic semiconductors[8] or the phenomenon of double exchange in magnets (a comparison of the latter with HTSCs can be found in Ref. 9), since in cuprates, as far as we know, the magnetic order (at least, the short-range) remains unchanged (i.e., antiferromagnetic) and collinear. In addition, in view of the ionic nature of the bonding in the crystals in question a charged state (doped carrier) can deform the initial structure (polaron effect) more strongly than an unchanged state (exciton). Such questions are beyond the scope of the present paper.

[5]In the standard notation in HTSC physics, these are t and t', respectively.

[6]For simplicity we shall drop the other relevant d state, $d_{3z^2-r^2} \equiv d_{z^2}$, which can also be occupied by both a pre-exising and a doped hole, and the role of which was analyzed in Refs. 12 and 18.

[7]In principle, such a conclusion agrees with the result of Akhiezer and Pomeranchuk, who showed that the exchange of magnons leads to repulsion between carriers in singlet channels.[30] On the other hand, the operator (4) can serve as a cause of the formation of magnetically ordered states and, accordingly, the appearance of a singularity in the quasiparticle density of states.[30,31]

[1] F. Damascelli, Z. Hussain, and Z.-X. Shen, Rev. Mod. Phys. **75**, 473 (2003).
[2] Z.-X. Shen, E-print archive: cond-mat/0305576 (2003).
[3] A. S. Davydov, *Theory of Molecular Excitons*, Plenum Press, New York (1971), Nauka, Moscow (1968).
[4] V. V. Eremenko, *Introduction to Optical Spectroscopy of Magnets* [in Russian], Naukova Dumka, Kiev (1975).
[5] É. G. Petrov, *Theory of Molecular Excitons* [in Russian], Naukova Dumka, Kiev (1976).
[6] Yu. B. Gaĭdideĭ, V. M. Loktev, and A. F. Prikhot'ko, Fiz. Nizk. Temp. **3**, 549 (1977) [Sov. J. Low Temp. Phys. **3**, 263 (1977)].
[7] V. V. Eremenko and V. N. Novikov, JETP Lett. **11**, 326 (1970).
[8] É. L. Nagaev, *Physics of Magnetic Semiconductors*, Mir, Moscow (1983), Nauka, Moscow (1979).
[9] V. M. Loktev and Yu. G. Pogorelov, Fiz. Nizk. Temp. **26**, 231 (2000) [Low Temp. Phys. **26**, 171 (2000)].
[10] M. Kastner, R. J. Birgeneau, G. Shirane, and Y. Endoh, Rev. Mod. Phys. **70**, 897 (1998).
[11] V. J. Emery, Phys. Rev. Lett. **58**, 2794 (1987).
[12] Yu. B. Gaididei and V. M. Loktev, Preprint ITP-87-127P, Bogolyubov Institute for Theoretical Physics, Kiev (1987); Phys. Status Solidi **147**, 307 (1988).
[13] V. M. Loktev, Fiz. Nizk. Temp. **19**, 375 (1992) [Low Temp. Phys. **19**, 263 (1992)]; Ukr. Fiz. Zh. (Oglyadin) **1**, 10 (2004).
[14] F. C. Zhang and T. M. Rice, Phys. Rev. B **37**, 3759 (1988).
[15] R. Hayn, V. Yushanhai, and S. Lovtsov, Phys. Rev. B **47**, 5253 (1993).
[16] V. I. Belinicher and A. L. Chernyshov, Phys. Rev. B **49**, 9746 (1994).
[17] N. M. Plakida, *High-Temperature Superconductors*, Berlin, Springer (1995).
[18] S. G. Ovchinnikov, Zh. Éksp. Teor. Fiz. **107**, 796 (1995) [JETP **80**, 451 (1995)]; JETP Lett. **64**, 25 (1996).

[19] N. M. Plakida, R. Hayn, and J.-L. Richard, Phys. Rev. B **51**, 16599 (1995).
[20] V. A. Moskalenko, P. Entel, M. Marinaro, and D. F. Digor, Zh. Éksp. Teor. Fiz. **124**, 700 (2003) [JETP **97**, 632 (2003)].
[21] P. W. Anderson, Science **235**, 1196 (1987).
[22] E. Dagotto, Rev. Mod. Phys. **66**, 763 (1994).
[23] V. G. Baryakhtar, V. M. Loktev, and D. A. Yablonskii, Physica C **156**, 667 (1988).
[24] Yu. A. Izyumov and Yu. N. Skryabin, *Basic Models in the Quantum Theory of Magnetism* [in Russian], Urals Division of the Russian Academy of Sciences, Ekaterinburg (2002).
[25] N. M. Plakida, JETP Lett. **74**, 303 (2001).
[26] Yu. A. Izyumov and R. P. Ozerov, *Magnetic Neutron Diffraction*, Plenum Press, New York (1970), Nauka, Moscow (1966).
[27] V. S. Babichenko and Yu. Kagan, JETP Lett. **56**, 378 (1992).
[28] V. V. Val'kov, T. A. Val'kova, D. M. Dzhebisashvili, and S. G. Ovchinnikov, JETP Lett. **75**, 378 (2002).
[29] V. V. Val'kov, D. M. Dzebisashvili, and V. A. Mitskan, *First International Conference on Fundamental Problems of High-T_c Superconductivity* [in Russian], October 18–22, Moscow-Zvenigorod, P. N. Lebedev Physics Institute of the Russian Academy of Sciences (2004), p. 11.
[30] A. I. Akhiezer and I. Ya. Pomeranchuk, Zh. Éksp. Teor. Fiz. **36**, 819 (1959) [Sov. Phys. JETP **9**, 605 (1959)].
[31] A. F. Barabanov, A. A. Kovalev, O. V. Urazaev, and A. M. Belomouk, Phys. Lett. A **265**, 221 (2000).
[32] S. Trugman, Phys. Rev. B **37**, 1597 (1988).
[33] A. F. Andreev, JETP Lett. **79**, 88 (2004).
[34] Yu. B. Gaididei and V. M. Loktev, Ukr. Phys. J. **50**, 401 (2005).
[35] V. M. Loktev and S. G. Sharapov, Fiz. Nizk. Temp. **26**, 1214 (2000) [Low Temp. Phys. **26**, 899 (2000)].
[36] V. M. Loktev, S. G. Sharapov, and H. Beck, Fiz. Nizk. Temp. **28**, 311 (2002) [Low Temp. Phys. **28**, 220 (2002)].
[37] V. P. Gusynin, V. M. Loktev, and S. G. Sharapov, JETP Lett. **69**, 141 (1999); Zh. Éksp. Teor. Fiz. **117**, 1143 (2000) [JETP **90**, 993 (2000)].

Translated by Steve Torstveit

Nonlinear interaction of an electromagnetic wave with a transport current in a hard superconductor

M. L. Nesterov, T. M. Slipchenko, and V. A. Yampol'skii*

A. Ya. Usikov Institute of Radio Physics and Electronics, National Academy of Sciences of Ukraine, Ul. Akademika Proskury 12, Kharkov 61085, Ukraine
(Submitted December 21, 2004; revised January 19, 2005)
Fiz. Nizk. Temp. **31**, 656–664 (June 2005)

It is predicted that the time dependence of the electric field at the surface of a superconducting slab carrying a transport current will have jumps that occur as a result of the interaction of the current with the field of the electromagnetic wave. A theoretical analysis of the phenomenon is carried out in a simple model for arbitrary monotonic dependence of the critical current density on the magnetic induction. The dependence of the value of the jump of the electric field on the amplitude of the wave and the strength of the transport current is investigated. The predicted effect can be observed experimentally by measuring the emf of a coil wound on the slab in the plane perpendicular to the external ac magnetic field. © *2005 American Institute of Physics.* [DOI: 10.1063/1.1943534]

1. INTRODUCTION

Nonlinearity of the constitutive relation between the current density and the electromagnetic field in a conducting medium leads to a breakdown of the superposition principle and, hence, to interaction of electromagnetic waves inside a sample. The specific character of the nonlinearity of the medium is manifested in features of this interaction. For example, in hard superconductors the interaction of waves can lead to the unusual effect of jumps on the time dependence of the electric field $E(t)$ at the surface of the sample.[1,2] The conditions for the appearance of jumps of the electric field and also the amplitude of the jumps of $E(t)$ depend on the amplitude of the interacting electromagnetic waves, their frequencies, and the initial phase difference. Jumps of the electric field can be observed in samples with different geometry. This phenomenon has been observed experimentally in cylindrical samples of YBCO.[1,2]

In the present paper we show theoretically that jumps of the electric field at the surface of a sample should also arise under other experimental conditions, when a *single* monochromatic electromagnetic wave interacts with the transport current.

The static and quasistatic electromagnetic properties of hard superconductors are usually considered on the basis of the critical state model, which is valid over a rather wide range of amplitudes and frequencies, when the leading role in the formation of the current-carrying capacity of a sample is played by magnetic flux pinning. In the framework of this model Maxwell's equation for the distribution of the magnetic induction **B** in a superconducting sample has the form

$$\text{Curl}\ \mathbf{B}=\frac{4\pi}{c}J_c(B)\frac{\mathbf{E}}{E}, \tag{1}$$

where $J_c(B)$ is the critical current density. This equation is substantially nonlinear. The nonlinearity is due to both the dependence $J_c(B)$ and the factor $\mathbf{E}/E$ on the right-hand side of (1). The latter cause of nonlinearity is of particular interest, since it is present only in hard superconductors and is not encountered in any other nonlinear media. The peculiar type of nonlinearity of hard superconductors leads to a number of unique effects, e.g., to collapse of the transport current[3–5] and of the magnetization of the sample.[6–8] The collapse of the transport current is an effect wherein an external ac magnetic field causes the critical current flowing in the subsurface region of the superconductor to be displaced into the interior of the sample. The collapse of the magnetization is also an effect brought on by an ac magnetic field. Because of the specific electrodynamic properties of a hard superconductor, with increasing amplitude of the ac magnetic field the dc magnetization can be completely suppressed, i.e., the sample becomes nonmagnetic. The phenomenon considered in this paper also occurs as a result of the peculiar nonlinearity of hard superconductors.

In this paper the critical state model, generalized to the case of an arbitrary monotonic magnetic-field dependence of the critical current density, is used in a detailed theoretical investigation of the jumps of the electric field that occur due to the interaction of the transport current with the ac magnetic field, and we analyze the conditions for their appearance. We study the dependence of the amplitude of the jumps on the parameters of the problem, such as the value of the critical current density, the wave amplitude, the sample thickness, etc. As an example we consider the jumps of the electric field in the limiting case when there is no dependence $J_c(B)$.

2. STATEMENT OF THE PROBLEM

We consider an infinite superconducting slab of thickness d with a transport current I flowing along it. We assume that all the fields and currents depend only on one spatial coordinate x along an axis directed perpendicular to the slab. The origin $x=0$ is placed at one of the surfaces of the sample. A specified current I flows along the y axis and creates at the surface of the sample a magnetic field oriented

 © 2005 American Institute of Physics

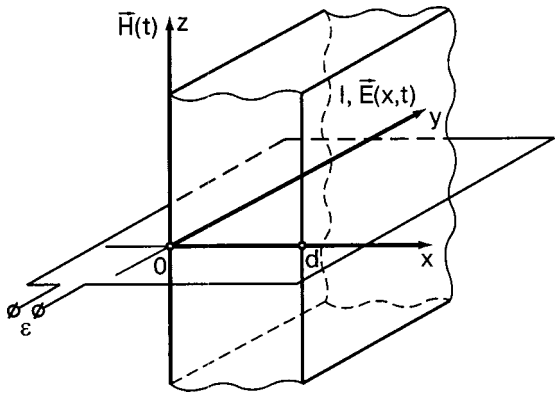

FIG. 1. Geometry of the problem.

along the z axis and equal to $\pm H_I$ ($H_I = 2\pi I/cD$, where D is the linear dimension of the sample along the self-magnetic field of the current).

The sample carrying transport current I is placed in an ac magnetic field $\mathbf{H}(t) = \mathbf{H}_0 \cos \omega t$ directed parallel to the surface of the sample along the self-magnetic field of the transport current $\mathbf{H}_I$ (along the z axis). The ac electric field that arises in this case is directed along the y axis (see Fig. 1).

To solve the problem it is convenient to write the critical current density in the form

$$J_c(B) = \frac{J_c(0)}{\psi(B)}. \tag{2}$$

We shall assume that the function $\psi(B)$ is smooth and monotonically increasing, with $\psi(0) = 1$.

In the geometry under consideration the system of Maxwell's equations has the form

$$\begin{cases} \dfrac{\partial F(B(x,t))}{\partial x} = -\dfrac{4\pi}{c} J_c(0)\,\mathrm{sgn}(E_y), \\ \dfrac{\partial E}{\partial x} = -\dfrac{1}{c}\dfrac{\partial B}{\partial t}, \end{cases} \tag{3}$$

where

$$F(B) = \int_0^B \psi(B^*)\, dB^*.$$

The boundary conditions on the system of Eqs. (3) are

$$B(0,t) = H_0 \cos \omega t + H_I,$$
$$B(d,t) = H_0 \cos \omega t - H_I. \tag{5}$$

Here we neglect the jump of the magnetic induction at the surface of the sample due to the Meissner currents. This can be done if the characteristic values of the magnetic fields are much greater than the first critical field H_{c1}.

The nondissipative transport current in the slab always has a value below the critical. It follows that $0 \leqslant H_I < H_p$, where H_p is the so-called penetration field. Its physical meaning is as follows. When the amplitude of the external ac magnetic field has the value H_p the electromagnetic wave penetrating into the sample just reaches the center of the sample. The value of H_p is the solution of the equation

$$F(H_p) = 2\pi J_c(0) d/c. \tag{6}$$

We note that in the case when the critical current density is independent of the magnetic induction, the function $\psi(B) = 1$ and $F(B) = B$. Then the penetration field takes the value $H_p = H_{p0} = 2\pi J_c(0) d/c$.

Below we shall consider only the case

$$H_I < H_p, \tag{7}$$

when there is a transport-current-free region near the center of the sample. As the following analysis shows, condition (7) is a necessary condition for the appearance of jumps in time of the electric field at the surface of the slab. Furthermore, it is necessary for the appearance of jumps that the amplitude of the ac signal H_0 exceed a certain threshold value $H_0^{(t)}$:

$$H_0 > H_0^{(t)}, \quad H_0^{(t)} = H_p - H_I. \tag{8}$$

For finding the distribution of the magnetic and electric fields in the sample it is convenient to introduce the dimensionless quantities

$$\xi = \frac{2x}{d}, \quad \tau = \omega t, \quad b(\xi,\tau) = \frac{B(x,t)}{H_{p0}}, \quad h_0 = \frac{H_0}{H_{p0}},$$
$$E_0 = \frac{\omega d H_{p0}}{2c}, \quad h_I = \frac{H_I}{H_{p0}}, \quad h_0^{(t)} = \frac{H_0^{(t)}}{H_{p0}}, \quad e = \frac{E}{E_0}. \tag{9}$$

The system of Eqs. (3) and the boundary conditions on it are written in the new notation as follows:

$$\begin{cases} \dfrac{\partial F(b(\xi,\tau))}{\partial \xi} = -\,\mathrm{sgn}(e(\xi,\tau)), \\ \dfrac{\partial e}{\partial \xi} = -\dfrac{\partial b(\xi,\tau)}{\partial \tau}; \end{cases} \tag{10}$$

$$b(0,\tau) = h_0 \cos \tau + h_I,$$
$$b(2,\tau) = h_0 \cos \tau - h_I. \tag{11}$$

3. EVOLUTION OF THE DISTRIBUTION OF THE MAGNETIC INDUCTION IN THE CASE OF LOW AMPLITUDES

Let us consider the evolution of the magnetic field distribution inside the sample. We begin with the case when there is no jump of the electric field at the surface:

$$H_0 < H_0^{(t)}, \quad h_0 < h_0^{(t)}. \tag{12}$$

According to the boundary conditions (11), at the time $\tau = 0$ the function $F(b)$ reaches its maximum values, equal to $F(h_0 \pm h_I)$, at the two boundaries of the slab. In accordance with the critical state model, at that time the electric field is equal to zero everywhere inside the superconductor. As time goes on, the magnetic induction $b(\xi,\tau)$ in the sample decreases, and an electric field is induced in the slab. Two subsurface regions with nonzero electric field appear. In these regions the sign of the derivative $\partial b(\xi,\tau)/\partial \xi$ is negative. In other regions the electric field remains equal to zero, and the distribution of the function $b(\xi,\tau)$ retains the shape it had at the initial time $\tau = 0$.

At the time $\tau = \pi$ the external magnetic field reaches its minimum value, the electric field inside the superconductor again goes to zero, and the distribution $F(b(\xi,\tau))$ takes the shape of broken line *3* in Fig. 2a. Then, in the interval $\pi < \tau < 2\pi$, the function $F(b(\xi,\tau))$ in the subsurface regions of

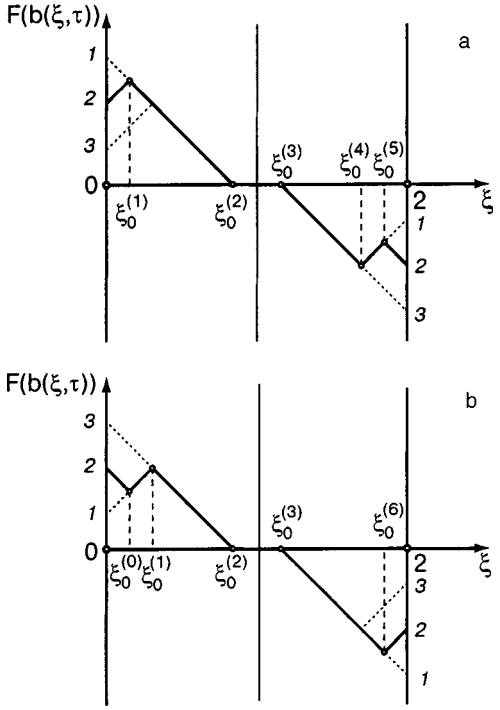

FIG. 2. Evolution of the distribution of the function $F(b\xi,\tau)$ inside the sample in the case of low amplitudes ($h_0<h_0^{(t)}$): in the time interval $0<\tau<\pi$ (a), for $\pi<\tau<2\pi$ (b).

the superconductor increases with time (see Fig. 2b). At the time $\tau=2\pi$ the external magnetic field again reaches a maximum value.

The solution of the equation of the critical state (10) with boundary conditions (11) gives the following results for the function $F(b(\xi,\tau))$:

$$F(b(\xi,\tau))=\pm\xi+\text{const}. \tag{13}$$

When the external magnetic field reaches a maximum value, at

$$\tau=0, \tag{14}$$

the distribution of the magnetic induction [more precisely, the function $F(b(\xi,\tau))$] is described by the expression

$$F(b(\xi,\tau))=\begin{cases} -\xi+F(h_I+h_0), & 0<\xi<\xi_0^{(2)},\\ 0, & \xi_0^{(2)}<\xi<\xi_0^{(3)},\\ -(\xi-2)+F(-h_I-h_0), & \xi_0^{(3)}<\xi<\xi_0^{(4)},\\ (\xi-2)+F(-h_I+h_0), & \xi_0^{(4)}<\xi<2. \end{cases} \tag{15}$$

The distribution is of the form given by line *1* in Fig. 2a, with three breaks:

$$\xi_0^{(2)}=F(h_I+h_0), \tag{16}$$

$$\xi_0^{(3)}=2+F(-h_I-h_0), \tag{17}$$

$$\xi_0^{(4)}=2+1/2[F(-h_I-h_0)-F(-h_I+h_0)]. \tag{18}$$

At subsequent times, for

$$0<\tau<\pi, \tag{19}$$

the field distribution $F(b(\xi,\tau))$ acquires two more breaks in addition to those already mentioned:

$$\xi_0^{(1)}=1/2[F(h_I+h_0)-F(h_I+h_0\cos\tau)], \tag{20}$$

$$\xi_0^{(5)}=2+1/2[F(-h_I+h_0\cos\tau)-F(-h_I+h_0)], \tag{21}$$

and takes the form shown by line *2* in Fig. 2a:

$$F(b(\xi,\tau))=\begin{cases} \xi+F(h_I+h_0\cos\tau), & 0<\xi<\xi_0^{(1)},\\ -\xi+F(h_I+h_0), & \xi_0^{(1)}<\xi<\xi_0^{(2)}\\ 0, & \xi_0^{(2)}<\xi<\xi_0^{(3)},\\ -(\xi-2)+F(-h_I-h_0), & \xi_0^{(3)}<\xi<\xi_0^{(4)},\\ (\xi-2)+F(-h_I+h_0), & \xi_0^{(4)}<\xi<\xi_0^{(5)},\\ -(\xi-2)+F(-h_I+h_0\cos\tau), & \xi_0^{(5)}<\xi<2. \end{cases} \tag{22}$$

The external magnetic field and, hence, the function $F(h(\tau))$ reaches a minimum when

$$\tau=\pi. \tag{23}$$

At that time the graph of the distribution $F(b(\xi,\tau))$ has the shape shown by line *3* in Fig. 2a:

$$F(b(\xi,\pi))=\begin{cases} \xi+F(h_I-h_0), & 0<\xi<\xi_0^{(1)},\\ -\xi+F(h_I+h_0), & \xi_0^{(1)}<\xi<\xi_0^{(2)},\\ 0, & \xi_0^{(2)}<\xi<\xi_0^{(3)},\\ -(\xi-2)+F(-h_I-h_0), & \xi_0^{(3)}<\xi<2 \end{cases} \tag{24}$$

with breaks at points that can be found from formulas (20), (16), and (17).

At subsequent time, for

$$\pi<\tau<2\pi, \tag{25}$$

$F(h(\tau))$ increases at the surface of the sample and the electric field also increases. The graph of the distribution $F(b(\xi,\tau))$ acquires two additional breaks at the points

$$\xi_0^{(0)}=1/2[F(h_I+h_0\cos\tau)-F(h_I-h_0)], \tag{26}$$

$$\xi_0^{(6)}=2-1/2[F(-h_I+h_0\cos\tau)-F(-h_I-h_0)], \tag{27}$$

and the distribution itself has the shape shown by line *2* in Fig. 2b:

$$F(b(\xi,\tau))=\begin{cases} -\xi+F(h_I+h_0\cos\tau), & 0<\xi<\xi_0^{(0)},\\ \xi+F(h_I-h_0), & \xi_0^{(0)}<\xi<\xi_0^{(1)}\\ -\xi+F(h_I+h_0), & \xi_0^{(1)}<\xi<\xi_0^{(2)},\\ 0, & \xi_0^{(2)}<\xi<\xi_0^{(3)},\\ -(\xi-2)+F(-h_I-h_0), & \xi_0^{(3)}<\xi<\xi_0^{(6)},\\ (\xi-2)+F(-h_I+h_0\cos\tau), & \xi_0^{(6)}<\xi<2. \end{cases} \tag{28}$$

The graph of the field distribution at the time

$$\tau=2\pi \tag{29}$$

is the same as at the initial time $\tau=0$ and coincides with line *1* in Fig. 2a.

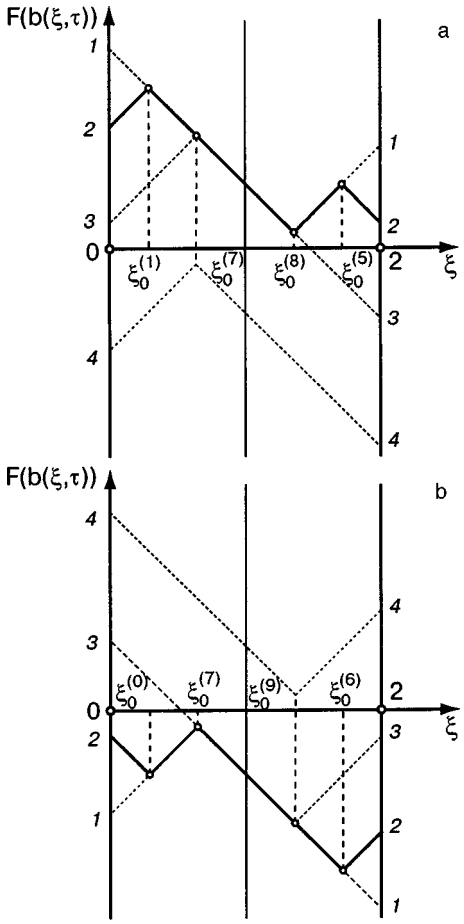

FIG. 3. Evolution of the distribution of the function $F(b\xi,\tau)$ inside a sample in the case of large amplitudes ($h_0>h_0^{(t)}$): in the time interval $0<\tau<\pi$ (a), for $\pi<\tau<2\pi$ (b).

4. EVOLUTION OF THE MAGNETIC FIELD DISTRIBUTION IN THE CASE OF LARGE AMPLITUDES

In this Section we consider the more interesting case

$$H_0>H_0^{(t)}, \quad h_0>h_0^{(t)}, \tag{30}$$

when a jump appears in electric field at the surface of the sample. As will be shown below, under conditions (30) at a certain instant $\tau=\tau_{\text{jump}}$ the position of the points separating the regions in which $\partial b(\xi,\tau)/\partial\tau=0$ and $\partial b(\xi,\tau)/\partial\tau\neq 0$ changes abruptly, and that implies a jump in the rate at which magnetic flux is "swept out" of the sample.

The solution of the equation of the critical state (10) with boundary conditions (11) gives the following results for the distribution of magnetic induction in different time intervals.

Broken line *1* in Fig. 3a illustrates schematically the distribution $F(b(\xi,\tau))$ in the slab at the starting time $\tau=0$. There is one break point, which is found from the equation

$$\xi_0^{(8)}=1+1/2[F(h_I+h_0)-F(-h_I+h_0)], \tag{31}$$

and the distribution itself has the form

$$F(b(\xi,0))=\begin{cases}-\xi+F(h_I+h_0), & 0<\xi<\xi_0^{(8)},\\ (\xi-2)+F(-h_I+h_0), & \xi_0^{(8)}<\xi<2.\end{cases} \tag{32}$$

At subsequent time, in the interval

$$0<\tau<\tau_{\text{jump}}^{(1)}, \tag{33}$$

the distribution $F(b\xi,\tau))$ is described by the formula

$$F(b(\xi,\tau))=\begin{cases}\xi+F(h_I+h_0\cos\tau), & 0<\xi<\xi_0^{(1)},\\ -\xi+F(h_I+h_0), & \xi_0^{(1)}<\xi<\xi_0^{(8)},\\ (\xi-2)+F(-h_I+h_0), & \gamma_0^{(8)}<\xi<\xi_0^{(5)},\\ -(\xi-2)+F(-h_I+h_0\cos\tau), & \xi_0^{(5)}<\xi<2\end{cases} \tag{34}$$

(see line *2* in Fig. 3a). The break points $\xi_0^{(1)}$ and $\xi_0^{(5)}$ that arise in this case were encountered previously above. Their values are found from formulas (20) and (21), respectively.

At the time

$$\tau=\tau_{\text{jump}}^{(1)} \tag{35}$$

the graph of the distribution $F(b\xi,\tau))$ takes the form shown by broken line *3* in Fig. 3a:

$$F(b(\xi,\tau_{\text{jump}}^{(1)}))=\begin{cases}\xi+F(h_I+h_0\cos\tau_{\text{jump}}^{(1)}), & 0<\xi<\xi_0^{(7)},\\ -(\xi-2)+F(-h_I+h_0\cos\tau_{\text{jump}}^{(1)}), & \xi_0^{(7)}<\xi<2\end{cases} \tag{36}$$

with a single break point

$$\xi_0^{(7)}=1/2[F(-h_I+h_0\cos\tau_{\text{jump}}^{(1)})-F(h_I+h_0\cos\tau_{\text{jump}}^{(1)})]+1. \tag{37}$$

A jump of the electric field arises at the time determined by the relation

$$\cos\tau_{\text{jump}}^{(1)}=1/h_0\{F^{-1}[F(h_I+h_0)-2]+h_I\}. \tag{38}$$

Here the symbol F^{-1} denotes the inverse function, and $[F(h_I+h_0)-2]$ is the argument of that function.

In the next time interval, for

$$\tau_{\text{jump}}^{(1)}<\tau<\pi, \tag{39}$$

the break point remains in its previous position, and the distribution $F(b\xi,\tau))$ takes the form

$$F(b(\xi,\tau))=\begin{cases}\xi+F(h_I+h_0\cos\tau), & 0<\xi<\xi_0^{(7)},\\ -(\xi-2)+F(-h_I+h_0\cos\tau), & \xi_0^{(7)}<\xi<2.\end{cases} \tag{40}$$

At the time $\tau=\pi$ the graph of the distribution has the form of broken line *4* in Fig. 3a and is described by the following expression:

$$F(b(\xi,\tau))=\begin{cases}\xi+F(h_I-h_0), & 0<\xi<\xi_0^{(7)},\\ -(\xi-2)+F(-h_I-h_0), & \xi_0^{(7)}<\xi<2.\end{cases} \tag{41}$$

In the time interval

$$\pi<\tau<\tau_{\text{jump}}^{(2)} \tag{42}$$

the distribution of the magnetic induction [more precisely, the function $F(b\xi,\tau))$] is given by the formulas

$$F(b(\xi,\tau))=\begin{cases}-\xi+F(h_I+h_0\cos\tau), & 0<\xi<\xi_0^{(0)},\\ \xi+F(h_I-h_0), & \xi_0^{(0)}<\xi<\xi_0^{(7)},\\ -(\xi-2)+F(-h_I-h_0), & \xi_0^{(7)}<\xi<\xi_0^{(6)},\\ (\xi-2)+F(-h_I+h_0\cos\tau), & \xi_0^{(6)}<\xi<2.\end{cases} \tag{43}$$

The graph of the distribution has the form of line *2* in Fig. 3b, with three breaks at the points $\xi_0^{(7)}$, $\xi_0^{(0)}$, and $\xi_0^{(6)}$. Their positions are found from formulas (37), (26), and (27), respectively.

When the condition $\tau=\tau_{\text{jump}}^{(2)}$ holds, the electric field at the surface of the sample again takes a jump. The time $\tau_{\text{jump}}^{(2)}$ can be found from the formula

$$\cos\tau_{\text{jump}}^{(2)}=1/h_0\{F^{-1}[F(-h_I-h_0)-2]-h_I\}. \tag{44}$$

At that instant the graph of the distribution $F(b(\xi,\tau))$ is as illustrated by line *3* in Fig. 3b:

$$F(b(\xi,\tau_{\text{jump}}^{(2)}))=\begin{cases}-\xi+F(h_I+h_0\cos\tau_{\text{jump}}^{(2)}), & 0<\xi<\xi_0^{(9)},\\ (\xi-2)+F(-h_I+h_0\cos\tau_{\text{jump}}^{(2)}), & \xi_0^{(9)}<\xi<2\end{cases} \tag{45}$$

with a single break point

$$\xi_0^{(9)}=1/2[F(-h_I+h_0\cos\tau)-F(h_I+h_0\cos\tau+h_I)]+1. \tag{46}$$

In the time interval

$$\tau_{\text{jump}}^{(2)}<\tau<2\pi \tag{47}$$

the external magnetic field grows to its maximum value. The graph of the distribution $F(b\xi,\tau))$ ''slides'' upward without changing shape, and the break point $\xi_0^{(9)}$ maintains its position. After the field reaches a maximum value the cycle described above repeats anew.

5. STUDY OF THE ELECTRIC FIELD AT THE SURFACE OF THE SAMPLE

In this Section we calculate the values of the electric field at the surface of the slab at different points in time and find the values of the jumps in it. We take as the observable quantity the electromotive force (emf) in a coil wound directly on the sample (see Fig. 1) in a plane perpendicular to the direction of the ac magnetic field. The value of the emf is related to the electric field at the surface of the sample by the relation

$$\varepsilon=[E(d)-E(0)]Ln, \tag{48}$$

where L is the length of the slab along the current, and n is the number of turns in the coil. In the case under discussion the emf is described by the formula

$$\varepsilon=-\frac{Ln}{c}\int_0^d\frac{\partial B}{\partial t}dx. \tag{49}$$

We introduce to dimensionless quantities. For this we normalize the emf of the induction to its characteristic value ε_0:

$$\varepsilon_0=E_0Ln,\quad e=\frac{E}{E_0}=\frac{\varepsilon}{\varepsilon_0}. \tag{50}$$

Then we rewrite Eq. (49) in the following way:

$$e=-\int_0^2\frac{\partial b(\xi,\tau)}{\partial\tau}d\xi. \tag{51}$$

For finding the emf of the induction we note that

$$\frac{\partial F(b(\xi,\tau))}{\partial\tau}=\psi(b(\xi,\tau))\frac{\partial b(\xi,\tau)}{\partial\tau}, \tag{52}$$

$$\frac{\partial F(b(\xi,\tau))}{\partial\xi}=\psi(b(\xi,\tau))\frac{\partial b(\xi,\tau)}{\partial\xi}=-\operatorname{sgn}(e(\xi,\tau)). \tag{53}$$

We first consider the case of low amplitudes (12), when no jump of the electric field occurs. Then during the first half period $0\leqslant\tau\leqslant\pi$, i.e., during a monotonic decrease of the external magnetic field, the emf of the induction is given by the expression

$$e=h_0\sin\tau[\psi(h_I+h_0\cos\tau)](-h_I+h_0\cos\tau+b^{(1)})-\psi(-h_I+h_0\cos\tau)(-h_I+h_0\cos\tau-b^{(5)}), \tag{54}$$

where $b^{(1)}$ and $b^{(5)}$ are the values of the magnetic induction at the corresponding break points. They can be expressed in terms of the inverse F functions:

$$b^{(1)}=F^{-1}\{1/2[F(h_I+h_0)+F(h_I+h_0\cos\tau)]\}, \tag{55}$$

$$b^{(5)}=F^{-1}\{1/2[F(-h_I+h_0)+F(-h_I+h_0\cos\tau)]\}. \tag{56}$$

In the second half period $\pi\leqslant\tau\leqslant2\pi$, when the external magnetic field is decreasing, the emf of the induction has the form

$$e=h_0\sin\tau[\psi(-h_I+h_0\cos\tau)](-h_I-h_0\cos\tau-b^{(6)})-\psi(h_I+h_0\cos\tau)(-h_I-h_0\cos\tau+b^{(0)}) \tag{57}$$

with the following values of the field at the break points:

$$b^{(0)}=F^{-1}\{1/2[F(h_I-h_0)+F(h_I+h_0\cos\tau)]\}, \tag{58}$$

$$b^{(6)}=F^{-1}\{1/2[F(-h_I-h_0)+F(-h_I+h_0\cos\tau)]\}. \tag{59}$$

Let us now turn to the case of large amplitudes. In the first half period, $0\leqslant\tau\leqslant\pi$, in the time interval (33) (up to the first jump) the behavior of the emf is described by the same formula (54) as for small amplitudes. In the interval (39) (after the first jump) the emf depends on time as

$$e=h_0\sin\tau[\psi(h_I+h_0\cos\tau)](-h_I-h_0\cos\tau+b^{(7)})-\psi(-h_I+h_0\cos\tau)(-h_I+h_0\cos\tau-b^{(7)}) \tag{60}$$

with the value of the field at the break point, which is found from the formula

$$b^{(7)}=F^{-1}\{1/2[F(h_0\cos\tau_{\text{jump}}-h_I)+F(h_I+h_0\cos\tau_{\text{jump}})]+1\}. \tag{61}$$

In the second half period we observe a picture symmetric to the one described above. Until the second jump the emf of the induction is described by the relation (57) found above, and after the second jump it is described by formula (60).

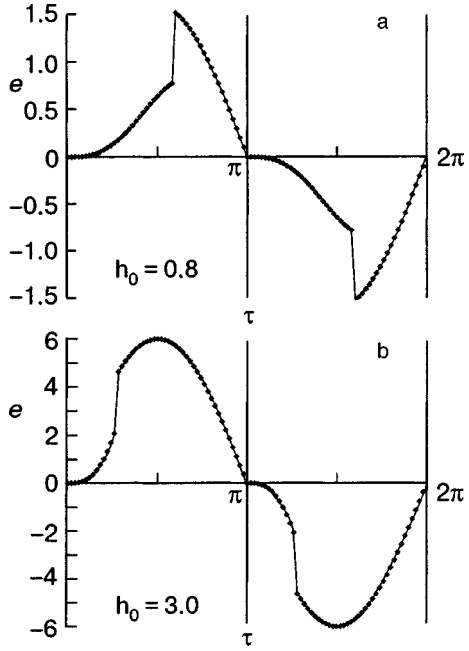

FIG. 4. Jumps in the time dependence of the emf at values of the amplitude of the ac field $h_0=0.8$ (a) and 3.0 (b).

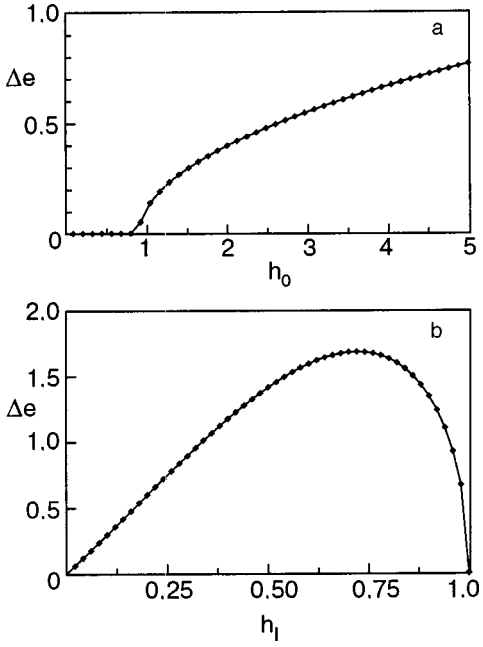

FIG. 5. Value of the emf jump as a function of the amplitude of the ac magnetic field $h_0=H_0/H_p$ for $h_I=0.5$ (a) and as a function of the transport current strength (the parameter h_I) for $h_0=1.5$ (b).

Let us determine the value of the jump of the emf. For this we find the difference of the emfs of the induction directly before and after the jump:

$$\Delta e = h_0 \sin\tau[\psi(h_I+h_0\cos\tau)](b^{(7)}-b^{(1)}) - \psi(-h_I+h_0\cos\tau)(b^{(7)}-b^{(5)}). \quad (62)$$

As an example, let us consider the limiting case when the critical current density is independent of field. Such a case can be realized, e.g., in the presence of an additional strong external magnetic field with a value much greater than H_p. In such a situation $\psi(b)=1$, $F(b)=b$. Then the condition for the appearance of jumps of the emf is

$$H_I<H_p, \quad H_0<H_0^{(t)}, \quad (63)$$

where $H_p=2\pi J_c d/c$, and $H_0^{(t)}=H_p-H_I$ is the threshold amplitude of the magnetic field. The formula for the value of the jump in emf takes the form

$$\Delta e = 4h_I\sqrt{(1-h_I)(h_0+h_I-1)}. \quad (64)$$

Analytical results obtained in neglect of the magnetic dependence of the critical current density are conveniently presented in graphic form. Figure 4 shows graphs of $e(\tau)$ for $h_I=0.5$ and two different amplitudes of the ac field. It is seen that the emf jumps appear more distinctly in Fig. 4a, i.e., in the case of not too low amplitudes. Figure 5a demonstrates the square-root growth of the jump with increasing amplitude of the ac magnetic field. Figure 5b shows the dependence of the value of the jump on the current strength (on the parameter h_I).

As is seen in Fig. 4, on average over the period of the magnetic field the emf in a coil wound on the sample is equal to zero. At the same time, it has been shown[9,10] that in the given situation the period-averaged electric field in the slab is nonzero. To see this, it is sufficient to do a simple analysis of the dynamics of the change of the distribution of the magnetic induction in the sample with the aid of Figs. 2 and 3. It is clear that in the course of each period of the ac field a certain magnetic flux is ''pumped through'' the sample from left to right, and its movement generates a dc component of the electric field. In the experiment proposed here the dc component of the field cannot be detected, since, according to Eq. (48), the coil actually registers the difference of the electric fields at the two opposite surfaces of the slab.

We conclude with a numerical estimate of the value of the emf jump in the proposed experiment. In a coil containing 100 turns wound on a ceramic sample 1 mm thick by 1 cm square, with a critical current density of 1 kA/cm^2 at a frequency of 100 Hz, an easily measurable emf jump of the order of 1–2 mV is induced.

The authors are grateful to E-H. Brandt, L. M. Fisher, and G. P. Mikitik for helpful discussions of the results of this study.

*E-mail: yam@ire.karkov.ua

[1] I. V. Baltaga, I. F. Voloshin, K. V. Il'enko, L. M. Kalinov, N. M. Makarov, L. M. Fisher, V. A. Yampol'skii, and M. Pinsky, Solid State Commun. **93**, 697 (1996).
[2] I. V. Baltaga, I. F. Voloshin, K. V. Il'enko, L. M. Kalinov, N. M. Makarov, F. Perez-Rodriguez, L. M. Fisher, and V. A. Yampol'skii, Physica C **251**, 50 (1995).
[3] I. V. Baltaga, I. F. Voloshin, N. V. Il'in, N. M. Makarov, L. M. Fisher, and V. A. Yampol'skii, Phys. Lett. A **148**, 213 (1990).
[4] I. F. Voloshin, N. V. Il'in, N. M. Makarov, L. M. Fisher, and V. A. Yampol'skiĭ, JETP Lett. **53**, 109 (1991).
[5] I. V. Baltaga, I. F. Voloshin, N. M. Makarov, L. M. Fisher, and V. A. Yampol'skii, Fiz. Nizk. Temp. **21**, 441 (1995) [Low Temp. Phys. **21**, 320 (1995)].
[6] I. V. Baltaga, I. F. Voloshin, K. V. Il'enko, L. M. Kalinov, L. M. Fisher, and V. A. Yampol'skii, Solid State Commun. **97**, 833 (1996).

[7] I. F. Voloshin, L. M. Kalinov, M. A. R. LeBlanc, S. E. Savel'ev, L. M. Fisher, S. Hirscher, and V. A. Yampol'skii, Physica C **278**, 169 (1997).
[8] I. F. Voloshin, K. V. Il'enko, L. M. Kalinov, M. A. R. LeBlanc, F. Perez-Rodriguez, S. E. Savel'ev, L. M. Fisher, and V. A. Yampol'skii, Phys. Rev. B **61**, 15382 (2000).
[9] V. V. Andrianov, V. B. Zenkevich, V. V. Kurguzov, V. V. Sychev, and F. F. Ternovskiĭ, Zh. Éksp. Teor. Fiz. **58**, 1523 (1970) [Sov. Phys. JETP **31**, 815 (1970)].
[10] G. P. Mikitik and E. N. Brandt, Phys. Rev. B **64**, 092502 (2001).

Translated by Steve Torstveit

LOW-TEMPERATURE MAGNETISM

Short-period oscillations of the resistivity and magnetoresistance in Co/Cu(111) superlattices on mica

V. V. Zorchenko* and A. N. Stetsenko

National Technical University "Kharkov Polytechnical Institute," ul. Frunze 21, Kharkov 61002, Ukraine

A. G. Anders

V. N. Karazina Kharkov National University, pl. Svobody 4, Kharkov 61077, Ukraine; B. Verkin Institute for Low Temperature Physics and Engineering, National Academy of Sciences of Ukraine, pr. Lenina 47, Kharkov 61103, Ukraine

K. V. Kutko

B. Verkin Institute for Low Temperature Physics and Engineering, National Academy of Sciences of Ukraine, pr. Lenina 47, Kharkov 61103, Ukraine

(Submitted June 29, 2004; revised September 28, 2004)
Fiz. Nizk. Temp. **31**, 665–678 (June 2005)

In a study of $[\mathrm{Co}(8\ \text{Å})/\mathrm{Cu}(d_{\mathrm{Cu}})(111)]_{20}$ superlattices grown by magnetron sputtering it is found that the resistivity ρ_s and relative magnetoresistance $\Delta R/R_s$ in magnetic fields $H=15$ kOe oriented parallel or perpendicular to the layers exhibit oscillations as the thickness of the copper spacer layers is varied in the range $d_{\mathrm{Cu}}=6-40$ Å. Extrema of ρ_s and $\Delta R/R_s$ are observed at $d_{\mathrm{Cu}}=nd_{(111)}$, where n is an integer or half-integer and $d_{(111)}=2.087$ Å is the distance between (111)Cu planes, with a distance between adjacent maxima or minima equal to 1, 1.5, 2, 2.5 and $3d_{(111)}$. When the magnetic field deviates from the plane of the layers the magnetic-field dependence of the resistivity exhibits an additional maximum due to a feature of the magnetization of the layers in the superlattice in an inclined field. The oscillations of ρ_s and $\Delta R/R_s$ are accompanied by oscillations of the magnetic anisotropy constants in synchrony with them. Analysis of the experimental data and theoretical calculations of the orientation of the magnetic moments of the layers when a magnetic field perpendicular to the layers is turned on allows one to explain the observed effects wherein the roughness of the interfaces between layers varies nonmonotonically with increasing d_{Cu}, leading to oscillations of the bilinear and biquadratic exchange interactions of the Co layers. © *2005 American Institute of Physics.*
[DOI: 10.1063/1.1943535]

1. INTRODUCTION

The giant magnetoresistance (MR) in multilayer systems of nonmagnetic and ferromagnetic metals is usually manifested in structures with an antiferromagnetic (AF) exchange interaction of neighboring magnetic layers across the nonmagnetic spacers.[1] In such structures the relative magnetoresistance $\Delta R/R_s$ (see below) and the exchange interaction energy J_1 of the layers are oscillatory functions of the thickness d_{nm} of the nonmagnetic spacers, and the maxima of $\Delta R/R_s$ are observed at the same values of d_{nm} as the maxima of J_1. In intervals of d_{nm} in which the ferromagnetic (F) interaction is manifested, $\Delta R/R_s$ takes on relatively small values. For a Co/Cu superlattice (SL) one observes 3–4 maxima of $\Delta R/R_s$ at values of d_{nm} which are multiples of ~ 9 Å,[2–7] in good agreement with the theoretical calculations of the period of the oscillations of the exchange interaction, first predicted in Ref. 8 (see also Refs. 9 and 10).

Numerous mechanisms have been proposed for explaining the giant MR, including bulk-spin-dependent and boundary-spin-dependent scattering of electrons, variation of the potential relief for electrons with opposite spin directions when the magnetic field is turned on, and scattering on structural defects (see, e.g., the review[11] and papers[12–14]). Furthermore, the same high level of MR has also been observed in Co/Cu superlattices in the absence of AF interaction of the Co layers;[15] this suggests the possibility of alternative mechanisms of giant MR. Despite detailed theoretical analysis, the main mechanism governing the level of MR in specific magnetic SLs, e.g., Co/Cu, still remains unclear.

In this paper we present data on new, never-before observed oscillations of the resistivity and magnetoresistance in Co/Cu superlattices as the thickness d_{Cu} of the Cu layers is varied, with anomalously small distances between maxima ($\sim 1-2$ monolayers of Cu). Ferromagnetic resonance (FMR) studies of these same SLs revealed oscillations of the magnetic anisotropy and resonance linewidth which were in synchrony with oscillations of the resistivity and magnetoresistance; these will be described in a separate paper.

2. STRUCTURE OF THE SAMPLES AND THE MEASUREMENT TECHNIQUE

The samples were grown by successive condensation of Co and Cu on a mica substrate at room temperature with the use of magnetron sputtering in a vacuum apparatus with a

 © 2005 American Institute of Physics

residual atmosphere of $\sim 10^{-6}$ torr at an argon pressure of 1.3×10^{-3} torr. The layer thicknesses were determined by multibeam optical interferometry with an accuracy of 2% or better. The samples, 10×0.15 mm in size, consisted of a copper underlayer (50 Å) on the mica, on top of which 20 Co/Cu bilayers were formed. The upper layer of copper for all the samples had a thickness of 12.5 Å. The thickness of the Co layers was fixed at 8 Å, and the thickness of the copper spacers was varied from 6 to 40 Å. The rate of condensation of Co and Cu were 0.45 and 0.58 Å/s, respectively.

According to electron microscope studies, the samples removed from the mica had a polycrystalline structure. The (111)Cu plane was parallel to the surface of the substrate without any preferred orientations of the other crystallographic planes of the grains with respect to the mica. The cobalt and copper layers grow epitaxially on each other. The grain boundaries pass through the whole thickness of the sample practically perpendicular to the mica surface (i.e., one grain spans the thickness of the sample). The grains have an equiaxed form in the plane of the sample. The grain sizes did not vary greatly, having values $\sim 80-100$ Å independently of d_{Cu}, although for $d_{\mathrm{Cu}}\geqslant 30$ Å one also encounters a small fraction of grains with sizes ~ 120 Å. These data suggest that the grain size is set by the first layer of copper condensed (the 50 Å layer), upon which the Co/Cu superlattice is formed. As a result, the crystal structure is a set of columnar grains highly elongated along the normal to the surface.

We note that our results correlate with the known published data. In particular, in Ref. 16 analogous columnar structure was obtained in the magnetron sputtering of $[\mathrm{Co}(10\ \text{Å})/\mathrm{Cu}(20\ \text{Å})]_{15}$ superlattices on an underlayer of copper 350 Å thick (the grain size was also ~ 350 Å). However, in the growth of $[\mathrm{Co}(11\ \text{Å})/\mathrm{Cu}(d_{\mathrm{Cu}})]_6$ on an underlayer of Ru (50 Å) under the same conditions of Co and Cu condensation by this same research group[17] the grain size was found to be strongly dependent on the thickness of the copper spacers; for example, at $d_{\mathrm{Cu}}=9$ and 43 Å the grain size was 30–50 Å and 100–200 Å, respectively, and several grains fit across the thickness of the sample; the formation of columnar grains was suppressed by recrystallization processes occurring directly during growth of the layers.

A low-angle $\vartheta-2\vartheta$ x-ray scan showed the presence of two peaks and a set of weakly damped oscillations of the intensity of the reflected x-ray beam, attesting to the uniformity of the thickness of the samples, the low roughness of the interfaces between layers, and the presence of periodicity in the superlattice.

Hysteresis loops were recorded using a vibromagnetometer. The magnetoresistance was measured in direct current at a field of up to 17 kOe directed parallel or perpendicular to the current in the plane of the sample or perpendicular to the SL layers. For some samples we measured the MR in magnetic fields directed perpendicular to the current and at an angle ϑ ($0-90°$) to the normal to the surface of the sample (this angle was set to an accuracy of $\sim 0.5°$).

The measurements showed that the Co/Cu structure has a relatively low coercive force H_c. For example, for the samples with $d_{\mathrm{Cu}}=8$, 13.5, and 37 Å it had values $H_c\approx 30$, 36, and 22 Oe, respectively. Their hysteresis loops had a ratio $M_r/M_s\sim 0.8$ (M_r is the remanent magnetization of the sample at $H=0$, and M_s is the saturation magnetization in a field $H=H_s$), and the magnetization of the samples varied rapidly in the field region below ~ 100 Oe and increased weakly at high fields. These facts suggest that the AF interaction of the Co layers in these SLs either is absent or is masked by regions with F interaction around magnetic shorts of Co atoms,[7,18,19] which should be localized in the region of large-angle grain boundaries and places where three grains come together. We note that weakening of the AF interaction is promoted by a relatively high pressure of the residual atmosphere[20,21] and, especially, of oxygen[20] during growth of Co/Cu SLs and also by nonoptimality of the Co layer thickness.[22] Under the vacuum conditions of the present experiment one cannot expect a strong AF interaction between Co layers.

3. OSCILLATIONS OF THE RESISTIVITY AND MAGNETORESISTANCE

Measurements of the magnetic-field dependence of the resistivity shows that the shape of the $R(H)$ curves depends on the orientation of the magnetic field relative to the plane of the sample and the current direction (Fig. 1). If the magnetic field lies in the plane of the sample perpendicular to the current, $R(H)$ has the usual shape for multilayers, with maxima at $H=\pm H_c$ (Refs. 2 and 17). When the magnetic field is parallel to the current one observes shallow minima in the low-field region $H\sim H_c$, apparently due to the anisotropic magnetoresistive effect in the Co layers, and then a maximum, after which the behavior of $R(H)$ differs little from that for the case of orthogonal orientation of the field and current.

In a magnetic field perpendicular to the plane of the sample, in addition to the small low-field maximum a second maximum, at $H=H^*$ ($\sim 1.76-6.24$ kOe), was observed for some of the samples (see Fig. 2). When the field direction

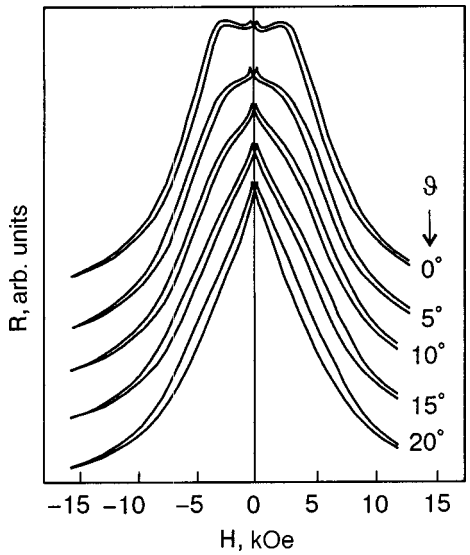

FIG. 1. Magnetoresistance $R(H)$ of a Co/Cu superlattice with a thickness of the copper spacer layers $d_{\mathrm{Cu}}=12$ Å for different angles of deviation ϑ of the magnetic field **H** from the direction normal to the surface of the sample in the the plane orthogonal to the current. The shape of the curves is qualitatively the same in the angle interval $\vartheta\sim 20-90°$.

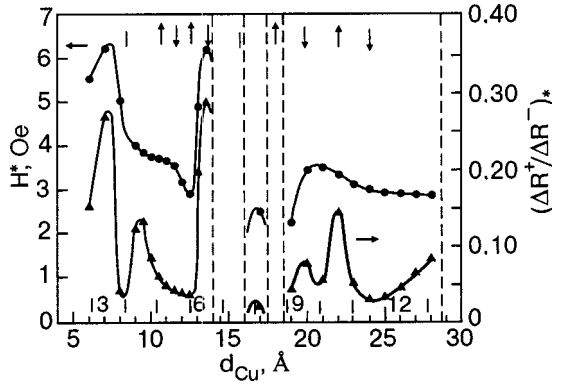

FIG. 2. Values of the field H^* at which the second maximum of $R(H)$ is observed and of the ratio $(\Delta R^+/\Delta R^-)_*$ for Co/Cu multilayers in a magnetic field perpendicular to the plane of the samples as functions of the thickness d_{Cu} of the copper spacer layers. Here and below, the vertical dashed lines show the values of $d_{Cu}=nd_{(111)}$, where n is an integer and $d_{(111)}=2.087$ Å is the distance between (111) Cu planes. The arrows directed upward and downward and the vertical hash marks indicate the positions of the maxima, minima, and inflection points of $(\Delta R/R_s)_*$ versus d_{Cu}.

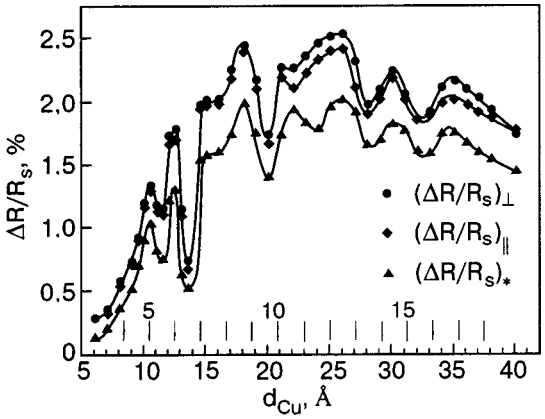

FIG. 3. Dependence of the relative magnetoresistance $\Delta R/R_s$ of Co/Cu superlattices on the thickness d_{Cu} of the copper spacers in a magnetic field lying in the plane of the sample perpendicular $(\Delta R/R_s)_\perp$ or parallel $(\Delta R/\Delta R_s)_\parallel$ to the current or directed normal to the plane of the samples $(\Delta R/R_s)_*$.

deviates from the normal to the surface of the sample in the plane perpendicular to the current by an angle $\vartheta \geqslant 3-15°$ the second maximum is smeared out, and only a hump remains on the $R(H)$ curve, and for $\vartheta \geqslant 10-35°$ that hump vanishes completely and the $R(H)$ curve takes the usual form. In regions near $d_{Cu} \approx 15$ and 18 Å and also for $d_{Cu} \geqslant 30$ Å, the second maximum on the $R(H)$ curves is absent (the boundaries of these regions are shown by the vertical dashed lines in Fig. 2). A similar form of modification of the $R(H)$ curves was observed previously in one of the first papers on giant MR for Ag/Co superlattices[23] when the magnetic field deviates from the normal to the sample in the plane passing through this normal and the current direction, but the authors did not offer any explanation for this effect. An analogous form of the $R(H)$ curves was obtained for $[(Ni_xFe_{(1-x)}Ag_{(1-y)}]$/Ag structures in a field perpendicular to the layers[24] and also for Fe/Gd superlattices in a magnetic field parallel to the layers,[25] and this was explained by a change of the angle between the magnetization of the originally antiferromagnetically oriented Fe and Gd layers, starting at some threshold field.

The dependence of the relative magnetoresistance $\Delta R/R_s$ on d_{Cu} for different orientations of the magnetic field is shown in Fig. 3. Here $\Delta R=\Delta R^+ + \Delta R^-$, where $\Delta R^+ = R^{max} - R_0$ and $\Delta R^- = R_0 - R(H_s)$, and R^{max} is the maximum value of $R(H)$, $R_0=R(H=0)$, $R(H_s)=R_s$ is the resistance of the samples in a field $H=15$ kOe, at which $R(H)$ is close to saturation. The relative MR has some characteristic features. The level of $\Delta R/R_s$ is rather low, which is not surprising in view of the nonoptimal conditions of sample preparation. In all of the intervals of thicknesses d_{Cu} the values of $\Delta R/R_s$ turned out to have its largest value for a field orientation perpendicular to the current in the plane of the sample except at the largest thicknesses of the copper spacers, and the smallest values when the magnetic field was directed perpendicular to the plane of the layers. In the case when the field was parallel to the current, the MR was somewhat smaller than in the case of a field perpendicular to the current in the plane of the sample. This difference has been mentioned in the literature[15,26] and was explained by two factors: the anisotropic magnetoresistive (AMR) effect for ferromagnetic materials,[27] and the intrinsic anisotropy of the giant magnetoresistance.[28–30] The $\Delta R/R_s$ curves for the different orientations of the magnetic field behave similarly except in the region $d_{Cu} \sim 20-25$ Å.

The most remarkable feature of the $\Delta R/R_s$ curves for all three magnetic-field orientations is their oscillatory character, with the extrema of the curves observed at values of the copper spacer thickness d_{Cu} equal to an integer or half-integer number of interplane distances for the Cu(111) planes: $d_{(111)}=2.087$ Å (the thicknesses $nd_{(111)}$ are shown in Figs. 2 and 3 by the vertical hash marks labeled by the number n above them. The distances between maxima (or between minima) of $\Delta R/R_s$ are very small, considerably less than the characteristic known period 9 Å for Co/Cu superlattices.[2–7] In particular, these distances are equal to 1, 1.5, 2, 2.5, and $3d_{(111)}$, i.e., the largest of them does not exceed ~ 6 Å. The smallest period of oscillations with respect to d_{Cu} that we know of was observed in a study[31] of photoemission from copper films on (001)Co and had a value equal to a thickness of 2.3 ± 0.1 atomic layers of (001)Cu (this corresponds to the theoretically expected value for the interlayer exchange coupling and the period of modulation of the density of states at the Fermi level for the corresponding quantum wells[8–10]). We note that for Fe/Cr(001) structures, short-period (2.1 atomic layers of Cr) oscillations of the exchange coupling[32] and magnetoresistance[33] have been observed which are due to features of the topology of the Fermi surface of Cr.[34] Theoretical calculations of the exchange interaction in Co/Cu superlattices[8–10] and quantum size effects for electronic states[35] cannot give such small ($\sim 1-1.5$ atomic layers) periods of oscillations of J_1 or of the electron density of states for any orientation of the copper layers, and it is therefore necessary to look for another explanation of the short-period oscillations of the relative MR.

The oscillations of $\Delta R/R_s = \Delta\rho/\rho_s$ are caused by oscillations of $\Delta\rho$ and ρ_s. Figure 4 shows plots of $\Delta\rho_\parallel^-$, $\Delta\rho_\parallel^+$, and $\rho_s^\parallel$. Here and below the sub/superscripts $\parallel$ and $\perp$ refer to orientations of the magnetic field in the plane of the layers parallel to and perpendicular to the current, and $*$ indicates

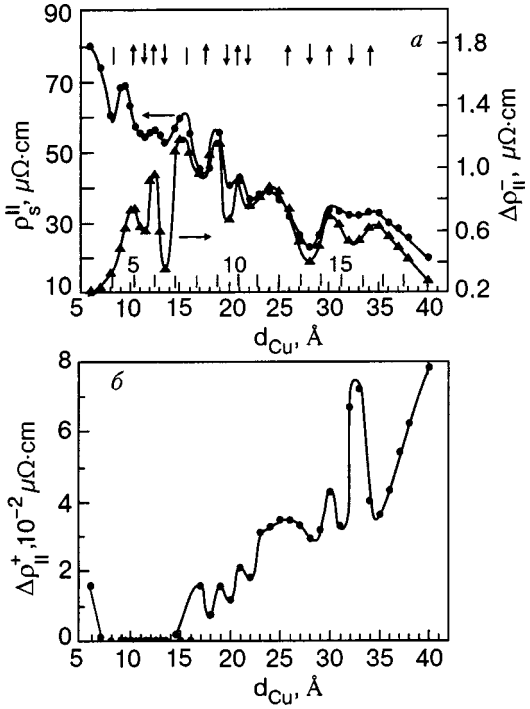

FIG. 4. Resistivity $\rho_s^{\parallel}$ of a Co/Cu superlattice in the state of saturation in a magnetic field $H=15$ kOe directed parallel to the current and the values of $\Delta\rho_{\parallel}^{-}$ (a) and $\Delta\rho_{\parallel}^{+}$ (b) as functions of the thickness d_{Cu} of the copper spacers. The arrows and hash marks indicate the position of the singular points of $(\Delta R/\Delta R_s)_{\parallel}$.

an orientation with the field perpendicular to the layers.

It is seen in Fig. 4 that the extrema of $(\Delta R/R_s)_{\parallel}$ correspond to the extrema of $\Delta\rho_{\parallel}^{-}$ and $\rho_s^{\parallel}$ (since the value of $\Delta\rho_{\parallel}^{+}$ is much smaller than $\Delta\rho_{\parallel}^{-}$, we shall focus mainly on the behavior of $\Delta\rho_{\parallel}^{-1}$) except for the maxima at $d_{Cu}=5d_{(111)}$ and $12.5d_{(111)}$ (for convenience in Fig. 4 the positions of the extrema of $\Delta R/R_s$ are indicated by arrows pointing up (maximum) or down (minimum). The inflection point on the step at $d_{Cu}=7.5d_{(111)}$ also corresponds to maxima of $\Delta\rho_{\parallel}^{-}$ and $\rho_s^{\parallel}$. For $d_{Cu}=9d_{(111)}$ all three quantities $\Delta\rho_{\parallel}^{-}$, $\Delta\rho_{\parallel}^{+}$, and $\rho_s^{\parallel}$ have a maximum, which apparently should correspond to a step in this region of d_{Cu} (not shown in Fig. 3). The positions of the extrema of $\Delta\rho_{\parallel}^{-}$ and $\rho_s^{\parallel}$ coincide completely starting at $d_{Cu}>5d_{(111)}$, while at smaller d_{Cu} they do not coincide. Remarkably, the extrema of $\Delta\rho_{\parallel}^{-}$ and $\rho_s^{\parallel}$ that do coincide with respect to d_{Cu} are of the same type, i.e., minima or maxima. An important circumstance is that the maxima and minima of $(\Delta R/\Delta R_s)_{\parallel}$ coincide with the maxima and minima of $\Delta\rho_{\parallel}^{-}$ and $\rho_s^{\parallel}$ except in the region $d_{Cu}<5d_{(111)}$ and the point $d_{Cu}=8.5d_{(111)}$ (near 18 Å), where minima of $\Delta\rho_{\parallel}^{-}$, $\Delta\rho_{\parallel}^{+}$, and $\rho_s^{\parallel}$ and a maximum of $(\Delta R/\Delta R_s)_{\parallel}$ are observed. The position of the extrema of $\Delta\rho_{\parallel}^{+}$, as a rule, also coincide with the extrema of $\Delta\rho_{\parallel}^{-}$ and $\rho_s^{\parallel}$ (see Fig. 4). In particular, the absence of an extremum of $\Delta\rho_{\parallel}^{+}$ at $d_{Cu}=11.5d_{(111)}$ has made its so that an extremum of $(\Delta R/\Delta R_s)_{\parallel}$ is not observed at that thickness d_{Cu}, although $\Delta\rho_{\parallel}^{-}$ and $\rho_s^{\parallel}$ have maxima there.

We note that our Co/Cu SLs have a higher level of resistivity $\rho_s^{\parallel}$ in comparison with the published data. For example, for $[\mathrm{Co}(11\ \text{Å})/\mathrm{Cu}(d_{Cu})]_{20}$ the value of $\rho(H=0)$ is approximately equal to 23 and 17 $\mu\Omega\cdot$cm for $d_{Cu}=9$ and 18 Å, respectively.[3] For a SL with $d_{Co}=15$ Å and $d_{Cu}=9$ Å prepared by another research group[4] a similar value, $\rho_s=20.3\ \mu\Omega\cdot$cm, was obtained. These values are approximately three times lower than the corresponding levels of $\rho_s^{\parallel}$ for our SLs.

Using the known relation[36] for copper, $\rho\lambda_{Cu}=750\ \mu\Omega\cdot\text{cm}\cdot$ Å (where λ_{Cu} is the mean free path of electrons in copper) and neglecting for estimation the difference between cobalt and copper, we obtain the following values of the electron mean free path for samples with $d_{Cu}=9$ Å ($\rho_s^{\parallel}=68.5\ \mu\Omega\cdot$cm), 18 Å ($\rho_s^{\parallel}=46\ \mu\Omega\cdot$cm), and 40 Å ($\rho_s^{\parallel}=20\ \mu\Omega\cdot$cm): $\lambda\approx 10.9$, 16.3, and 37.5, respectively. In the whole range of d_{Cu} from 6 to 40 Å the value of λ is less than the superlattice period $\Lambda=d_{Cu}+d_{Co}$ and close to d_{Cu} (sometimes larger and sometimes smaller than d_{Cu}). This suggests strong scattering of electrons on impurities and interfaces in the SL. The cause of this scattering cannot be grain boundaries, since the mean size of the grains is much greater than λ. It is clear that at such small values of λ even in the presence of AF ordering of the Co layers one cannot expect an appreciable value of the MR and relative MR in our SLs, since the appearance of giant MR requires that λ at least be considerably larger than Λ.

In this regard we note that in choosing the argon pressure P_{Ar} for the sputtering of the Co and Cu targets we took into account the circumstance[37,38] that the value of $\Delta R/R_s$ is strongly dependent on P_{Ar}. For example, in Ref. 37 for a $[\mathrm{Co}(19\ \text{Å})/\mathrm{Cu}(9.5\ \text{Å})]_{40}$ superlattice, decreasing P_{Ar} led to an increase of $\Delta R/R_s$ (at room temperature) from ~2% at $P_{Ar}\approx 11.25$ mtorr to ~39% at $P_{Ar}=3$ mtorr. Record values of $\Delta R/R_s$ for Co/Cu SLs have been obtained at $P_{Ar}=3.25$ mtorr ($\Delta R/R_s=65\%$)[39] and $P_{Ar}=3.75$ mtorr (>80%)[20] (in the latter case, for a Co/Cu(111) SL, decreasing P_{Ar} to 1.5 mtorr led to a drop of $\Delta R/R_s$ to 75%).[40]

Furthermore, decreasing the argon pressure led to a decrease of the roughness of the interfaces between Co and Cu layers, although it was accompanied by some enhancement of the mixing of the Co and Cu layers.[37] For this reason we decided to investigate what will happen at a low argon pressure in the hope of obtaining structures with extremely smooth layers in view of the absence of roughness on a substrate of fluorophlogopite. Apparently our too severe regime of deposition of the Co and Cu layers led to a certain mixing of the layers and to high resistivity of the samples.

We note that for many SLs, e.g., Al/Ni, Al/Ag,[41] Ni/Cu,[42] and Pd/Au,[43] the resistivity ρ is inversely proportional to the SL period; this relationship, which agrees with the predictions of the theory of the classical size effect for superlattices,[43] holds under the condition that the main mechanism of electron scattering is due to the interfaces between layers. For our samples $\rho_s^{\parallel}(\Lambda)$ can apparently be considered to be a more complicated function of $1/\Lambda$, containing a term proportional to $1/\Lambda$ and an oscillatory admixture (see Fig. 5).

For the magnetic SLs Ni/Cu (Ref. 44) and Co/Ni (Ref. 45) in zero magnetic field one observes oscillations of ρ_0 as a function of the layer thickness, the nature of which has not been conclusively established. For Co/Ni this effect is apparently due to features of the electron spectrum of the SL.[45] For a Co/Cu SL[3] the oscillations are due to oscillations of the

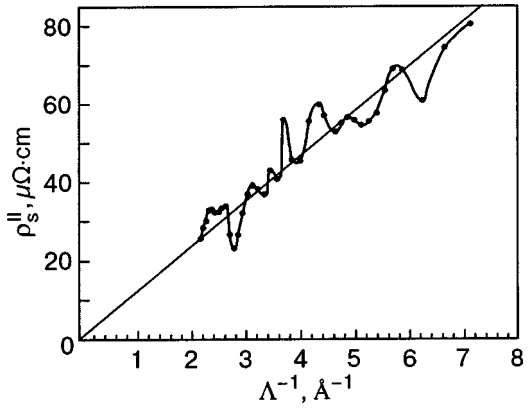

FIG. 5. Plot of the resistivity $\rho_s^{\parallel}$ of a Co/Cu superlattice (see Fig. 4) as a function of Λ^{-1}, the reciprocal of the multilayer period $\Lambda = d_{\mathrm{Cu}} + d_{\mathrm{Co}}$.

AF interaction of the Co layers. We do not know of any papers on metallic SLs in which thickness oscillations of ρ_s are described except for Ref. 45 on Co/Ni SLs, where the period of the oscillations with respect to d_{Co} and d_{Ni} were approximately 20 Å.

4. DISCUSSION OF THE RESULTS

Let us examine the possible explanations for the observed oscillations of $\Delta R/R_s$, $\Delta\rho$, and ρ_s. In the theory of the giant MR, oscillatory dependence on thickness due to superlattice effects of quantization of the electron spectrum have been considered in a number of papers,[46] but those theoretical models did not take into account the concrete form of the energy bands of the SL. When recently developed methods of calculating the MR with the real energy structure of the SL taken into account are applied to the Co/Cu system,[47–49] they apparently cannot give oscillations of the MR with a period of one or two atomic layers. It is therefore natural to look for another explanation for the oscillations of $\Delta R/R_s$, $\Delta\rho$, and ρ_s.

In the theoretical analysis of the causes of the oscillations of ρ and the MR it can be assumed that there exist several mechanisms governing the level of resistance which depend on the magnetic field. The first of these, which is responsible for the giant MR in antiferromagnetically ordered SLs, is due to the spin-dependent scattering of electrons in the interior of the layers and at the interfaces between them, and the effective manifestation of this mechanism requires that the electrons cross several interfaces before scattering (i.e., $\Lambda < \lambda_{SL}$). The contribution of this mechanism to the resistance is determined by the angle φ between the directions of the magnetic moments of adjacent layers $\mathbf{M}_1$ and $\mathbf{M}_2$, and in the case when $\mathbf{M}_1$ and $\mathbf{M}_2$ are parallel to the layers it is well described by the relation

$$[\rho(H) - \rho_s] \sim \sin^2(\varphi/2) (\varphi = 0 \ \text{ at } \ \rho(H) = \rho_s).$$

This relation has been confirmed experimentally for current directions both parallel to and perpendicular to the SL layers,[28,29,50] although some deviations from this dependence are also observed. This dependence has been justified theoretically in the framework of the classical[51,52] and quantum-mechanical[47,52,53] calculations of the conductivity of magnetic SLs (more-complex behavior of the MR is also theoretically possible, with the appearance of a maximum at a certain value of φ).[52,53] In the case of AF ordering of the magnetic layers at $H = 0$ the angle $\varphi = \pi$, and the value of $[\rho(H) - \rho_s]$ (and thereby $\Delta\rho_{\parallel}^{-}$) reaches its maximum possible value. In the case of ferromagnetic ordering of the layers $\varphi = 0$, and the this contribution vanishes.

The presence of a rather strong biquadratic interaction of the layers (see Appendix) can lead to an additional noticeable rotation of the magnetic moments of adjacent layers by a certain angle, so that the angle $\varphi(H = 0) = \varphi_0$ turns out to be less than 180° in the case of an antiferromagnetic interaction and greater than zero for a ferromagnetic interaction, and therefore in the AF case the biquadratic interaction will lower the value of $\Delta\rho_{\parallel}$, while in the F case, on the contrary, it will give rise to magnetoresistance.

As a rule, the value of $\Delta R/R_s$ is small in the case of a ferromagnetic interaction of the SL layers, but a case is known[15] in which a Co/Cu SL grown by molecular beam epitaxy exhibited giant MR of the same scale ($\sim$40%) in the absence of AF interaction as for a SL with AF coupling. In that case the giant MR effect is due to suppression by the magnetic field of electron scattering on thermal fluctuations of groups of spins of the Co atoms, which are apparently localized at monoatomic steps or are islands of Co atoms on the surface of smooth parts of the Co films. Furthermore, an external magnetic field should suppress the scattering of electrons on fluctuations of the magnetic field generated by steps[54] and superparamagnetic complexes of Co atoms.

A third mechanism is that of anisotropic spin-orbit scattering, which leads to the well-known AMR effect,[27] and when the magnetic moment **M** deviates from the current direction it gives a negative (for Co) contribution to the resistance which is proportional to the square of the sine of the angle between the moment **M** and the current.

To explain the oscillations of $\Delta\rho$, ρ_s, and $\Delta R/R_s$, we shall make two main assumptions. The first is that the roughness of the interfaces in our SL is an oscillatory function of d_{Cu}. For copper films it has been predicted theoretically that their roughness oscillates as the film thickness increases, with a characteristic oscillation step of one or two atomic layers of copper.[55] Such oscillations should be observed in the case of a sufficiently high surface mobility of the atoms being condensed (in our case this condition is satisfied) and a layer-by-layer mechanism of film growth. According to theoretical estimates,[56] they should lead to noticeable corresponding oscillations of the resistance of the film. Analogous effects should also be manifested in superlattices.[57] The second assumption is the presence of an appreciable biquadratic interaction of neighboring magnetic layers in our SLs, which leads to a change of the angle φ between $\mathbf{M}_1$ and $\mathbf{M}_2$ in the absence of magnetic field.

The energies of the bilinear J_1 and biquadratic J_2 interactions depends strongly on the roughness of the interfaces between layers. One of the main mechanisms proposed for the formation of J_2 is directly related to this roughness[58] (the growth of J_2 when roughness appears). In particular, experiments on a $[\mathrm{Co}(10\ \text{Å})/\mathrm{Cu}(9\ \text{Å})]_{50}$ superlattice (the first AF peak of $\Delta R/R_s$) have shown that for smooth layers the relative MR reaches 65% at room temperature and falls to 31% with increasing roughness of the interfaces.[59] Here the rela-

tionship between J_1 and J_2 changes from $J_1/J_2 \approx 2.7$ to $J_2/J_1 \approx 3$. Calculations of the orientation of the magnetic moments of neighboring layers $\mathbf{M}_1$ and $\mathbf{M}_2$ for our SLs in a magnetic field perpendicular to the layers are given in the Appendix. It follows from those calculations that under the condition $|J_1|/2J_2 < 1$ the biquadratic interaction will lead to a change of the angle φ_0. The value of this change, which influences the value of the first contribution to the MR, will increase with increasing interfacial roughness and will be an oscillatory function of d_{Cu}, according to our first assumption.

These assumptions can also account for the appearance of the second maximum on the $R(H)$ curves for magnetic fields orthogonal to the substrate and the oscillatory behavior of the field $H^*(d_{\mathrm{Cu}})$ at which the second maximum of $R(H)$ is observed. Indeed, if the biquadratic interaction is relatively weak, i.e., $|J_1|/2J_2 > 1$, then the angle φ_0 for the AF and F interactions of the layers will equal 180° and zero, respectively. With increasing magnetic field the angle θ between the field direction and the magnetic moments of the layers will gradually decrease from 90° to zero (for a constant angle $\psi = \varphi_0$ between the projections of $\mathbf{M}_1$ and $\mathbf{M}_2$ on the plane of the sample), and there is no reason for a maximum to appear on $R(H)$. If, however, $|J_1|/2J_2 < 1$, then the angle φ_0 is different from 180° or zero, and with increasing field (up to a certain value) a decrease of θ occurs, the angle φ remains equal to φ_0, and the angle ψ tends toward 180° for either sign of the bilinear interaction. In this field region one expects a decrease of $R(H)$ due to the AMR effect if the contribution of the first mechanism to the MR depends only on the angle φ. Starting with a certain value of the field there can be a situation in which the angle φ starts to grow ($\varphi > \varphi_0$), reaching a maximum (at $\psi = 180°$), and then falls monotonically to zero at high fields for which the magnetic moments of the layers will be oriented along the field. In this case the nonmonotonic trend of φ will give rise to the corresponding maximum of $R(H)$. In the case of large roughness and/or small $|J_1|$, when the angle φ_0 is close to 90°, the maximum should vanish. Then only a ''hump''—a feature in the form of a smeared step—remains on the $R(H)$ curve. The dependence of the field H^* on d_{Cu} should be largely determined by the parameter $|J_1|/2J_2$, i.e., by the dependences $J_1(d_{\mathrm{Cu}})$ and $J_2(d_{\mathrm{Cu}})$, which, in turn, are intimately related to the interfacial roughness.

Let us analyze the dependence of $\Delta\rho$ and ρ_s on the interfacial roughness. For a ferromagnetic interaction of the magnetic layers enhancement of the roughness should lead to growth of $\Delta\rho$ for any orientation of the magnetic field owing to an increase of the angle φ_0 and the contribution of the first MR mechanism, the enhancement of the scattering on the ''dangling'' spins of Co atoms found at the interfaces of the layers, and to a slight decrease of $\Delta\rho$ because of the AMR effect, which because of the relative smallness of the contribution in our case [which is attested to by the smallness of the difference $(\Delta R/R_s)_\perp - (\Delta R/R_s)_\parallel$] should not alter the overall picture of the growth of $\Delta\rho$ with increasing roughness. In the case of an AF interaction, with increasing roughness the second and third mechanisms will alter $\Delta\rho$ in the same direction as for the F interaction. However, the contribution of the first mechanism to $\Delta\rho$ should decrease because of the decrease of the angle φ_0 and of the electron mean free path λ with increasing roughness. The value of ρ_s increases with increasing roughness in all cases.

Thus in the case of a ferromagnetic interaction of the layers or for an antiferromagnetic interaction if the first MR mechanism is not the governing one, growth of the roughness should case a simultaneous synchronous growth of $\Delta\rho$ and ρ_s. A decrease of $\Delta\rho$ and increase of ρ_s with increasing roughness is a sign of AF interaction. We note, however, that in the general case this assertion can be incorrect. One can imagine a situation in which $\varphi = 180°$ and the layers of the ferromagnetic and nonmagnetic metals are ideally smooth, so that the reflection of electrons from the interfaces is almost total and specular. In this case the first MR mechanism is ineffective, since the electrons will be pent up in the ferromagnetic and nonmagnetic layers. Then the appearance of roughness should lead to growth of $\Delta\rho$ and ρ_s. It can therefore be assumed that for AF interaction of the layers the largest relative MR should be achieved at a low, optimal level of roughness, since strong roughness sharply limits the value of λ and lowers the giant MR effect. The conjecture that there is an optimal structure of the Co/Cu interfaces from the standpoint of magnetoresistance was first made in Ref. 60 on the basis of experimental data. In view of what we have said, the conjecture that specular scattering of electrons at the interfaces between layers is possible is confirmed by quantum-mechanical calculations for Co/Cu(111) structures,[49] which showed that part of the electrons found in the copper layers are pent up in these layers and cannot leave them (if the interfaces are sufficiently smooth), and this ''channeling'' effect can be one of the main mechanisms of the giant MR. On the other hand, calculations[13] in which the spin-dependent potential relief for electrons is taken into account but the scattering inside the layers is assumed to be independent of spin give a MR that increases with increasing roughness. In Ref. 12 it was predicted that spin-dependent interfacial scattering would be enhanced with increasing roughness and with interchanges of Co and Cu atoms at the interfaces. It is seen from the examples given that the question of the role of roughness in the formation of the MR is by no means closed.

In our case the interfaces are far from optimal, and therefore in the antiferromagnetic case we would expect growth of ρ_s and a decrease of $\Delta\rho$ with increasing roughness for our SLs. It can also be shown that in the case of a ferromagnetic interaction the value of $\Delta R/R_s$ should behave with changing roughness in a manner qualitatively similar to $\Delta\rho$ and ρ_s.

The relations presented above can be used to explain the behavior of the d_{Cu} dependence of $\Delta R/R_s$, $\Delta\rho_\parallel^-$, and $\rho_s^\parallel$, including the breakdown of synchrony of their oscillations in the region 15 Å $\leqslant d_{\mathrm{Cr}} \leqslant$ 18 Å and also the noncoincidence of the maxima of $\Delta\rho_\parallel^-$ and $\rho_s^\parallel$ in the region $d_{\mathrm{Cu}} \approx 5d_{(111)}$. It is natural to suppose that the maxima (minima) of $\rho_s^\parallel$ also correspond to the maxima (minima) of the roughness. Then synchrony in the behavior of $\Delta\rho_\parallel^-$ and $\rho_s^\parallel$ for $d_{\mathrm{Cu}} > 5d_{(111)}$ should mean either that the layers are ferromagnetically coupled or that in this interval of d_{Cu} the second MR mechanism is the main one. It is also natural to suppose that the layers have a ferromagnetic type of exchange interaction in almost the whole interval of d_{Cu} values investigated (this

agrees with the synchrony of the oscillations of $\Delta R/R_s$, $\Delta\rho_{\parallel}^{-}$, and $\rho_s^{\parallel}$). Then the maximum of $H^*(d_{\mathrm{Cu}})$ (Fig. 2) at $d_{\mathrm{Cu}}=6.5d_{(111)}$ should correspond to a minimum of the roughness (and, apparently, to a minimum of J_1) and to minima of $\Delta\rho_{\parallel}^{-}$ and $\rho_s^{\parallel}$, as is observed. With decreasing d_{Cu} there is a sharp increase in roughness, accompanied by a sharp drop of H^* and vanishing of the second maximum of $R(H)$ in the region $d_{\mathrm{Cu}}\sim 15$ Å, where apparently the sign of J_1 changes from negative to positive, i.e., the ratio $|J_1|/2J_2$ decreases sharply. Then the roughness decreases to thicknesses $d_{\mathrm{Cu}}\approx 8.5d_{(111)}$, and a peak appears on the $H^*(d_{\mathrm{Cu}})$ curve at around 17 Å; this can be explained by two competing processes—a decrease of the roughness, leading to a decrease of J_2 and growth of H^*, and an increase of J_1, leading to weakening of the influence of J_2 and a decrease of the field H^*. At the point $d_{\mathrm{Cu}}=18$ Å the $R(H^*)$ curve is qualitatively similar to $R(H^{\parallel})$, and not only is there no sign of the second peak of $R(H^*)$ but the curve is not even convex there. Clearly the second peak of the AF interaction lies in this region. In this same region lie the maximum of $(\Delta R/\Delta R_s)_{\parallel}$ and the minima of $\Delta\rho_{\parallel}^{-}$ and $\rho_s^{\parallel}$. Apparently it is the change of the type of coupling of the layers that has led to the disruption of the synchrony of the behavior of these quantities. Despite the AF type of interaction in this region the quantities $\Delta\rho_{\parallel}^{-}$ and $\rho_s^{\parallel}$ behave in synchrony, and therefore the second mechanism of MR should definitely be operating here.

On further increase of d_{Cu} in the interval from ~ 18 to ~ 19 Å the growth of the roughness and the decrease of J_1 combine to give rise to a second maximum of $R(H)$ and to growth of H^*, which continues till $d_{\mathrm{Cu}}\approx 20$ Å, apparently because of the decrease of J_1 and of the roughness in the interval $\sim 19-20$ Å. For $d_{\mathrm{Cu}}\geqslant 30$ Å the second maximum is not observed; this is due to a decrease of the parameter $|J_1|/2J_2$, since the value of J_1, according to theory,[58] should fall off faster than J_2 with increasing d_{Cu}.

The appearance of the first AF peak of the exchange coupling in the region $d_{\mathrm{Cu}}\approx 5d_{(111)}$ can also explain the disagreement of the curves $\Delta\rho_{\parallel}^{-}$ and $\rho_s^{\parallel}$ in the interval $d_{\mathrm{Cu}}=9-10.5$ Å, where the first MR mechanism is apparently the main one. Data on the magnetic anisotropy of our multilayers, which were presented in a separate paper, completely confirm the conclusions of our analysis of the behavior of the resistivity and MR and the energies J_1 and J_2. They show that an AF exchange interaction is manifested in the regions $d_{\mathrm{Cu}}=8-11$ Å and ~ 18 Å, with maxima at $d_{\mathrm{Cu}}\sim 9-10$ Å and ~ 18 Å, in agreement with the known data.[1–10]

That $\Delta\rho$ and ρ_s are related to the roughness is also supported by data on the differences $\gamma=(\Delta R/R_s)_{\perp}-(\Delta R/R_s)_{\parallel}$ and $\beta=(\Delta R/R_s)_{\perp}-(\Delta R/R_s)_{*}$ (see Fig. 6). It is seen from Fig. 6 that these differences are oscillatory functions of d_{Cu} and that β oscillates around a level of $\sim 0.35\%$. The oscillations of β and $\rho_s^{\parallel}$ (i.e., of the roughness) are in synchrony except in the regions $d_{\mathrm{Cu}}\leqslant 12$ Å and $d_{\mathrm{Cu}}=15-17$ Å. For γ there is not as clear a correlation with $\rho_s^{\parallel}$. One notices that the maxima and minima of γ and β and also the plateau regions on the $\gamma(d_{\mathrm{Cu}})$ curves are found at approximately the same level. These results are clear evidence of anisotropy of the giant MR in respect to the orientation of the magnetic field, which was discussed, for example, in Refs. 29 and 30.

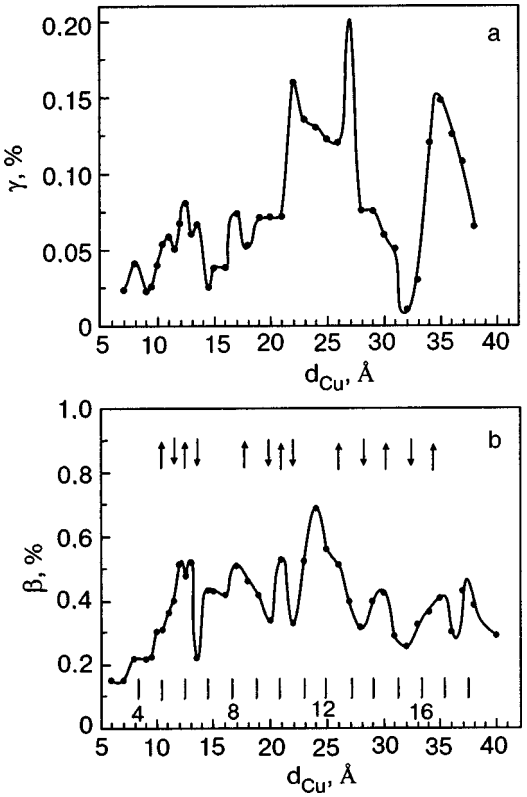

FIG. 6. The quantities $\gamma=(\Delta R/R_s)_{\perp}-(\Delta R/R_s)_{\parallel}$ (a) and $\beta=(\Delta R/R_s)_{\perp}-(\Delta R/R_s)_{*}$ (b) for Co/Cu superlattices as functions of the thickness d_{Cu} of the copper spacers. The arrows and vertical hash marks indicate the position of the extrema and inflection points of $(\Delta R/R_s)_{\perp,\parallel}$.

Remarkably, the oscillations of γ and β are not attenuated with increasing d_{Cu}, i.e., $\Delta\rho$ varies in proportion to ρ_s (Refs. 29 and 30). Completely different behavior of the $\gamma(d_{\mathrm{Cu}})$ curve was observed for Co(70 Å)/Cu(d_{Cu})/NiFe(50 Å)/FeMn(100 Å) spin valves.[29] In this case γ was practically independent of d_{Cu}, in agreement with the predictions of the theory.[30] That theory implies that the sign of γ can change, and for our SLs that occurs in the region $d_{\mathrm{Cu}}\sim 39$ Å.

The difference of β (and γ) can be represented in the form $\beta=\beta^{+}+\beta^{-}$, $\beta^{\pm}=(\Delta R^{\pm}/R_s)_{\perp}-(\Delta R^{\pm}/R_s)_{*}$. If we assume for simplicity that the domain structure of the sample at $H=0$ is the same for the MR measurements in fields $H_{\perp}$ and H_{*}, then $\beta^{-}\approx R_s^{*}/R_s^{\perp}-1$. Since $\beta^{+}\ll\beta^{-}$, the oscillations of β are determined mainly by the ratio $R_s^{*}/R_s^{\perp}$, which oscillates in synchrony with the roughness. If it is assumed that the AMR contribution to the resistance R_s is the same for these magnetic field orientations, it can be concluded from this that the R_s^{*} is more sensitive than $R_s^{\perp}$ to a change of roughness. The relatively large value of β ($\sim 0.2-0.5\%$) may be due to the large difference in the efficiency of processes of magnetic-field suppression of thermal fluctuations of the spins of the Co atoms for the two different field orientations. For γ one cannot neglect the component γ^{+}, which gives an appreciable contribution and apparently causes the asynchrony in the behavior of γ and the roughness.

We note that when the magnetic field deviates from the direction normal to the sample by an angle ϑ the relative MR $(\Delta R/R_s)(\vartheta)$ for samples with $d_{\mathrm{Cu}}=7$ and 12 Å, for angles $\vartheta\geqslant 20°$ is well described by the relation $(\Delta R^{-}/R_s)(\vartheta)$

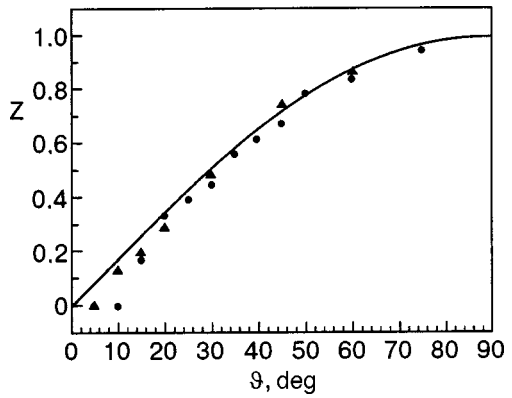

FIG. 7. Plot of the ratio $Z=[(\Delta R^-/R_s)(\vartheta)-(\Delta R^-/R_s)_*]/[(\Delta R^-/R_s)_\perp-(\Delta R^-/R_s)_*]$ for Co/Cu superlattices with copper spacer thicknesses $d_{Cu}=7$ (▲) and 12 Å (●) as a function of the angle ϑ between the magnetic field, perpendicular to the current, and the normal to the plane of the multilayers. The values at $\vartheta=5°$ are $Z=-3.53\times10^{-4}$ and -1.15×10^{-3} for $d_{Cu}=7$ and 12 Å, respectively (the value at $\vartheta=10°$ is $Z=1.77\times10^{-4}$ for the sample with $d_{Cu}=7$ Å). The curve shows the function $\sin\vartheta$.

$-(\Delta R^-/R_s)_*=A\sin\vartheta$, while for smaller angles one observes a minimum of this dependence at angles $\sim5°$ (Fig. 7). We note that for Co/Ag superlattices[23] the largest value of $(\Delta R/R_s)(\vartheta)$ was observed at $\vartheta=45°$. For a Fe/Cr(001) superlattice,[61] in which because of the biquadratic exchange interaction the magnetizations of neighboring Fe layers were noncollinear in zero magnetic field, the resistance of the samples decreases monotonically with increasing field. At angles $\vartheta\leqslant25°$ the form of the $R(H,\vartheta)$ curves changed, the resistance of the samples increased in proportion to H^2, reached a maximum at $H\leqslant8$ kOe, and then fell rapidly, and the maximum of $R(H)$ was reached at the point of a second-order phase transition.[61] Although the authors did not give any data for $(\Delta R/R_s)(\vartheta)$, it is clear that the relative MR reaches the highest values in the region of angles $\vartheta<25°$. We have not yet found an explanation for the behavior of γ, β, and the angular dependences of the MR; all of these questions require further analysis. Apparently one can say that the appearance of features in the form of extrema (in fields $H\gg H_c$) on the $R(H,\vartheta)$ curves for $\vartheta<90°$ is due to the rather high level of biquadratic interaction of the magnetic layers.

5. CONCLUSION

For Co/Cu(111) superlattices with a fixed thickness of the Co layers (8 Å), deposited on mica by magnetron sputtering, it is found that the resistivity at saturation ρ_s (at $H=15$ kOe), the magnetoresistance $\Delta\rho$, and the relative magnetoresistance $\Delta R/R_s$ exhibit unusual oscillations as the thickness d_{Cu} of the copper spacers is increased from 6 to 40 Å. The extrema of ρ_s, $\Delta\rho$, and $\Delta R/R_s$ occur at thicknesses d_{Cu} which are integer or half-integer numbers of copper monolayers (i.e., $d_{(111)}=2.087$ Å is the distance between (111)Cu planes), and the distance between adjacent maxima or minima are equal to 1, 1.5, 2, 2.5, and $3d_{(111)}$. The magnetic anisotropy constant κ_m and the ferromagnetic resonance linewidth undergo analogous oscillations, which will be described in detail in a separate paper, and complete synchrony of the oscillations of ρ_s, $\Delta\rho$, $\Delta R/R_s$, and κ_m is observed. The behavior of the curves of the resistance of the samples as a function of magnetic field, $R(H)$, changes qualitatively when the field deviates from the plane of the samples. Besides the maxima of $R(H)$ at fields $H=\pm H_c$ (H_c is the coercive force of the samples), a second broad maximum or a characteristic ''hump'' appears at fields $H\gg H_c$.

Theoretical calculations of the direction of the magnetic moments of the layers in a field orthogonal to the plane of the sample and an analysis of the experimental data suggest that the cause of the oscillations of ρ_s, $\Delta\rho$, and $\Delta R/R_s$ and the magnetic anisotropy constants is the nonmonotonic variation of the roughness of the interfaces between layers and the resulting oscillations of the bilinear (J_1) and biquadratic (J_2) exchange interactions of neighboring ferromagnetic layers. The change of the shape of the $R(H)$ curves when the field deviates from the plane of the samples is due to the appreciable value of the biquadratic interaction and evidently should be observed for samples with $|J_1|/2J_2<1$, since for samples with thickness values d_{Cu} for which this inequality does not hold, no modification of the $R(H)$ curves is observed. The same conclusion was reached by the authors of Ref. 58, where analogous behavior of $R(H)$ was observed. Therefore the study of the angular and field dependence of ρ_s, $\Delta\rho$, and $\Delta R/R_s$ in conjunction with theoretical calculations allows one in principle to draw contains about the processes of magnetization in superlattices and the variation of the bilinear and biquadratic interactions of the layers as the thickness of the magnetic and nonmagnetic consituents of the superlattices are varied.

The authors thank B. A. Avramenko and Yu. P. Pershin of the staff of the National Technical University ''Kharkov Polytechnical Institute'' for measurement of the magnetic characteristics and x-ray studies of the samples.

This study was supported by the National Academy of Sciences of Ukraine in the framework of the program ''Nanostructure systems, nanomaterials, nanotechnology,'' Grant No. 3-026/2004.

APPENDIX

Field dependence of the orientation of the magnetic moments of layers in structures of the Co/Cu(111) type in a magnetic field perpendicular to the substrate

We consider N magnetic layers coupled by exchange interactions across spacers of a nonmagnetic material. In the case $N\gg1$ or for spin-valve structures with $N=2$ the energy functional has the typical form for a two-sublattice magnet. We write the energy functional in the form used in Ref. 62 (the magnetic field and the z axis are perpendicular to the layers):

$$F=\sum_{i=1}^{2}\left\{k[(n_i^xn_i^y)^2+(n_i^zn_i^y)^2+(n_i^xn_i^z)^2]+\frac{m}{2}(n_i^z)^2-h(n_i^z)\right\}+\frac{1}{2}J_1(\mathbf{n}_1\cdot\mathbf{n}_2)+\frac{1}{2}J_2(n_1\cdot n_2)^2. \tag{A1}$$

Here J_1 is the Heisenberg (bilinear) energy energy, J_2 is the energy of the biquadratic interaction, k is the cubic anisotropy energy, h is the Zeeman energy in an external field, m is

the magnetization energy, and $\mathbf{n}_i$ is a unit vector in the direction of the magnetic moment $\mathbf{M}_i$ of the layer.

In a coordinate system in which the normal to the sample is directed along the [111] axis and the axes x and y are oriented along the $[1\bar{1}0]$ and $[11\bar{2}]$ directions, respectively, we have

$$F=\sum_{i=1}^{2}\left\{k\left(\frac{1}{4}\sin^4\vartheta_i+\frac{1}{3}\cos^4\vartheta_i-\frac{\sqrt{2}}{3}\sin^3\vartheta_i\sin 3\varphi_i\right)+\frac{m}{2}\cos^2\vartheta_i-h\cos\vartheta_i\right\}+\frac{1}{2}J_1[\ldots]+\frac{1}{2}J_2[\ldots]^2,\quad [\ldots]=\cos\vartheta_1\cos\vartheta_2+\sin\vartheta_1\sin\vartheta_2\cos\psi,\quad \psi=\varphi_1-\varphi_2. \tag{A2}$$

Here we have used a spherical coordinate system in which θ_i is the angle between the magnetic moment $\mathbf{M}_i$ of layer i and the z axis, φ_i is the angle between the projection of $\mathbf{M}_i$ on the plane of the layers and the x axis. Because the regions with uniform magnetization (domains) are much larger (by many orders of magnitude) than the grain size in Co/Cu superlattices and there are no preferred orientations of the $[1\bar{1}0]$ and $[11\bar{2}]$ directions relative to the substrate, the functional F must be averaged over all the grains within a domain, and that causes the contribution of the third term in the sum (A2) for F to vanish. Thus the functional F is dependent on three variables: ϑ_1, ϑ_2, and ψ.

Analysis of the minima of the functional (A2) gives the following results. Stable states of the magnetization correspond to equality of the angles ϑ_1 and ϑ_2, i.e., $\vartheta_1=\vartheta_2=\vartheta$. All possible states of the magnetic structure lie in four regions on the phase diagram in the coordinates (J_1,J_2), shown in Fig. 8 (it has been shown experimentally and theoretically that the value of the biquadratic interaction J_2 is non-negative). The boundaries of regions I–IV are determined by the straight line $|\beta|=1$, where the parameter $\beta=J_1/2J_2$ is a measure of the relative strength of the Heisenberg and biquadratic interactions.

In region I ($J_1<0$, $|\beta|>1$), with a ferromagnetic exchange interaction of the layers, at arbitrary magnetic field the angle ψ between the projections $\mathbf{M}_1$ and $\mathbf{M}_2$ on the plane of the layers remains constant and equal to zero ($\cos\psi=1$). The relation between the angle ϑ and the magnetic field h is

$$\cos\vartheta=\frac{h}{m}+\delta,\ \delta\cong\left(\frac{h}{m}\right)\left(\frac{k}{m}\right)\left(1-\frac{7}{3}\frac{h^2}{m^2}\right),\ |\delta|\ll\left|\frac{h}{m}\right|. \tag{A3}$$

With increasing field the magnetic moments $\mathbf{M}_1$ and $\mathbf{M}_2$ deviate from the plane of the layers, and at fields $h\geqslant m+4k/3$ they are aligned perpendicular to the substrate. Analogous processes occur in the case of AF interaction of the layers ($J_1>0$) in region III ($\beta>1$, $\cos\psi=-1$), for which

$$\cos\vartheta=\frac{h}{m}+\delta+\Delta,\quad \Delta=\left(\frac{h}{m}\right)\left(\frac{2J_2}{m}\right)\left[(1-\beta)-2\frac{h^2}{m^2}\right],\quad |\delta+\Delta|\ll\frac{h}{m}. \tag{A4}$$

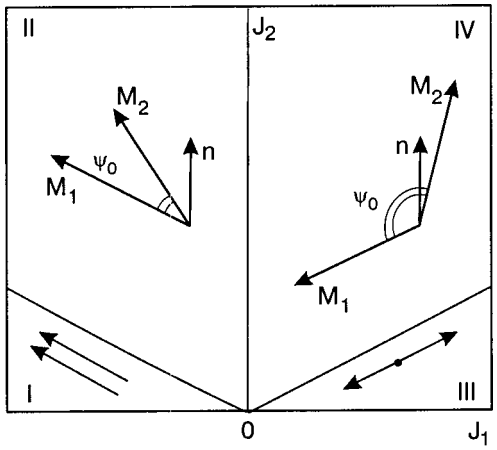

FIG. 8. Diagram of the magnetic states of Co/Cu superlattices for different relationships between the energies of the bilinear (J_1) and biquadratic (J_2) exchange interactions.

However, in regions II, III, and IV the magnetization of the layers will be perpendicular to the plane of the sample at fields $h\geqslant m+4k/3+(J_1+2J_2)$.

In regions II and IV the magnetic moments of the layers are noncollinear, and at zero magnetic field the angle $\psi(H=0)=\psi_0$ is determined by the relation $\cos\psi=-\beta$, i.e., with increasing J_2 this angle changes from zero to 90° (at $J_2\to\infty$) in region II and from 180° to 90° ($J_2\to\infty$) in region IV. The dependence of the angles ψ and ϑ on magnetic field is determined by relation (A3) and the equation

$$\cos\psi=-\frac{\beta+\cos^2\vartheta}{\sin^2\vartheta}, \tag{A5}$$

which correspond to stable states of the magnetic structure for $cos^2\vartheta\leqslant(1-\beta)/2$. Here the equals sign determines that value h_{cr} of the magnetic field at which the angle ψ reaches its largest possible value, equal to 180° (i.e., $\cos\psi=-1$). On the other hand, the stable state with $\cos\psi=-1$ is also reached in the field region in which $\cos^2\vartheta\geqslant(1-\beta)/2$, and the relation between ϑ and h is given by Eq. (4). We note that the stable states corresponding to a minimum of the functional F are possible under the condition $m+7k(h/m)^2>0$ in the region of angles $90°>\vartheta\geqslant 0$. Since expressions (A3) and (A4) differ from each other by the term Δ, at the field $h=h_{cr}$ a transition should occur from the branch of the function $\cos\vartheta(h)$ described by relation (A3) to the "high-field" branch (A4). When the field reaches h_{cr} the angle ϑ will jump to a larger (if $\Delta(h_{cr})<0$) or smaller (if $\Delta(h_{cr})>0$) value. Substituting the value

$$\frac{h_{cr}}{m}\cong\sqrt{\frac{1-\beta}{2}}\left\{1-\left(\frac{k}{m}\right)\left[1-\frac{7}{6}(1-\beta)\right]\right\} \tag{A6}$$

into the function Δ, we obtain

$$\Delta(h_{cr})\cong(1-\beta)\sqrt{\frac{1-\beta}{2}}\left(\frac{2J_2}{m}\right)\left(\frac{2k}{m}\right)\left[1-\frac{7}{6}(1-\beta)\right]. \tag{A7}$$

It follows from (A7) that $\Delta(h_{cr})<0$ if $k[7\beta-1]<0$, i.e., if $\beta<0$, $k>0$; $\beta>1/7$, $k<0$, or $\beta<1/7$, $k>0$. After the jump (for $h>h_{cr}$) the angle ϑ gradually decreases to zero according to the law (A4).

In regions III and IV the jump in ϑ mentioned above should be reflected in the form of the field dependence of the resistance. For the first MR mechanism we can use for estimation the relation

$$R = R_s + \Delta R \sin^2(\varphi/2), \tag{A8}$$

where φ is the angle between $\mathbf{M}_1$ and $\mathbf{M}_2$:

$$\cos\varphi = \sin^2\vartheta \cos\psi + \cos^2\vartheta. \tag{A9}$$

In the field region $h \leqslant h_{cr}$ we obtain, using Eq. (5), $\cos\psi = -\beta = \cos\psi_0$, i.e., the angle φ remains constant and equal to ψ_0. For $h > h_{cr}$ we have $\cos\varphi = 2\cos^2\vartheta - 1$. The jump of $\cos\varphi$ for $\Delta(h_{cr}) < 0$ causes a spike of $\sin^2(\varphi/2)$ and of the resistance, and therefore the first MR mechanism can give rise to a second maximum on $R(H)$ at $k > 0$, while in the AF region $d_{Cu} \sim 10.5$ Å for $J_1 < 2(J_2/7)$. Here from Eq. (6), taking into account that $k/m \ll 1$, we obtain $h_{cr}/m \sim \sqrt{1-\beta}$, i.e., upon an increase of the roughness, leading to an increase of J_2, the values of $|\beta|$ and h_{cr} decrease for $\beta < 0$, i.e., the field H^* in the ferromagnetic region should increase when the interfaces between layers become smoother (see the peak of H^* at $d_{Cu} = 13.5$ Å in Fig. 2). In the AF region (e.g., near $d_{Cu} = 10.5$ Å), on the contrary, growth of the roughness should cause an increase in H^*.

The contribution to the resistance from the AMR effect is proportional to $\sin^2\Omega$, where Ω is the angle between the magnetization and current:

$$R_{AMR} - \Delta R_{AMR} \sin^2\Omega. \tag{A10}$$

For each of the magnetic layers

$$\sin^2\Omega = \cos^2\vartheta + \sin^2\vartheta \sin^2\left(\frac{\psi}{2} + n\frac{\pi}{2}\right), \tag{A11}$$

where $n = 0$ for $\psi \leqslant 90°$ and $n = 1$ for $\psi > 90°$. Here we have taken into account the circumstance that our samples have a highly elongated shape. The energy due to the shape anisotropy will make it so that for $\psi \leqslant 90°$ the projection of the magnetic moments $\mathbf{M}_1$ and $\mathbf{M}_2$ of the layers on the plane of the sample will be directed at equal angles to the axis of the sample in the absence of magnetic field. As the field is increased (in regions II and IV) the angle ψ will increase, and at $\psi = 90°$ an additional, jumplike 90° rotation of the projections of the moments will occur. Analysis of the behavior of the AMR resistance as a function of ψ shows that when ψ increases from ψ_0 to 90° the resistance decreases, and at $\psi = 90°$ a small downward jump of the resistance occurs. Then in the interval $180° \geqslant \psi > 90°$ the AMR resistance will remain constant. At $\psi = 180°$ a jumplike increase in the resistance will occur (for $\Delta(h_{cr}) < 0$), followed by a smooth decrease. Thus the AMR mechanism of MR should also lead to a second maximum of $R(H^*)$. The second MR mechanism, due to scattering on thermal fluctuations of the spins of the Co ions, apparently should also lead to a spike of the MR for $\Delta(h_{cr}) < 0$. Thus all three of the main MR mechanisms can explain the appearance of the second maximum. Since the first mechanism and the AMR mechanism are not dominant in our case, the field dependence of the resistance does not exhibit regions of constant resistance because of the influence of the the second, main mechanism of MR. In addition, because of the finite number of layers there can be noticeable deviations of the behavior of their magnetizations in comparison with the case of an infinite number of layers.

*E-mail: zorch@kpi.kharkov.ua

[1] R. E. Camley and R. L. Stamps, J. Phys.: Condens. Matter **5**, 3727 (1993).
[2] S. S. P. Parkin, R. Bhadra, and K. P. Roche, Phys. Rev. Lett. **66**, 2152 (1991).
[3] S. S. P. Parkin, A. R. Modak, and D. J. Smith, Phys. Rev. B **47**, 9136 (1993).
[4] D. H. Mosca, F. Petroff, A. Fert, P. A. Schroeder, W. P. Pratt, Jr., and R. Laloee, J. Magn. Magn. Mater. **94**, L1 (1991).
[5] S. S. P. Parkin, R. F. Marks, R. F. C. Farrow, G. R. Harp, Q. H. Lam, and R. J. Savoy, Phys. Rev. B **46**, 9262 (1992).
[6] C. Dupas, E. Kolb, K. Le Dang, J. P. Renard, P. Veillet, E. Velu, and D. Renard, J. Magn. Magn. Mater. **128**, 361 (1993).
[7] S. K. J. Lenczowski, M. A. M. Gijs, J. B. Giesbers, R. J. M. van de Veerdonk, and W. J. M. de Jonge, Phys. Rev. B **50**, 9982 (1994).
[8] P. Bruno and C. Chappert, Phys. Rev. Lett. **67**, 1602 (1991); **67**, 2592 (1991); Phys. Rev. B **46**, 261 (1992).
[9] P. Bruno, J. Appl. Phys. **78**, 6972 (1994); Phys. Rev. B **52**, 411 (1995).
[10] N. N. Lathiotakis, B. L. Györffy, J. B. Staunton, and B. Ujfalussy, J. Magn. Magn. Mater. **185**, 293 (1998).
[11] P. M. Levy, Solid State Phys. **47**, 367 (1994).
[12] S. Zhang and P. M. Levy, Phys. Rev. Lett. **77**, 916 (1996).
[13] T. N. Todorov, E. Yu. Tsymbal, and D. G. Pettifor, Phys. Rev. B **54**, R12685 (1996).
[14] E. Yu. Tsymbal and D. G. Pettifor, Phys. Rev. B **54**, 15314 (1996); J. Appl. Phys. **81**, 4579 (1997); J. Magn. Magn. Mater. **202**, 163 (1999).
[15] D. Barlett, F. Tsui, D. Glick, L. Lauhon, T. Mandrekar, C. Uher, and R. Clarke, Phys. Rev. B **49**, 1521 (1994).
[16] A. R. Modak, D. J. Smith, and S. S. P. Parkin, Phys. Rev. B **50**, 4232 (1994).
[17] A. R. Modak, S. S. P. Parkin, and D. J. Smith, J. Magn. Magn. Mater. **129**, 415 (1994).
[18] G. Rupp and K. Schuster, J. Magn. Magn. Mater. **121**, 416 (1993); G. Rupp and H. A. M. van den Berg, IEEE Trans. Magn. **29**, 3102 (1993).
[19] D. B. Fulghum and R. E. Camley, Phys. Rev. B **52**, 13436 (1995); J.-F. Bobo, M. Piecuch, and E. Snoeck, J. Magn. Magn. Mater. **126**, 440 (1993).
[20] K. Kagawa, H. Kano, A. Okabe, A. Suzuki, and K. Hayashi, J. Appl. Phys. **75**, 6540 (1994).
[21] C. H. Marrows, B. J. Hickey, M. Herrmann, S. McVitie, and J. N. Chapman, J. Magn. Magn. Mater. **198–199**, 408 (1999).
[22] A. M. Shukh, D. H. Shin, and H. Hoffmann, J. Appl. Phys. **78**, 6507 (1994); Y. Kobayashi, Y. Aoki, H. Sato, A. Kamijo, and M. Abe, J. Magn. Magn. Mater. **126**, 501 (1993); D. J. Kubinski and H. Holloway, J. Appl. Phys. **79**, 1661 (1996).
[23] D. H. Mosca, A. Barthelemy, F. Petroff, A. Fert, P. A. Schroeder, W. P. Pratt, Jr., R. Laloee, and R. Cabanel, J. Magn. Magn. Mater. **93**, 480 (1991).
[24] R. F. C. Farrow, R. F. Marks, T. A. Rabedeau, M. T. Toney, D. Dobbertin, R. Beyers, and S. S. P. Parkin, J. Appl. Phys. **76**, 3688 (1994).
[25] M. Vaezzadeh, B. George, and G. Marchal, Phys. Rev. B **50**, 6113 (1994).
[26] D. Greig, M. J. Hall, C. Hammond, B. J. Hickey, H. P. Ho, M. A. Howson, M. J. Walker, N. Wiser, and D. G. Wright, J. Magn. Magn. Mater. **110**, L239 (1992); G. R. Harp, S. S. P. Parkin, R. F. C. Farrow, R. F. Marks, M. F. Toney, Q. H. Lam, T. A. Rabedeau, and R. J. Savoy, Phys. Rev. B **47**, 8721 (1993).
[27] I. A. Campbell, A. Fert, and O. Jaoul, J. Phys. C: Metal Phys. **3**, S95 (1970); T. R. McGuire and R. I. Potter, IEEE Trans. Magn. **11**, 1018 (1975).
[28] B. Dieny, V. S. Speriosu, S. S. P. Parkin, B. A. Gurney, D. R. Wilhoit, and D. Mauri, Phys. Rev. B **43**, 1297 (1991); A. Chaiken, P. Lubitz, J. J. Krebs, G. A. Prinz, and M. Z. Harford, Appl. Phys. Lett. **59**, 240 (1991).
[29] B. Dieny, C. Cowache, A. Nossov, P. Dauguet, J. Chaussy, and P. Gandit, J. Appl. Phys. **79**, 6370 (1996).
[30] Th. G. S. M. Rijks, R. Coehoorn, M. J. M. de Jong, and W. J. M. de Jonge, Phys. Rev. B **51**, 283 (1995).
[31] R. Kläsges, D. Schmitz, C. Carbone, W. Eberhardt, P. Lang, R. Zeller, and P. H. Dederichs, Phys. Rev. B **57**, R696 (1998).
[32] J. Unguris, R. J. Celotta, and D. T. Pierce, Phys. Rev. Lett. **67**, 140 (1991); S. T. Purcell, W. Folkerts, M. T. Johnson, N. W. E. McGee, K. Jager, J. aan de Stegge, W. B. Zeper, W. Hoving, and P. Grünberg, Phys. Rev. Lett. **67**,

903 (1991); D. T. Pierce, J. A. Stroscio, J. Unguris, and R. J. Celotta, Phys. Rev. B **49**, 14564 (1994).
[33] C. D. Potter, R. Schad, P. Beliën, G. Verbanck, V. V. Moshchalkov, Y. Bruynseraede, M. Schäfer, R. Schäfer, and P. Grünberg, Phys. Rev. B **49**, 16055 (1994).
[34] M. D. Stiles, Phys. Rev. B **54**, 14679 (1996).
[35] J. E. Ortega, F. J. Himpsel, G. J. Mankey, and R. F. Willis, Phys. Rev. B **47**, 1540 (1993).
[36] C. Kittel, *Introduction to Solid State Physics*, Wiley, New York (1996), p. 217.
[37] R. J. Highmore, W. C. Shih, R. E. Somekh, and J. E. Evetts, J. Magn. Magn. Mater. **116**, 249 (1992).
[38] S. Honda, S. Ohmoto, R. Imada, and M. Nawate, J. Magn. Magn. Mater. **126**, 419 (1993).
[39] S. S. P. Parkin, Z. G. Li, and D. J. Smith, Appl. Phys. Lett. **58**, 2710 (1991).
[40] H. Kano, K. Kagawa, A. Suzuki, A. Okabe, K. Hayashi, and K. Aso, Appl. Phys. Lett. **63**, 2839 (1993).
[41] H. Sato, I. Sakamoto, and C. Fierz, J. Phys.: Condens. Matter **3**, 9067 (1991).
[42] H. Sato, T. Matsudai, W. Abdul-Razzaq, C. Fierz, and P. A. Schroeder, J. Phys.: Condens. Matter **6**, 6151 (1994).
[43] P. F. Carcia and A. Suna, J. Appl. Phys. **54**, 2000 (1983).
[44] S. Kim and I. K. Schuller, Phys. Rev. B **58**, 2240 (1998).
[45] D. Lederman, J. M. Gallego, S. Kim, and I. K. Schuller, J. Magn. Magn. Mater. **183**, 261 (1998).
[46] A. Vedyayev, C. Cowache, N. Ryzhanova, and B. Dieny, J. Phys.: Condens. Matter **5**, 8289 (1993); A. Vedyayev, M. Chshiev, and B. Dieny, J. Magn. Magn. Mater. **184**, 145 (1998); B. R. Bulka and J. Barnas, Phys. Rev. B **51**, 6348 (1995); J. Barnas and Y. Bruynseraede, Phys. Rev. B **53**, 5449 (1996).
[47] R. H. Brown, D. M. C. Nicholson, W. H. Butler, X.-G. Zhang, W. A. Shelton, T. C. Schulthess, and J. M. McLaren, Phys. Rev. B **58**, 11146 (1998).
[48] K. M. Schep, P. J. Kelly, and G. E. W. Bauer, Phys. Rev. Lett. **74**, 586 (1995); T. Kai, Y. Ohashi, and K. Shiki, J. Magn. Magn. Mater. **183**, 292 (1998).
[49] W. H. Batler, X.-G. Zhang, D. M. C. Nicholson, T. C. Schulthess, and J. M. MacLaren, Phys. Rev. Lett. **76**, 3216 (1996); J. Appl. Phys. **79**, 5282 (1996).
[50] P. Dauguet, P. Gandit, J. Chaussy, S. F. Lee, A. Fert, and P. Holody, Phys. Rev. B **54**, 1083 (1996); L. B. Steren, A. Barthélémy, J. L. Duvail, A. Fert, R. Morel, F. Petroff, P. Holody, R. Loloee, and P. A. Schroeder, Phys. Rev. B **51**, 292 (1995); S. Mao, M. Plumer, A. Mack, Z. Yang, and E. Murdock, J. Appl. Phys. **85**, 5033 (1999).
[51] S. Zhang, P. M. Levy, and A. Fert, Phys. Rev. B **45**, 8689 (1992); L. Sheng, D. Y. Xing, Z. D. Wang, and J. Dong, Phys. Rev. B **55**, 5908 (1997); R. Y. Gu, D. Y. Xing, and Z. D. Wang, Phys. Rev. B **58**, 11142 (1998).
[52] J. Barnas, O. Baksalary, and A. Fert, Phys. Rev. B **56**, 6079 (1997).
[53] A. Vedyayev, B. Dieny, N. Ryzhanova, J. B. Genin, and C. Cowache, Europhys. Lett. **25**, 465 (1994); A. Vedyayev, B. Dieny, N. Ryzhanova, and J. B. Genin, Phys. Lett. A **185**, 117 (2004); A. Vedyayev, N. Ryzhanova, B. Dieny, P. Dauguet, P. Gandit, and J. Chaussy, Phys. Rev. B **55**, 3728 (1997); K. Wang, S. Zhang, and P. M. Levy, Phys. Rev. B **54**, 11965 (1996).
[54] E. Tsymbal, J. Magn. Magn. Mater. **130**, L6 (1994).
[55] U. Jacob, J. Vancea, and H. Hoffmann, Phys. Rev. B **41**, 11852 (1990).
[56] Z. Tešanović, M. V. Jarić, and S. Maekawa, Phys. Rev. Lett. **57**, 2760 (1986); N. Trivedi and N. W. Ashcroft, Phys. Rev. B **38**, 12298 (1988); G. Fishman and D. Calecki, Phys. Rev. B **43**, 11581 (1991); A. E. Meyerovich and I. V. Ponomarev, Phys. Rev. B **65**, 155413 (2002).
[57] A. E. Meyerovich and I. V. Ponomarev, Phys. Rev. B **67**, 165411 (2003).
[58] J. C. Slonczewski, Phys. Rev. Lett. **67**, 3172 (1991); J. Appl. Phys. **73**, 5957 (1993); S. Demokritov, E. Tsymbal, P. Grünberg, W. Zinn, and I. K. Schuller, Phys. Rev. B **49**, 720 (1994).
[59] C. H. Marrows, R. Loloee, and B. J. Hickey, J. Magn. Magn. Mater. **184**, 137 (1998).
[60] Y. Saito, K. Inomata, A. Goto, and H. Yasuoka, J. Magn. Magn. Mater. **126**, 466 (1993); J. Phys. Soc. Jpn. **62**, 1450 (1993); C. Blaas, L. Szunyogh, C. Weinberger, C. Sommers, P. M. Levy, and J. Shi, Phys. Rev. B **65**, 134427 (2003).
[61] V. V. Ustinov, N. G. Bebenin, L. N. Romashev, V. I. Minin, M. A. Milyaev, A. R. Del, and A. V. Semerikov, Phys. Rev. B **54**, 15958 (1996).
[62] V. V. Kostyuchenko and A. K. Zvezdin, J. Magn. Magn. Mater. **176**, 155 (1997); Phys. Rev. B **57**, 5951 (1998).

Translated by Steve Torstveit

Description of a Heisenberg ferromagnet above the Curie point as a spin liquid

E. V. Kuz'min*

Tavricheskii National University, pr. Vernadskogo 4, Simferopol 95007, Ukraine
(Submitted October 11, 2004; revised November 5, 2004)
Fiz. Nizk. Temp. **31**, 679–686 (June 2005)

A Heisenberg ferromagnet (F) with spin $S=1/2$, found in a spin-liquid (SL) state at temperatures above the Curie point τ_C, is considered. In this spin-liquid state there is no long-range magnetic order but the short-range order is preserved, and the spin correlation functions are isotropic. The spin liquid is described in the framework of a second-order theory by the method of temperature Green functions. The main thermodynamic characteristics of the spin liquid are found as the result of a self-consistent numerical solution of a system of three integral equations. The Curie point τ_C^+, at which the dc magnetic susceptibility at wave vector $\mathbf{q}=0$ diverges, is determined. A comparison of the thermodynamic characteristics of the system in the F state ($\tau \leqslant \tau_C$, spin-wave theory) and in the SL state ($\tau \geqslant \tau_C^+$) is made. It is shown that $\tau_C^+ > \tau_C$, and a modification of spin-wave theory in which τ_C reaches the value τ_C^+ is indicated. At the point of the F-SL phase transition the spin correlation functions suffer a finite discontinuity, and with increasing temperature they fall off $\propto 1/\tau$. The heat capacity of the ferromagnet at $\tau \to \tau_C$ goes to infinity, while in the SL state the heat capacity remains finite at the point τ_C^+ and falls off for $\tau \gg \tau_C^+$ in proportion to $1/\tau^2$. The susceptibility obeys the Curie-Weiss law. © *2005 American Institute of Physics.* [DOI: 10.1063/1.1943536]

1. INTRODUCTION

The Heisenberg model with the Hamiltonian

$$\mathcal{H}=-\frac{1}{2}I\sum_{\mathbf{f},\boldsymbol{\Delta}} S_{\mathbf{f}}S_{\mathbf{f}+\boldsymbol{\Delta}}, \quad S=1/2, \tag{1}$$

where $I>0$, $\mathbf{f}$ are sites of the three-dimensional crystal lattice, and $\boldsymbol{\Delta}$ are vectors joining the z nearest neighbors, has been intensively studied for many decades. Although an exact ferromagnetic ground state is known, there is still no exact solution of the model at arbitrary temperature. Below the Curie temperature T_C, in the ferromagnetic state, a spin-wave description is used, while above T_C, in the nonmagnetic state, the characteristics of the system are calculated with the aid of high-temperature expansions (thermodynamic perturbation theory). Both theoretical approaches are presented in Tyablikov's book,[1] where the efficiency of the two-time temperature Green function method for describing the properties of a ferromagnet at $T \leqslant T_C$ is demonstrated.

In this paper we make the assumption that above the Curie point the system goes to a spin-liquid (SL) state, i.e., an F-SL phase transition occurs. The SL state is characterized by isotropicity of the spin correlators, so that in this phase the symmetry of the Hamiltonian is recovered. The spin liquid is described by the Green function method in the framework of a second-order theory.[2–4] From the system of self-consistent equations we calculate the thermodynamic properties of the SL. A comparison of the characteristics of the system in the F state at $T \to T_C$ (from below) and in the SL state at $T \to T_C$ (from above) shows that a jump (discontinuity) of the correlation functions and heat capacity occurs at the Curie point.

From here on we shall use the dimensionless Hamiltonian $h=\mathcal{H}/zI$; all the energy parameters are rendered dimensionless by dividing by zI, including the temperature: $\tau=k_BT/zI$, $\tau_C=k_BT_C/zI$. The energy of the system per bond in units of I is written in the form

$$\epsilon(\tau)=\frac{\langle H\rangle}{\frac{1}{2}zNI}=-[K_1(\tau)+L_1(\tau)], \tag{2}$$

where

$$K_1=\frac{1}{N}\sum_{\mathbf{f}}\frac{1}{z}\sum_{\boldsymbol{\Delta}}\langle S_{\mathbf{f}}^+S_{\mathbf{f}+\boldsymbol{\Delta}}^-\rangle,$$

$$L_1=\frac{1}{N}\sum_{\mathbf{f}}\frac{1}{z}\sum_{\boldsymbol{\Delta}}\langle S_{\mathbf{f}}^zS_{\mathbf{f}+\boldsymbol{\Delta}}^z\rangle \tag{3}$$

are the transverse and longitudinal correlators in the first coordination zone (for nearest neighbors), N is the number of sites in the lattice, and the thermodynamic limit $N\to\infty$ is understood. Representation (2) is formally exact. The behavior of the correlators is substantial different in the F ($\tau \leqslant \tau_C$) and SL ($\tau \geqslant \tau_C$) states.

It should be stressed that we use a dimensionless temperature τ and dimensionless Curie temperature τ_C, so that it is possible to apply the theory to a wide class of substances. In magnetic insulators the value of the Curie temperature T_C can vary widely, from tens to hundred of kelvin. One can point to ferromagnets with rather low values of T_C: for example, in $CuV_xCr_{2-x}S_4$ compounds $T_C=8-75$ K, depending on the doping, and the compounds of divalent europium EuF_2, EuI_2, and EuSe have Curie temperatures $T_C=2$, 5, and 7 K, respectively,[6] etc.

 © 2005 American Institute of Physics

2. FERROMAGNETIC STATE AND SPIN-WAVE THEORY

To avoid having to cite the far-flung standard references for the spin-wave theory of ferromagnetism, let us give an account of its main consequences. It is well known that it is a second-order theory (linear theory of spin waves), as the equation of motion for the spin operator $S_{\mathbf{f}}^{+}$ is linearized with the use of the Tyablikov decoupling. The commutator Green function has the form

$$\langle\langle S_{\mathbf{q}}^{+}|S_{-\mathbf{q}}^{-}\rangle\rangle_{\omega}^{F}=\frac{2\overline{s}}{\omega-\varepsilon_{\mathbf{q}}},\quad \varepsilon_{\mathbf{q}}=\overline{s}(1-\gamma_{\mathbf{q}}), \tag{4}$$

where $\overline{s}=\overline{s}(\tau)=\langle S_{\mathbf{f}}^{z}\rangle$, $\overline{s}(0)=1/2$ (the averages are understood in the sense of Bogolyubov quasi-averages), $S_{\mathbf{q}}^{+}$ is the Fourier transform of the spin operator, and

$$\gamma_{\mathbf{q}}=\frac{1}{z}\sum_{\boldsymbol{\Delta}}\exp(i\mathbf{q}\cdot\boldsymbol{\Delta}).$$

Using the spectral theorem, we obtain an equation for the order parameter $\overline{s}$:

$$\overline{s}=\frac{1/2}{\frac{1}{N}\Sigma_{\mathbf{q}}\coth\left(\frac{\overline{s}(1-\gamma_{\mathbf{q}})}{2\tau}\right)} \tag{5}$$

and an expression for the transverse correlator:

$$K_1(\tau)=2\overline{s}\frac{1}{N}\sum_{\mathbf{q}}\frac{\gamma_{\mathbf{q}}}{e^{\varepsilon_{\mathbf{q}}/\tau}-1},\quad K_1(0)=0. \tag{6}$$

At low temperatures Eq. (5) implies the Bloch 3/2 law. The Curie temperature τ_C is defined as the critical temperature at which the magnetization of the ferromagnet vanishes, i.e., $\overline{s}\to 0$ at $\tau\to\tau_C$. In this limit, expanding the hyperbolic cotangent in a series, we obtain from (5) and (6)

$$\tau_C=\frac{1}{4W},\quad K_1(\tau_C)=\frac{W-1}{2W}, \tag{7}$$

where

$$W=\frac{1}{N}\sum_{\mathbf{q}}\frac{1}{1-\gamma_{\mathbf{q}}} \tag{8}$$

is the Watson integral ($W=1.516$ for a simple cubic lattice). In the neighborhood of τ_C the order parameter goes to zero in a square-root manner:

$$\overline{s}(\tau)=A\sqrt{\tau_C-\tau},\quad A=\sqrt{3},\quad \tau\to\tau_C. \tag{9}$$

Unfortunately, a correct definition of the correlator L_1 in the framework of spin-wave theory does not exist (its behavior will be discussed below). Therefore, the energy of the ferromagnet is treated as that of an ideal Bose gas of magnons with a dispersion law $\varepsilon_{\mathbf{q}}$:

$$\epsilon_F(\tau)=\epsilon_F(0)+\frac{1}{N}\sum_{\mathbf{q}}\varepsilon_{\mathbf{q}}n(\varepsilon_{\mathbf{q}}),$$

$$n(\varepsilon_q)=\left[\exp\left(\frac{\varepsilon_{\mathbf{q}}}{\tau}\right)-1\right]^{-1}, \tag{10}$$

where $\epsilon_F(0)=-1/4$ is the ground-state energy. Expanding the solution $\overline{s}(\tau)$ of Eq. (5), one can calculate the specific heat

$$c_F(\tau)=k_B\frac{\partial\epsilon_F}{\partial\tau}=\begin{cases}a\left(\dfrac{\tau}{\tau_C}\right)^{3/2}+b\left(\dfrac{\tau}{\tau_C}\right)^{5/2}+\ldots, & \tau\ll\tau_C,\\ \dfrac{\sqrt{3}}{4}\dfrac{\tau_C}{\sqrt{\tau_C-\tau}}, & \tau\to\tau_C,\end{cases} \tag{11}$$

which diverges at the Curie point τ_C.

In the ferromagnetic state the transverse correlator $K_1(0)=0$ is an increasing function of temperature ($K_1\propto\tau^{3/2}$ for $\tau\to 0$) and reaches a maximum at the phase transition point τ_C. The longitudinal correlator has the opposite behavior: it is maximum in the ground state $L_1(0)=1/4$ and decreases with increasing temperature, although the temperature dependence $L_1(\tau)$ in general is unknown. If we use the exact expression for the first moment

$$M_1=\frac{1}{N}\sum_{\mathbf{f}}\left\langle\left(\frac{\partial S_{\mathbf{f}}^{+}}{\partial t}\right)S_{\mathbf{f}}^{-}\right\rangle=\frac{\overline{s}}{2}+\frac{K_1}{2}+L_1$$

and its spectral representation in terms of Green function (4)

$$M_1^{\mathrm{Sp}}=\int_{-\infty}^{\infty}\omega J(\omega)d\omega,$$

$$J(\omega)=\frac{1}{N}\sum_{q}\frac{\exp(\omega/\tau)}{\exp(\omega/\tau)-1}\times\left(-\frac{1}{\pi}\right)\mathrm{Im}\langle\langle S_{\mathbf{q}}^{+}|S_{-\mathbf{q}}^{+}|S_{-\mathbf{q}}^{-}\rangle\rangle_{\omega+i0}^{F},$$

then from the equality $M_1=M_1^{\mathrm{Sp}}$ we obtain

$$\frac{\overline{s}}{2}+\frac{K_1}{2}+L_1=2\overline{s}^{2}\left[1+\frac{1}{N}\sum_{\mathbf{q}}(1-\gamma_{\mathbf{q}})n(\varepsilon_{\mathbf{q}})\right]. \tag{12}$$

Relation (12) allows us to establish the temperature behavior of the longitudinal correlator L_1 in the framework of spin-wave theory. For $\tau\to\tau_C$, $\overline{s}\to 0$ the right-hand side of (12) goes to zero and, consequently, $L_1(\tau_C)=-K_1(\tau_C)$, i.e., the longitudinal correlator becomes negative. This effect (the appearance of short-range "antiferromagnetic" order) has been criticized repeatedly (see Ref. 1) and attests to the approximate character of the linear theory of spin waves. More serious grievances against this theory are the fact that as the Curie point τ_C is approached, the interaction of spin waves and their damping are manifested in an essential way. It is customarily assumed[5,6] that the spin-wave theory is valid for $\tau\leqslant(2/3)\tau_C$. Nevertheless, its results will serve as a guide for comparison with the spin-liquid theory.

3. SPIN LIQUID. GREEN FUNCTION AND CORRELATION FUNCTIONS

At temperatures above the Curie point a ferromagnet goes into a nonmagnetic state with short-range order. It is assumed that a spin liquid state arises. A spin liquid is defined as a spatially homogeneous (on average) spin system in which the correlation functions are isotropic,

$$K_R=\langle S_{\mathbf{f}}^{+}S_{\mathbf{f}+\mathbf{R}}^{-}\rangle=2\langle S_{\mathbf{f}}^{z}S_{\mathbf{f}+\mathbf{R}}^{z}\rangle,\quad \langle S_{\mathbf{f}}^{z}\rangle=\overline{s}\equiv 0, \tag{13}$$

depend only on the modulus of the distance between sites, $R=|\mathbf{R}|$ ($K_0=1/2$ for spin $S=1/2$), and the average for any

component of the spin operator at a lattice site is equal to zero, $\langle S_{\mathbf{f}}^{\alpha}\rangle = 0$, $\alpha = +, -, z$. The expression for the energy (2) in the SL state takes the form

$$\epsilon_{SL}(\tau) = -\frac{3}{2}K_1(\tau), \quad \tau > \tau_C. \tag{14}$$

The SL then is based on the second-order equations of motion for the spin operators and their linearization with correction factors. The Green function has the form

$$\langle\langle S_{\mathbf{q}}^{+} | S_{-\mathbf{q}}^{-}\rangle\rangle_{\omega}^{SL} = \frac{2K_1(1-\gamma_{\mathbf{q}})}{\omega^2 - \Omega_{\mathbf{q}}^2},$$

$$\Omega_{\mathbf{q}}^2 = \lambda^2 E_{\mathbf{q}}^2, \quad E_{\mathbf{q}}^2 = (1-\gamma_{\mathbf{q}})(1+\delta-\gamma_{\mathbf{q}}). \tag{15}$$

Here K_1 is the transverse correlator for nearest neighbors ($K_1 \geqslant 0$), $\lambda^2 = \alpha_1 K_1$, where α_1 is the correction factor arising in the decoupling of the three-center averages, and $(1+\delta)$ is a rather involved combination of correction functions in an "expanded" cluster (in the second and third coordination zones). The Green function (15) depends on three temperature-dependent parameters, $K_1(\tau)$, $\lambda(\tau)$, and $\delta(\tau)$ (or α_1, λ, and δ), which are to be calculated self-consistently.

The Green function (15) corresponds to the spectral intensity

$$J_{SL}(\mathbf{q},\omega;\tau) = \frac{\exp(\omega/\tau)}{\exp(\omega/\tau)-1}\frac{K_1(1-\gamma_{\mathbf{q}})}{\Omega_{\mathbf{q}}}[\delta(\omega-\Omega_{\mathbf{q}}) - \delta(\omega+\Omega_{\mathbf{q}})], \tag{16}$$

according to which we find the Fourier transform of the correlation function

$$\langle S_{\mathbf{q}}^{+} S_{-\mathbf{q}}^{-}\rangle \equiv K(\mathbf{q}) = \int_{-\infty}^{\infty} J_{SL}(\mathbf{q},\omega;\tau)\,d\omega = \frac{K_1(1-\gamma_{\mathbf{q}})}{\Omega_q}\coth\left(\frac{\Omega_{\mathbf{q}}}{2\tau}\right), \quad \tau > \tau_C. \tag{17}$$

Expanding expression (17), we can calculate any spatial correlation functions

$$K_{\mathbf{R}} = \frac{1}{N}\sum_{\mathbf{q}} e^{i\mathbf{q}\cdot\mathbf{R}}K(\mathbf{q}), \quad K(\mathbf{q}) = \sum_{\mathbf{R}} e^{-i\mathbf{q}\cdot\mathbf{R}}K_{\mathbf{R}}, \tag{18}$$

including

$$K_0 = \frac{1}{2} = \frac{1}{N}\sum_{\mathbf{q}} K(\mathbf{q}) = \frac{K_1}{\lambda}I_0(\lambda,\delta;\tau), \tag{19}$$

$$K_1 = \frac{1}{N}\sum_{\mathbf{q}} \gamma_{\mathbf{q}}K(\mathbf{q}) = \frac{K_1}{\lambda}I_1(\lambda,\delta;\tau), \tag{20}$$

$$K_t = \frac{1}{z^2}\sum_{\boldsymbol{\Delta},\boldsymbol{\Delta}'} K^{\boldsymbol{\Delta}-\boldsymbol{\Delta}'} = \frac{1}{N}\sum_{\mathbf{q}} \gamma_{\mathbf{q}}^2 K(\mathbf{q}) = \frac{K_1}{\lambda}I_2(\lambda,\delta;\tau), \tag{21}$$

where

$$I_n(\lambda,\delta;\tau) = \frac{1}{N}\sum_{\mathbf{q}} \frac{1-\gamma_{\mathbf{q}}}{E_{\mathbf{q}}(\delta)}\gamma_{\mathbf{q}}^n \coth\left(\frac{\lambda E_{\mathbf{q}}(\delta)}{2\tau}\right), \tag{22}$$

$$E_{\mathbf{q}}(\delta) = \sqrt{(1-\gamma_{\mathbf{q}})(1+\delta-\gamma_{\mathbf{q}})}, \quad n = 0,1,2.$$

Analysis shows[2–4] that Eqs. (19)–(21) are insufficient for self-consistent calculation of the parameters K_1, λ, and δ, and one more equation is needed. This is the equation for the second moment, the exact expression for which (i.e., the result of an exact calculation) in the SL state has the form

$$M_2 = \frac{1}{N}\sum_{\mathbf{f}} \left\langle \left(-\frac{\partial^2 S_{\mathbf{f}}^{+}}{\partial t^2}\right) S_{\mathbf{f}}^{-} \right\rangle = \frac{1}{2}\left(K_t - \frac{K_1}{z}\right), \quad \tau > \tau_C. \tag{23}$$

On the other hand, M_2 can be calculated from the spectral representation

$$M_2^{\mathrm{Sp}} = \frac{1}{N}\sum_{\mathbf{q}} \int_{-\infty}^{\infty} \omega^2 J(\mathbf{q},\omega;\tau)\,d\omega,$$

$$J(\mathbf{q},\omega;\tau) = \frac{\exp(\omega/\tau)}{\exp(\omega/\tau)-1}\left(-\frac{1}{\pi}\right)\mathrm{Im}\langle\langle S_{\mathbf{q}}^{+} | S_{-\mathbf{q}}^{-}\rangle\rangle_{\omega+i0}.$$

Using formula (16) for $J_{SL}(\mathbf{q},\omega;\tau)$, we find

$$M_2^{\mathrm{Sp}} = \lambda K_1 P(\lambda,\delta;\tau),$$

$$P(\lambda,\delta;\tau) = \frac{1}{N}\sum_{\mathbf{q}} (1-\gamma_{\mathbf{q}})E_{\mathbf{q}}(\delta)\coth\left(\frac{\lambda E_{\mathbf{q}}(\delta)}{2\tau}\right). \tag{24}$$

Equating $M_2 = M_2^{\mathrm{Sp}}$, we obtain the equation

$$I_2 - \frac{I_1}{z} = 2\lambda^2 P \tag{25}$$

(the arguments of the functions have been dropped).

Thus a closed description of the properties of the spin liquid is obtained by a self-consistent solution of the system of three integral equations (19), (20), and (25). We write this system of equations in terms of λ, δ, and α_1 in the form ($K_1 = \lambda^2/\alpha_1$)

$$\left.\begin{aligned} \frac{1}{2} &= \frac{\lambda}{\alpha_1}I_0(\lambda,\delta;\tau), && A \\ \lambda &= I_1(\lambda,\delta;\tau), && B \\ 2\lambda^2 P(\lambda,\delta;\tau) &= I_2(\lambda,\delta;\tau) - \frac{I_1(\lambda,\delta;\tau)}{z}, && C \end{aligned}\right\}. \tag{26}$$

In the calculations the summation over the Brillouin zone is replaced by integral with a density of states $D(\gamma)$ corresponding to the dispersion law γ_q in the three-dimensional lattice. The expressions that figure into (26) take the form

$$I_n(\lambda,\delta;\tau) = \int_{-1}^{1} D(\gamma)\frac{1-\gamma}{E(\gamma,\delta)}\gamma^n \coth\left(\frac{\lambda E(\gamma,\delta)}{2\tau}\right)d\gamma, \quad n = 0,1,2;$$

$$P(\lambda,\delta;\tau) = \int_{-1}^{1} D(\gamma)(1-\gamma)E(\gamma,\delta) \times \coth\left(\frac{\lambda E(\gamma,\delta)}{2\tau}\right)d\gamma, \tag{27}$$

$$E(\gamma,\delta) = \sqrt{(1-\gamma)(1+\delta-\gamma)}.$$

Thus instead of high-temperature expansions for $\tau > \tau_C$ we have a temperature description of the system based on the concept of the spin liquid and its consequences, in the form the system of equations (26).

4. MAGNETIC SUSCEPTIBILITY AND CURIE TEMPERATURE OF A SPIN LIQUID

The dimensionless dynamic magnetic susceptibility, by definition,[1] is equal to

$$\chi^{+-}(\mathbf{q},\omega) = -\langle\langle S^{+}_{\mathbf{q}} | S^{-}_{-\mathbf{q}} \rangle\rangle_{\omega+i0}. \tag{28}$$

In the SL state, because of the isotropy of the spin correlators $\chi^{zz}(\mathbf{q},\omega) = \chi^{+-}(\mathbf{q},\omega)/2$.

The static susceptibility ($\omega = 0$) of a spin liquid is found from the Green function (15):

$$\chi^{+-}(\mathbf{q};0) \equiv \chi(\mathbf{q};\tau) = \frac{2}{\alpha_1}\frac{1}{1-\gamma_{\mathbf{q}}+\delta}, \quad \tau > \tau_C, \tag{29}$$

where $\alpha_1 = \alpha_1(\tau)$, $\delta = \delta(\tau)$. We define the Curie temperature τ_C^+ of the spin liquid by the relation

$$\chi^{-1}(0;\tau_C^+) = 0, \tag{30}$$

which means that the static susceptibility at $\mathbf{q=0}$ diverges at $\tau \to \tau_C^+$ (from above, i.e., with decreasing temperature). Since $\gamma_0 = 1$, it follows from (29) and (30) that $\delta(\tau_C^+) = 0$. In the vicinity of the τ_C^+ we have the following behavior of the susceptibility:

$$\chi(0;\tau) = \frac{2}{\alpha_1(\tau_C^+)\delta'(\tau_C^+)}\frac{1}{\tau-\tau_C^+}, \tag{31}$$

where $\delta'(\tau)$ is the derivative of the function at the point τ_C^+.

To calculate τ_C^+ it is necessary to solve the system of equations (26) at $\delta = 0$. The quantities $\lambda(\tau_C^+)$, $\alpha_1(\tau_C^+)$, and τ_C^+ are subject to calculation. A numerical solution of the system for a simple cubic (sc) lattice with $z = 6$ leads to the result

$$\tau_C^+ = 0.171, \quad \lambda(\tau_C^+) = 0.403,$$
$$\alpha_1(\tau_C^+) = 1.332, \quad K_1(\tau_C^+) = 0.422. \tag{32}$$

The ferromagnetic Curie point calculated according to spin-wave theory for an sc lattice has the value $\tau_C = 0.165$, and $K_1(\tau_C) = 0.174$. A comparison of the results of spin-wave theory and spin-liquid theory (32) shows that $\tau_C^+ > \tau_C$; this inequality is typical for high-temperature expansions.[1,5,6]

Although the value obtained for the difference $\Delta\tau = \tau_C^+ - \tau_C = 0.006$ is small, it can be assumed that the true Curie point is τ_C^+. One can propose a variant of the theory in which τ_C reaches the value τ_C^+. If the spin-wave theory is constructed using Callen decoupling,[1] then the following modification of the spectrum is obtained:

$$\varepsilon_{\mathbf{q}} \to \varepsilon_{\mathbf{q}} = \overline{s}(1+aK_1)(1-\gamma_{\mathbf{q}}), \tag{33}$$

where a is the *a priori* unknown Callen decoupling parameter, the choice of which is nonunique. Equation (5) with spectrum (33) leads to the following expression for the Curie temperature:

$$\tau_C = \frac{1+aK_1(\tau_C)}{4W}, \tag{34}$$

where the value of $K_1(\tau_C)$ remains as before [see Eq. (7)]. From the condition $\tau_C = \tau_C^+ = 0.171$ (for an sc lattice) one can find the Callen decoupling parameter a; it is equal to 0.213. In this manner we match the values of the Curie points, eliminating the "no-man's land" Δt. Then in relation (9) the coefficient $a^2 = 3/1.037 = 2.89$. The jump $\Delta K_1 = 0.052$ at the Curie point has fundamental significance.

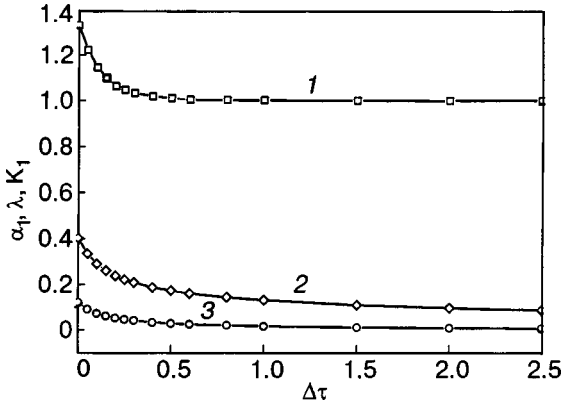

FIG. 1. Dependence of the decoupling parameter α_1 (*1*), the "stiffness" parameter of the spectrum, λ (*2*), and the transverse correlator between nearest neighbors, K_1 (*3*), on the temperature difference $\Delta\tau = \tau - \tau_C^+$ in the spin-liquid state.

The expression for the susceptibility (31) in a small neighborhood of the point τ_C^+ has the form of a Curie–Weiss law. The high-temperature asymptotics for $\chi(\tau) = 2/\alpha_1(\tau)\delta(\tau)$ for $\tau \gg \tau_C$ can be found analytically. In this limit $\alpha_1(\tau) \to 1$ (the spins become practically uncorrelated), $\delta(\tau) \gg (1-\gamma_q)$, and the argument of the hyperbolic cotangent $\lambda E_q(\varepsilon)/2\tau \ll 1$. Expanding the hyperbolic cotangent in a series, we obtain from Eqs. (19) and (20) or, equivalently, from (A) and (B) of system (26),

$$\delta(\tau) \to 4\tau, \quad \lambda(\tau) \to \frac{1}{\sqrt{8z\tau}}, \quad K_1(\tau) \to \frac{1}{8z\tau}, \quad \tau \gg \tau_C. \tag{35}$$

These asymptotic expressions imply the Curie law $\chi(\tau) \to 1/2\tau$, and also the boundedness of the spectrum of excitations $\Omega_q = \lambda E_q(\delta) \to \sqrt{(1-\gamma_q)/2z}$.

5. RESULTS OF A NUMERICAL CALCULATION OF THE THERMODYNAMIC PROPERTIES OF THE SPIN LIQUID

The system of equations (26) was solved numerically with the Mathcad program for a value $\tau_C = \tau_C^+ = 0.171$ in terms of the temperature $t = \tau - \tau_C$. The values of the parameters $\lambda(t)$, $\alpha_1(t)$, and $K_1(t)$ are presented in Fig. 1. The parameter $\delta(t)$ is a practically linear function of t. Below we derive the main characteristics of the spin liquid.

Susceptibility. The inverse susceptibility $\chi^{-1}(\tau) = \alpha_1(\tau)\delta(\tau)/2$ is linear in the entire temperature range and obeys the Curie-Weiss law

$$\chi^{-1}(\tau) = 2(\tau - \tau_C^+).$$

Spin correlations between nearest neighbors are described by the transverse correlator $K_1(\tau)$. The jump of the transverse correlator at the phase transition point has the value $\Delta K_1(\tau_C) = 0.052$, and its temperature behavior (with the asymptotics $\propto 1/\tau$) is presented in Fig. 2.

The heat capacity of a spin liquid,

$$c_{SL}(\tau) = k_B\left(\frac{\partial \in_{SL}}{\partial\tau}\right) = k_B\frac{3}{2}\left(-\frac{\partial K_1(\tau)}{\partial\tau}\right), \tag{36}$$

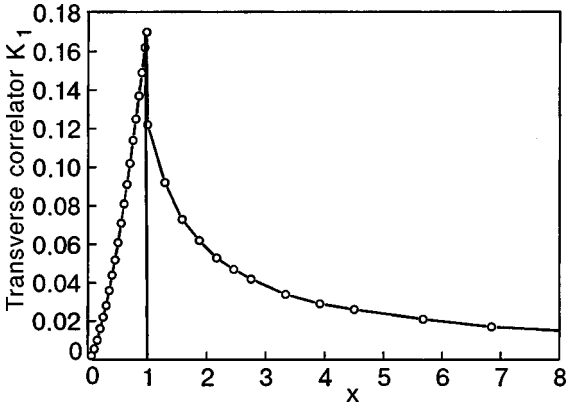

FIG. 2. Dependence of the transverse correlator K_1 on the relative temperature $x=\tau/\tau_C$.

has the asymptotics $c_{SL}(\tau)\propto 1/\tau^2$, and at the phase transition point its numerical value is

$$c_{SL}(\tau_C)=\frac{3}{2}k_B 0.6=0.9k_B.$$

The heat capacity in the ferromagnetic phase for $\tau\to\tau_C$ diverges, in accordance with formula (11), so that we have an infinite jump of the heat capacity at the phase transition point. The behavior of the specific heat c/k_B in the entire temperature interval is shown in Fig. 3. The results presented for the temperature behavior of $\chi(\tau)$, $K_1(\tau)$, and $c_{SL}(\tau)$ characterize the spin liquid rather fully.

The long-range spatial spin correlations are conveniently characterized by the *correlation length*. In accordance with formulas (17) and (18) we have

$$K_{\mathbf{R}}=\frac{1}{N}\sum_{\mathbf{q}} e^{i\mathbf{q}\cdot\mathbf{R}}\frac{K_1(1-\gamma_{\mathbf{q}})}{\Omega_{\mathbf{q}}}\coth\left(\frac{\Omega_{\mathbf{q}}}{2\tau}\right),$$

where the summation is over the Brillouin zone. The sum is replaced by an integral, and the leading contribution to the integral is given by the region around $\mathbf{q}=0$, where $1-\gamma_{\mathbf{q}}\approx\mathbf{q}^2/z$ (for a sc lattice) and $\Omega_{\mathbf{q}}/2\tau\ll 1$. Using the expansion of the hyperbolic cotangent for small values of the argument, we obtain

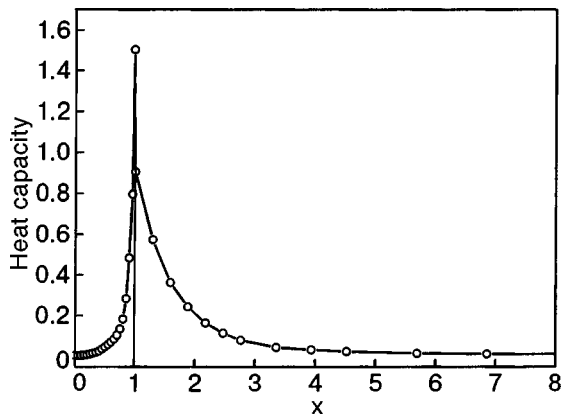

FIG. 3. Dependence of the specific heat on the relative temperature $x=\tau/\tau_C$.

$$K_{\mathbf{R}}\approx\frac{v}{(2\pi)^3}\int d^3\mathbf{q}e^{i\mathbf{q}\cdot\mathbf{R}}\frac{K_1(1-\gamma_{\mathbf{q}})}{\Omega_{\mathbf{q}}}\frac{2\tau}{\Omega_{\mathbf{q}}}$$
$$=\frac{2\tau z}{\alpha_1(\tau)}\frac{v}{(2\pi)^3}\int d^3\mathbf{q}\frac{e^{i\mathbf{q}\cdot\mathbf{R}}}{\mathbf{q}^2+\boldsymbol{\kappa}^2}. \quad (37)$$

In expression (37) the correlation length ξ (in units of the lattice constant) has been introduced in the integrand in accordance with its definition:

$$\frac{1}{\xi^2}=\boldsymbol{\kappa}^2=z\delta;\quad \xi(\tau)=\frac{1}{\sqrt{z\delta(\tau)}}=\frac{1}{2\sqrt{z}}-\frac{1}{\sqrt{\tau-\tau_C^+}}. \quad (38)$$

The integral in expression (37) is well known (see, e.g., Ref. 6) and for large values of R we have

$$K^{\mathbf{R}}\approx\frac{2\tau z}{\alpha_1(\tau)}\frac{\exp(-R/\xi(\tau))}{R}. \quad (39)$$

The divergence of the correlation length at $\tau\to\tau_C^+$ is evidence of a phase transition of the spin liquid to a ferromagnetic state with long-range order.

Let us consider still another characteristic of the system—the average value of the square of the total spin, $\langle S_{\text{tot}}^2\rangle$, expressed in terms of its value per spin, i.e., the function

$$S^2(\tau)\equiv\frac{1}{N}\langle\mathbf{S}_{\text{tot}}^2\rangle. \quad (40)$$

In the ferromagnetic ground state the square of the total spin is equal to $S(S+1)\approx N^2/4$; $S^2(0)=N/4$ is a macroscopically large quantity, and in the thermodynamic limit $S^2(0)\to\infty$. We write the function $S^2(\tau)$ in explicit form as

$$S^2(\tau)=\frac{1}{N}\left\langle\sum_{\mathbf{f},\mathbf{m}} S_{\mathbf{f}}S_{\mathbf{m}}\right\rangle=\sum_{\mathbf{R}}\frac{1}{N}\sum_{\mathbf{f}}\langle S_{\mathbf{f}}S_{\mathbf{f}+\mathbf{R}}\rangle$$
$$=\frac{3}{2}\sum_{\mathbf{R}} K_{\mathbf{R}}(\tau), \quad (41)$$

where we have used the property of isotropicity of the spin correlators, which is a characteristic trait of the spin liquid. Comparing Eq. (41) with the definitions (18), we obtain

$$S^2(\tau)=\frac{3}{2}\lim_{\mathbf{q}\to 0}K(\mathbf{q})=\frac{3}{2}K(0). \quad (42)$$

From expressions (17) for $K(\mathbf{q})$ we find in the given limit

$$\lim_{\mathbf{q}\to 0}K(\mathbf{q})=\frac{2\tau}{\alpha_1(\tau)\delta(\tau)}=\chi(\tau)\tau,$$

$$S^2(\tau)=\frac{3}{2}\chi(\tau)\tau,\quad \tau\geqslant\tau_C^+. \quad (43)$$

It follows from expression (43) that at the threshold of ferromagnetic instability for $\tau\to\tau_C^+$ the function $S^2(\tau)$ diverges (becomes macroscopically large, as in the F state), and at $\tau\to\infty$ ($\tau\gg\tau_C^+$) the function $S^2(\tau)\to 3/4$, i.e., we have a system of independent spins (a true paramagnet).

In the SL state all of the spatial spin correlators are positive; in particular, the longitudinal correlator for the nearest neighbors $L_1=K_1/2>0$. However, according to spin-wave

theory $L_1(\tau_C)<0$. How can one interpret the sign of L_1? Let us consider the wave function of a pair of nearest-neighbor spins (1 and 2) in the nonmagnetic state:

$$|\Psi)=\alpha|\uparrow\uparrow)+\beta|\downarrow\downarrow)+\gamma|\uparrow\downarrow)+\delta|\downarrow\uparrow).$$

From the condition $(\Psi|S^z_{1,2}|\Psi)=0$ it follows that $\alpha^2=\beta^2$, $\gamma^2=\delta^2$. The longitudinal and transverse correlators, respectively, are equal to

$$L_1=(\Psi|S^z_1S^z_2|\Psi)=\frac{1}{2}(\alpha^2-\gamma^2),$$

$$K_1=(\Psi|S^+_1S^-_2|\Psi)=\gamma\delta.$$

Solutions $\delta=\pm\gamma$ are possible. In the case under consideration $K_1=\gamma^2>0$. The sign of L_1 is determined by the difference of the statistical weights of the states with parallel (α^2) and antiparallel (γ^2) spins. In the case of a positive exchange interaction a ''memory'' of the ferromagnetic ordering should persist at the phase transition point (and above it), and therefore $\alpha^2>\gamma^2$, $L_1>0$. The result of the spin-wave theory for L_1 in the vicinity of the phase transition point (''antiferromagnetic'' short-range order) is incorrect. This conclusion once again emphasizes the approximate character of the spin-wave theory.

6. CONCLUSION

We have proposed a description of the Heisenberg ferromagnet (exchange parameter $I>0$ for nearest neighbors) above the Curie point as a spin-liquid state. We are actually dealing with a disordered system. Although the exchange interaction is short-ranged, cooperative phenomena nevertheless arise in the system—the interaction is transported to the whole lattice in a ''relay'' manner. Although long-range magnetic order is established in the F state, in the SL state order is established only over finite distances, i.e., we have *intermediate* or *short-range* order.

Both states (the F state for $\tau\leqslant\tau_C$ and the SL state for $\tau\geqslant\tau^+_C$) are described by the method of temperature Green functions in the framework of a linear theory of first and second order, respectively. This method gives a complete and self-consistent description of the thermodynamic properties of the spin liquid. It should be stressed that here we have only made a comparison of the results of the spin-wave theory of ferromagnetism and the theory of the spin liquid: at the phase transition point a jump of the spin correlation functions and of the heat capacity is observed. Although, as was noted by Mattis,[7] there is still no closed theory that could reliably predict the critical temperature of an arbitrary three-dimensional ferromagnet, its behavior in this temperature interval can be described approximately with the aid of a combination of the theory of spin waves and the proposed spin-liquid theory in the framework of a unified Green function method.

The author is grateful to V. N. Berzhankii for helpful discussions.

*E-mail: ekuz@crimea.edu

[1] S. V. Tyablikov, *Methods in the Quantum Theory of Magnetism* [transl. of 1st Russ. ed.], Plenum Press, New York (1967), cited Russ. 2nd ed., Nauka, Moscow (1975). Metody kvantovoĭ teorii magnetizma, Nauka, Moscow (1976).
[2] E. V. Kuz'min, Fiz. Tverd. Tela (St. Petersburg) **44**, 1075 (2002) [Phys. Solid State **44**, 1122 (2002)].
[3] E. V. Kuz'min, Zh. Éksp. Teor. Fiz. **123**, 149 (2003) [JETP **96**, 129 (2003)].
[4] E. V. Kuz'min, Fiz. Nizk. Temp. **29**, 764 (2003) [Low Temp. Phys. **29**, 571 (2003)].
[5] S. V. Vonsovskiĭ, *Magnetism*, Vols. 1 and 2, Wiley, New York (1974), Nauka, Moscow (1971).
[6] *Magnetic Semiconductors and Chalcogenide Spinels* [in Russian], Izd-vo MGU, Moscow (1981).
[7] D. C. Mattis, *The Theory of Magnetism*, Harper and Row, New York (1965), Mir, Moscow (1967).

Translated by Steve Torstveit

Phase transitions in a ferromagnet with biquadratic exchange and hexagonal single-ion anisotropy

Yu. A. Fridman,* O. A. Kosmachev, and B. L. Eingorn

V. I. Vernadskii Tavricheskii National University, pr. Vernadskogo 4, Simferopol 95007, Ukraine
(Submitted October 11, 2004; revised December 8, 2004)
Fiz. Nizk. Temp. **31**, 687–694 (June 2005)

The phase states and the spectra of elementary excitations of a ferromagnet with a biquadratic exchange interaction and a spin-2 magnetic ion are investigated. The phase diagrams of the system are constructed for different relationships among the material constants. It is shown that the phase diagram is substantially altered at large values of the single-ion anisotropy constants and biquadratic exchange constant. © *2005 American Institute of Physics.*
[DOI: 10.1063/1.1943537]

INTRODUCTION

Magnets with pronounced quantum properties, primarily systems with large single-ion anisotropy or magnets in which the biquadratic exchange interaction plays a substantial role (so-called Heisenberg magnets), have drawn steady research interest from both theorists and experimentalists.[1,2] This is because in such magnets the quantum properties of individual spins in the effective magnetic field play a decisive role in the formation of the dynamic and thermodynamic properties. When a large single-ion anisotropy (comparable to or even exceeding the exchange interaction) is taken into account together with a biquadratic exchange, a number properties appear which are unusual from the standpoint of the phenomenological theory. First, when anisotropy and the interactions of higher multipoles are taken into account exactly for high-spin systems, the single-ion spectrum becomes substantially nonequidistant and additional branches appear in the spectrum of elementary excitations. In addition, quadrupolar phases can exist and may be the ground state of the system in the case when the biquadratic exchange exceeds the Heisenberg exchange.

It is known[3–13] that a large number of magnetic compounds (consisting of regularly arranged magnetic ions with an interaction of fixed sign and intensity between them) nevertheless remain nonmagnetic down to temperature $T=0$. The reason for the absence of magnetic order in these cases is the existence of strong anisotropy of the form $\beta\Sigma_n(S_n^z)^2$, where the constant β is comparable to or even greater than the exchange interaction J_0. The theoretical investigation of such systems dates back to the paper by Moriya,[14] where it was shown that for $\beta/2J_0>1$ even at absolute zero temperature in the absence of an external field a nonmagnetic quadrupole-ordered (QU) ground state is realized. In was shown in Ref. 15 that the competition of the two types of interactions—single-ion anisotropy and exchange—leads to the existence of peculiar types of spin structures at $T=0$: the single-ion anisotropy also creates an effective field but of a quadrupolar rather than ferromagnetic type. The corresponding quadrupole order in this case can be represented as a chaotic ordering of spins in the plane perpendicular to the axis of ferromagnetism, selected by an external field, for example, and can be characterized by a quadrupole order parameter $q=3\langle(S^z)^2\rangle-S(S+1)$. Thus, despite the absence of vector magnetic order, the corresponding structures are spin-ordered: the order in them is determined by tensor characteristics. For this reason their properties differ from those of paramagnets—in particular, they are close to those of antiferromagnets (specifically, those that are uniaxial in a field parallel to the axis of anisotropy). Another mechanism (besides uniaxial anisotropy) that leads to the existence of quadrupolar phases can be the presence of biquadratic exchange.[2,16,17]

Studies of this type are actively being done for spin-1 systems. The interest in such systems is obvious: first because spin 1 is the minimum spin of a magnetic ion for which single-anisotropy anisotropy is realized in a system, and also because the quantum properties of a magnet are manifested most clearly at small values of the spin.

However, taking into account single-ion anisotropy more complex than uniaxial requires consideration of magnetically ordered systems with a spin of the magnetic ion greater than 1.[18,19] Such systems include rare-earth magnets such as TmCd,[20] $DyVO_4$, and $TmVo_4$.[21] The goal of the present paper is to study the phase states and spectral properties of a ferromagnet with biquadratic exchange, high uniaxial anisotropy, and a spin of the magnetic ion $S=2$.

MODEL

As the model system we consider a ferromagnet with a biquadratic exchange interaction and hexagonal single-ion anisotropy in zero external field. The Hamiltonian of such a system can be written in the form

$$\mathcal{H}=-\sum_n (B_2^0O_{2n}^0+B_4^0O_{4n}^0)-\frac{1}{2}\sum_{n\neq n'}[J(n-n')\mathbf{S}_n\cdot\mathbf{S}_{n'} + K(n-n')(\mathbf{S}_n\cdot\mathbf{S}_{n'})^2], \quad (1)$$

where B_2^0 and B_4^0 are single-ion anisotropy constants, O_j^i are Stevens operators, S_n^i are spin operators at site n, and $J,K>0$ are the Heisenberg and biquadratic exchange in constants, respectively.

In the general case the magnetic moment of a system described by Hamiltonian (1) is oriented at an angle τ to the

 © 2005 American Institute of Physics

OZ axis. We diagonalize the initial Hamiltonian by rotating the coordinate system around the OY axis so that the magnetic moment coincides with the OZ axis:

$$\mathcal{H}(\theta)=U\mathcal{H}U^{+},\quad U(\theta)=\prod_{n}\exp(i\theta S_n^y). \tag{2}$$

In the new variables the Hamiltonian of the single-ion anisotropy has the form

$$\begin{aligned}\mathcal{H}_{OA}=&-B_2^0\left(\frac{2-3\sin^2\theta}{2}O_2^0-\frac{3}{2}O_2^{zx}\sin 2\theta+\frac{3}{2}O_2^2\sin^2\theta\right)\\&-B_4^0\left(\frac{8-40\sin^2\theta+35\sin^4\theta}{8}O_4^0\right)\\&-B_4^0\left[\frac{5}{2}\sin 2\theta(7\sin^2\theta-4)O_4^1+\frac{5}{2}\sin^2\theta(6\right.\\&\left.-7\sin^2\theta)O_4^2-\frac{35}{2}O_4^3\sin 2\theta\sin^2\theta+\frac{35}{8}O_4^4\sin^4\theta\right],\end{aligned} \tag{3}$$

where

$$O_2^0=3(S^z)^2-6;\quad O_2^{ij}=[S^i,S^j]_+;$$

$$O_2^2=\frac{1}{2}((S^+)^2+(S^-)^2);$$

$$O_4^0=35(S^z)^4-155(S^z)^2+72;$$

$$O_4^1=\frac{1}{4}[7(S^z)^3-19S^z,(S^++S^-)]_+;$$

$$O_4^2=\frac{1}{4}[7(S^z)^2-11,((S^+)^2+(S^-)^2)]_+;$$

$$O_4^3=\frac{1}{4}[S^z,((S^+)^3+(S^-)^3)]_+;$$

$$O_4^4=\frac{1}{2}((S^+)^4+(S^-)^4);\quad S^{\pm}=S^x\pm iS^y. \tag{4}$$

In terms of the Stevens operators the exchange part of the Hamiltonian can be written in the form

$$\begin{aligned}\mathcal{H}_{\rm int}=&-\frac{1}{2}\sum_{n\neq n'}\left(J(n-n')-\frac{K(n-n')}{2}\right)(\mathbf{S}_n\cdot\mathbf{S}_{n'})\\&-\frac{1}{4}\sum_{n\neq n'}K(n-n')\left(\frac{1}{3}O_{2n}^0O_{2n'}^0\right.\\&\left.+\sum_{t=2,xy,yz,zx}O_{2n}^tO_{2n'}^t\right).\end{aligned} \tag{5}$$

After separating out from the exchange Hamiltonian (5) in the standard way a self-consistent field due to ordering of the magnetic moment and an additional field $\langle O_{2n}^p\rangle=q_2^p$ due to the quadrupole ordering, the single-ion Hamiltonian with allowance for (3) takes the form

$$\begin{aligned}\mathcal{H}_0=&\overline{\varepsilon}_0-\overline{H}S^z-\frac{K_0}{2}\left(\frac{1}{3}q_2^0O_2^0+\sum_{t=2,xy,yz,zx}q_2^tO_2^t\right)\\&+\mathcal{H}_{OA}(\theta),\end{aligned} \tag{6}$$

where

$$\begin{aligned}\overline{\varepsilon}_0=&-6K_0-\frac{1}{2}\left(J_0-\frac{K_0}{2}\right)\langle S^z\rangle^2+\frac{K_0}{4}\left(\frac{1}{3}(q_2^0)^2\right.\\&\left.+\sum_{t=2,xy,yz,xz}(q_2^t)^2\right),\quad \overline{H}=\left(J_0-\frac{K_0}{2}\right)\langle S^z\rangle.\end{aligned}$$

Taking the quantum properties of the system under study into account requires a mathematical formalism adequate to the task. The best approach for this purpose is the diagram technique for the Hubbard operators,[22,23] the application of which[24] makes it possible to develop a regular procedure for calculating the thermodynamic and dynamic characteristics of anisotropic Heisenberg ferromagnets. As was mentioned in Ref. 24, in the Hubbard operator representation all systems with a pair interaction take the same form, which is certainly a convenience for developing a general formalism. Since the Heisenberg magnet model is a system of spin moments with binary interaction, the diagram technique for the Hubbard operators is an adequate mathematical formalism that permits taking the single-ion anisotropy into account exactly by incorporating it in the single-ion Hamiltonian. This procedure makes it possible to avoid the difficulties arising in the use of spin operators. In addition, the Hubbard operator technique permits taking a number of purely quantum effects into account.[25–28]

The Hubbard operators $X^{M'M}\equiv|\psi(M')\rangle\langle\psi(M)|$ (Refs. 23 and 24) describe the transition of a magnetic ion from state M to state M'. In the case under consideration $M=-2,-1,0,1,2$. We construct these operators on the basis of the eigenfunctions of the operator S_n^z. The relation between the spin operators and the Hubbard operators is given by the expression

$$\begin{aligned}&S_n^+=2(X_n^{21}+X_n^{-1-2})+\sqrt{6}(X_n^{10}+X_n^{0-1}),\\&S^-=(S^+)^+,\quad S_n^z=2(H_n^2-H_n^{-2})+(H_n^1-H_n^{-1}),\end{aligned} \tag{7}$$

where the $H^M\equiv X^{MM}$ are the diagonal Hubbard operators. The Hubbard operator algebra is defined by the commutation relations

$$\begin{aligned}&[H^M,X^{kl}]=(\delta_{Mk}-\delta_{Ml})X^{kl}=\alpha^M(k,l)X^{kl};\\&[X^{pl},X^{lp}]=H^p-H^l;\quad [X^{\alpha},X^{-\alpha}]=(\boldsymbol{\alpha}\cdot\mathbf{H})\end{aligned} \tag{8}$$

where $\boldsymbol{\alpha}$ denotes the root vectors.[24]

In the Hubbard operator representation the one-site Hamiltonian (6) can be written in the form

$$\mathcal{H}_0=\sum_M E_MH^M+\sum_{p,q}V_{pq}X^{pq}, \tag{9}$$

where E_M and V_{pq} have the following form:

$$\begin{aligned}&E_{\pm 2}=-6(\tilde{B}_2^0+2\tilde{B}_4^0)\mp 2\overline{H};\\&E_{\pm 1}=3(\tilde{B}_2^0+16\tilde{B}_4^0)\mp\overline{H};\quad E_0=6(\tilde{B}_2^0-12\tilde{B}_4^0),\\&V_{pq}=V_{qp}^*;\end{aligned} \tag{10}$$

$$V_{21}=V_{12}=-V_{-2-1}=-V_{-1-2}=-3(\tilde{B}_2^1+\tilde{B}_4^1);$$

$$V_{20}=V_{02}=V_{-20}=V_{0-2}=-\sqrt{6}(\tilde{B}_2^2+3\tilde{B}_4^2);$$

$$V_{2-1}=V_{-12}=-V_{-21}=-V_{1-2}=-3(\tilde{B}_4^3);$$

$$V_{10}=V_{01}=-V_{-10}=-V_{0-1}=-\frac{\sqrt{6}}{2}(\tilde{B}_2^1-6\tilde{B}_4^1);$$

$$V_{2-2}=V_{-22}=-12(\tilde{B}_4^4);\quad V_{-11}=V_{1-1}=-3(\tilde{B}_2^2-4\tilde{B}_4^2);$$

$$\tilde{B}_2^0=B_2^0(\theta)+\frac{1}{6}K_0q_2^0;\quad \tilde{B}_2^2=B_2^2(\theta)+\frac{1}{2}K_0q_2^2;$$

$$\tilde{B}_2^1=B_2^1(\theta)+\frac{1}{2}K_0q_2^{zx};$$

$$\tilde{B}_4^0=B_4^0\frac{8-40\sin^2\theta+35\sin^4\theta}{8};$$

$$\tilde{B}_4^1=\frac{5}{2}B_4^0\sin 2\theta(7\sin^2\theta-4);$$

$$\tilde{B}_4^2=\frac{5}{2}B_4^0\sin 2\theta(6-7\sin^2\theta);$$

$$\tilde{B}_4^3=-\frac{35}{2}B_4^0\sin 2\theta\sin^2\theta;\quad \tilde{B}_4^4=\frac{35}{2}B_4^0\sin^4\theta;$$

$$B_2^0(\theta)=B_2^0\left(\frac{2-3\sin^2\theta}{2}\right);\quad B_2^1(\theta)=-\frac{3}{2}B_2^0\sin 2\theta;$$

$$B_2^2(\theta)=\frac{3}{2}B_2^0\sin^2\theta.$$

In the general case, for an arbitrary relation between the exchange constants and the single-ion anisotropy constants, diagonalization of the one-site Hamiltonian (9) is extremely difficult. For certain relations among the material constants, however, this procedure can be carried out successfully.

LOW ANISOTROPY

Let us begin by considering the case when the single-ion anisotropy is substantially smaller than the exchange interaction constants, i.e., $B_i^0 \ll J_0, K_0$. Furthermore, we shall assume that effects due to ordering of the multipole degrees of freedom are small:[29] the Heisenberg exchange is larger than the biquadratic ($J_0 \gg K_0$). In this approximation the modulus of the magnetization does not vary, and any possible phase changes of the state of the system involve only rotation of the magnetization vector.

In this approximation the correction to the ground state of the magnetic ion in the small parameter B_i^0/J_0 has the form

$$E_2^{(1)}=3(3B_2^0+20B_4^0)\sin^2\theta-\frac{105}{2}B_4^0\sin^4\theta. \tag{11}$$

In the low-temperature case under consideration ($T \ll T_C$, where T_C is the Curie temperature) it is sufficient to take into account in the expression for the free energy density

$$F=-T\ln\left(\sum_{M=-2}^{2}\exp(-E_M/T)\right)$$

only the lowest energy level:

$$E_2=-6(\tilde{B}_2^0+2\tilde{B}_4^0)-2\overline{H}+3(3B_2^0+20B_4^0)\sin^2\theta-\frac{105}{2}B_4^0\sin^4\theta.$$

Analysis of the free energy density shows that when the anisotropy constant $B_4^0<0$ the following phase states are realized in the system.

1. A state in which the magnetization vector is parallel to the OZ axis (the angle $\theta=0$). We call this phase state the easy-axis (EA) phase.

2. A state in which the magnetization vector lies in the plane perpendicular to the OZ axis (the XOY plane, the angle $\theta=\pi/2$). We call this the easy-plane (EP) state.

3. A canted phase (CP), in which the equilibrium angle of orientation of the magnetization vector is determined by the expression

$$\sin\theta=\sqrt{\frac{3B_2^0+20B_4^0}{35B_4^0}}. \tag{12}$$

From an analysis of the free energy density one can easily determine the line of phase transitions from the easy-axis to the canted phase, $3B_2^0+20B_4^0=0$, and from the easy-plane to the canted phase, $B_2^0-5B_4^0=0$.

In the case when $B_4^0>0$, the canted phase becomes unstable, and a phase transition between the easy-axis and easy-plane phases is a first-order transition.[30] From the equality of the free energies in the easy-axis and easy-plane phases one can find the line of the easy-axis to easy-plane phase transition:

$$6B_2^0+5B_4^0=0.$$

The results obtained for the case of a small single-ion anisotropy enable one to construct the phase diagram shown in the inset to Fig. 1. In the case under consideration the phase transitions involve rotation of the magnetization vector. We note that our results are in complete agreement with the results of Ref. 30, which were obtained for a hexagonal crystal with an single-ion anisotropy energy of the form

$$U_a=K_1\sin^2\theta+K_2\sin^4\theta.$$

HIGH SINGLE-ION ANISOTROPY

Let us now consider the more interesting situation where the single-ion anisotropy constants are assumed to be greater than the energy interaction constants ($B_i^0 \gg J_0, K_0$). In this case quantum effects are clearly manifested in the system: first, the quantum spin contraction effect, wherein the magnetization decreases in modulus at the site,[27] and second, the possibility that quadrupolar phases characterized by tensor order parameters q_2^t can be realized in the system.[31] As before, we assume that the temperatures are low.

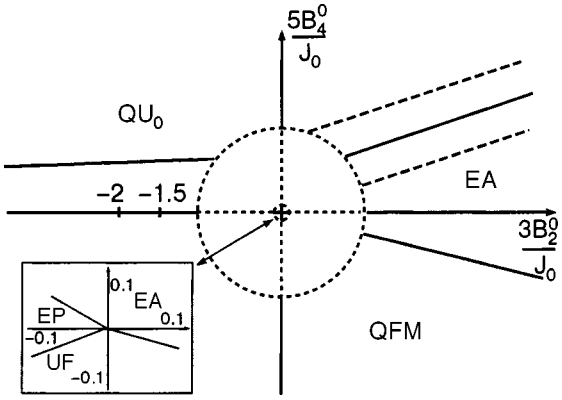

FIG. 1. Phase diagram of a ferromagnet with biquadratic exchange in the case of large values of the single-ion anisotropy constants and predominant Heisenberg exchange ($B_i^0 > J_0 > K_0$).

As we have mentioned above, the incorporation of quantum effects requires taking the single-ion anisotropy into account exactly, as can be done in terms of the Hubbard operators. These operators are constructed on the basis of eigenfunctions of the one-site Hamiltonian (9). For diagonalization of this Hamiltonian we use the method of unitary transformations for the Hubbard operators:[22]

$$U_{mn}^{\alpha} = \exp(\alpha X^{nm} - \alpha^* X^{mn}), \tag{13}$$

where $\alpha \equiv |\alpha| \exp(i\mu)$ is the parameter of the unitary transformation. Taking the commutation relations (8) into account, we define the transformation laws for the Hubbard operators upon a unitary rotation (13):

$$X^{pq} \to U_{nm}(\alpha,\beta,\gamma,\delta) X^{pq} U_{nm}^{+}(\alpha,\beta,\gamma,\delta) \equiv X^{pq}(\alpha,\beta,\gamma,\delta),$$

and the unitary transformation operator in this case has the form

$$U_{nm}(\alpha,\beta,\gamma,\delta) = U_{1-1}(\delta) U_{-20}(\gamma) U_{20}(\beta) U_{2-2}(\alpha),$$
$$U_{ij}(\varphi) = 1 - (1-\cos\varphi)(X^{ii} + X^{jj}) + \sin\varphi (X^{ij} - X^{ji}), \tag{14}$$

where $\varphi = \alpha, \beta, \delta, \gamma$.

For diagonalization of the single-ion Hamiltonian (9) we do the unitary transformations (13), (14) and require that the off-diagonal matrix elements $V_{pq}(\alpha,\beta,\gamma,\delta)$ vanish. This condition allows us to obtain a system of equations for the parameters of the unitary transformations: α, β, γ, δ, the solution of which will allow us to determine the dependence of the ''angles of rotation'' of the system on the constants of the single-ion anisotropy and exchange interactions.

The eigenvectors and eigenvalues of the single-ion Hamiltonian (9) are given by the relations

$$|\psi_{-2}\rangle = b|2\rangle - \cos\beta \sin\gamma |0\rangle + a|-2\rangle;$$
$$|\psi_{-1}\rangle = -\sin\delta |1\rangle + \cos\delta |-1\rangle;$$
$$|\psi_0\rangle = -c|2\rangle + \cos\beta\cos\gamma |0\rangle + d|-2\rangle;$$
$$|\psi_1\rangle = \cos\delta |1\rangle + \sin\delta |-1\rangle;$$
$$|\psi_2\rangle = \cos\alpha\cos\beta |2\rangle + \sin\beta |0\rangle + \sin\alpha\cos\beta |-2\rangle, \tag{15}$$

where

$$a = \cos\alpha\cos\gamma + \sin\alpha\sin\beta\sin\gamma,$$
$$b = \cos\alpha\sin\beta\sin\gamma - \sin\alpha\cos\gamma,$$
$$c = \cos\alpha\sin\beta\cos\gamma + \sin\alpha\sin\gamma,$$
$$d = \cos\alpha\sin\gamma - \sin\alpha - \sin\beta\cos\gamma.$$
$$\tilde{E}_2 = E_2\cos^2\alpha\cos^2\beta + E_0\sin^2\beta + E_{-2}\sin^2\alpha\cos^2\beta + (V_{20}\cos\alpha + V_{0-2}\sin\alpha)\sin 2\beta + V_{2-2}\sin 2\alpha\cos^2\beta;$$
$$\tilde{E}_0 = E_2 c^2 + E_0\cos^2\beta\cos^2\gamma + E_{-2}d^2 - 2cV_{20}\cos\beta\cos\gamma + 2dV_{0-2}\cos\beta\cos\gamma - 2cdV_{2-2};$$
$$\tilde{E}_{-2} = E_2 b^2 + E_0\cos^2\beta\sin^2\gamma + E_{-2}a^2 - 2bV_{20}\cos\beta\sin\gamma - 2aV_{0-2}\cos\beta\sin\gamma + 2abV_{2-2};$$
$$\tilde{E}_1 = E_1\cos^2\delta + E_{-1}\sin^2\delta + V_{1-1}\sin 2\delta;$$
$$\tilde{E}_{-1} = E_1\sin^2\delta + E_{-1}\cos^2\delta - V_{1-1}\sin 2\delta, \tag{16}$$

and E_M is determined by expressions (10). In the general case the explicit form of the parameters of the system is quite complex. However, in the case of low temperatures we can limit consideration to only the lowest energy level, allowing us to obtain an expression for the order parameters of the system. It follows from expressions (10) and (16) that in the case under discussion the lowest energy level is E_2. Then the ground state of the magnetic ion is described by the eigenvector $|\psi_2\rangle$:

$$|\psi_2\rangle = \cos\alpha\cos\beta |2\rangle + \sin\beta |0\rangle + \sin\alpha\cos\beta |-2\rangle.$$

The order parameter of the system in this case has the form

$$\langle S^z\rangle = 2\cos 2\alpha\cos^2\beta, \quad q_2^0 = 6\cos 2\beta,$$
$$q_2^2 = \sqrt{6}\sin 2\beta(\sin\alpha + \cos\alpha). \tag{17}$$

It follows from expressions (17) that in the case when the Heisenberg exchange is predominant ($2J_0 \gg K_0$), the following phase states are realized in the system.

1. If the unitary transformation parameters $\alpha = \beta = 0$, then it follows from Eq. (17) that the order parameters have the form

$$\langle S^Z\rangle = 2, \quad q_2^0 = 6, \quad q_2^2 = 0. \tag{18}$$

These values are characteristic of ferromagnetic ordering in the system, and the given magnetic order is the easy-axis (EA) phase.

2. For $\beta = \pi/2$ a phase with quadrupolar ordering (QU_0) is realized in the system. The order parameters of the system in this phase have the form

$$\langle S^z\rangle = 0, \quad q_2^0 = -6, \quad q_2^2 = 0. \tag{19}$$

In the case of predominant biquadratic exchange ($K_0 \gg 2J_0$) the magnetic phases become unstable, and only the

quadrupolar phases can be realized in the system. For $\alpha = \pi/4$, $\beta = 0$ the system will be found in quadrupolar phase QU_1, the order parameters of which have the form

$$\langle S^z \rangle = 0, \quad q_2^0 = 6, \quad q_2^2 = 0. \tag{20}$$

PHASE DIAGRAM

To construct the phase diagram it is necessary to determine the lines of phase transitions. This is done most simply from an analysis of the spectra of elementary excitations. It is well known that the spectra of elementary excitations of a system are determined by the poles of the Green function:[32]

$$G^{\alpha\alpha'}(n,n';\tau,\tau') = -\langle \hat{T} X_n^{\alpha}(\tau) X_{n'}^{\alpha'}(\tau') \rangle,$$

where $\hat{T}$ is the Wick operator, $X_n^{\alpha}(\tau)$ is the Hubbard operator in the Heisenberg representation, and the averaging is done using the total Hamiltonian.

The dispersion relation determining the spectra of elementary excitations is analogous to the Larkin equation, and a detailed derivation of it is given in Ref. 27. We note that since we have taken the one-site correlators into account exactly, the dispersion relation is valid both for arbitrary values of the single-ion anisotropy constants and for an arbitrary relationship between the constants of the exchange interactions. For studying the spectral properties of the magnet in the vicinity of the phase transitions, we restrict analysis to the solutions of the dispersion relation in the corresponding phases.

Let us analyze the dispersion relation in the case when the Heisenberg exchange interaction is predominant ($J_0 > K_0$).

We assume that the parameters of the system are such that the EA phase is realized in the magnet, so that the order parameter is determined by relations (18). In that case the elementary excitations in the EA phase have the form

$$\varepsilon_1(k) = 6\gamma k^2 + 4(J_0 + K_0) + 12B_2^0 - 60B_4^0;$$

$$\varepsilon_2(k) = 2\alpha k^2 + (9B_2^0 + 60B_4^0), \tag{21}$$

where $\alpha = J_0 R_0^2$ and $\gamma = K_0 \tilde{R}_0^2$, with R_0 and $\tilde{R}_0$ being the radii of the Heisenberg and biquadratic exchange interactions, respectively.

Analogously, in the QU_0 phase (with Eq. (19) taken into account), the magnon spectra have the form

$$\varepsilon_3(k) = 3\sqrt{(\gamma k^2 - B_2^0 + 40B_4^0)[2\alpha k^2 + 2(K_0 - J_0) - B_2^0 + 40B_4^0]};$$

$$\varepsilon_4(k) = 12\sqrt{(\gamma k^2 - B_2^0 + 5B_4^0)(K_0 - B_2^0 + 5B_4^0)}. \tag{22}$$

Analysis of the free energy in the EA and QU_0 phases shows that the phase transition between them is a first-order transition. Equating the expressions for the free energy in the EA and QU_0 phases, we can determine the line of the phase transition: $60B_4^0 - 12B_2^0 - 2J_0 + K_0 = 0$.

It is well known that the spectra of elementary excitations do not have any features on a first-order phase transition line. However, on lines of stability these spectra soften. From the expressions for $\varepsilon_1(k)$ and $\varepsilon_4(k)$ we obtain the following expressions for the line of stability of the EA and QU_0 phases:

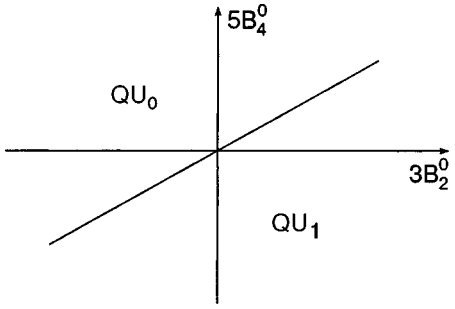

FIG. 2. Phase diagram of a ferromagnet with predominant biquadratic exchange ($K_0 \gg J_0$) and arbitrary values of the single-ion anisotropy constants.

$$3B_2^0 - 15B_4^0 + J_0 + K_0 = 0, \quad B_2^0 - 5B_4^0 = 0. \tag{23}$$

The vanishing of the energy gap in the spectrum $\varepsilon_2(k)$ allows us to determine the line of the second-order phase transition EA-QFM [quadrupolar-ferromagnetic (or canted) phase]:

$$3B_2^0 + 20B_4^0 = 0.$$

On the line of the second-order phase transition QU_0-QFM, given by $40B_4^0 - B_2^0 + 2(K_0 - J_0) = 0$, the gap in the spectrum $\varepsilon_3(k)$ vanishes.

The corresponding phase diagram is presented in Fig. 1. The region bounded by the dashed circle corresponds to small values of the single-ion anisotropy constants. The dashed line correspond to lines of stability of the first-order QU_0-EA phase transition.

It is also of interest to consider the case of large biquadratic exchange ($K_0 \gg 2J_0$). When the biquadratic exchange becomes dominant, the magnetic phases with $\langle S^z \rangle \neq 0$ become unstable and energetically unfavorable, and only the quadrupolar phases QU_0 and QU_1 can be realized in the system. Here, unlike the case when the Heisenberg exchange is dominant, the QU phases are realized for arbitrary values of the single-ion anisotropy constants.

In the QU_1 phase the spectra of excitations with allowance for the order parameter (2) have the form

$$\varepsilon_5(k) = 12\sqrt{(\gamma k^2 + B_2^0 - 5B_4^0)(K_0 + B_2^0 - 5B_4^0)};$$

$$\varepsilon_6(k) = 3\sqrt{(3\gamma k^2 + 3B_2^0 + 20B_4^0)(2\alpha k^2 + 8K_0 - J_0 + 9B_2^0 + 60B_4^0)}. \tag{24}$$

On the line of the $QU_1 - QU_0$ phase transition the gap in the magnon spectrum $\varepsilon_5(k)$ vanishes, and the line of this phase transition has the form

$$B_2^0 - 5B_4^0 = 0. \tag{25}$$

The phase transition from the QU_0 phase to the QU_1 phase occurs along the magnon branch $\varepsilon_4(k)$. From the vanishing of the gap in the spectrum $\varepsilon_4(k)$ we obtain a phase transition line that coincides with Eq. (25). This attests to the second-order nature of the $QU_1 - QU_0$ phase transition. We note that this phase transition involves rotation of the principal axes of the quadrupole moment tensor. The corresponding phase diagram is presented in Fig. 2.

The authors thank the Ministry of Education and Science of Ukraine for financial support (Project No. 235/03).

*E-mail: frid@tnu.crimea.ua

[1] É. L. Nagaev, Usp. Fiz. Nauk **136**, 61 (1982) [Sov. Phys. Usp. **25**, 31 (1982)].
[2] É. L. Nagaev, *Magnets with Complicated Exchange Interaction* [in Russian], Nauka, Moscow (1988).
[3] T. Tsurento and T. Murano, Physica **51**, 186 (1971).
[4] C. Ishikawa and Y. J. Endo, Prog. Theor. Phys. **55**, 650 (1976).
[5] V. G. Borisenko and Yu. V. Pereverzev, Fiz. Nizk. Temp. **11**, 730 (1985) [Sov. J. Low Temp. Phys. **11**, 400 (1985)].
[6] K. M. Diederix, H. A. Algra, J. P. Groen *et al.*, Phys. Lett. A **60**, 247 (1977).
[7] V. P. D'yakonov, É. E. Zubov, F. P. Onufrieva, A. V. Saĭko, and I. M. Fita, Zh. Éksp. Teor. Fiz. **93**, 1775 (1987) [Sov. Phys. JETP **66**, 1013 (1987)].
[8] F. Varret, J. Phys. Chem. Solids **37**, 257 (1976).
[9] I. I. Smit, L. I. de Jongh, and D. de Klerk *et al.*, Physica **86**, 1147 (1977).
[10] N. Wada, K. Amaja, and T. Haseda, J. Phys. Soc. Jpn. **43**, 341 (1977).
[11] H. A. Algra, I. Bartolome, L. I. de Jongh *et al.*, Physica **93**, 35 (1978).
[12] W. G. Bos, T. O. Klassen, N. J. Pouks, and R. I. Carlin, J. Magn. Magn. Mater. **15–18**, 464 (1980).
[13] R. L. Carlin and V. van Duyneveldt, J. Acc. Chem. Res. **13**, 231 (1980).
[14] T. Morija, Phys. Rev. **117**, 635 (1960).
[15] F. P. Onufrieva, Zh. Éksp. Teor. Fiz. **89**, 2270 (1985) [Sov. Phys. JETP **62**, 1311 (1985)].
[16] H. H. Chen and P. M. Levy, Phys. Rev. Lett. **27**, 1383 (1971).
[17] V. M. Matveev, Zh. Éksp. Teor. Fiz. **65**, 1626 (1973) [Sov. Phys. JETP **38**, 813 (1974)].
[18] M. Dudzinski and J. Sznajd, Eur. Phys. J. B **5**, 745 (1998).
[19] J. Sznajd and M. Dudzinski, Phys. Rev. B **59**, 4176 (1999).
[20] R. Aleonard and P. Morin, Phys. Rev. B **19**, 3868 (1979).
[21] P. M. Levy, P. Morin, and D. Schmitt, Phys. Rev. Lett. **42**, 1417 (1979).
[22] V. V. Val'kov, Teor. Mat. Fiz. **76**, 321 (1988).
[23] J. Hubbard, Proc. R. Soc. London, Ser. A **281**, 401 (1964).
[24] R. O. Zaĭtsev, Zh. Éksp. Teor. Fiz. **68**, 207 (1975) [Sov. Phys. JETP **41**, 100 (1975)].
[25] F. P. Onufrieva, Zh. Éksp. Teor. Fiz. **80**, 2372 (1981) [Sov. Phys. JETP **53**, 1241 (1981)].
[26] V. V. Val'kov and T. A. Val'kova, Teor. Mat. Fiz. **59**, 453 (1984).
[27] V. V. Val'kov, T. A. Val'kova, and S. G. Ovchinnikov, Zh. Éksp. Teor. Fiz. **88**, 550 (1985) [Sov. Phys. JETP **61**, 970 (1985)].
[28] V. V. Val'kov and S. G. Ovchinnikov, Zh. Éksp. Teor. Fiz. **85**, 1600 (1983) [Sov. Phys. JETP **58**, 775 (1983)].
[29] V. M. Loktev and V. S. Ostrovskiĭ, Fiz. Nizk. Temp. **20**, 983 (1994) [Low Temp. Phys. **20**, 775 (1994)].
[30] L. D. Landau and E. M. Lifshitz, *Electrodynamics of Continuous Media*, 2nd ed., rev. and enl., by E. M. Lifshitz and L. P. Pitaevskii, Pergamon Press, Oxford (1984), Nauka, Moscow (1982).
[31] Yu. A. Fridman, O. A. Kosmachev, and B. L. Eingorn, Fiz. Nizk. Temp. **29**, 744 (2003) [Low Temp. Phys. **29**, 555 (2003)].
[32] Yu. A. Izyumov and Yu. N. Skryabin, *Statistical Mechanics of Magnetically Ordered Systems*, Plenum Press (1990), Nauka, Moscow (1987).

Translated by Steve Torstveit

Interplay between the spin state of manganese and the stability of the crystal structure of MnAs and MnP compounds

V. I. Valkov* and A. V. Golovchan

A. A. Galkin Donetsk Physicotechnical Institute, ul. R. Lyuksemburg 72, Donetsk 83114, Ukraine
(Submitted November 22, 2004)
Fiz. Nizk. Temp. **31**, 695–702 (June 2005)

Starting from first principles, a study of the ground states of manganese arsenide and manganese phosphide, which have a hexagonal $B8_1$ and a distorted rhombohedral $B31$ crystal structure, is made by the FP–LMTO method. It is shown that in these compounds a continuous transition from a high-spin to a low-spin state occurs as the volume of the lattice is changed, and it turns out that the magnetic moment of the manganese atoms is the same at equal volumes. Starting from the results of a calculation of the total energy of these systems as a function of the parameters of the structural distortions, it is established that the high-spin state suppresses the structural distortions, while the low-spin state enhances them. It is shown that the difference of the crystal and magnetic structures of manganese arsenide and phosphide is due solely to the different lattice volumes, i.e., the substitution of arsenic by phosphorus is equivalent to the application of external hydrostatic pressure. It is conjectured that a qualitative interpretation of the mechanism of magnetostructural transitions in MnAs should proceed from the idea that the leading role is the degree of occupation of the ''antibonding'' state of the itinerant carriers of magnetism. © *2005 American Institute of Physics.*
[DOI: 10.1063/1.1943538]

INTRODUCTION

The pnyctides of $3d$ transition metals, MnAs, MnP, and NiAs, in particular, have been studied for decades with unabated interest, which recently has intensified in connection with the possibility of the technological use of the properties of MnAs–GaAs, MnFeAs–Mn–FeP–MnFeSi alloys.[1–3] From the pnyctides themselves researchers have moved on to quasibinary systems based on them, and in recent years experiments on pnyctide-semiconductor films has become a priority. One of the characteristic features of this class of compounds is the close interplay between the magnetic and structural subsystems, the study of which is the main goal of the present paper.

At atmospheric pressure and low temperatures, manganese arsenide has a hexagonal close packed (hcp) crystal structure $B8_1$ (symmetry group $P6_3/mmc$) and possesses high-spin (HS) ferromagnetic (FM) order. Raising the temperature leads to a sequence of magnetic and structural phase transitions. At $T_C=313$ K a first-order transition occurs from the ferromagnetic HS state[4,5] (manganese magnetic moment $|\mathbf{m}|=m_H=3.4\mu_B$) to a HS paramagnetic (PM) state.[6] This transition is accompanied by a change of the crystal structure from hcp $B8_1$ ($P6_3/mmc$) to rhombohedral $B31$ (symmetry group P_{nma}).[7] The hexagonal structure is recovered as a result of a second-order structural phase transition $B31(\mathrm{PM})-B8_1(\mathrm{PM})$ at $T_t=399$ K.

The rhombohedral $B31$ structure can be treated as a distorted hcp $B8_1$ structure, pictured in a rhombohedral derivative (Fig. 1). A qualitative measure of the distortions is the parameter $\phi=\pm|g_z|/a\sqrt{3}$, $e=\pm|g_x|/c\ll\phi$ for manganese and $\phi_1=\pm|a_{1x}|/c$, $e_1=\pm|a_{1z}|/a\sqrt{3}\ll\phi_1$ for arsenic,[7]

$$\mathbf{g}=\mathbf{u}_1-\mathbf{u}_2+\mathbf{u}_3-\mathbf{u}_4,$$
$$\mathbf{a}=\mathbf{u}_1-\mathbf{u}_2-\mathbf{u}_3+\mathbf{u}_4, \tag{1}$$

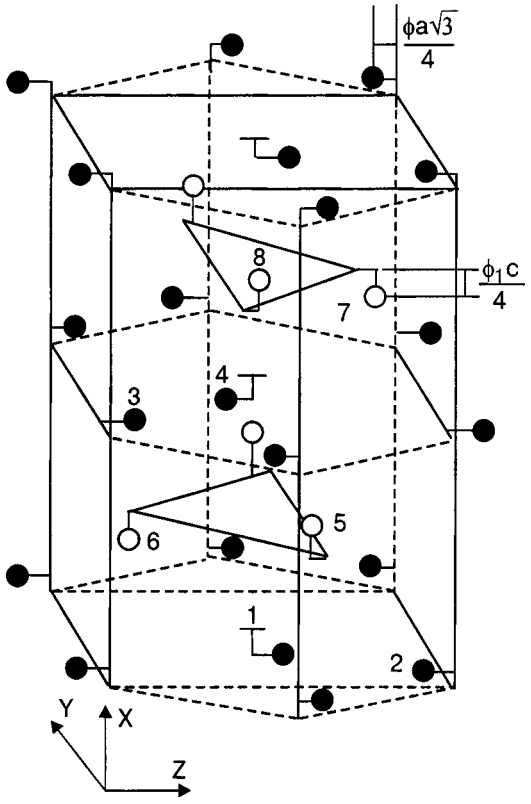

FIG. 1. Crystalline unit cell of MnAs in the rhombohedral derivation. The Mn (●) and As (○) atoms are shown displaced from their position in the initial nickel arsenide lattice; a and c correspond to the designations of the lattice parameters for the $B8_1$ structure.

 © 2005 American Institute of Physics

TABLE I. Parameters of the crystal lattice of the compounds MnAs, MnP, and NiAs.

Compound	a($B8_1$), Å	c($B8_1$), Å	a($B31$), Å	$b(B31)$, Å	$c(B31)$, Å	V_0/форм. ед., Å	r_{MT}(Mn), Å	r_{MT}(As), Å
MnAs	3.72	5.72	5.72	3.72	6.4356	33.72	1.2573	1.30866
MnP	–	–	5.917	3.173	5.260	24.689	1.1187	1.164
NiAs	3.5218	4.913	–	–	–	–	–	–

$$\mathbf{g}_1=\mathbf{u}_5-\mathbf{u}_6+\mathbf{u}_8-\mathbf{u}_7,$$
$$\mathbf{a}_1=\mathbf{u}_5-\mathbf{u}_6+\mathbf{u}_7-\mathbf{u}_8, \quad (2)$$

where $\mathbf{u}_n$ is the displacement vector of the atoms of the nth sublattice, and a and $c\|x$ are the lattice parameters for the $B8_1$ structure.

The structural phase transition $B8_1 \leftrightarrow B31$ can be described approximately by choosing ϕ and ϕ_1 as the structural order parameters.

In the region of high pressures $P>P_k=2.2$ kbar and low temperatures $T<220$ K, low-spin (LS) magnetically ordered phases (including a ferromagnetic phase)[3,4] with the $B31$ structure are observed in MnAs.

The ground state of MnP has the $B31$ lattice, and, independently of the type of magnetic order and the pressure, is always low-spin ($|m|=m_L\approx 1.3\mu_B$).[8] At $T_N\simeq 47$ K$<T<T_c\simeq 290$ K, MnP is a ferromagnet, while for $T<T_N$ the magnetic order corresponds to a helicoidal structure of the double-spiral (DS) type.[8,9] To understand the role of the interatomic distance in the formation of the magnetic state and the electronic properties of these pnyctides and to obtain information about the microscopic mechanism of the structural transformations in MnAs, it is of interest to do a theoretical study of the stability of the structural and spin states of MnAs and MnP as the volume of the unit cell is varied.

1. BACKGROUND INFORMATION AND THE CALCULATION TECHNIQUE

Since the complete first-principles calculation of manganese arsenide[5,10] was restricted to the $B8_1$ structure and we do not know of any other studies in which the possibility of a structural phase transition $B8_1 \leftrightarrow B31$ and the formation of the low-spin FM phase $B31$ has been investigated, we thought it a topical problem to calculate the energies of the spin-polarized state of the compounds MnAs and MnP as a function of the structural order parameters ϕ and ϕ_1 as the unit cell volume V_0 is varied. Such an approach makes it possible to reveal the features of the formation of the interplay between the magnetic state of the system and the type of crystal structure.

Calculations were done by the full-potential nonrelativistic FP–LMTO method,[11] which takes into account effects of asphericity of the electron density and the crystalline potential, which govern the displacive-type structural phase transition. The spin-orbit interaction for the valence states was not taken into account. The maximum values of the angular momentum in the expansions of the basis functions in spherical harmonics within the MT spheres, in the reexpansions of the MT orbitals outside the MT spheres, and also in the expansion of the crystalline potential and charge density were equal to 2, 4, and 6, respectively. The integration over the Brillouin zone was done with the use of its irreducible part: $50(B8_1)$ and $45(B31)k$ points. The local density approximation (LDA)[12] was used for the exchange-correlation energy in the calculations.

2. RESULTS OF THE CALCULATIONS

In the study of manganese arsenide the parameters of the initial $B8_1$ structure (see Table 1) were chosen close to the experimental parameters of the $B8_1$ crystal lattice at room temperature and atmospheric pressure,[13] corresponding to a volume per formula unit $V_0=33.72$ Å^3.

The influence of the unit cell volume on the structure of the density of states of nonmagnetic and ferromagnetic MnAs is shown in Figs. 2a,b. Basically, compression of the lattice leads to widening of the conduction band and to a certain change of shape of the peaks of the density of states. The appearance of structural distortions causes a qualitative change of the shape of the density of states—the formation of a set of narrow peaks (Fig. 2c). This behavior is due to lifting of the degeneracy of the branches of the energy spectrum at the new boundaries of the Brillouin zone, which arise upon a change of symmetry of the crystal lattice. Common to all the curves of the density of states is their finite value at the Fermi level in both subbands. This attests to the metallic character of the ferromagnetism in these compounds, which makes them fundamentally different from compounds with a semimetallic character of the ferromagnetism, where the density of states in one of the spin subbands at the Fermi level goes to zero.[1]

Analysis of the density of states of MnP (Figs. 2d,e,f) shows that the electronic structure of MnP behaves in relation to pressure and structural distortions in the same way as MnAs at a similar volume.

In hypothetical nonmagnetic MnAs at $V=V_0$ a calculation of the total energy of the system as a function of the two structural order parameters, $E(\phi,\phi_1)$ (Fig. 3), showed that the minimum of the total energy corresponds to the $B31$ structure with the parameters $\phi=0.16$ and $\phi_1=0.14$. From now on we shall neglect the difference between these values and investigate the stability of the crystal lattice with respect to structural distortions only along the line $\phi=\phi_1$.

In this case at atmospheric pressure and for the nonmagnetic (NM) state there is a minimum of the energy $E(\phi,\phi_1=\phi)$ for $\phi=\phi_1=0.15$, corresponding to the $B31$ structure (Fig. 4a). By the nonmagnetic state we mean a state degenerate with respect to spin (the densities of states with spin up and spin down are identical). In a self-consistent calculation of the exchange splitting, the minimum of energy corresponds to the high-spin state with the $B8_1$ structure (ϕ

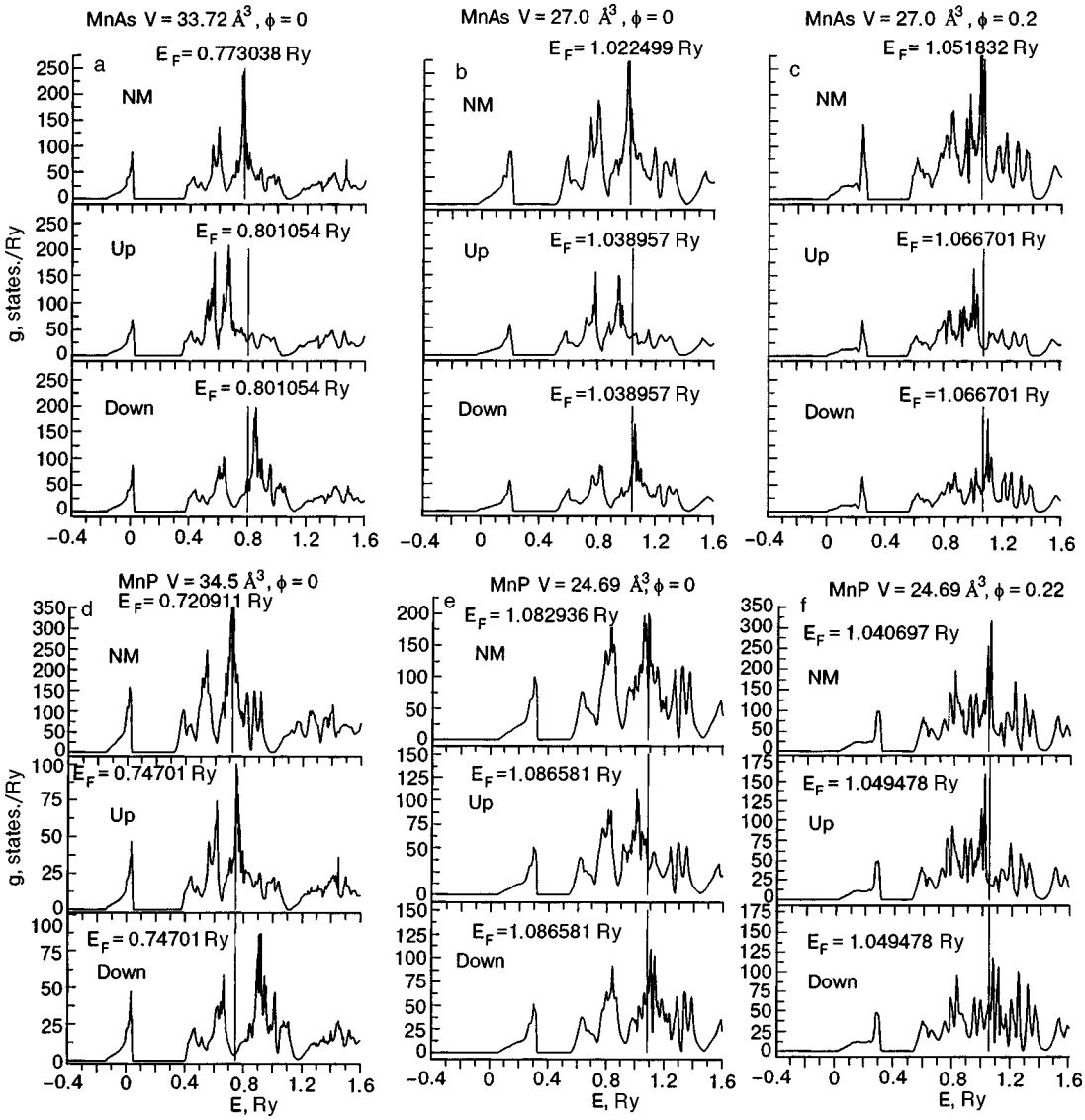

FIG. 2. Influence of the unit cell volume V and structural distortions ϕ on the density of states of MnAs and MnP. The vertical line shows the Fermi level. NM is the density of states in the nonmagnetic case.

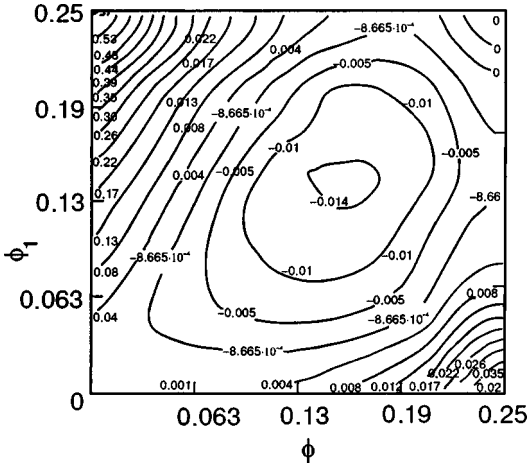

FIG. 3. Dependence of the total energy $E(\phi,\phi_1)-E(0,0)$ on the value of the structural distortions for manganese arsenide (ϕ is the displacement of Mn, and ϕ_1 is the displacement of As).

$=\phi_1=0$). Here the calculated value of the magnitude of the magnetic moment of manganese in the high-spin state corresponds to $m(\phi=0)=m_H=2.95\mu_B$.

Analogous calculations for the ''hydrostatically'' compressed MnAs ($V/V_0=0.8$; Fig. 4b) shows that the minimum of the total energy corresponds to the low-spin ($m_L \approx 1.5\mu_B$) ferromagnetic $B31$ structure. Here the formation of the LSFM is a stabilizing factor for the $B31$ lattice. It is seen in Fig. 4b that the equilibrium values of the structural order parameters in the LSFM state are larger than in the NM state.

In a study of manganese phosphide the parameters of the initial $B31$ structure (Table I) were chosen close to the experimental parameters of the $B31$ crystal lattice (at room temperature),[13] which corresponds to a unit cell volume per formula unit $V_0=24.69$ Å^3. As is seen from Table I, the unit cell volume per formula unit is smaller for MnP than for MnAs.

The influence of ''hydrostatic'' dilatation on the interplay of the magnetic and structural order parameters in MnP is shown in Fig. 5. As in Fig. 4, here the total energy of the system is given as a function of the structural order param-

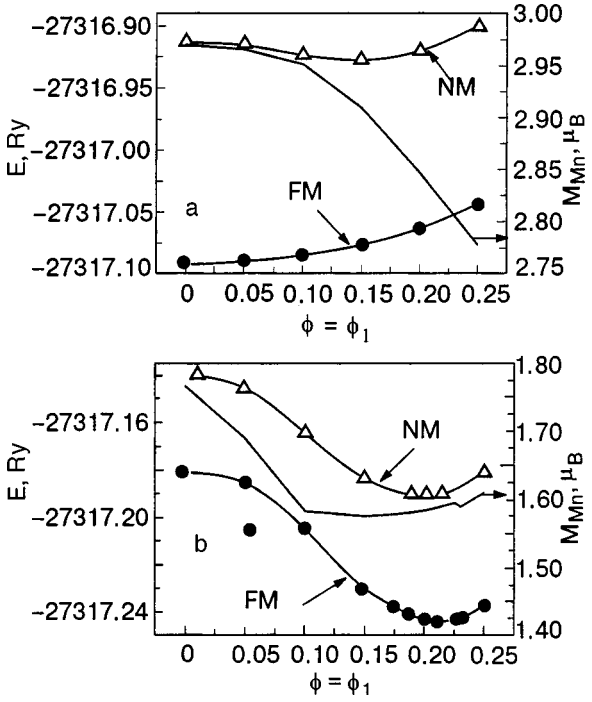

FIG. 4. Dependence of the total energy and magnetic moment of Mn on the value of the structural distortions for manganese arsenide along the line $\phi = \phi_1$; $V = V_0 = 33.72$ Å^3 (a), $V = 0.8V_0 = 27$ Å^3 (b).

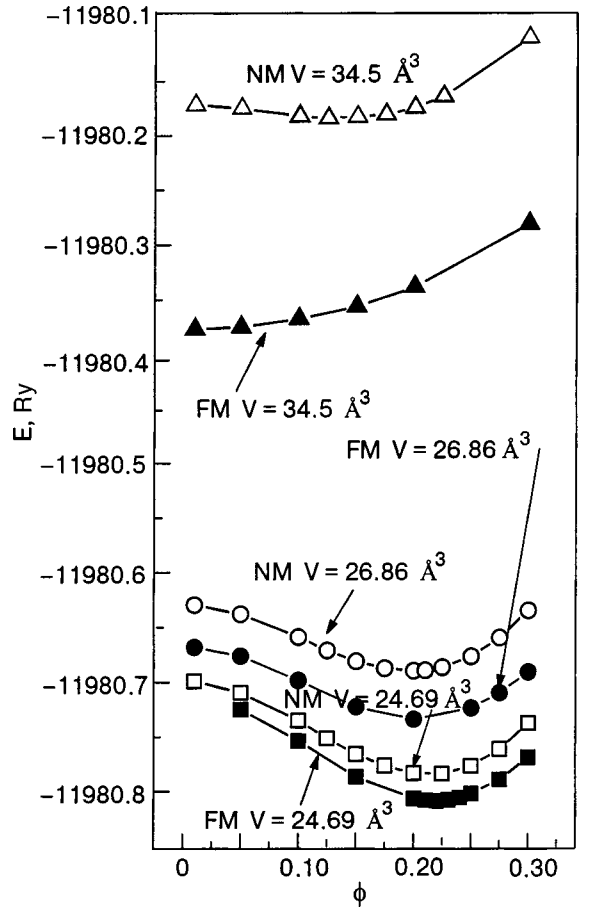

FIG. 5. Dependence of the total energy of the Mn atoms in the FM phase on the value of the structural distortions along the line $\phi = \phi_1$ for different volumes of the unit cell for manganese phosphide.

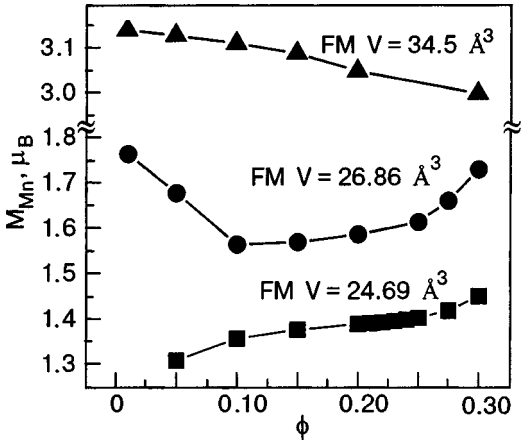

FIG. 6. Dependence of the magnetic moment of the Mn atoms in the FM phase on the value of the structural distortions along the line $\phi = \phi_1$ for different unit cell volumes for manganese phosphide.

eters for different unit cell volumes. At atmospheric pressure ($V = V_0 = 24.59$ Å^3) in MnP a distorted low-spin B31 (FM) structure is realized (Fig. 5), with a manganese magnetic moment $m = m_L = (1.3–1.4)\mu_B$ (Fig. 6). The hypothetical nonmagnetic ($m = 0$) state also has a minimum corresponding to the distorted crystal structure. However, the presence of magnetic order in the system leads to growth of the structural distortions and to a lowering of the energy of the system. Increasing the volume V leads to an increase of the magnetic moment m_L and a decrease of the structural distortions. The formation of the high-spin FM state ($m(\phi = 0) = m_H = 3.1\mu_B$) at $V = 34.5$ Å^3 suppresses the structural distortions and effects a stabilization of the distorted crystal structure $B8_1$ ($\phi = 0$). At the same time, the nonmagnetic state admits the existence of structural distortions, but as in MnAs at a similar volume, the high-spin ferromagnetic state with the distorted crystal structure $B8_1$ turns out to be energetically favorable.

The dependence of the self-consistent magnetic moment m on the value of the structural distortions ϕ at different volumes is shown in Fig. 6. These calculated curves help one to identify the spin state of the system.

3. ANALYSIS OF THE RESULTS

As a result of the numerical simulation we have obtained the following results.

1. In manganese arsenide at atmospheric pressure the high-spin FM order does not admit the existence of a stable $B31$ structure. The minimum of the total energy corresponds to the ''high-spin'' FM phase with the $B8_1$ crystal structure.

2. Decreasing the unit cell volume (this can be achieved experimentally by the application of hydrostatic pressure or by doping of the MnAs with iron, cobalt, chromium, vanadium, or phosphorus)[14] is a stabilizing factor for the structural distortions. Starting at a certain ''critical'' volume $V < V_C < V_0$ the minimum of the total energy corresponds to the low-spin FM phase with the $B31$ structure.

3. In manganese phosphide at atmospheric pressure $V_0 < V_C$ a low-spin FM phase with the $B31$ structure is realized. However, in the model manganese phosphide with a volume

$V > V_C$ the minimum of the total energy corresponds to the high-spin FM phase with the undistorted crystal structure.

Thus the change of the magnetic properties of manganese arsenide on substitution of the arsenic by phosphorus is mainly due to compression of the crystal lattice.

According to these results, the qualitative interpretation of the mechanism of magnetostructural transitions in MnAs should, in our view, be based on the idea that the leading role is played by the occupation $N(m)$ of the ''antibonding'' d states. By ''antibonding states'' we mean those that lie above the middle of the d band in the nonmagnetic case. When these states are sufficiently occupied, in excess of a certain critical value N_c, which arises in the high-spin phase (for the ''spin-up'' subband), the Mn–Mn energy bonds cause a minimum of the total energy for the nickel arsenide lattice ($\phi = \phi_1 = 0$). In the low-spin phase the degree of occupation of the antibonding states, $N(m_l) < N(m_H)$, is insufficient for stabilization of the $B8_1$ structure.

A similar point of view can be the basis for understanding the magnetostructural $B8_1$(FM)–$B31$(PM) and structural $B31$(PM)–$B8_1$(PM) transformations realized in the high-spin region of the phase diagram of manganese arsenide with increasing temperature.[3]

Since the FM–PM transition in MnAs is a pronounced first-order transition with a relatively weak change of the magnetic characteristics below the transition temperature T_C, one can assume that the increase of the amplitude of thermal fluctuations of atoms in the range $0 < T < T_C$ has a weak effect on the electronic and structural characteristics. The vanishing of the magnetization $M = \langle m_z \rangle$ at $T = T_C$ leads to a decrease of the local mean magnetic moment $\langle m^2(M) \rangle^{1/2}$ (Refs. 15 and 16). The decrease of this quantity comes about as a result of a transition of part of the electrons from the antibonding to free states. For itinerant magnetism $\langle m^2(M) \rangle^{1/2}$ is determined by the exchange splitting of the local density of states at the site and varies weakly as a function of M (Ref. 16). Therefore the high-spin state of the manganese ions and the PM phase is preserved. Nevertheless, such a significant decrease of the degree of occupation of the antibonding states, accompanied by a decrease of $\langle m^2 \rangle^{1/2}$, can lead to destabilization of the $B8_1$ initial structure and to the realization of a magnetic phase transition as a magnetostructural transformation $B8_1$(FM)–$B31$(PM). (Obviously the emptying of the antibonding states with increasing pressure occurs in full measure at an isothermal high-spin-low-spin transition, when the value of $\langle m^2(M) \rangle^{1/2}$ changes by almost a factor of two.[17] It is easy to see that in this case the main contribution to the mechanism of the structural transformation is due solely to the redistribution of the electron density over the states, since the influence of the phonon subsystem can be eliminated.)

It should be noted that in a system with localized carriers of magnetism $\langle m^2 \rangle^{1/2}$ is a constant quantity, and the destruction of the magnetic order is not due to the redistribution of the electron density and therefore cannot entail a significant change of the binding energy between atoms.

A subsequent increase of the temperature from T_C is accompanied not only by further growth of the amplitude of the thermal vibrations of the atoms but also by an increase in the occupation of the antibonding states (this is evidenced by

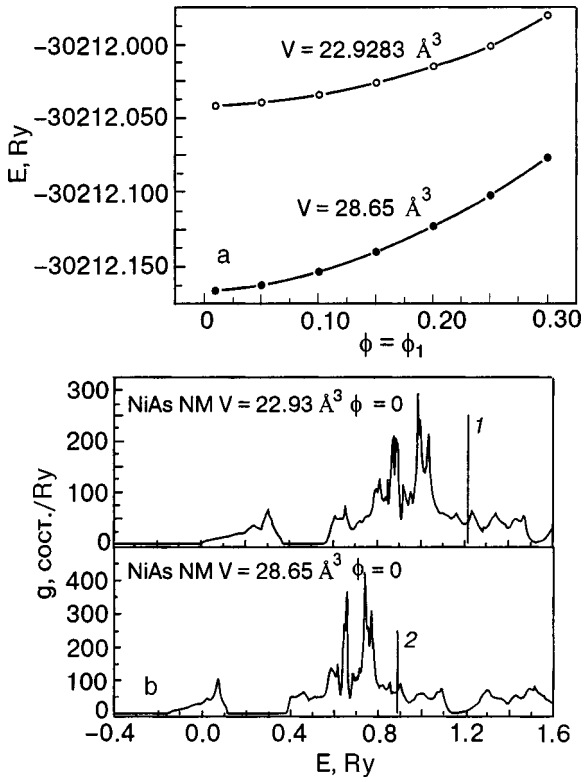

FIG. 7. Influence of the unit cell volume on the stability of the crystal structure (a) and on the density of states (b) of nonmagnetic nickel arsenide. $E_F = 1.209391$ Ry (*1*), $E_F = 0.889218$ Ry (*2*).

an increase in the quantity $\langle m^2(0) \rangle^{1/2}$; Refs. 15 and 16). Therefore at a certain temperature $T_t \ll E_F$ the preservation of the nonzero average displacements $\langle u_n \rangle$, which determine the structural order parameter parameter (2), becomes energy unfavorable.[18] As a result, the more symmetric $B8_1$ structure is restored. Such a mechanism of paramagnetic structural transition $B31$(PM)$\leftrightarrow B8_1$(PM) in MnAs can be manifested as the unfreezing of certain phonon modes.[19]

In manganese phosphide, which at atmospheric pressure is found in the low-spin states, the occupation of the antibonding states is insignificant ($N \ll N_C$), and the $B31$ structure is energetically more favorable from the start. Therefore the temperature destruction of the structural order parameter ϕ as a result of the increase of the amplitude of the thermal vibrations of atoms is improbable (T_t may exceed the melting temperature of the compound MnP).

The change of the spin state from LS to HS accompanying an increase in volume is accompanied by an increase in the degree of occupation of the antibonding states above the critical value N_c, which leads to a change of the lattice type from $B31$ to $B8_1$. On the other hand, if regardless of the presence of magnetic order the antibonding states are sufficiently occupied, then the appearance of the $B31$ structure should be ruled out in principle. In practice such a situation is realized in nickel arsenide, which has the $B8_1$ lattice. The Ni atom has eight $3d$ electrons, i.e., the antibonding states of the d band are almost completely occupied, and therefore, according to our ideas, the $B31$ crystal structure should not arise there. Calculations of the dependence of the total energy of NiAs as a function of the structural order parameters confirm this. The dependence $E(\phi = \phi_1)$ on compression to

$V=0.8V_0$ has a single minimum, $\phi=0$ (Fig. 7a).

In conclusion we note that the results correct the symmetry ideas about the role of magnetic order in the formation of the lattice structure. The symmetry description of the magnetostructural transition in manganese arsenide takes into account the coupling of the magnetic and lattice subsystems through interaction of the magnetic and structural order parameters.[20] On the basis of what we have discussed above, this interaction can indeed by distinguished on the basis of the ideas about the redistribution of the energy density over the bonding and antibonding states. However, the source of the existence of such an interaction is the change of the degree of occupation of the *d* bands. Thus at half filling of the *d* band the change of the magnetic moment and magnetization strongly alter the degree of filling of the antibonding states, which leads to a structural transition. When the *d* band is considerably more than half filled the appearance or disappearance of a magnetic moment and magnetic order does not fundamentally alter the degree of occupation of the antibonding states and therefore does not lead to a change of the type of crystal structure.

*E-mail: valkov@dpms.fti.ac.donetsk.ua

[1] B. Sanyal, L. Bergqvist, and O. Eriksson, cond-mat/0308524.
[2] G. D. Samolyuk and V. P. Antropov, J. Appl. Phys. **93**, 6882 (2003).
[3] O. Tegus, E. Bruck, W. Dagula, X. W. Li, L. Zhang, K. H. J. Buschow, and F. R. de Boer, J. Appl. Phys. **93**, 7655 (2003).
[4] N. Menyk, J. A. Kafalas, K. Dwight, and J. B. Goodenough, Phys. Rev. **177**, 177 (1969).
[5] L. M. Sandratskii, R. F. Egorov, and A. A. Berdyshev, Phys. Status Solidi B **103**, 511 (1981); E. Sasioglu, I. Galanakis, L. M. Sandratskii, and P. Bruno, cond-mat/0503713.
[6] S. Haneda, N. Kazama, Y. Yamaguchi, and H. Watanabe, J. Phys. Soc. Jpn. **42**, 1211 (1977); S. Haneda, N. Kazama, Y. Yamaguchi, and H. Watanabe, J. Phys. Soc. Jpn. **42**, 1212 (1977); S. Haneda, N. Kazama, Y. Yamaguchi, and H. Watanabe, J. Phys. Soc. Jpn. **42**, 31 (1977).
[7] V. I. Val'kov and A. V. Golovchan, Fiz. Nizk. Temp. **30**, 945 (2004) [Low Temp. Phys. **30**, 711 (2004)].
[8] E. E. Huber, Jr. and D. H. Ridgley, Phys. Rev. **135**, A 1033 (1964).
[9] J. B. Forsyth, S. J. Pichart, and P. J. Brown, Proc. Phys. Soc. **88**, 333 (1966).
[10] S. Sanvito and N. A. Hill, cond-mat/0004184.
[11] S. Yu. Savrasov and D. Yu. Savrasov, Phys. Rev. B **46**, 12181 (1992); MindLab, http://physics.njit.edu/savrasov/.
[12] S. H. Vosko, L. Wilk, and M. Nusair, Can. J. Phys. **58**, 1200 (1980).
[13] É. A. Zavadskiĭ and V. I. Val'kov, *Magnetic Phase Transitions* [in Russian], Naukova Dumka, Kiev (1980).
[14] K. Selt, A. Kjekshus, A. Andresen, and A. Zieba, J. Phys. Chem. Solids **38**, 719 (1977).
[15] T. Moriya, *Spin Fluctuations in Itinerant Electron Magnetism*, Springer-Verlag, Berlin (1985), Mir, Moscow (1988).
[16] V. I. Grebennikov, Yu. I. Prokop'ev, O. V. Sokolov, and E. A. Turov, Fiz. Met. Metalloved. **52**, 679 (1981).
[17] V. I. Val'kov, E. G. Galkina, É. A. Zavadskiĭ, V. I. Kamenev, and B. M. Todris, Dokl. Akad. Nauk Ukr. SSR, No. 12, 52 (1981).
[18] M. B. Smirnov and J. Hlinka, Fiz. Tverd. Tela (St. Petersburg) **42**, 2219 (2000) [Phys. Solid State **42**, 2288 (2000)].
[19] G. L. Hua, T. R. Welberry, and R. L. Withers, J. Phys. C **21**, 3863 (1988).
[20] I. M. Vitebskiĭ, V. I. Kamenev, and D. A. Yablonskiĭ, Fiz. Tverd. Tela (Leningrad) **23**, 215 (1981) [Sov. Phys. Solid State **23**, 121 (1981)].

Translated by Steve Torstveit

LOW-DIMENSIONAL AND DISORDERED SYSTEMS

Energy pumping in a quantum nanoelectromechanical system

T. Nord* and L.Y. Gorelik

Department of Applied Physics, Chalmers University of Technology and Göteborg University, SE-412 96 Göteborg, Sweden

(Submitted September 14, 2004)
Fiz. Nizk. Temp. **31**, 703–707 (June 2005)

The fully quantized mechanical motion of a single-level quantum dot coupled to two voltage-biased electronic leads is studied. It is found that there are two different regimes, depending on the applied voltage. If the bias voltage is below a certain threshold (which depends on the energy of the vibrational quanta) the mechanical subsystem is characterized by a low level of excitation. Above a threshold the energy accumulated in the mechanical degree of freedom increases dramatically. The distribution function for the energy level population and the current through the system in this regime is calculated. © *2005 American Institute of Physics.*
[DOI: 10.1063/1.1943539]

During the past few years, the experimental methods of physics have seen an advancing capability to manufacture smaller and smaller structures and devices. This has lead to many new interesting investigations of nanoscale physics. Examples include, for instance, observation of the Kondo effect in single-atom junctions,[1] manufacturing of single-molecular transistors,[2] and so on. There has also been a great interest in the promising field of molecular electronics.[3] One of the main features of the conducting nanoscale composite systems is its susceptibility to significant mechanical deformations. This results from the fact that on the nanoscale level the mechanical forces controlling the structure of the system are of the same order of magnitude as the capacitive electrostatic forces governed by charge distributions. This circumstance is of the utmost importance in the so called electromechanical single-electron transistor (EM-SET), which has been in focus of recent research. The EM-SET is basically a double junction system where the additional (mechanical) degree of freedom, describing the relative position of the central island, significantly influences the electronic transport. Experimental work in relation to EM-SET structures range from the macroscopic[5] to the micrometer scale[6–8] and down to the nanometer scale.[9] Various aspects of electronic transport in such systems have been investigated theoretically in a series of articles.[11–20]

In Refs. 4 and 15 it was, among other things, shown that coupling the mechanical degree of freedom of an EM-SET to the nonequilibrium bath of electrons constituted by the biased leads can lead to dynamical self-excitations of the mechanical subsystem and, as a result, bring the EM-SET to the shuttle regime of charge transfer. This phenomena is usually referred to as a shuttle instability. In these papers the grain dynamics are treated classically and the key issue is that the charge of the grain, $q(t)$, is correlated with its velocity, $\dot{x}(t)$, in such a way that the time average, $\overline{q(t)\dot{x}} \neq 0$.

Decreasing the size of the central island in the EM-SET structure to the nanoscale level results in the quantization of its mechanical motion. Charge transfer in this regime was studied theoretically in Ref. 10. However, the strong additional dissipation in the mechanical subsystem suggested in this paper keeps the mechanical subsystem in the vicinity of its ground state and prevents the the mechanical instability from developing. The aim of our paper is to investigate the behavior of the EM-SET system in the quantum regime when its interaction with the external thermodynamic environment generating additional dissipation processes can be partly ignored in such a manner that the mechanical instability becomes possible.

We will show that in this case at relatively low bias voltages, intrinsic dissipation processes bring the mechanical subsystem to the vicinity of the ground state. But if the bias voltage exceeds some threshold value, the energy of the mechanical subsystem, initially located in the vicinity of the ground state, starts to increase exponentially. We have found that intrinsic processes alone saturate this energy growth at some level of excitation. The distribution function for the energy level population and the current through the system in this regime is calculated.

We will consider a model EM-SET structure consisting of a one-level quantum dot situated between two leads (see Fig. 1). To describe such a system we use the Hamiltonian

$$H=\sum_{k,\alpha} E_{k,\alpha} a^{\dagger}_{k,\alpha} a_{k,\alpha} + \left(E_0 - D\frac{\hat{X}}{x_0} \right) c^{\dagger}c + \frac{1}{2m}\hat{P}^2 + \frac{1}{2} m\omega_0^2 \hat{X}^2 + T_{k,\alpha}(\hat{X})[a^{\dagger}_{k,\alpha} c + c^{\dagger} a_{k,\alpha}]. \quad (1)$$

The first term describes electronic states with energies $E_{k,\alpha}$; the $a^{\dagger}_{k,\alpha}$ ($a_{k,\alpha}$) are creation (annihilation) operators for these noninteracting electrons with momentum k in the left ($\alpha = L$) or right ($\alpha = R$) lead. The second term describes the influence of the electric field on the electronic level so that $c^{\dagger}$ (c) is the creation (annihilation) operator for the level electrons and E_0 is the energy level. The scalar D represents

 © 2005 American Institute of Physics

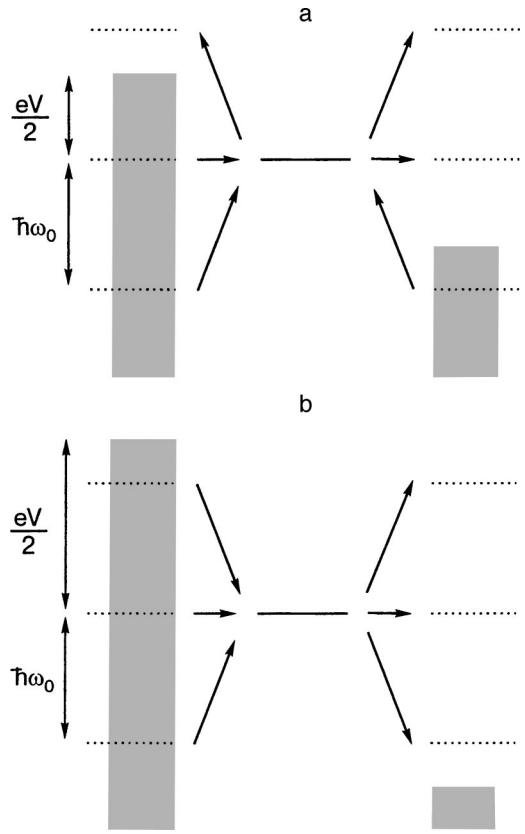

FIG. 1. Model system consisting of a one-level quantum dot placed between two leads. The level of the dot equals the chemical potential of the leads, and a bias voltage of V is applied between the leads. The center-of-mass movement of the dot is in a harmonic oscillator potential with the vibrational quanta $\hbar\omega_0$. The applied bias voltage is such that $eV/2<\hbar\omega_0$ (a). Same as (a) but with the applied bias voltage larger than $2\hbar\omega_0/e$ (b).

the strength of the Coulomb force acting on a charged grain, $\hat{X}$ is the position operator, and $x_0=\sqrt{\hbar/m\omega_0}$ is the harmonic oscillator length scale for an oscillator with mass m and angular frequency ω_0. The third and fourth terms describe the center-of-mass movement in a harmonic oscillator potential, so that $\hat{P}$ is the center-of-mass momentum operator. The last term is the tunneling interaction between the lead states and the level and $T_{k,\alpha}(\hat{X})$ is the tunneling coupling strength. We will consider the case when the tunneling coupling depends exponentially on the position operator $\hat{X}$, i.e., $T_{k,R}(\hat{X})=T_R\exp\{\hat{X}/\Lambda\}$ and $T_{k,L}(\hat{X})=T_L\exp\{-\hat{X}/\Lambda\}$, where T_R and T_L are constants and Λ is the tunneling length.

To introduce a connection to the quantized vibrational states of the oscillator we perform a unitary transformation of the Hamiltonian (1) so that $UHU^\dagger=\tilde{H}$, where $U=\exp(i\hat{P}d_0c^\dagger c/\hbar)$. In this paper we consider the situation when $\tilde{H}$ has the most symmetric form:

$$\tilde{H}=\sum_{k,\alpha}E_{k,\alpha}a^\dagger_{k,\alpha}a_{k,\alpha}+\tilde{E}_0c^\dagger c+\hbar\omega_0\left(b^\dagger b+\frac{1}{2}\right)$$
$$+T_0\sum_k\left[a^\dagger_{k,R}c\exp(x_-b+x_+b^\dagger)\right.$$
$$\left.+a^\dagger_{k,L}c\exp(-x+b-x_-b^+)\right]+\text{h.c.} \quad (2)$$

Here $b^\dagger$ (b) is a bosonic creation (annihilation) operator for the vibronic degree of freedom, and the dimensionless parameters $x_\pm=1/\sqrt{2}(x_0/\Lambda\pm d_0/x_0)$ (where $d_0=D/(x_0m\omega_0^2)$ characterize the strength of the electromechanical coupling. Furthermore, T_0 is the renormalized tunneling coupling constant, and $\tilde{E}_0=E_0-Dd_0/(2x_0+m\omega^2d_0^2/2)$ is the shifted dot level. For simplicity, but without loss of generality, we choose $\tilde{E}_0$ equal to the chemical potential of the leads at zero bias voltage.

First let us study the situation when the mechanical subsystem is characterized by a low level of excitation. We will consider the case of small electromechanical coupling. This means that the dimensionless parameters $x_\pm\ll1$ and that only elastic electronic transitions and transitions accompanied by emission or absorption of a single vibronic quantum (single-vibronic processes) are important. If the applied voltage is smaller than $2\hbar\omega_0/e$ and the temperature is equal to zero, the six allowed transitions of this type are the ones described in Fig. 1a. Here we see that only elastic tunneling processes and tunneling processes in which the vibronic degree of freedom absorbs one vibronic quantum are allowed, and, as a result, the rate equation for the distribution function of the energy level population $P(n,t)$ has the form:

$$\Gamma^{-1}\partial_tP(n,t)=P(n,t)+(x_+^2+x_-^2)(n+1)P(n+1,t)$$
$$-(1+n(x_+^2+x_-^2))P(n,t),$$

where $\Gamma=2\pi T_0^2\nu/\hbar$ and ν is the density of states in the leads.

It is straightforward to solve these equations and find that the solution exponentially fast approaches the stable solution $P(0)=1$ and $P(n)=0$ for all $n>0$. As a result, the dimensionless average extra energy excited in the vibronic subsystem,

$$E(t)=\sum_{n=0}^{\infty}nP(n,t), \quad (3)$$

goes to 0.

If the applied bias voltage is increased above the threshold value $V_c=2\hbar\omega_0/e$, we instead get the allowed transitions described in Fig. 1b, i.e., two absorption processes have changed into emission processes where the energy quantum $\hbar\omega_0$ is transferred to the vibronic degree of freedom. These transitions lead to the following equation for $P(n)$:

$$\Gamma^{-1}\partial_tP(n,t)=-(1+x_-^2+(n+1)x_+^2)P(n,t)$$
$$+x_-^2(n+1)P(n+1,t)+P(n,t)$$
$$+x_+^2nP(n-1,t). \quad (4)$$

One can find from this equation that the time evolution of the exited energy is given by the formula:

$$E(t)=\frac{x_+^2}{x_+^2-x_-^2}[\exp(\Gamma(x_+^2-x_-^2)t)-1], \quad (5)$$

i.e., energy is continuously pumped into the mechanical subsystem, which is strong evidence that the low exited regime is unstable if the bias voltage exceeds the critical value V_c.

Furthermore, it is necessary to remark here that for this case we thus have a linear increase in the energy as a function of time even when x_+^2 approaches x_-^2.

As the excitation of the vibronic subsystem increases, multi-vibronic processes become important. They give rise to an additional dissipation which saturates the energy growth induced by the single-vibronic processes. As a result, the system comes to a stationary regime which is characterized by a significant level of excitation of the vibronic subsystem. To demonstrate this we will now expand our analysis by taking into account electronic transitions accompanied by the emission or absorption of two vibronic quanta (two-vibronic processes). To describe such transitions one has to take into account second-order terms in $b^\dagger$ and b in the tunneling part of the Hamiltonian (2). As illustrated in Fig. 2, these terms will generate four processes in which two vibrational quanta are absorbed by the electron during the tunneling event. There is also a renormalization of the elastic channel coming from the inclusion of these terms. Now the equation for the distribution function of the energy level population has the form:

$$\Gamma^{-1}\partial_t P(n,t) = nP(n-1,t) - [\varepsilon n^2 + (\alpha-\varepsilon+1)n + 1]P(n,t) + \alpha(n+1)P(n+1,t) + \varepsilon(n+1)(n+2)P(n+2,t) = 0, \tag{6}$$

where we have introduced the constants $\varepsilon = (x_+^4 + x_-^4)/4x_+^2$ and $\alpha = x_-^2/x_+^2$.

To find the stationary solution of this equation we introduce the generating function:

$$\mathcal{P}(z) = \sum_{n=0}^{\infty} z^n P(n),$$

where z is a complex number inside the unit circle. Rewriting Eq. (6), we find the equation for $\mathcal{P}(z)$

$$\varepsilon(z+1)\partial_z^2\mathcal{P}(z) + (\alpha - z)\partial_z\mathcal{P}(z) - \mathcal{P}(z) = 0.$$

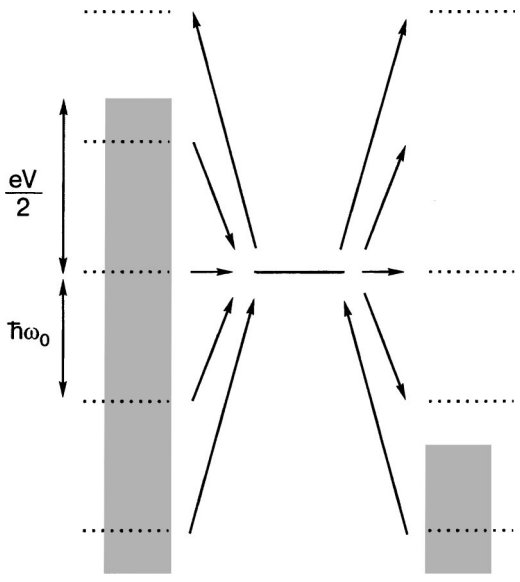

FIG. 2. Illustration of the second order case where elastic tunneling and inelastic tunneling exchanging two or less vibrational quanta are included. The level of the dot is equal to the chemical potential and the bias voltage is set so that $2\hbar\omega_0/e < V < 4\hbar\omega_0/e$.

The solution to this equation is

$$\mathcal{P}(z) = \exp\left(-\int_1^z dz' \frac{\alpha-\varepsilon-z'}{\varepsilon(z'+1)}\right) \times \left\{\int_{z_0}^z dz' \exp\left(\int_1^{z'} dz'' \frac{\alpha-\varepsilon-z''}{\varepsilon(z''+1)}\right)\frac{C_1}{\varepsilon(z'+1)}\right\},$$

where C_1 and z_0 are constants. Since the probabilities $P(n)$ are positive and normalized, the sum $\Sigma_{n=0}^{\infty}(-1)^n P(n) = \mathcal{P}(z=-1)$ converges absolutely. This is true only for $z_0 = -1$. The second constant C_1 can be determined from the normalization condition $\mathcal{P}(z=1)=1$ to be $C_1 = \varepsilon 2^\gamma / \int_{-1}^1 dx \exp((1-x)/\varepsilon)(x+1)^{\gamma-1}$, where we have introduced the constant $\gamma = (\alpha-\varepsilon+1)/\varepsilon$. Therefore the final expression for $\mathcal{P}(z)$ is

$$\mathcal{P}(z) = \frac{C_1}{\varepsilon}\frac{\exp\left(\frac{z-1}{\varepsilon}\right)}{(z+1)^\gamma}\int_{-1}^z dz' \exp\left(\frac{1-z'}{\varepsilon}\right)(z'+1)^{\gamma-1}. \tag{7}$$

We can now calculate the average energy excited in the harmonic oscillator, which is just $\partial_z\mathcal{P}(z)$ calculated at $z=1$,

$$E = \frac{1}{2\varepsilon}(2 + C_1 - \varepsilon\gamma). \tag{8}$$

One can show that $C_1(\varepsilon)$ decays exponentially as $\exp(-\text{const}/\varepsilon)$ when $\varepsilon \to 0$, so for small ε we get $E = (1-\alpha)/2\varepsilon + O(1)$.

To see how the energy pumped into the harmonic oscillator affects the charge transport we calculate the current I through the system in units of $e\Gamma$. For voltages below V_c the current is only mediated by the elastic channel and is thus $I = 1/2$.

For voltages in the range $2\hbar\omega_0/e < V < 4\hbar\omega_0/e$ the current can be calculated to leading order in ε as

$$I = \left(\frac{1}{4}(x_-^4 - x_+^4) + x_+^2 x_-^2\right)\mathcal{P}''(z=1) + (x_+ - x_-)^2 P'(z=1) + 1. \tag{9}$$

In Fig. 3 we have chosen a set of numerical values and

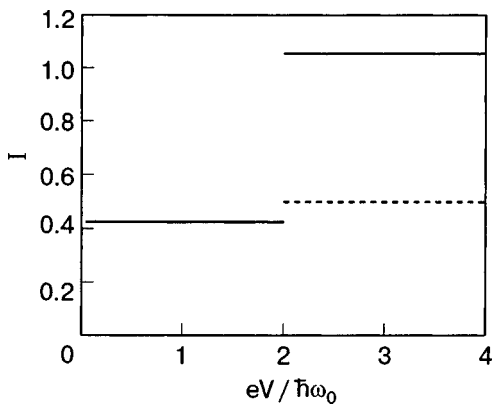

FIG. 3. The current as plotted as a function of the bias voltage (solid line). The current makes a jump as the non-elastic channel is opened at $V = 2\hbar\omega_0/e$. We have also plotted (dashed line) the current as a function of voltage for the high dissipation limit, where the harmonic oscillator goes to the ground state between tunneling events.

plotted (solid line) the calculated current as a function of the bias voltage. For comparison we have also plotted (dashed line) the current as given in the high dissipation limit, where the harmonic oscillator goes to the ground state between tunneling events. It is clear that the current is much greater in the regime characterized by a high level of excitation than the regime of low excitation.

In conclusion, we have studied the fully quantized mechanical motion of a single-level quantum coupled to two voltage-biased electronic leads. We have shown that above a certain threshold voltage the energy accumulated in the mechanical subsystem increases dramatically.

We have also shown that second-order inelastic tunneling events are enough to stabilize this pumping of energy. Finally the current through the system was calculated, and it was found that the development of the mechanical instability is accompanied by a dramatic increase in the current.

The authors would like to thank Robert Shekhter, Jari Kinaret, and Anatoli Kadigrobov, for valuable discussions related to this manuscript.

This work was supported in part by the European Commission through project FP-003673 CANEL of the IST Priority. The views expressed in this publication are those of the authors and do not necessarily reflect the official European Commission's view on the subject.

Financial support from Swedish SSF and Swedish VR is also gratefully acknowledged.

*E-mail: nord@fy.chalmers.se

[1] J. Park, A. N. Pasupathy, J. I. Goldsmith, C. Chang, Y. Yaish, J. R. Petta, M. Rinkoski, J. P. Sethna, H. D. Abruña, P. L. McEuen, and D. C. Ralrh, Nature (London) **417**, 722 (2002).
[2] W. Liang, M. P. Shores, M. Bockrath, J. R. Long, and H. Park, Nature (London) **417**, 725 (2002).
[3] C. Joachim, J. K. Gimzewski, and A. Aviram, Nature (London) **408**, 541 (2000).
[4] L. Y. Gorelik, A. Isacsson, M. V. Voinova, B. Kasemo, R. I. Shekhter, and M. Jonson, Phys. Rev. Lett. **80**, 4526 (1998).
[5] M. T. Tuominen, R. V. Krotkov, and M. L. Breuer, Phys. Rev. Lett. **83**, 3025 (1999).
[6] D. V. Scheible, A. Erbe, and R. H. Blick, New J. Phys. **4**, 86.1 (2002).
[7] A. Erbe, C. Weiss, W. Zwerger, and R. H. Blick, Phys. Rev. Lett. **87**, 096106 (2001).
[8] A. Erbe, R. H. Blick, A. Kriele, and J. P. Kotthaus, Appl. Phys. Lett. **73**, 3751 (1998).
[9] H. Park, J. Park, A. K. L. Lim, E. H. Anderson, A. P. Alivisatos, and P. L. McEuen, Nature (London) **407**, 57 (2000).
[10] K. D. McCarthy, N. Prokof'ev, and M. Tuominen, cond-mat/0205419.
[11] N. Nishiguchi, Phys. Rev. Lett. **89**, 066802 (2002).
[12] A. D. Armour and A. MacKinnon, Phys. Rev. B **66**, 035333 (2002).
[13] D. Mozyrsky and I. Martin, Phys. Rev. Lett. **89**, 018301 (2002).
[14] T. Nord, L. Y. Gorelik, R. I. Shekhter, and M. Jonson, Phys. Rev. B **65**, 165312 (2002).
[15] D. Fedorets, L. Y. Gorelik, R. I. Shekhter, and M. Jonson, Europhys. Lett. **58**, 99 (2002).
[16] N. Nishiguchi, Phys. Rev. B **65**, 035403 (2001).
[17] A. Isacsson, Phys. Rev. B **64**, 035326 (2001).
[18] D. Boese and H. Schoeller, Europhys. Lett. **54**, 668 (2001).
[19] L. Y. Gorelik, A. Isacsson, Y. M. Galperin, R. I. Shekhter, and M. Jonson, Nature (London) **411**, 454 (2001).
[20] C. Weiss and W. Zwerger, Europhys. Lett. **47**, 97 (1999).

This article was published in English in the original Russian journal. Reproduced here with stylistic changes by AIP.

Nondissipative current in a quantum wire

N. M. Guseinov and S. M. Seyid-Rzayeva*

Institute of Physics of the National Academy of Sciences of Azerbaijan, Baku, Az-1143, Azerbaijan
(Submitted October 27, 2004)
Fiz. Nizk. Temp. **31**, 708–711 (June 2005)

A theoretical study is made of the nondissipative current of a two-dimensional degenerate electron gas in a planar quantum wire with a parabolic confining potential in a magnetic field perpendicular to the plane of the wire. With the aid of a solution of the equation of the density matrix an expression for the nondissipative conductivity in a magnetic field of arbitrary strength is obtained. It is found that the conductivity has metallic properties and the quantum Hall effect should not arise in a wire with a parabolic confining potential. At high magnetic fields the expression for the nondissipative conductivity corresponds to the ''classical'' one. At low fields the conductivity is directly proportional to the first power of the magnetic field strength. © *2005 American Institute of Physics.* [DOI: 10.1063/1.1943540]

1. INTRODUCTION

There have now been many theoretical papers devoted to the study of the Hall effect in quantum wires (see, e.g., Refs. 1–10). Quantum wires (QWs) of different geometry and with different types of confining potentials have been studied. In Refs. 9 and 10 this problem is considered for electronic states in the presence of a nonuniform magnetic field. As a rule, the confining potential considered is either a quantum well[4,7] or a parabolic potential.[2,3,5,6] The energy spectrum of an electron in a QW in the presence of a transverse magnetic field has been studied in Refs. 11 and 12 for such models of the confining potential as a potential well with an infinitely high barrier and a barrier of finite height and also for a parabolic potential well. The case of a parabolic potential in the presence of an unrestricted magnetic field was considered in Refs. 9 and 10.

The magnetic moment and other thermodynamic quantities for a QW in a transverse magnetic field for a parabolic confining potential were investigated in Refs. 5 and 13. The parabolic potential model is popular because it leads to an exactly solvable problem. Furthermore, a parabolic potential can be fully implemented in a real quantum wire.

In Ref. 14 it was noted that a QW with a wide parabolic confining potential could be made with existing technology. Wires having a parabolic well over 1000 Å wide were fabricated. A feature of the parabolic potential model as opposed to the quantum well model is that the influence of the boundaries of the QW is felt by all electrons regardless of their distance from the boundaries. This is not the case for the model of a quantum well with infinite walls at high magnetic fields, when the magnetic length is much smaller than the width of the well. In such a case the influence of the boundaries is felt only by those electrons found in a narrow layer with a width of the order of ℓ near the boundaries of the wire. Thus the Hall current in a wide planar wire will be practically the same as in a two-dimensional film without confinement.

Our goal in this paper is to investigate the nondissipative current of degenerate two-dimensional electrons confined by a parabolic potential in a planar wire in the presence of a magnetic field perpendicular to the plane of the wire.

Despite the extremely simple statement of the problem, the authors do not know of any published solutions except for Ref. 15, where the Kubo formulas were used to obtain an expression for the nondissipative conductivity for a system consisting of independent parabolic wires. In the present paper the nondissipative current in the QWs in the presence of a transverse magnetic field is studied using the solution of the equation for the density matrix.[17–20]

2. NONDISSIPATIVE CURRENT

We consider a two-dimensional degenerate electron gas in a planar QW. The y axis is chosen along the length of the wire. In the direction of the x axis the motion of an electron is confined by a parabolic potential $m\omega_0^2 x^2/2$ with a frequency ω_0 (m is the effective mass of the electron). A magnetic field H is directed along the z axis, perpendicular to the plane of the wire. In an external magnetic field the electrical current causes a redistribution of charge near the edges of the wire, creating a Hall field $\mathcal{E}_x$. If the width of the wire is much greater than the de Broglie wavelength, then the electron density inside the wire (in the electric field) remains practically unchanged[21] (although the redistribution of charge far from the edges of the wire has been taken into account in some papers[1,6,7,22]). We shall assume that the fields $\mathcal{E}_x$ and $\mathcal{E}_y$ are uniform. The inclusion of the electric fields will be treated as a perturbation.

In the absence of electric fields the spectrum of the electron and its wave function are well known:

$$E_\alpha = \hbar\omega\left[n + \frac{1}{2} + \frac{1}{2}\left(\frac{\omega_0}{\omega_c}\right)^2\left(\frac{x_0}{\ell}\right)^2\right], \tag{1}$$

where $\alpha=(n,x_0)$ is a set of quantum numbers, $n=0,1,2,\ldots$, $x_0=\ell^2 k_y/\beta$ is the position of the center of gyration of the electron, k_y is the y component of the wave vector of the electron, ω_c is the cyclotron frequency, $\beta=(1$

 © 2005 American Institute of Physics

$+\omega_0^2/\omega_c^2)^{1/2}$, and $\omega=(\omega_c^2+\omega_0^2)^{1/2}$. The quantity $\overline{\ell}$ is related to the magnetic length $\ell=(h/m\omega_c)^{1/2}$ by the relation $\overline{\ell}=\ell/\beta$.

For a vector potential chosen in the form $\mathbf{A}=(0,Hx,0)$ the electron wave function is written as

$$\varphi_\alpha=\frac{1}{\sqrt{L_y}}\chi_\alpha(\xi)\exp(ik_y y), \tag{2}$$

$$\chi_\alpha(\xi)=\frac{H_n(\xi)}{\sqrt[4]{\pi}}\sqrt{\frac{e^{-\xi^2}}{2^n n!\overline{\ell}}}$$

where L_y is the length of the wire, $\xi=(x-x_0)/\overline{\ell}$, and $H_n(\xi)$ are Hermite polynomials.

The current density in the direction of the y axis is expressed in terms of the density matrix $\rho_{\alpha'\alpha}$ as follows:

$$j_y(x)=\sum_{\alpha,\alpha'} j^y_{\alpha\alpha'}\rho_{\alpha'\alpha}. \tag{3}$$

In the general case the matrix elements of the current density $\mathbf{j}_{\alpha\alpha'}$, expressed in terms of the wave functions ψ_α and $\psi_{\alpha'}$, are

$$\mathbf{j}_{\alpha\alpha'}=-\frac{i|e|h}{2m}(\psi_{\alpha'}\nabla\psi^*_\alpha-\psi^*_\alpha\nabla\psi_{\alpha'})-\frac{e^2}{mc}\mathbf{A}\psi_{\alpha'}\psi^*_\alpha. \tag{4}$$

Since it will turn out that the density matrix elements corresponding to the nondissipative current in the representation of the wave functions (2) are diagonal with respect to the quantum number x_0, it is sufficient to determine only the elements

$$j_{n,n'}=j^y_{(n,x_0)(n',x_0)}.$$

Taking Eqs. (2) and (4) into account, we obtain

$$j_{n,n'}=-\frac{|e|}{L_y}[(\beta^2-1)\omega_c x_0-\overline{\ell}\omega_c\xi]\chi_{n'}(\xi)\chi_n(\xi). \tag{5}$$

Using the method proposed by Arora in Refs. 17–19, one can obtain the following expression for the matrix elements of the density matrix in the zeroth approximation in the scattering:

$$\rho_{\alpha'\alpha}=f_0(E_\alpha)\delta_{\alpha'\alpha}+|e|\mathcal{E}_x\overline{\ell}\langle\alpha'|\xi|\alpha\rangle\frac{f_0(E_{\alpha'})-f_0(E_\alpha)}{E_{\alpha'}-E_\alpha}, \tag{6}$$

where $f_0(E_\alpha)=1/\exp(E_\alpha-\eta)/T+1$ is the equilibrium Fermi distribution function, and η is the chemical potential corresponding to the equilibrium state for $\mathcal{E}_x,\mathcal{E}_y=0$.

For the matrix elements $\langle\alpha'|\xi|\alpha\rangle$ we have the following relation:

$$\langle\alpha'|\xi|\alpha\rangle=\left[\left(\frac{n}{2}\right)^{1/2}\delta_{n-1;n'}+\left(\frac{n+1}{2}\right)^{1/2}\delta_{n+1;n'}\right]\delta_{x_0,x'_0}.$$

Substituting (5) and (6) into (3), we obtain the nondissipative current density

$$j_y(x)=-\frac{e^2\overline{\ell}}{L_y}\sum_{n,n',x_0}[(\beta^2-1)\omega_c x_0-\overline{\ell}\omega_c\xi]\times\left[\left(\frac{n}{2}\right)^{1/2}\delta_{n-1,n'}+\left(\frac{n+1}{2}\right)^{1/2}\delta_{n+1,n'}\right]\times\chi_{n'}(\xi)\chi_n(\xi)\frac{f_0(E_{\alpha'})-f_0(E_\alpha)}{E_{\alpha'}-E_\alpha}\mathcal{E}_x.$$

To obtain an expression for the total nondissipative current J_y we integrate the above expression over x and sum it over n'. Taking into consideration that $E_{n+1,x_0}-E_{n,x_0}=\hbar\omega$, we obtain

$$J_y=-\frac{e^2\mathcal{E}_x}{m\omega_c L_y\beta^2}\sum_{n,x_0}(n+1)[f_0(E_{n+1,x_0})-f_0(E_{n,x_0})]. \tag{7}$$

Let n_0 be the number of filled subbands. In the case of high degeneracy $f_0(E_{n_0+1,x_0})=0$. Taking this into account, we obtain

$$\sum_{n,x_0}(n+1)[f_0(E_{n+1,x_0})-f_0(E_{n,x_0})]=-\sum_{n,x_0}f_0(E_{n,x_0})=-N,$$

where N is the total number of electrons. It follows from (7) that the expression for the nondissipative current takes the form

$$J_y=-\frac{e^2N\mathcal{E}_x}{m\omega_c L_y d\beta^2}.$$

Taking this last expression into account, we obtain the following expression for the element σ_{yx} of the conductivity tensor

$$\sigma_{yx}=-\frac{e^2}{h}\frac{1}{1+\frac{\omega_0^2}{\omega_c^2}}\nu, \tag{8}$$

where the electron filling factor $\nu=2\pi n_e\ell^2$, and the density of the two-dimensional electron gas $n_e=N/L_y d$. Using the known symmetry properties $\sigma_{xy}=-\sigma_{yx}$, we obtain an expression that agrees with that given in Ref. 15.

3. CONCLUSION

Using the usual definition of ω_0 in the parabolic confining potential model, we define the Fermi level η as

$$\eta=\frac{m\omega_0^2(d/2)^2}{2}.$$

Using this definition, we obtain from Eq. (1)

$$\frac{E_\alpha}{\hbar\omega}=n+\frac{1}{2}+\beta^2\frac{\eta}{\hbar\omega}\left(\frac{x_0}{d/2}\right)^2. \tag{9}$$

Since $\beta^2>1$, it follows from Eq. (9) that the Fermi level η always intersects some subband at the points $|x_0|<d/2$. This means that free states always exist above the Fermi level, and consequently the conductivity has a metallic property. Thus in this case the quantum Hall effect should not arise in a QW with a parabolic confining potential.

The value of the magnetic field depends either on the value of the parameter ω_c/ω_0 or on d/ℓ. The characteristic magnetic field H_c is defined by the relation $d \simeq \ell$. Fields $H < H_c$ are considered weak. For $d = 100$ Å one can estimate that $H_c \cong 10$ T. It follows from Eq. (8) that in a weak magnetic field $\sigma_{yx} \sim H$. At high magnetic fields $\omega_0/\omega_c \ll 1$, and the conductivity (8) corresponds to the ''classical'' one.

In closing, the authors thank Prof. F. M. Gashimzade for fruitful discussions of this work.

*E-mail: S-Nisa@rambler.ru

[1] W. X. Lai and S. Das Sarma, Phys. Rev. B **33**, 8874 (1986).
[2] X. C. Xie and S. Das Sarma, Solid State Commun. **68**, 697 (1988).
[3] G. Kirczonov, Phys. Rev. B **38**, 10958 (1988).
[4] H. Akera and T. Ando, Phys. Rev. B **39**, 5508 (1989).
[5] Y. Meir, O. Entin-Wohlman, and Y. Gefen, Phys. Rev. B **42**, 8351 (1990).
[6] Q. Li and D. J. Thouless, Phys. Rev. Lett. **65**, 767 (1990).
[7] D. P. Chu and P. N. Butcher, J. Phys.: Condens. Matter **5**, 397 (1993).
[8] A. Yu. Alekseev, V. V. Cheianov, and J. Frohlich, Phys. Rev. B **54**, 17320 (1996).
[9] Y. Takagaki and K. Ploog, Phys. Rev. B **53**, 3885 (1996).
[10] S. M. Badalyan and F. M. Peeters, Phys. Rev. B **64**, 155303 (2001).
[11] W. Tan, J. C. Jukson, and G. P. Srivastova, Semicond. Sci. Technol. **9**, 1305 (1994).
[12] A. Lorenzoni and L. G. Andreani, Semicond. Sci. Technol. **14**, 1169 (1999).
[13] Y. Ishikawa and H. Fukuyama, J. Phys. Soc. Jpn. **68**, 2405 (1999).
[14] E. G. Cwinn, R. M. Westervelt, P. F. Hopkins, and A. J. Rimberg, Phys. Rev. B **39**, 6260 (1989).
[15] U. Wulf, J. Kucera, and A. H. MacDonald, Phys. Rev. B **47**, 1675 (1993).
[16] D. S. Fisher and P. A. Lee, Phys. Rev. B **23**, 6851 (1981).
[17] V. K. Arora and R. L. Peterson, Phys. Rev. B **12**, 2285 (1975).
[18] V. K. Arora, Phys. Status Solidi B **105**, 707 (1981).
[19] V. K. Arora and F. G. Awad, Phys. Rev. B **23**, 5570 (1981).
[20] E. N. Adams and T. D. Halstein, J. Phys. Chem. Solids **10**, 254 (1959).
[21] A. G. Aronov and G. E. Pikus, Fiz. Tverd. Tela (Leningrad) **6**, 506 (1964) [Sov. Phys. Solid State **6**, 399 (1964)].
[22] A. H. Macdonald, T. M. Rice, and W. F. Brinkman, Phys. Rev. B **28**, 3648 (1983).

Translated by Steve Torstveit

LOW-TEMPERATURE PHYSICS OF PLASTICITY AND STRENGTH

Low-temperature anomalies of the physico-mechanical characteristics of pseudoamorphous titanium nickelide

A. S. Bakai, V. V. Brik, V. M. Kuzmenko, M. V. Lazareva,* I. M. Neklyudov, Ya. D. Starodubov, T. P. Chernyaeva, and V. M. Gorbatenko

National Research Center "Kharkov Physico-Technical Institute," ul. Akademicheskaya 1, Kharkov 61108, Ukraine

(Submitted September 22, 2004; revised November 29, 2004)
Fiz. Nizk. Temp. **31**, 712–717 (June 2005)

A study is made of the structure, mechanical properties, and electrical resistance of crystalline and pseudoamorphous (obtained by rolling at 300 K by 50 and 90%) titanium nickelide in both the initial state and after annealing to different temperatures in the interval 513–893 K. It is found that the resistivity of polyamorphous Ti–Ni exceeds 200 $\mu\Omega\cdot$cm, falls off monotonically with increasing annealing temperature, and has a minimum in the low-temperature region 4.2–50 K ($T_{\min}=17-19$ K). In the temperature interval 4.2–20 K a nonmonotonic temperature dependence of the ultimate strength of polyamorphous Ti–Ni is observed which increases with increasing degree of deformation by rolling of the investigated material. The results are analyzed. It is conjectured that the observed anomaly of the temperature dependences of the ultimate strength and resistivity are due to low-temperature polyamorphism of the pseudoamorphous Ti-Ni in the temperature interval 10–20 K. © *2005 American Institute of Physics.* [DOI: 10.1063/1.1943541]

INTRODUCTION

Titanium nickelide [a titanium-nickel alloy of an equiatomic composition (Ti–Ni)] possess a shape memory effect and is a reference material for the study and practical use of this effect.[1,2] In recent years, along with intensive investigation of the shape memory effect, superelasticity, and superplasticity of this material in the crystalline state, papers reporting the preparation of Ti–Ni in amorphous and amorphous-crystalline states have appeared.[3–10] It has also been established that Ti–Ni is amorphized by irradiation.[3] Amorphization is also achieved by strong plastic deformation.[4,5] It is of significant interest to study the properties of Ti–Ni in an amorphous state in which the short-range order does not extend more than 3 nm.

The goal of the present study was to investigate the structure, electrical, and mechanical properties of deformed titanium nickelide in the temperature interval 4.2–77 K and the change of the structure after annealing in the range 513–873 K.

MATERIAL AND EXPERIMENTAL TECHNIQUES

Studies were carried out on samples in the form of foils that had undergone annealing at 723 for 1 hour (c-Ti–Ni). Then these foils were rolled at room temperature by 50 and 90% (d^{50}-Ti–Ni and d^{90}-Ti–Ni, respectively).

The samples for electron microscope and electron diffraction studies were prepared by jet polishing. Structural studies were done on a JEOL JEM-100CX electron microscope at room temperature both in bright-field and dark-field images in reflections of the most intense diffraction ring.

In the electron diffraction studies two methods we used to obtain the diffraction patterns of the samples: microdiffraction from a region 1 μm in diameter, and micro-beam diffraction, which permitted obtaining the diffraction pattern from a region 0.1 μm in diameter. Thus a general idea of the structure of titanium nickelide in the annealed and deformed states was obtained, and a detailed study of individual local regions was done.

The resistivity measurements were made by the four-probe method in the temperature range 4.2–77 K and at a temperature above 293 K.

The temperature dependence of the ultimate strength was investigated under tensile testing at a rate of $\dot{\varepsilon}\cong 10^{-3}$ s^{-1} at temperatures in the range 4.2–77 K on the apparatus described in Ref. 11. The mechanical testing was done on slab-like samples 0.2 mm thick for the initial state and 0.1 and 0.02 mm for the 50% and 90% deformed samples, respectively. The width of the samples was 1.5–2 mm, and the length of the working part was 15 mm.

STRUCTURE OF TITANIUM NICKELIDE IN THE ANNEALED AND DEFORMED STATES

Titanium nickelide, which in the annealed state has an intensively twinned monoclinic martensitic structure (Fig. 1), when deformed at room temperature by 50–90% acquires a two-phase structure (in respect to both the level of dispersedness and the phase state; Fig. 2).

The microstructure of Ti–Ni in the initial (c-Ti–Ni state and the microdiffraction pattern corresponding to it are presented in Fig. 1. The microdiffraction pattern from regions 1

 © 2005 American Institute of Physics

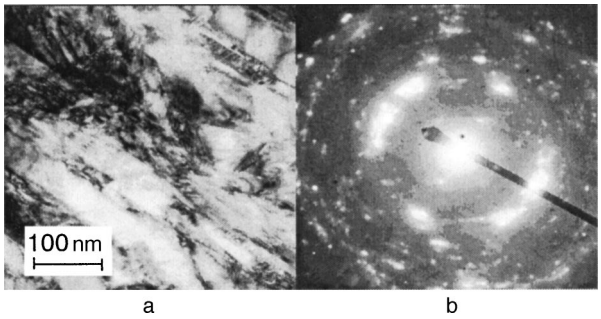

FIG. 1. Microstructure of Ti–Ni in the initial (c-Ti–Ni) state (a) and the corresponding microdiffraction pattern (b).

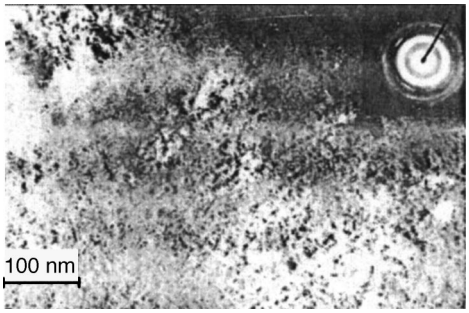

FIG. 3. Microstructure of deformed titanium nickelide after annealing at 595 K and cooling to room temperature.

μm in diameter consist of individual reflections and discontinuous arcs.

The deformed material has a completely different structure (Fig. 2): on the bright-field images of the structure one can see a continuous gray background without regular and distinct interfaces (the amorphous component d-Ti–Ni), against which microcrystallites 3–15 nm in size (occasionally as large as 25 nm) appear in the form of darker or lighter segregations, and the microdiffraction patterns exhibit rather bright diffuse rings of the microcrystalline component.

According to its state, d-Ti–Ni can be classed as a conglomerate structure in which microcrystallites of size 3–14 nm are immersed in a medium with a less perfect amorphous matrix consisting of structural elements not greater than 3 nm in size.

To determine the structural state of d^{90}-Ti–Ni (the superscript here denotes the degree of deformation) the structure of this material was investigated after each step of its restoration by isochronous annealing at temperatures of 513, 573, 593, 637, 723, and 873 K at a rate of 1–3 K/min and cooling to room temperature at the same rate. These studies showed that heating to 513 K produced no substantial change of the structure except for an inverse martensitic transformation in the regions of the monoclinic martensite. At $T \sim 573$ K the crystallization process apparently begins—zones with different degree of disperseness appear in the structure (Fig. 3).

It is seen in the figure that at such an annealing temperature the intense formation of a single-crystal austenitic structure occurs, with a crystallite size of 5–30 nm. The main structural component is the high-temperature phase (bcc). When the temperature is increased to 673 K the degree of homogeneity increases, and crystallization extends over almost the entire volume of the material. After annealing at 637 and 673 K the grain size is 30 and 51 nm, respectively, the rhombohedral phase has become the main component, and at a temperature of 723 K the process of crystallization of the d^{90}-Ti–Ni is practically complete. When the annealing temperature is increased further to 873 K the grain size reaches ~ 70 nm, and the main phase is monoclinic martensite.

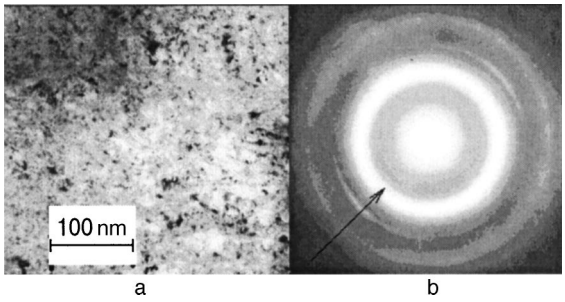

FIG. 2. Microstructure (a) and microdiffraction pattern (b) of titanium nickelide deformed by 90% (the arrow indicates the halo from the amorphous component).

ELECTRICAL RESISTANCE

Measurements of the resistance R of d-Ti–Ni were made in two temperature intervals: 298–673 K (Fig. 4), and 4.2–50 K (Fig. 5). Measurements at high temperatures permit observation of the characteristic temperature dependence of the resistance for disordered alloys and also to establish the boundaries of the temperature interval in which the crystal structure of Ti–Ni is restored on annealing. As to the low-temperature behavior of the resistance, it is sensitive to structural features and structural rearrangements, when the scattering length on phonons exceeds the scattering length on structural inhomogeneities.

These studies have shown that as in amorphous metals obtained by the methods of quenching of melts and condensation of metal vapors, the d^{90}-Ti–Ni samples have a high resistivity ρ ($>200\mu\Omega\cdot$cm).

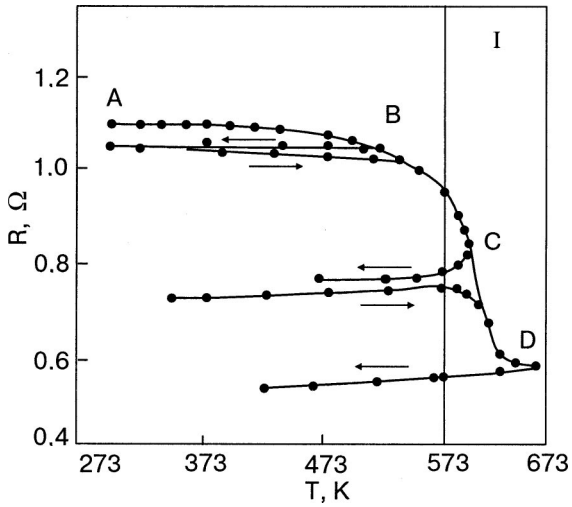

FIG. 4. Temperature dependence of the electrical resistance of 90%-deformed titanium nickelide; I is the crystallization region.

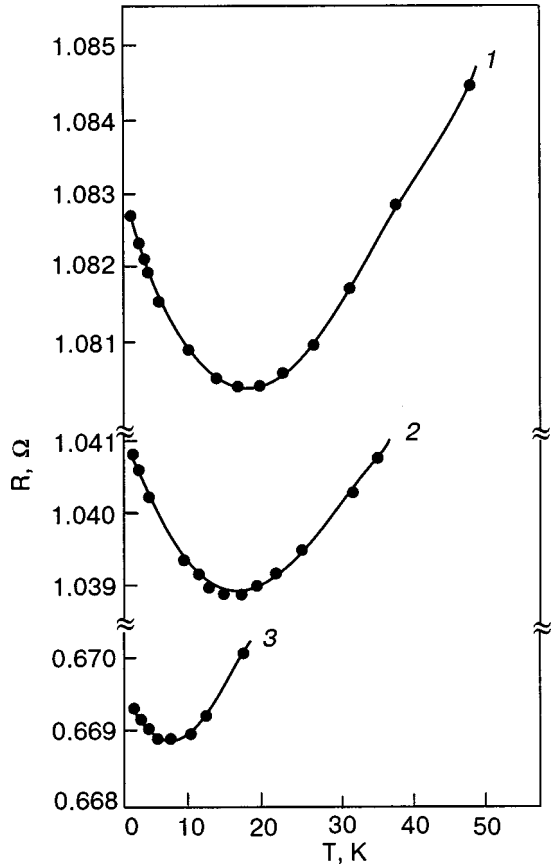

FIG. 5. Temperature dependence of the resistance of d^{90}-Ti–Ni in the region 4.2–50 K; curves *1*, *2*, and *3* correspond to resistance measurements, where the heating was stopped (Fig. 4, points *B*, *C*, and *D*).

Figure 4 shows the temperature dependence of the resistance of d^{90}-Ti–Ni in the temperature interval 298–673 K on heating at a rate of $\approx$3 K/min. The resistance decreases slowly with increasing temperature from 298 to 516 K on account of relaxation processes in the amorphized matrix of the sample. An abrupt change of the slope of the temperature dependence $R(T)$ at $T\approx 573$ K attests to a process of crystallization of the amorphous component of the sample.

The temperature interval of crystallization is $\approx$573–673 K. At $T>673$ K the resistance begins to grow, i.e., the heating curve emerges with a positive temperature coefficient of the resistance (TCR). The letters on the $R(T)$ curve in Fig. 4 indicate the places where the heating was stopped and the measurement (shown in Fig. 5) of the resistance of the d^{90}-Ti–Ni samples was made in the low-temperature region.

As is seen in Fig. 5, for the deformed samples (curve *1*) a rather narrow peak and a deep minimum of the resistance is observed in the 17–19 K region. On a subsequent raising of the annealing temperature to 513 K (curve *2*) the position of the minimum remains practically unchanged; when the temperature of the preliminary annealing is raised to 593 K the depth of the resistance minimum decreases significantly, and it is is shifted to lower temperatures by 6–8 K (curve *3*). On a subsequent increase of the temperature to 693 K the minimum on the $R(T)$ curve vanishes completely. This suggest that this mechanism owes its existence to the amorphous component *d*-Ti–Ni.

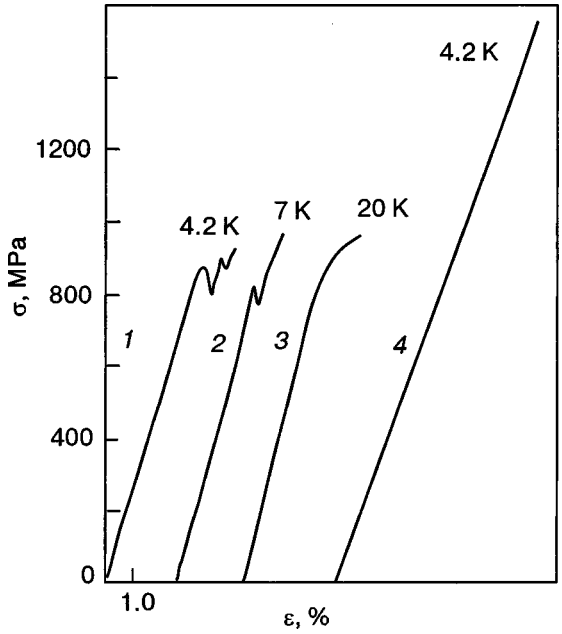

FIG. 6. Deformation curves of Ti–Ni samples in the initial state (*1*, *2*, *3*) and after a 50% deformation by rolling at 300 K (*4*).

MECHANICAL PROPERTIES OF TITANIUM NICKELIDE IN THE INTERVAL RANGE 4.2–77 K

Figure 6 shows the deformation curves of the samples in the initial state (*c*-Ti–Ni), and after deformation by rolling the strength increases noticeably but plasticity is absent and the hardening coefficient is decreased somewhat.

Figure 7 shows the temperature dependence of the ultimate strength of the samples in the initial state and after rolling by 50 and 90%. It is seen that the ultimate strength at 4.2 K of the deformed material is almost twice its initial value. The initial material has a maximum in the region 12–19 K, while the deformed samples have a minimum in this same interval, the depth of the minimum increasing with increasing degree of reduction by rolling, equalling 250 and 800 MPa for the samples rolled by 50 and 90%, respectively.

The character of the destruction of the samples is also different: the samples rolled by 50% at 4.2 K fracture at an angle of $\approx$45°, while after rolling by 90% the fracture of the samples occurs simultaneously at two places with the forma-

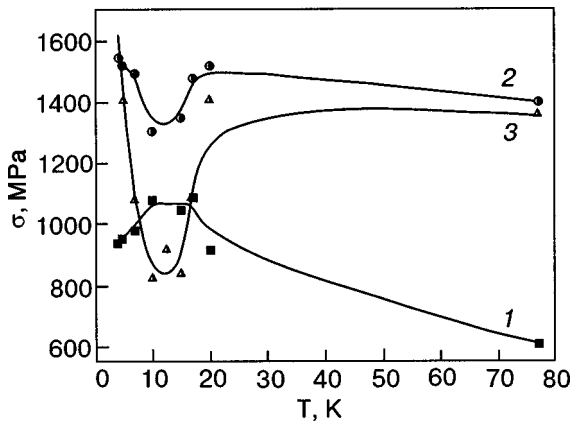

FIG. 7. Temperature dependence of the ultimate strength for the initial Ti–Ni sample (*1*) and for samples rolled by 50% (*2*) and 90% (*3*).

tion of a ''corrugation'' on the edges of the crack; this may be due to the occurrence of a localized plastic deformation in microvolumes of the samples. We call attention to the fact that in the temperature interval 10–20 K the temperature dependence of the resistance also exhibits a minimum of the resistance for the deformed samples.

DISCUSSION OF THE RESULTS

As a result of these studies it has been established that the behavior of the resistance of highly deformed d-Ti–Ni on annealing is similar in character to the change of the resistance for amorphous materials obtained by the methods of quenching of the melt and condensation on a cold substrate.[12,13] On heating at a rate of 3 K/min (Fig. 4) in the temperature interval 298–516 K the resistance slowly decreases. This temperature interval corresponds to the stage of irreversible structural relaxation, which is confirmed by electron microscope studies mentioned above and by return measurements of $R(T)$. Further increase of the annealing temperature to 573 K leads to a sharp drop of the resistance—crystallization of the material occurs (see Fig. 3). An austenitic structure is formed, with a crystallite size of up to 30 nm. The high-temperature bcc phase becomes the main structural component. When the annealing temperature is increased to 673 K the degree of homogeneity increases; the crystallization extends practically through the whole volume of the material. After annealing at 637 and 673 K the grain size is 30 and 51 nm, respectively, and the rhombohedral phase is the main component, and at a temperature of 723 K the crystallization process for d^{90}-Ti–Ni is complete. Upon further increase of the annealing temperature (to 873 K) the grain size is $\sim$70 nm and the main phase is monoclinic martensite.

The most remarkable feature of the low-temperature behavior of $R(T)$ for d^{90}-Ti–Ni is the presence of a narrow (with a half-width less than 10 K) minimum at $T \approx 17$ K. Here the resistivity has a high value $\sim 200\ \mu\Omega \cdot$cm, which corresponds to the Ioffe–Regel limit, according to which the scattering length is comparable to the interatomic distance (see Refs. 12 and 13).

The resistance minimum in Fig. 5 can have several explanations. A mixed amorphous-crystalline state of d^{90}-Ti–Ni and its annealed (at temperatures below the temperature of complete crystallization) modifications are the most probable cause of the appearance of the minimum on the $R(T)$ curve. In this case the minimum of the temperature coefficient of resistance is the result of a competition between the negative TCR of the amorphous phase[14] and the positive TCR of the crystalline phase. Therefore with decreasing concentration of the amorphous component during annealing of the samples the temperature and depth of the minimum decrease, and after completion of the crystallization the minimum vanishes. The negative TCR of the the high-resistance amorphous alloys is usually attributed to quantum corrections to the Boltzmann conductivity, taking into account the effects of weak localization and electron-electron interaction.[15]

One can also assume that for $T \leqslant 20$ K a process of polyamorphous transition begins in the amorphized component of titanium nickelide, with the appearance of a more resistive phase, which leads to an increase in the resistance of the sample. The structural rearrangement in deformed Ti-Ni is suggested by the substantial softening of the samples in the temperature interval of the observed resistance minimum. The proposed restructuring should occur in the amorphous component, since the behavior described is absent in the annealed titanium nickelide. Qualitatively the picture resembles the phenomenon of low-temperature deformation polymorphism, which has been observed on a number of deformed single-component metals,[16] with the difference, however, that in the present case this phenomenon is observed in an amorphized alloy.

We note that low-temperature polyamorphism has recently been observed in oriented glasses based on C_{60} fullerite doped with various gases.[17] The nature of the polyamorphism is discussed in that same paper. If our assumption of low-temperature polyamorphism of the amorphized alloy Ti–Ni is confirmed by further structural and thermodynamic studies, it will be possible to conclude that this phenomenon is inherent to many disordered systems.

*E-mail: mlazarev@kipt.kharkov.ua

[1] I. I. Kornilov, D. K. Belousov, and E. V. Kachur, *Titanium Nickelide and Other Shape-Memory Alloys* [in Russian], Nauka, Moscow (1977).
[2] I. I. Sasovskaya and V. G. Pushin, Fiz. Met. Metalloved. **64**, 896 (1987).
[3] V. L. Drimhall, H. E. Rissinger, and A. R. Pelton, Radiat. Eff. **90**, 241 (1985).
[4] V. B. Fedorov, V. G. Kurdyumov, D. K. Khakimova *et al.*, Dokl. Akad. Nauk SSSR **269**, 885 (1983).
[5] E. V. Tat'yanin, V. G. Kurdyumov, and V. B. Fedorov, Fiz. Met. Metalloved. **62**, 133 (1986).
[6] J. L. Brimhall, Nucl. Instrum. Methods Phys. Res. B **7/8**, Part 1, 26 (1985).
[7] R. Saito and M. Jwaki, Nucl. Instrum. Methods Phys. Res. B **7/8**, Part 2, 625 (1985).
[8] B. M. Clements, Less Common. Metals **140** (1988).
[9] R. B. Schwarz, R. R. Petrich, and C. K. Saw, J. Non-Cryst. Solids **76**, 281 (1985).
[10] D. E. Polk, A. Celka, and B. C. Giessen, Acta Metall. **26**, 1097 (1978).
[11] I. A. Gindin, S. F. Kravchenko, Ya. D. Starodubov, and G. G. Chechel'nitskiĭ, Prib. Tekh. Éksp., No. 2, 240 (1967).
[12] P. Kout and L. Maizel, in *Glassy Metals*, H. J. Güntherodt and H. Beck (eds.), Springer-Verlag, Berlin (1981), Mir, Moscow (1983).
[13] S. R. Elliot, *Physics of Amorphous Materials*, Longmal, London-New York (1984).
[14] S. Kanemaki, M. Suzuki, Y. Yamada, and U. Mizutani, J. Phys. F: Met. Phys. **18**, 105 (1988).
[15] M. A. Howson and B. L. Gallagher, Phys. Rep. **170**, 266 (1988).
[16] I. A. Gindin, B. G. Lazarev, Ya. D. Starodubov, and V. I. Khotkevich, *Some Problems of the Strength of Solids* [in Russian], Izd-vo Akad. Nauk SSSR, Moscow-Leningrad (1959).
[17] F. N. Aleksandrovskii, A. V. Dolbin, V. B. Esel'son, V. G. Gavrilko, V. G. Manzhelii, B. G. Udovidchenko, A. S. Bakai, G. E. Gadd, S. Moricca, and B. Sundqvist, Fiz. Nizk. Temp. **29**, 432 (2004) [Low Temp. Phys. **29**, 324 (2004)].

Translated by Steve Torstveit

PERSONALIA

Viktor Nikitich Grigor'ev (on his 75th birthday)

June 3, 2005 is the 75th birthday of the experimental physicist Prof. Viktor Nikitich Grigor'ev, DSc Phys/Math. The scientific activity of Prof. Grigor'ev is devoted to basic research in the field of quantum liquids and quantum crystals. He played a part in the discovery of quantum diffusion in crystals, which has become widely known and acknowledged throughout the world. His pioneering research on the kinetics of liquid and solid helium has been awarded the State Prize of Ukraine in Science and Engineering. In recent years he has obtained new fundamental results on the kinetics of nucleation and phase separation in quantum mixed crystals.

Grigor'ev's scientific achievements are reflected in his numerous papers and conference reports and in the four monographs and handbooks he has co-authored. His 75th birthday finds him in the flower of his creative force and scientific activity. He holds a high reputation in the scientific community, and his work is often cited. A talented scientist and admirable person, Prof. Grigor'ev collaborates actively with young colleagues and passes on his experience to them; he has served as an advisor to many Candidates of Science.

We heartily congratulate Viktor Nikitich on his birthday and wish him good health, success in his scientific endeavors, and inexhaustible creative energy.

Editorial Board

 © 2005 American Institute of Physics